ABSTRACT

Title of Dissertation:	DEVELOPMENT OF FUNCTIONAL METAL OXIDE THIN FILMS VIA HIGH-THROUGHPUT PULSED LASER DEPOSITION FOR ADVANCED ENERGY APPLICATIONS
	Yangang Liang, Doctor of Philosophy 2018
Dissertation directed by:	Professor Ichiro Takeuchi, Department of Materials Science and Engineering

High-throughput methodologies are effective for rapid exploration of new materials with enhanced physical properties. In this thesis, we combine high-throughput pulsed laser deposition (HT-PLD) synthesis with rapid characterization techniques (X-Ray Diffraction, Atomic Force Microscopy, Electrochemical Impedance Spectroscopy, etc.) to quickly optimize metal oxide materials for energy conversion devices.

The solid oxide fuel cell (SOFC) is one of the most promising energy conversion technologies. Despite years of concerted efforts by the research community, widespread commercialization of SOFCs is hindered by their high operating temperature requirements (>800 °C). Currently, there are limitations on the performance of electrolyte and cathode materials, which prevent a significant reduction

in this operating temperature. To this end, we developed all-thin-film SOFC structures to probe fundamental transport properties via out-of-plane measurements in epitaxial electrolyte films with idealized interfaces. A highly conducting and thermally stable bottom electrode is combined with a library of top microelectrodes ($30\mu m \leq d \leq 500\mu m$), in a Cox and Strack-like geometry, which enables a direct and high-spatial-resolution investigation of the intrinsic transport properties of the model electrolyte $Sm_{0.2}Ce_{0.8}O_{2-\delta}$ (SDC20). This work demonstrated the utility of prototypical out-of-plane all-thin-film heteroepitaxial electrochemical devices as a model platform which can be extended to high-throughput investigations.

We have used the high-throughput thin film formalism to develop a fundamental understanding of surface oxygen reduction reaction (ORR) mechanisms in mixed-conducting cathode materials by fabricating thin-film microelectrode arrays of $La_{0.6}Sr_{0.4}Co_{1-x}Fe_xO_{3-\delta}$ ($0 \leq x \leq 1$) on a YSZ (100) substrate. The electrochemical properties of these microelectrode stacks are investigated via scanning impedance spectroscopy, and reveal that electrochemical resistance is dominated by surface oxygen exchange reactions on the electrode through a two-phase boundary pathway. A monotonic increase in electrochemical resistance is observed in $La_{0.6}Sr_{0.4}Co_{1-x}Fe_xO_{3-\delta}$ from x =0 to x =1 along with a decrease in chemical capacitance corresponding to a decrease in oxygen vacancy concentration. A pO_2 dependence of R_s and k^q for the whole spread film with the m in a range of 0.5 to 0.75 is observed, indicating that the oxygen vacancy transport to surface-adsorbed oxygen intermediates is the rate-determining step for mixed conducting cathodes. This study demonstrates the rich

insights obtained via high-throughput methodologies and the promise of applying such techniques to discover highly active solid-state cathode materials.

We have also looked at $PrBa_{0.5}Sr_{0.5}Co_{1.5}Fe_{0.5}O_{5+\delta}$ (PBSCF) as a double-perovskite cathode material, which exhibits the combined conduction of e^-, O^{2-}, and H^+. The high capacity of PBSCF to adsorb H_2O at high temperature (Proton concentration: 1.7 mol% at 600 °C) and its excellent ORR performance can facilitate the cathodic electrochemical reaction in proton conducting SOFCs (p-SOFCs). A thin-film library was used to investigate the ORR mechanism for PBSCF by systematically varying the size of the microelectrode arrays. By combining a chemically stable electrolyte, $BaZr_{0.4}Ce_{0.4}Y_{0.1}Yb_{0.1}O_3$ (BZCYYb4411) with a thin dense PLD PBSCF interface layer between the cathode material and the electrolyte, we have demonstrated breakthrough performance in p-SOFCs with a peak power density of 548 mW/cm^2 at 500 °C and an unprecedented stability under CO_2. The behavior of this p-SOFC can compete with that of high performance oxide-ion-conducting SOFCs. Such performance can create new avenues for incorporating fuel cells into a sustainable energy future.

We have further developed a high-throughput pulsed laser deposition approach to grow phase pure and high quality crystalline $V_{1-x}W_xO_2$ ($0 \leq x < 4\%$) thin films on different substrates, which is challenging because of the complex phase diagram of vanadium oxides where there are many polymorphs of VO_2. We systematically study how tungsten doping affects the poorly-understood phase transition hysteresis via a composition-spread approach. We have demonstrated for the first time that a composition of $V_{1-x}W_xO_2$ ($x \approx 2.4\%$) satisfies unique 'cofactor conditions' based on

geometric nonlinear theory. Our findings inform a strategy for developing more reliable vanadium dioxide materials. In addition, the potential application of $V_{1-x}W_xO_2$ thin films in lithium-ion rechargeable batteries were systematically studied based on the tungsten concentration dependence of electrical properties of $V_{1-x}W_xO_2$.

DEVELOPMENT OF FUNCTIONAL METAL OXIDE THIN FILMS VIA HIGH-THROUGHPUT PULSED LASER DEPOSITION FOR ADVANCED ENERGY APPLICATIONS

by

Yangang Liang

Dissertation submitted to the Faculty of the Graduate School of the
University of Maryland, College Park, in partial fulfillment
of the requirements for the degree of
Doctor of Philosophy
2018

Advisory Committee:
Professor Ichiro Takeuchi, Chair
Professor Sang Bok Lee
Professor Eric Wachsman
Professor Lourdes G. Salamanca-Riba
Assistant Professor Yifei Mo

Dedication

To my parents, my wife, and my daughters.

Acknowledgements

First and foremost, I would like to thank my advisor, Professor Ichiro Takeuchi, for his consistent support and encouragement throughout my research at University of Maryland. Thanks to him for giving me the research opportunity of exploring functional materials through a combinatorial synthesis and rapid characterization methodology. Professor Ichiro Takeuchi helped me come up with my thesis topic, supported me during the difficult times, and gave me more freedom to do my research and visit my family. I do feel lucky to work in his group, and it's been an honor to be his Ph.D. student.

I would also like to take this opportunity to thank my dissertation committee members, Professor Sang Bok Lee, Professor Eric Wachsman, Professor Lourdes G. Salamanca-Riba, Professor Yifei Mo, and Professor Bryan Eichhorn for their support and helpful comments during my thesis work. Besides my advisor and committee members, I would like to thank Professor Sossina M. Haile, Dr. Sihyuk Choi, and Dr. Chris J. Kucharczyk, who are in Northwestern University, for our wonderful cooperation to finish the ARPA-E project.

Many people have helped and taught me in our group. Thanks to Dr. Xiaohang Zhang, Dr. Sunghun Lee, and Dr. Tieren Gao for sharing their knowledge and experience with me. A special acknowledgement goes to my office mates: Eric MarksZ and Naila Al Hasan. And I would like to thank Dr. Yunhui Gong, who has been supportive in every way, although we are in different group.

Finally, but by no means least, thanks to my family (parents, wife, and daughters) for their unconditional support and understanding during the four years at

UMD. A very special thanks to my wife. Without her motivation and encouragement, I would not have decided to pursue a graduate career at UMD. She is always there for me, supported me and made me believe in myself. I also knew that I owe my daughters too much because I did not accompany them in the past four years.

Table of Contents

List of Tables

List of Figures

Chapter 1: Introduction

1.1 Motivations

According to the US Energy Information Administration (EIA), the fossil fuels, such as petroleum, natural gas, and coal, will continue to provide about 80% of total U.S. energy consumption until 2040.[1] However, the fossil fuels are nonrenewable energy sources, and the usage of fossil fuels can release greenhouse gases (e.g. CO_2) and pollute our environment. To reduce the usage of fossil fuels and meet the increasing demand for energy, new power generation and energy storage technologies are in demand.[2] Solid oxide fuel cells (SOFCs) have been regarded as clean and efficient energy conversion electrochemical technology. The rechargeable battery, in particular lithium-ion battery (LIB), is also considered one of the most promising and suitable technologies for the development of efficient, safe, and cheap energy storage devices.[3] Even though both SOFCs and LIBs have been studied extensively, there are still many technical issues, such as performance, cost, safety, etc., which limit their further applications. For example, the high operating temperatures of SOFCs (>800 °C) greatly limit their commercialization process;[3] the cathode material is the limiting factor in the performance of LIBs due to its high cost and low capacity.[4] The key to successful breakthroughs in their applications lie in the development of novel materials.

Among the functional materials, metal oxide thin films have received significant attention due to their versatile functional properties.[5] The demand for materials is endlessly growing, but the conventional materials discovery is impeded by high costs and time-consuming synthesis processes.[6] Furthermore, a high-quality metal

oxide thin film with controlled chemical and structural features at the atomic level is necessary for developing understanding of the composition-structure-property relationship of the material. Having a solid understanding will help efficiently utilize the properties of the material for technological applications and guide the development of novel materials. For example, the development of multiferroic materials by studying the $BaTiO_3$-$CoFe_2O_4$ artificial multilayer spreads.[7]

To this end, a high-throughput pulsed laser deposition methodology is used to develop functional metal oxide films in this thesis work. Using physical moving masks, a library of metal oxide thin films with different compositions or thicknesses are fabricated in a single experiment, which can not only save time as compared to the one-by-one process, but can also accelerate the optimization of experimental parameters. The functional properties of metal oxide thin films are investigated in the context of applications in SOFCs and LIBs. In addition, the phase transition characteristics of vanadium dioxide based materials was systematically studied. Furthermore, we demonstrated that pulsed laser deposition can be used to grow high quality organic-inorganic hybrid perovskite materials successfully for applications in perovskite solar cells (PSCs).[8]

1.2 Metal oxide thin films

As the most abundant materials in the Earth's crust, metal oxides typically contain oxygen anions (O^{2-}) and display insulating, semiconducting, and metallic properties depending on the composition and their crystal structures.[9] Metal oxide thin films have been studied extensively for both fundamental and application-oriented

research, and demonstrated numerous applications in photovoltaic, transistor, energy conversion, energy storage, etc. as shown in Figure 1.1 (a). Metal oxide thin films can display additional or enhanced functionalities compared to their bulk counterparts due to the possibility of interface engineering and nano-layering.[9] For example, Garcia-Barriocanal et al.[10] reported that oxygen ionic conductivity of the YSZ in YSZ/STO heterostructures was measured to be about eight orders of magnitude higher than that of bulk YSZ near room temperature due to strain- and interface-enhanced disorder of the O sublattice.

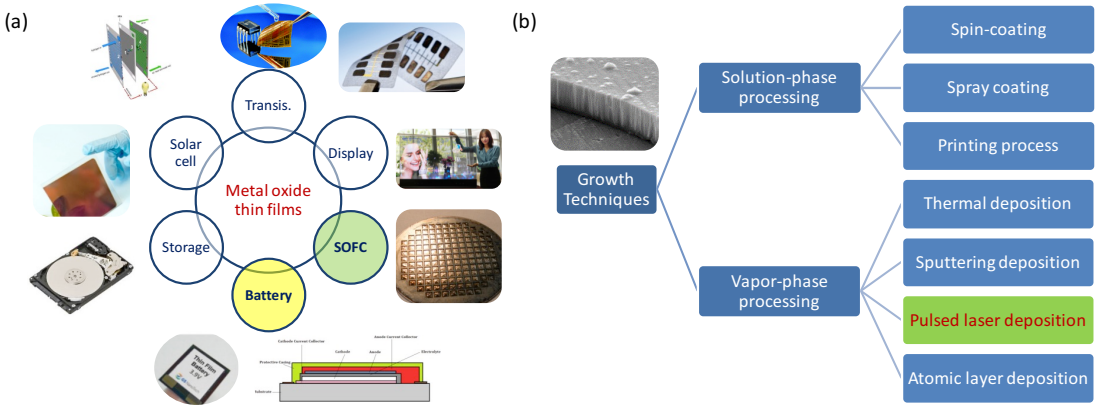

Figure 1.1 (a) The different applications of metal oxide thin films. (b) The general thin film fabrication methods.

Metal oxides cover a wide range of materials with a spectrum of functionalities including photocatalyst TiO_2, superconductor yttrium barium copper oxide (YBCO), ferroelectric $BaTiO_3$, transparent conducting oxide indium tin oxide (ITO), etc. Metal oxide thin films can be routinely made in thickness range of a nanometer to several micrometers. The film features, such as crystallinity, microstructure, defect, etc., determine its functional properties and potential applications.[9] For example, enhanced ionic conductivity and robust thermal stability have already been demonstrated in

epitaxial electrolyte thin films.[10,11] Therefore, many thin film growth techniques have been developed to meet different requirements. As shown in Figure 1.1 (b), there are solution-phase based and vapor-phase based thin film deposition techniques. Each deposition method has its own advantages and disadvantages, such as the sputtering deposition, it is easy to sputter and deposit elements, alloys and compounds, however, its sputtering rate is low compared to that attained in thermal evaporation. Pulsed laser deposition (PLD) is one of the most popular thin film deposition techniques for scientific purposes due to its stoichiometry transfer from the target material to the film and its versatile operational flexibility.[12] We take advantage of its versatility to use it as the deposition tool for high-throughput combinatorial methodology. Chapter 2 gives a detailed introduction to the method of high-throughput pulsed laser deposition.

In this dissertation, we focus on the development of high quality metal oxide thin films using a high-throughput pulsed laser deposition methodology and investigating their applications in clean energy technologies, namely solid oxide fuel cells (SOFCs) and lithium-ion batteries (LIBs). The following section gives introduction to SOFCs.

1.3 Introduction to SOFCs

Development of clean, efficient, and environmentally friendly power generation technologies has attracted great attention in both academia and industry in the past two decades because such technologies are needed to help slow down the processes of global warming and energy crisis. One such technology is fuel cells, which

provide a clean method of power generation as compared to other methods of hydro, thermal, and nuclear power generation.[13]

A fuel cell is an electrochemical device which converts chemical energy of fuels directly into electrical energy. There are many kinds of fuel cells based on different electrolytes, such as polymer electrolyte membranes (PEM), alkaline (AFC), phosphoric acid (PAFC), molten carbonate (MCFC), and solid oxide fuel cells (SOFCs).[14] The fuel cell principle was first discovered by Christan Friedrich Schönbein in 1838, and the first prototype was developed by Sir William Grove in 1845. The first commercial use of fuel cells was in NASA Apollo program to generate power for probes, satellites, and space capsules in 1960. The ceramic fuel cells using zirconium oxide and calcium oxide were studied at Westinghouse in 1962.

Among the fuel cells, SOFCs show many advantages: the highest efficiency (fuel input to electricity output: 60-65%, >70% integrated with reforming/heat recovery processes), fuel flexibility (H_2, CH_4, CO, etc.), easy installation/operation (all solid components), and a potential long lifetime (>40,000 hours). [14,15]

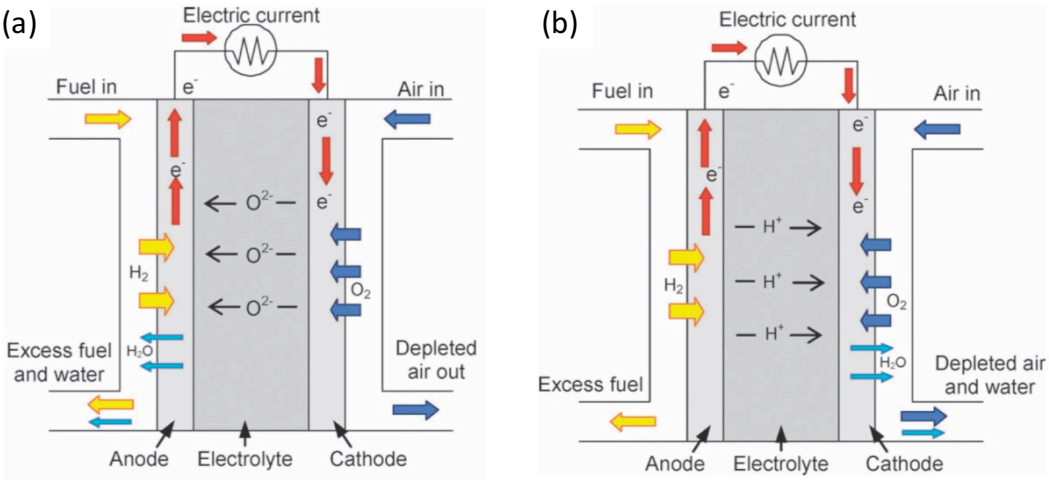

Figure 1.2 Concept diagrams of SOFC based on oxygen-ion conductors (a), and on proton conductors (b).[16]

SOFCs are based on the concept of oxygen ion conducting electrolytes through which the oxide ions migrate from the cathode side to the anode side where the water was produced by the reaction between the oxygen and the fuel (H_2, CH_4, CO, etc.) as shown in Figure 1.2(a). Alternatively, in proton conducting SOFCs (p-SOFCs), protons migrate from the anode side to the cathode side where the water was produced by the reaction between the oxygen and the fuel as shown in Figure 1.2(b). A typical SOFC consists of three components: anode, electrolyte, and cathode. The SOFC is usually operated in the temperature range of 800 °C to 1000 °C. The high operating temperature of SOFCs helps overcome the problem of using precious metal catalysts in traditional fuel cells.[16] In SOFCs, dense ceramic metal oxides are used as electrolytes (such as YSZ, gadolinium doped ceria (GDC)). Both electrodes are porous metal, metal oxides, or composite materials. For an oxygen ion conducting SOFC using hydrogen fuel, the hydrogen is oxidized to protons at the anode by the reaction of $H_2 \rightarrow 2H^+ + 2e$, the two electrons are forced to flow through the external circuit to the cathode side, where the oxygen in air is reduced to oxygen ions by the reaction of $\frac{1}{2}O_2 + 2e \rightarrow O^{2-}$. Driven by the difference in oxygen chemical potential (the gradient of oxygen partial pressures (pO_2)) between cathode and anode, the oxygen ions move through the electrolyte to the anode side, where the water is produced by the reaction of $2H^+ + O^{2-} \rightarrow H_2O$. The performance of the cell is evaluated by the output voltage which is given by the Nernst Equation:[17]

$$E = E^0 + \frac{RT}{2F}\ln\left(\frac{p_{H_2}p_{O_2}^{1/2}}{p_{H_2O}}\right) \qquad (1.1)$$

$$E^0 = -\frac{\Delta G^0}{2F} = \frac{\Delta H^0 - T\Delta S^0}{2F} \qquad (1.2)$$

Where E^0 is the standard potential difference between the electrode reactions and is given by Equation 1.2 representing the standard Gibbs free energy change for the overall reaction of hydrogen and oxygen, R is the gas constant, F is the Faraday's constant, 2 is the number of electrons transferred in the half cell reaction, and the terms in natural logarithmic are the partial pressure of the reactants and the products of the reaction.

SOFCs have shown many advantages, but the progress in the development of cost-competitive SOFC applications has been slow in the past 20 years. The main problem is that the current SOFCs operate at temperatures of more than 800 °C. The high operating temperatures lead to a high cost of materials due to the issues such as the sealing problem, thermal mismatch between materials, and the accelerated coarsening of electrodes.[3] Hence, lowering operating temperatures of SOFCs has been recognized worldwide as an important research direction for a more economical, efficient, and reliable SOFC technology. Lowering the operating temperature of SOFCs could also shorten the startup time and decrease energy loss from heat radiation. However, low operating temperature will lead to a poor cell performance: there is ≈12% drop in cell performance with a 10% decrease in temperature.[18] This is because the ionic conductivity of electrolytes decreases rapidly with decreasing temperature due to high activation energy as shown in Figure 1.3. The slope of each line in Figure 1.3 has a corresponding activation energy of the electrolyte by following the Arrhenius Equation (1.3):[15]

$$\sigma \cdot T = A \cdot \exp\left(-\frac{E_a}{k \cdot T}\right) \qquad (1.3)$$

Where T is the operation temperature (K), A is a pre-exponential term, k is the Boltzmann constant, and E_a is the activation energy. A typical E_a value for oxygen ion conductors is about 1 eV, while a big change in conductivity activation energy can also be observed due to the order-disorder transition such as DWSB at ~ 600 °C as shown in figure 1.3.[19]

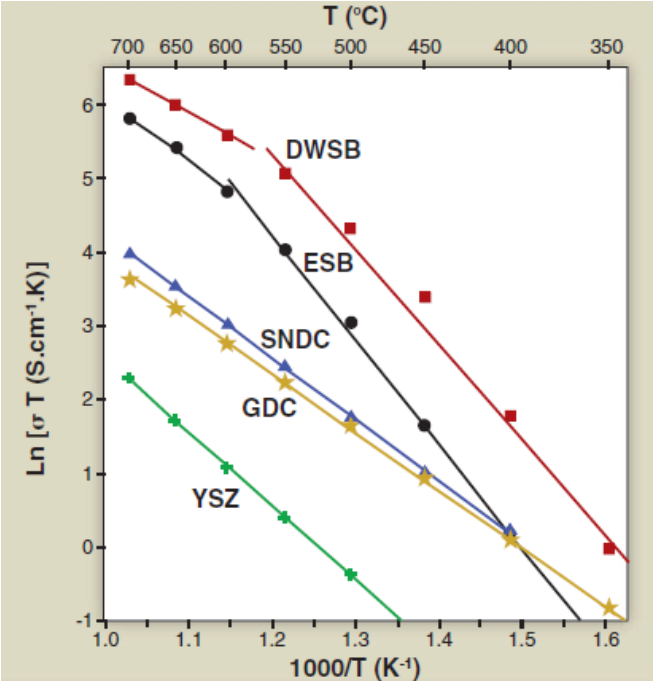

Figure 1.3 The ionic conductivity of various solid oxide electrolytes.[19]

The electrode activity also decreases drastically with decreasing temperature, especially for the cathode part, which is the main component of the power losses due to the polarization resistance at the cathode/electrolyte interface.[20] Oxygen reduction reaction (ORR) at the cathode is a thermally activated and quite a complicated process, which involves many intermediate steps depending on specific conditions. For instance, the multistep processes usually include adsorption of chemical species on the

electrode surface, surface or bulk diffusion of intermediate species, and charge transfer reactions at the electrode-electrolyte interface. In addition, the ORR mechanism on cathodes is still not well understood, and there are very few studies focusing on the cathode materials for proton conducting SOFCs (p-SOFCs).

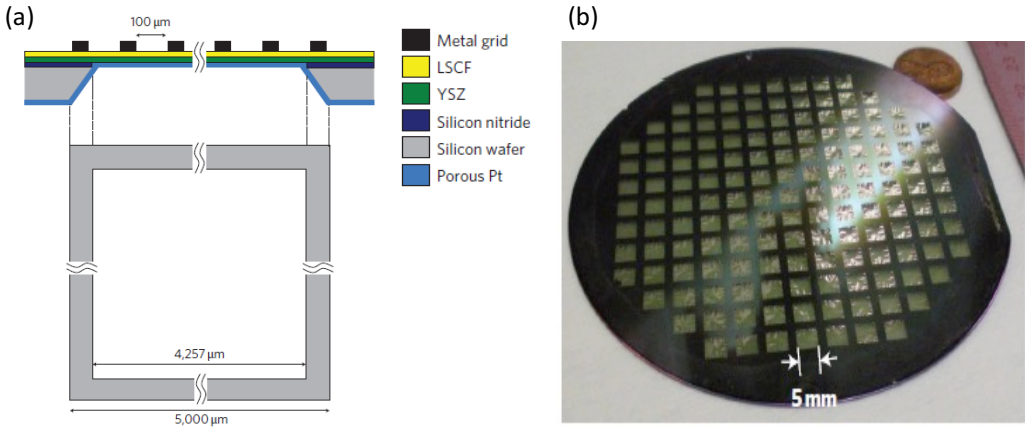

Figure 1.4 (a) Schematic of grid-supported 5 mm × 5 mm membranes. (b) An image of a 4-inch wafer with grid-supported micro-SOFCs.[21]

To solve the issues for low and intermediate temperature SOFCs (300 °C - 800 °C), many solutions have been proposed. For the electrolyte part, two main routes have been used to attain comparable performance to the high temperature SOFCs. One route is through the development of high ionic conducting electrolytes at low temperatures. As compared to the traditional YSZ electrolyte, some higher performance electrolytes have been reported as shown in Figure 1.3. However, there is a long way to go before these new electrolytes are commercialized due to the problems of cost, stability, and compatibility with other components of SOFCs.[22] Recently, high-temperature proton conductors have attracted great attention as an alternative to oxygen ion conductors due to their lower activation energy for proton conduction. In such a material a higher

conductivity than that of traditional oxygen-ion conductors at relatively low temperatures can be achieved.[23] The studies on proton conducting materials have mainly focused on $BaCeO_3$ and $BaZrO_3$ as these electrolyte materials possess considerable proton conductivity and stability.[23] The second strategy is the development of thin film electrolytes, because the area specific resistance (ASR) of the fuel cell can be reduced by decreasing the thickness of the electrolyte layer. Therefore, researchers are focusing on reducing the resistance of electrolyte to improve the performance of SOFCs at low temperatures by applying thin film technology. Fabricating thin film electrolytes can also benefit in miniaturization of SOFCs, which have potential applications in portable power sources for electronic consumer or medical devices.[24] So far many studies have been reported to fabricate YSZ electrolyte thin films using various physical or chemical thin film technologies, such as radio-frequency (RF) sputtering, PLD, atomic layer deposition (ALD), spin coating method, etc.[25] Also, some proof-of-concept thin-film SOFCs have been demonstrated. A power density of 155 mW/cm^2 at 510 °C has been reported by Masaru *et al.* on a scalable nanostructured membrane SOFC as shown in Figure 1.4.[21] However, there are still some disadvantages for these methods, such as relatively high cost and difficulty of scale-up, and further improvements are needed.

For the cathode part, the performance of electrodes can be improved by developing more active electrode materials and applying microstructure/nanostructure engineering techniques. Another important research direction is the studies of understanding the oxygen transport mechanisms and exploration of structure-property-performance correlations.[14] For most of the reported cathode materials, their

performance vary tremendously because of several unknown variable factors (fabrication and operation). For example, the porosity of a cathode has important effect on its performance. In particular, the ORR mechanism is very difficult to deduce in porous cathodes due to irregular or poorly defined morphology and geometries.[26] Thus, using dense thin film cathodes with a well-defined geometry can provide a better understanding of the rate limiting step for cathodic reaction mechanism under different conditions such as chemical composition, temperature, and oxygen partial pressure.

Lowering the operating temperatures of SOFCs is now a worldwide research trend. However, the high ionic conducting resistance of electrolytes and high polarization resistance of electrodes at low temperatures have become the key limiting factors for improving the performance of low temperature SOFCs. To this end, this dissertation mainly focuses on the development of an evaluation method for out-of-plane electrochemical transport properties in thin-film electrolytes, the fabrication of a dense thin-film cathode on oxygen ion conductors as a model system to investigate the ORR mechanisms, and the development of high-performance cathode materials for p-SOFCs.

1.4 Objectives and dissertation outline

The objective of this dissertation is to develop functional metal oxide thin films via a high-throughput pulsed laser deposition methodology and investigate their applications for energy conversion and energy storage, namely SOFCs. In addition, a goal of this thesis work is to investigate tuning of the phase transition characteristics of VO_2 through systematic doping. The sharp metal-insulator transition associated with the structural transition can be the basis of novel energy storage materials. Following

the systematic tuning results, we briefly discuss its potential application for LIBs, which will help develop their advanced applications in future. In addition to the work on metal oxide thin films, a novel pulsed laser deposition based method was developed to fabricate high quality organic-inorganic hybrid perovskite materials for next generation of solar cell applications.

With these objectives, the dissertation includes eight chapters. Chapter 1 gives a briefly background introduction to the research motivations, metal oxide thin films, and SOFCs. Chapter 2 introduces the research methodology and characterization techniques used in this dissertation. Chapter 2 includes an overview of the pulsed laser deposition (PLD) method and the high-throughput PLD system developed in our group, and a brief introduction to a series of materials characterization techniques.

Five chapters describe our experimental results. Chapter 3, Chapter 4, and Chapter 5 focus on materials development for SOFCs. Chapter 6 focuses on the phase transition characteristics and possible applications of VO_2 based materials. Chapter 7 focuses on a novel PLD-based hybrid fabrication method for organic-inorganic perovskite thin films.

In Chapter 3, we have fabricated all-thin-film solid oxide fuel cell (SOFC) structures in order to probe fundamental transport properties of SOFC electrolytes in an out-of-plane measurement geometry using epitaxial films with ideal model interfaces. Epitaxial multilayer thin-film structures consisting of a bottom electrode ($SrRuO_3$ (SRO) or $Ba_{0.93}La_{0.07}SnO_3$ (BLSO)) and an electrolyte $Sm_{0.2}Ce_{0.8}O_{2-\delta}$ (SDC20) (600 nm - 1000 nm) on $SrTiO_3$ (100) single crystal substrates were fabricated using pulsed laser deposition. The heteroepitaxy of the multi-layer structures was

confirmed by X-ray diffraction and high-resolution scanning transmission electron microscopy, and atomically sharp and structurally coherent interfaces were observed in the electrolyte/electrode bilayers. Electrochemical impedance spectroscopy (EIS) measurements of the devices at temperature range of 623 K to 823 K in air reveal electrochemical properties of SDC20 which are quantitatively consistent with known bulk transport properties of SDC20. This work demonstrates the utility of prototypical out-of-plane all-thin-film heteroepitaxial electrochemical devices as a model platform for directly investigating intrinsic transport properties of electrochemical materials in single-crystal-like structures with well-defined sharp interfaces.

In Chapter 4, we discuss the development of a fundamental understanding of surface oxygen reduction reactions (ORR) mechanisms in mixed-conducting cathode materials. The development of cathode materials with high catalytic activity for the oxygen reduction reaction plays an important role in determining the performance of solid oxide fuel cells (SOFCs) at relatively low temperatures. The mixed ionic-electronic perovskite-type oxide $La_{0.6}Sr_{0.4}Co_{1-x}Fe_xO_{3-\delta}$ is a state-of-the-art cathode material for intermediate temperature SOFCs, but there is no consensus on the mechanisms for oxygen reduction reactions (ORR) at the surface of mixed conducting cathode materials, possibly due to the different and complex geometries and microstructures of samples prepared by various research groups. To this end, in Chapter 4, we report a novel methodology which combines a high-throughput pulsed laser deposition of compositional spread thin films and an automatic scanning impedance spectroscopy for characterization of electrodes. Using this technique, the fundamental properties of multiple electrode compositions are systematically studied in order to

understand the surface oxygen reduction process. A library of isolated circular $La_{0.6}Sr_{0.4}Co_{1-x}Fe_xO_{3-\delta}$ ($0 \leq x \leq 1$) thin-film microelectrodes ranging from 80-500 μm in diameter was fabricated by HT-PLD and standard photolithographic techniques on a (100)-oriented 8 mol% Y_2O_3-ZrO_2 electrolyte substrate. The electrochemical properties of these geometrically well-defined, dense thin-film model microelectrodes were investigated by a scanning impedance spectroscopy as a function of iron content, diameter of microelectrodes, temperature, and oxygen partial pressure. The comparative study reveals that the electrochemical resistance is dominated by the oxygen exchange reaction at the surface of the electrode through a two-phase boundary electrochemical pathway. A monotonic increase in electrochemical resistance is observed in $La_{0.6}Sr_{0.4}Co_{1-x}Fe_xO_{3-\delta}$ from x =0 to x =1 along with a decrease in chemical capacitance corresponding to a decrease in oxygen vacancy concentration. A very similar power law dependence of both $\log(R_s)$ and $\log(k^q)$ on pO_2 in a double-logarithmic plot was observed to be in a range of 0.5 to 0.75, indicating that the approach of an oxygen vacancy to oxygen intermediates adsorbed on the surface is the rate determining step for mixed conducting cathode materials. This case study demonstrates the rich insights that can be obtained from this high-throughput methodology and its promising application toward searching for highly active cathodes for the oxygen reduction reaction in the field of solid-state electrochemistry.

In Chapter 5, we demonstrate the performance breakthrough in proton conducting SOFCs (p-SOFCs) based on a high performance cathode material. Proton conducting SOFCs have been demonstrated to be the highly efficient, environmentally sustainable, and cost-effective energy conversion devices at intermediate temperatures

(400-600 °C). However, the power output from these devices has lagged behind predictions based on electrolyte conductivity due to the poor performance of the traditionally used cathode materials and the stability challenge of proton conductors under H_2O/CO_2 atmosphere. Here we identify a double perovskite (PBSCF) that possesses the combined conduction of e^-, O^{2-}, and H^+ by investigating the geometrically well-defined microelectrodes. Combining with a chemically stable electrolyte, $BaZr_{0.4}Ce_{0.4}Y_{0.1}Yb_{0.1}O_3$ (BZCYYb4411) and a thin dense PLD PBSCF interface layer between the cathode material and the electrolyte, we achieved a peak power density of 548 mW/cm^2 at 500 °C and an unprecedented stability under CO_2.

Vanadium dioxide (VO_2) has been extensively studied previously due to its fully reversible first-order metal-insulator transition associated with a structural phase transition at about 340 K. Such a transition can be the basis for novel functional devices. In this work, we focused on tuning of the phase transition through systematic doping. One major challenge in VO_2 research on thin films is to fabricate phase pure thin films because of the complex phase diagram of vanadium oxides where there are many polymorphs of VO_2. One of the most effective chemical dopants for tuning the metal−insulator transition in vanadium dioxide is tungsten. In Chapter 6, we developed a high-throughput pulsed laser deposition approach to grow phase pure and high quality crystalline $V_{1-x}W_xO_2$ ($0 \leq x < 4\%$) thin films on different substrates. In particular, the concentration of W ions had a directional variation from 0% to 4% across each film. It is widely reported that tungsten dopants are able to effectively reduce the phase transition temperature. However, the underlying mechanism, especially how the tungsten dopants affect the hysteresis of the phase transition, is poorly understood.

Based on our experimental results, we found that the 'cofactor conditions', which are strongest lattice-structure compatibility conditions (of high temperature and low temperature phases) proposed based on the geometric nonlinear theory of first order phase transition recently, can be used to explain the relation between the doping concentration of tungsten ions and the hysteresis characteristics of the structural transition of $V_{1-x}W_xO_2$ films. Specifically, the cofactor condition was found to be satisfied in $V_{1-x}W_xO_2$ when x is around 2.4%. A minimum transition hysteresis width consistently observed in both epitaxial and polycrystalline $V_{1-x}W_xO_2$ films at the same tungsten concentration (x ~2.4%) showed for the first time that the geometric nonlinear theory (previously applied to shape memory alloys) is also applicable to oxide materials. The potential application of $V_{1-x}W_xO_2$ thin films in rechargeable lithium batteries were systematically studied based on the tungsten concentration dependence of electrical properties of $V_{1-x}W_xO_2$. Their potential use as dual functional cathode materials (host of lithium ions and conductor of electron) for rechargeable lithium batteries has been demonstrated in proof-of-concept experiments.

As another application of PLD for energy conversion materials, we have demonstrated a novel PLD-based hybrid fabrication method for organic-inorganic perovskite thin films. This is discussed in Chapter 7. We report on fabrication of organic-inorganic perovskite thin films using a hybrid method consisting of pulsed laser deposition (PLD) of lead iodide and spin-coating of methylammonium iodide. Smooth and highly crystalline $CH_3NH_3PbI_3$ thin films have been fabricated on silicon and glass coated substrates with fluorine doped tin oxide using this PLD-based hybrid method. Planar perovskite solar cells with an inverted structure have been successfully

fabricated using the perovskite films. Because of its versatility, the PLD-based hybrid fabrication method not only provides an easy and precise control of the thickness of the perovskite thin films, but also offers a straightforward platform for studying the potential feasibility in using other metal halides and organic salts for formation of the organic-inorganic perovskite structure.

In Chapter 8, we present the summary of different work we performed in this thesis and possible future projects.

Chapter 2: Pulsed Laser Deposition and Characterization Techniques

2.1 Introduction to high-throughput PLD

Pulsed Laser Deposition (PLD) is one of the most promising thin film growth techniques, especially for metal oxide materials which play important roles in energy applications. As one of the physical vapor deposition (PVD) techniques, PLD is an extremely simple thin film fabrication method where an external high power pulsed laser is used to vaporize the target material to form a thin film on a substrate inside a high vacuum chamber.[27]

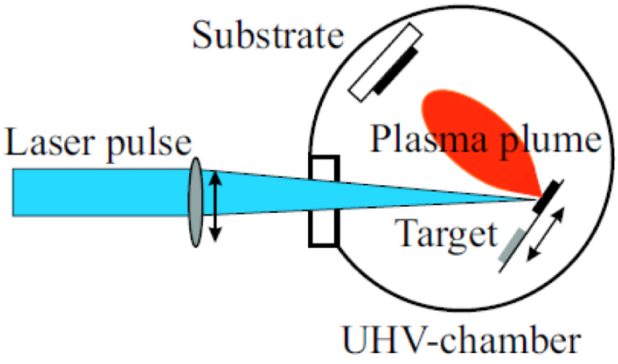

Figure 2.1 Schematic diagram of a typical laser deposition set-up.[28]

PLD has been widely recognized as a very promising, versatile and efficient method for thin-film formation and nanofabrication since it was successfully used for the in-situ growth of epitaxial high-temperature superconductor films in 1987.[29] A typical PLD set-up mainly includes an external pulsed laser, an ultrahigh vacuum (UHV) chamber, target holders, and a substrate stage as schematically illustrated in

Figure 2.1. In the UHV chamber with a flow of a reactive gas (e.g., oxygen or nitrogen gasses), alloy or oxide targets are struck by a pulsed and focused laser beam with an incident angle of 45°. During the process, the electromagnetic energy of the laser pulses is converted into electronic excitation and then into thermal, chemical, and even mechanical energy to cause evaporation, ablation, excitation, and plasma plume formation. The plasma plume consisting of a mixture of energetic species including atoms, molecules, electrons, ions, and clusters is blocked by the substrate and then a thin film is formed on the surface of substrate.[30]

PLD shows many fascinating advantages: 1) It usually ensures stoichiometry transfer between target and film; 2) It allows easy control of the film growth by optimizing the laser energy density, pulse repetition rate, substrate temperature, and deposition pressure; 3) It can make use of targets much smaller than that used in conventional sputtering techniques.

There are also some drawbacks in using this deposition technique. One of the major disadvantage is the presence of micro-sized particulates on the substrates due to the sub-surface boiling.[30] The particulates will greatly affect the growth of the subsequent layers as well as the electrical properties of the films. Another problem is the narrow angular distribution of the ablated species, which leads to limited film uniformity. In view of these problems, some strategies such as inserting a shadow mask to block off large particulates and rotating both the target and the substrate to produce larger uniform films have been proposed to improve the quality of the films formed by the PLD technique.[12]

PLD has been successfully employed for the deposition of simple and complex metal oxide materials with desired composition, structure, physical and chemical properties for applications in semiconductor, solid-state electrochemical, and ferroelectric devices because of the above-mentioned advantages.[30] However, the conventional trial-and-error synthesis approach has been a major rate-limiting step during the systematic investigation of increasingly complex materials for the development of new technologies.[6] In this thesis, we use a high-throughput (combinatorial) PLD technique to perform a systematic investigation of the relationship between compositions, functional properties, and crystal structures.

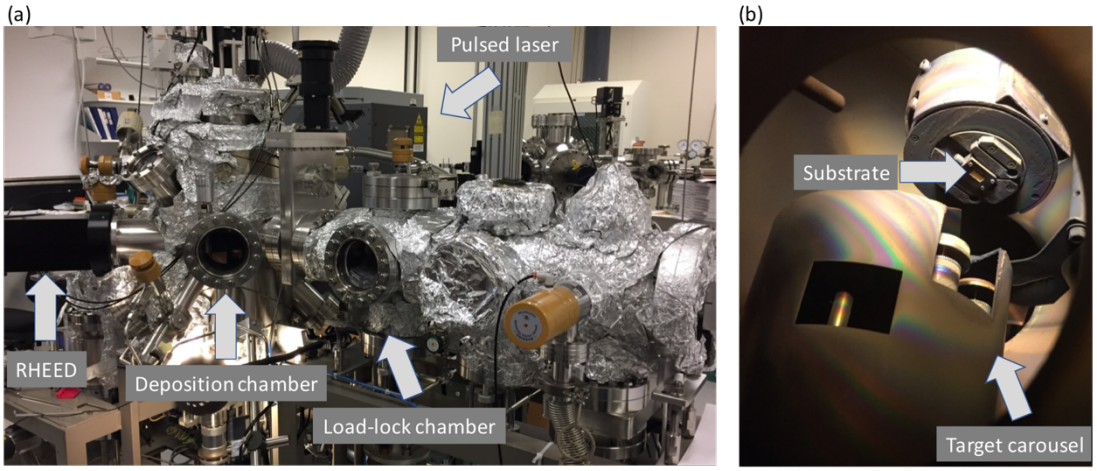

Figure 2.2 (a) A photograph of the combinatorial pulsed laser deposition system in our lab. (b) The inside photograph of the deposition chamber.

The combinatorial approach is to synthesize a large number of compounds by reacting a set of components in the pre-designed combinations in a single experiment. The concept was first developed in the field of organic and bio-organic synthesis, and then successfully extended to the field of solid-state materials.[31] A "library" sample that contains variations of the materials parameter of interest (composition,

temperature, thickness. etc.) is fabricated and evaluated with high-throughput measurements to quickly identify the most promising candidates. In 1995, Xiang *et al.*[32] proposed a method that combines thin film deposition and physical masking techniques for the parallel synthesis of spatially addressable libraries of solid-state materials, which initiated a research focus on novel electronic, magnetic, and optical materials by a combinatorial approach. However, this PLD-based combinatorial approach is a mixing-after-deposition process, this will lead to some problems such as phase separation and a complicated operation process (multiple mask alignments). In our lab, an updated PLD system (HT-PLD) is used for film deposition. As shown in Figure 2.2, the HT-PLD system is equipped with 6 rotatable target stages and a movable mask for combinatorial synthesis. The HT-PLD system demonstrates many important advantages such as high-efficiency, no physical pattern mask, and in-situ phase formation, etc.

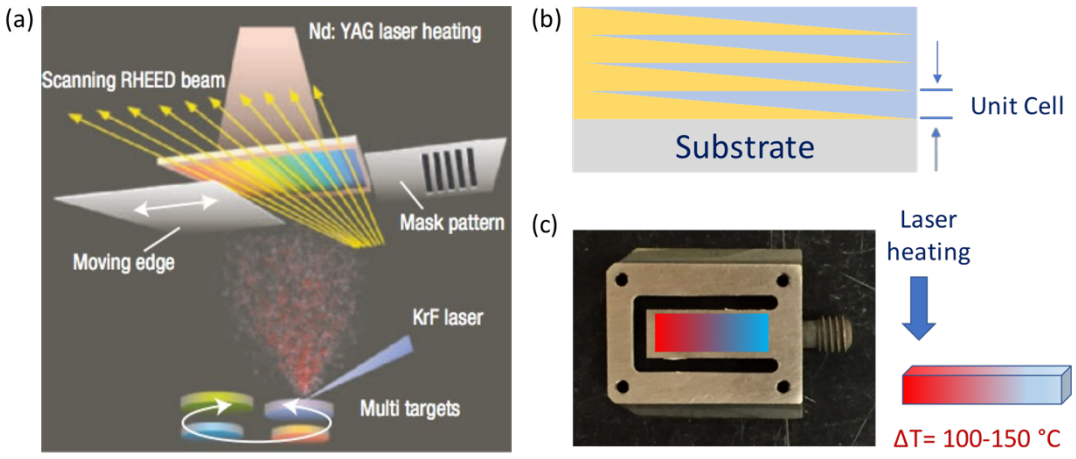

Figure 2.3 (a) The deposition scheme for fabricating a compositional spread sample.[6] (b) A schematic cross-sectional view of a compositional spread sample. (c) Schematic views of the fabrication of a temperature gradient sample.

Figure 2.3 shows schematic diagrams for preparing a compositional spread sample and a temperature gradient sample. As shown in Figure 2.3(a), the continuous composition variation is realized through the thickness gradient (wedge shape) of the two materials (corresponding to the two targets) introduced by moving a mask during deposition. Further, by using a LabVIEW program to control the deposition process, it is easy to have a rapid sequential deposition of each component at a rate of less than a monolayer per cycle at an optimal substrate temperature, resulting in a pseudo-binary or pseudo-ternary film without the post-annealing.

Optimizing the deposition temperature is particularly important because it is critical to the film crystallization and the surface morphology. However, the traditional "one-by-one" method is extremely time consuming and possibly misses some important data points. In our HT-PLD system, we can screen the deposition temperature in a temperature range of about 150 °C in a single experiment based on conventional radiative heating of a metallic substrate holder as shown in Figure 2.3(c).

The HT-PLD method combining with high-throughput measurements provides a powerful tool for the high throughput materials science methodology, which enables rapid materials synthesis and optimization.

2.2 Introduction to Epitaxy

Epitaxy of PLD thin films is the focus of this dissertation. Hence, we give a brief introduction to the features of epitaxy in this section.

Epitaxy means the deposition of a crystalline film on a crystalline substrate, which includes homoepitaxy and heteroepitaxy.[33] The requirement for epitaxial film

growth is that the film and substrate lattice planes have networks of identical or quasi-identical form/spacings. If a film is deposited on a substrate of the same composition, the process is called homoepitaxy; otherwise it is called heteroepitaxy.[30] To minimize the total interfacial energy by aligning the crystal structure of films with that of the substrates is the driving force for the epitaxy. The epitaxial formation of films has important advantages in terms of uniformity in the composition and controlled growth parameters.[30] These advanced structures have been used in lasers, light emitting diodes, detectors, transistors, etc. [30] Epitaxial growth techniques are the key to a successful manipulation of the heterostructures. In this dissertation, the PLD technique is the main tool for the growth of the heterostructures.

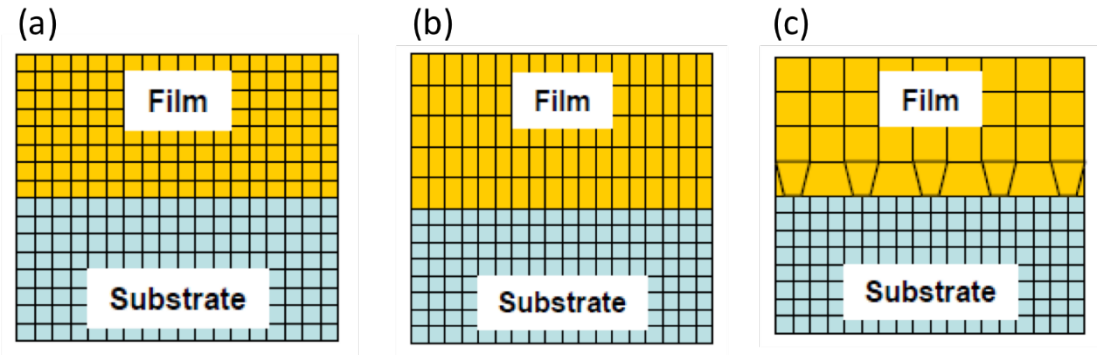

Figure 2.4 Schematic views of the lattice strains between the film and substrate. (a) Matched lattices with homoepitaxy. (b) Strain induced due to the lattice mismatch. (c) Relaxed epitaxy film and dislocation formed.[33]

Figure 2.4a shows a structure of matched lattices, which is desired to minimize defects and increase transport properties for many applications. When the lattice mismatch gets larger, as shown in Figure 2.4b, the film may be stretched or compressed during the initial stage of the film formation to accommodate the lattice structure of the substrate. Figure 2.4c shows the relaxed film epitaxy, where the film returns to its

original lattice structure away from the interface. The dislocation defects form at the interface due to the weak strain accommodation. The lattice misfit is defined as: $f = (a_s - a_f)/a_f$, where a_s and a_f are the lattice constants of the substrate and the film, respectively. If f is negative, the strain is compressive, f is positive, the strain is tensile.[33] For the 2D film, the strain is along xx at the interface, here, $\epsilon_{xx} = f$. When the thickness of film is at a critical thickness h_c, the dislocation starts to form. By solving the strain equilibrium equation: $\epsilon_{xx} = \frac{b}{8\pi f(1+v)}\left\{\log\left(\frac{h}{b}\right) + 1\right\}$, where b is the Burger's vector, h is the film thickness, v is the Poisson's ratio, and h_c is obtained. When $h < h_c$, the film is fully strained; $h > h_c$, the film is partially relaxed; When $h = h_c$, the dislocations start to form. [33] Typically, if the lattice mismatch is less than ~9%, the initial layers of film are fully strained. Therefore, when a film is very thin, the films may be elastically strained to have the same inter-atomic spacing as the substrate. As a film gets thicker, the lattice constants of the film may return to that in the bulk, and thus a relaxed structure is gradually formed as the position departs away from the interface. During the growth process of an epitaxial film, the substrate plays an important role in determining the quality of the epitaxial films and their microstructures. Therefore, it is very important to properly select a substrate for epitaxial growth of a film.

2.3 Characterization techniques

The high throughput methodologies are expected to facilitate the discovery of novel materials. A fast characterization method for library screening and a suitable software for experimental design, experimental control, and data analysis play

important roles in determining the success of the high throughput methodology. Thus, highly automatic characterization instruments are in need. However, compared with the improved pace of the synthesis methods, the development of high-throughput measurement methods becomes one bottle-neck.[34] In this thesis, I will make extensive use of specific instrumental tools to characterize various composition spread samples. In particular, various characterization methods, such as scanning electron microscope (SEM), transmission electron microscopy (TEM), physical property measurement system (PPMS), etc., together with some high-throughput characterization techniques of X-ray diffractions (XRD), atomic force microscope (AFM), electrochemical impedance spectroscopy (EIS), etc. were used for material characterization in this work. Moreover, a programmable x-y-z stage is used for most of the high-throughput characterization techniques, some will be discussed in each chapter.

2.3.1 X-ray diffraction (XRD)

X-ray diffraction (XRD) is non-destructive method used to identify the crystalline structures of materials. Specifically, the short wavelength x-rays in the range of a few angstroms to 0.1 angstrom (1 keV - 120 keV) are used.[35] This wavelength of x-rays is comparable to the size of atoms such that probing the structural arrangement of atoms and molecules in a wide range of materials may be possible. The energetic x-rays can penetrate deep into the materials and thus provide information about the bulk structure.

The XRD technique is based upon the Bragg's law, i.e., $2d \sin\theta = n\lambda$, where d is the distance between parallel lattice planes, θ is the incident angle of incidence, n

is a positive integer, and λ is the wavelength of the incident wave (λ = 1.5405 Å in this thesis work). The law yields various peak positions in the XRD spectrum after the X-rays are scattered by a crystalline material. As shown in Figure 2.5a, the path difference for X rays reflected from adjacent planes is 2dsinθ. According to the Bragg's law, constructive interference of the radiation from any two consecutive planes occurs when the path difference is an integral number of the wavelengths λ. Moreover, based on the equation of Bragg's law, the Bragg diffraction condition requires $\lambda \leq 2d$. [35]

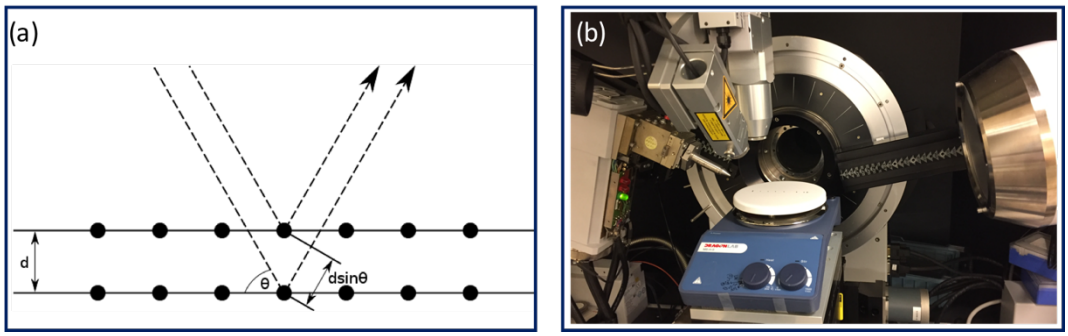

Figure 2.5 (a) A schematics diagram of the Bragg diffraction. (b) An image of a C2 Discover parallel beam diffractometer with HiStar area detector used in the crystallinity characterization of the thin film samples for this study.

In this thesis, only 2θ-θ scans were performed for most of the thin film samples, and from the XRD results, the relation between the film structure and the substrate structure can be obtained. As shown in Figure 2.5b, a diffractometer with an automatic x-y-z stage was used to characterize the crystal structure of the fabricated thin film samples. In addition, a heating plate can be installed onto the moving stage for *in-situ* heating to allow the study of temperature dependence of diffraction spectra. The rocking curve measurement can be used to estimate the film mosaic spread in the film.

In a rocking curve geometry, the angle between the incident ray and the surface of the sample is the Bragg's angle of θ, and the detector is positioned at the 2θ Bragg position. The value of Full Width at High Maximum (FWHM) of a rocking curve indicates how the grains are titled in the film. A smaller FWHM value means a higher crystal quality of the film and a lower degree of crystallographic disorder in the film. [35]

2.3.2 Atomic Force Microscopy (AFM)

Atomic force microscopy (AFM) is used for topological imaging and surface roughness characterization based on a mechanical probe. It has a high resolution (1 Å) and can generate a 3D map of the sample surface. AFM measurements can be operated under the ambient atmosphere. The key part of AFM technique is the mechanical probe, which consists of a cantilever with a sharp tip at its end to scan the surface profile. Approaching the tip to the surface of a sample induces an interaction force between the tip and the surface, leading to a deflection of the cantilever. To measure the deflection of the cantilever, the most conventional method is an optical deflection measurement in which the displacement of a laser beam reflected from the back side of the cantilever is detected by a position-sensitive photodiode detector.[36] Figure 2.6 shows the AFM system used in this work. The sample stage of the AFM system is an automated programmable x-y-z stage, and thus, it is highly efficient in measuring numerous sample points on a single 3-inch wafer. For a regular $5 \times 5\ \mu m^2$ scanning, a single position takes about 5 minutes to measure.

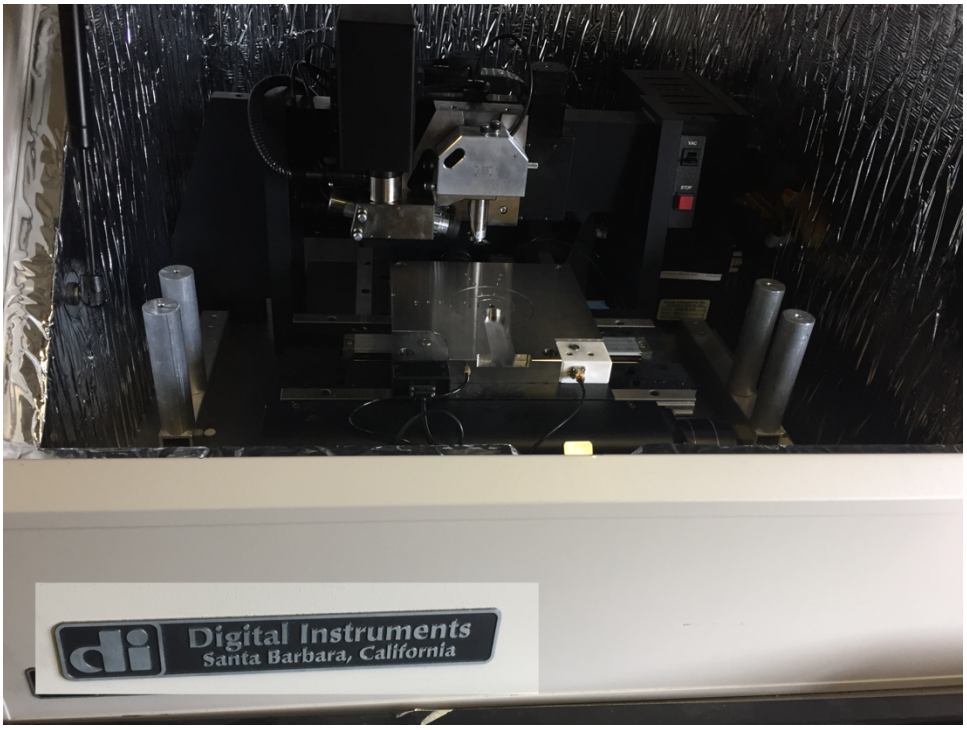

Figure 2.6 An image of the Atomic Force Microscopy used for determining surface roughness of the thin films fabricated in this study.

In general, an AFM system can be operated in three different modes: Contact mode, where the tip is in contact with the surface of the sample to scan the defined area; Non-contact mode, where the tip is very close to but does not touch the surface, and the cantilever is oscillated at or above the resonance frequency; Tapping mode, where the tip does not touch the surface, but the cantilever oscillates slightly lower than the resonance frequency. In tapping mode, damages to both tip and surface are limited compared to that in the contact mode.[36] We usually used the tapping mode in this thesis, and the model of the tips is Tap300Al-G-50-300 kHz, 40 N/m Tapping Mode from NanoAndMore USA, Inc.

2.3.3 Electrochemical Impedance Spectroscopy (EIS)

Electrochemical impedance spectroscopy (EIS) is a powerful method for characterizing the electrical properties of materials and their interfaces with electronically conducting electrodes.[37] The most common and standard approach is to apply an electrical stimulus to the electrodes and observe the response as a function of temperature, a partial gas pressure, and an applied static voltage or current bias. Any intrinsic property that may affect the conductivity of the electrodes and the electrolytes, especially in solid oxides fuel cell systems, can be studied by EIS.[38] The interpretation of a spectrum of impedance is based on the comparison between the spectrum of impedance and an "equivalent circuit" defined by a model. Although EIS is a highly valuable technique by its own, the analysis of complicated systems must be in connection with other experimental information to verify whether the defined equivalent circuit is physically reasonable. A more thorough treatment of impedance spectroscopy can be found in Reference[38].

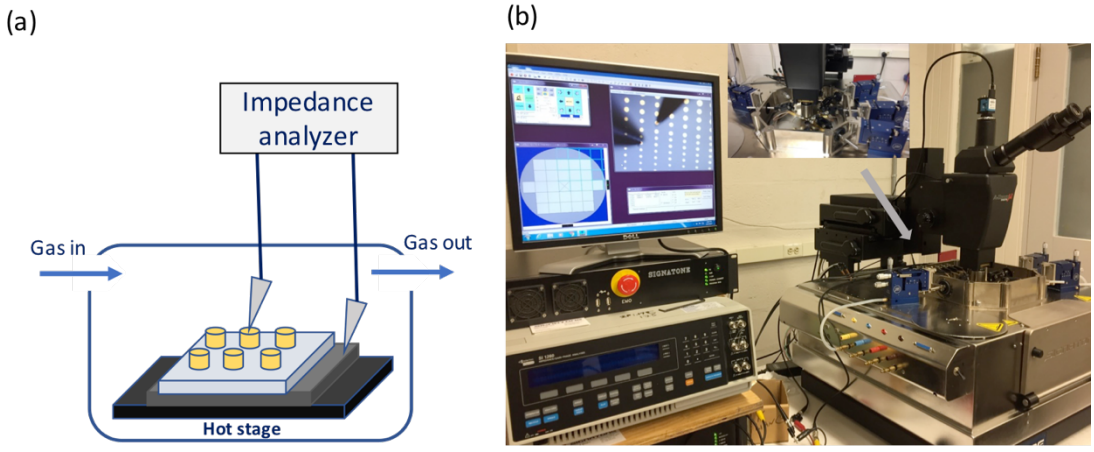

Figure 2.7 (a) Schematic of the EIS measurement setup inside the chamber of probe station. (b) Image of the EIS-Probe station system used for electrochemical measurements in this study.

The conventional DC measurements with two inert metal electrodes are difficult to probe the ionic conductivity of electrolytes due to the blocking of ions at the electrolyte/electrode interfaces. However, but the ionic conductivity can be easily obtained through the EIS measurements. The EIS measurements can also be used to identify the reaction mechanism of an electrochemical process. For instance, the EIS measurements can be used to determine the rate-limiting step in oxygen reduction reaction of cathode materials in an SOFC device.[39]

As shown in Figure 2.7a, a Solartron 1260 impedance analyzer with a two-probe measurement geometry was used in this work. The amplitude of a typical perturbation voltage signal for our SOFC materials was in a range of 10 to 50mV. Moreover, as shown in Figure 2.7b, the programmed probe station used in this work can automatically measure multiple devices fabricated on a single substrate.

Chapter 3: Out-of-Plane Electrochemical Transport in All-Thin-Film Heteroepitaxial Solid Oxide Fuel Cell Structures

3.1 Abstract

We have fabricated all-thin-film solid oxide fuel cell (SOFC) structures in order to probe fundamental transport properties of SOFC electrolytes in an out-of-plane measurement geometry using epitaxial films with ideal model interfaces. Epitaxial multilayer thin-film structures consisting of a bottom electrode ($SrRuO_3$ (SRO) or $Ba_{0.93}La_{0.07}SnO_3$ (BLSO)) and an electrolyte $Sm_{0.2}Ce_{0.8}O_{2-\delta}$ (SDC20) (600 nm - 1000 nm) on $SrTiO_3$ (100) single crystal substrates were fabricated using pulsed laser deposition. The heteroepitaxy of the multi-layer structures was confirmed by X-ray diffraction and high-resolution scanning transmission electron microscopy, and atomically sharp and structurally coherent interfaces were observed in the electrolyte/electrode bilayers. Electrochemical impedance spectroscopy (EIS) measurements of the devices at temperature range of 623 K to 823 K in air reveal electrochemical properties of SDC20 which are quantitatively consistent with known bulk transport properties of SDC20. This work demonstrates the utility of prototypical out-of-plane all-thin-film heteroepitaxial electrochemical devices as a model platform for directly investigating intrinsic transport properties of electrochemical materials in single-crystal-like structures with well-defined sharp interfaces.

3.2 Introduction

An important research direction in the field of multilayer thin films is the investigation of the ionic transport, which plays an essential role in the development of miniaturized solid oxide fuel cells (SOFCs). [21,40,41] Multilayer thin-film configurations offer the possibility to scale up the device size and reduce the operating temperatures of SOFCs, thus leading to potential applications of SOFCs in portable devices. [24,25,42-45] Indeed, enhanced ionic conductivity and robust thermal stability have already been demonstrated in epitaxial electrolyte thin films. [10,11]

A thin-film electrolyte layer impedes electron transport but facilitates the transfer of O^{2-}/H^{+} between the electrode layers. [46] Its high ohmic resistance for the thermally driven ionic charge transfer process results in low power density and low efficiency of SOFCs, and limits the deployment of SOFCs at low temperatures (573 K to 873 K). [19] Much efforts have been made to minimize the thickness of electrolytes from tens of micrometers to sub-micrometers in order to reduce the ohmic resistance at low temperatures. [24,25,42-45] A promising approach to fabrication of high-performance electrolytes involves synthesis of epitaxial thin films with controlled strain and orientations. Such materials have the potential to dramatically improve the transport properties of thin-film electrolytes. [47,48]

Most studies of electrolyte thin films to date are, however, based on in-plane transport measurements. The in-plane methods pose several problems, including: 1) the contribution of the film-substrate interface to the conduction, [49,50] 2) unavoidable influence of the parallel stray capacitance of the substrate on the impedance measurements, [51,52] and 3) the fact that in-plane transport is not the actual transport

geometry for real SOFCs. [13,53] In comparison, out-of-plane measurements in heteroepitaxial multilayer structures can be used to probe ionic transport through atomically sharp interfaces with well-defined geometries.

Unfortunately, performing out-of-plane conductivity measurements on electrolyte thin films with submicron thicknesses can be challenging due to frequently occurring shorts through pinholes and the fact that the film dimensions are drastically different from those of typical bulk devices. [54,55] To date, there have only been a handful of studies investigating the out-of-plane transport of thin-film electrolytes. [42,43,56-59] In these previous studies, polycrystalline electrolyte thin films were deposited on metal bottom electrode layers (e.g., Pt), [56] or free-standing electrolyte thin films were prepared through etching processes with Pt bottom contact layers deposited afterward. [43,59] Alternatively, niobium (Nb) doped $SrTiO_3$ (Nb:STO), an n-type semiconductor, [60] has been employed as a substrate for fabrication of epitaxial electrolyte thin films. [61,62] In other areas of oxide electronics such as ferroelectric thin film devices, [63,64] Nb:STO substrates are also frequently used, but they have been known to lead to formation of Schottky barriers at the interface influencing the overall performance of the devices, [63,64] and the role of such barriers which may form at the electrolyte/Nb:STO in electrochemical measurements has not been elucidated. [61] Here, we propose to use high-conductivity perovskite metal oxides, $SrRuO_3$ (SRO) and La-doped $BaSnO_3$ (BLSO), as bottom electrodes for epitaxial growth of electrolyte layers.

Conducting SRO epitaxial thin films are routinely used as electrodes for a variety of devices including ferroelectric capacitors, semiconductor devices, and lithium battery structures. [65-67] SRO is an ideal bottom electrode because of its

relatively low resistivity (≈300 μΩ·cm at 300K), [68] and its pseudo-cubic structure (a = 0.393 nm) which allows its epitaxial growth on common single crystal substrates such as STO, $LaAlO_3$ (LAO), MgO, and yttria-stabilized zirconia (YSZ). [68-71] The epitaxial SRO films have also been reported to be stable at a temperature up to 993 K under a moderate oxygen pressure (>100 Pa) and at ~1193 K in an oxidizing or inert atmosphere, [72] compatible with the operating conditions of SOFCs. In terms of the thermal stability, SRO is better than Pt, which has been observed to lead to damage to the electrolyte layer due to the coarsening of thin films at 1073 K. [58]

We have also looked at La-doped $BaSnO_3$ (BLSO) thin films. They are known to display high transparency in the visible range with high electrical conductivity, making them a good candidate for high-performance transparent conductors. [73-75] BLSO has already been demonstrated as a novel alternative anode material for oxide-ion low-temperature SOFCs. [76] Herein, we look at $Ba_{0.93}La_{0.07}SnO_3$ (BLSO) as an alternative epitaxial bottom electrode.

3.3 Experimental

3.3.1 Thin-film fabrication

Strontium ruthanate pellet (1.0" Dia. x 0.250" Thick) was obtained from Kurt J. Lesker Company. $BaSnO_3$, $La_2Sn_2O_7$, and $Sm_{0.2}Ce_{0.8}O_{2-\delta}$ pellets were sintered for PLD targets via a conventional powder pressing and sintering method. Barium carbonate, tin oxide, and lanthanum oxide were obtained from Sigma-Aldrich. Commercial $Sm_{0.2}Ce_{0.8}O_{2.0-\delta}$ (SDC20) powders were purchased from NexTech

Materials. Using these targets, $SrRuO_3$, $Ba_{0.93}La_{0.07}SnO_3$, and SDC20 thin films were grown on (001) oriented $SrTiO_3$ or $LaAlO_3$ single crystals (5 × 10 mm, CrysTec GmbH) by PLD with a KrF excimer laser (248 nm, fluence 0.8 J/cm^2, distance between target and substrate ~55mm) at a repetition rate of 5 Hz. All the single crystal substrates were ultrasonically cleaned in acetone and methanol prior to insertion into a dual-chamber UHV system. The optimized deposition temperature and oxygen pressure for the epitaxial SRO thin films on STO (001) substrates were 913 K and 13.3 kPa, respectively. The epitaxial BLSO films were grown on STO (001) or LAO (001) substrates by a monolayer-by-monoloayer growth method via controlling the deposition pulses of BSO and LSO targets under an optimized deposition temperature of 973 K and oxygen pressure of 7 kPa. SDC20 thin films were *in situ* grown on a SRO or BLSO layer under an optimized deposition temperature of 913 K and oxygen pressure of 4 kPa. Using X-Ray Reflectometry (XRR) or a stylus profilometry tool (Dektak), the deposition rates of SRO, BLSO, and SDC20 were determined to be 0.01 nm/s, 0.03 nm/s, and 0.05 nm/s, respectively. Following the depositions of SDC20, the samples were left in the PLD chamber with an oxygen background of 4 kPa during the cool-down period (5 °C/min). The fabrication process of the thin-film heterostructure is schematically shown in Figure 3.1 (a), where the substrate is STO (001) or LAO (001), the electrode is SRO or BLSO, and the electrolyte layer is SDC20.

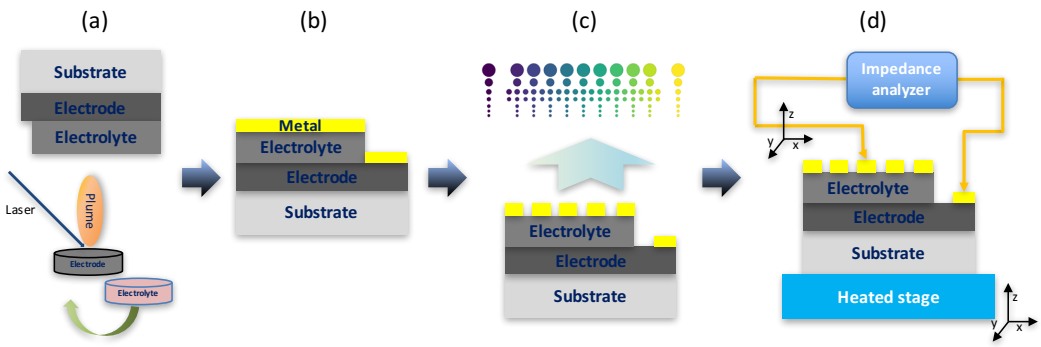

Figure 3.1 Schematic illustration of the fabrication process and measurement setup. (a) Heteroepitaxial films grown on single crystal substrates by a pulsed laser deposition system. (b) Metal electrodes fabricated onto thin films by a thermal evaporation of Cr and Au. (c) A library of microelectrodes defined through photolithography and ion milling. (d) Electrochemical impedance measured by a semi-automatic probe station system.

3.3.2 Microdot electrodes patterning

The top metal layers were deposited onto the films by thermal evaporation of chromium (Cr) and gold (Au) at a base pressure of 2.6×10^{-4} Pa (Figure 3.1 (b)). The metal layer served as the top electrodes and current collectors. Its total thickness was around 100 nm including the very thin layer of chromium (5nm) as the adhesive material. The gold layer was then patterned into a library of microelectrodes using photolithography and ion milling. Specifically, the sample was coated with a photoresist (Shipley 1813) by a regular spin coating method (4000 rpm for 50 s). After spin coating, the photoresist was baked at 373 K for 2 min. Following an exposure to UV radiation for 12 s through a photomask, it was developed in Shipley 352 developer for 40 s. The sample then underwent ion milling for 20 min, resulting in a milling depth of ≈110 nm. In the final step, the residual photoresist was stripped using acetone. In

this manner, a circular microelectrode array with diameters of 30 to 500 μm was defined as the top contact of the device. The layout of a library of circular microelectrodes was shown in Figure 3.1(c), where the color indicates the different distances from the side.

3.3.3 Characterization

X-ray diffraction was performed on a Bruker D8 Discover with 4 bounce monochromator (40 kV, 40 mA, Cu Kα) in geometries of θ-2θ and phi (φ) scans before and after EIS measurements. High angle annular dark field (HAADF)-STEM images were acquired from the prepared lamellas using a probe corrected FEI Titan 80–300 microscope operated at 300 kV. The probe is typically corrected to 20 mrad, providing a spatial resolution of 0.1 nm. The probe convergence angle is 24 mrad, and the HAADF inner and outer collection angles are 70 and 400 mrad, respectively. Atomic force microscopy (AFM, Digital Instruments Nanoscope III and Dimension 5000) was used to characterize the as grown films. Scanning electron microscopy (SEM) of the post-tested device was performed using a Hitachi SU-70 with field emission gun.

3.3.4 Electrical measurement and data analysis

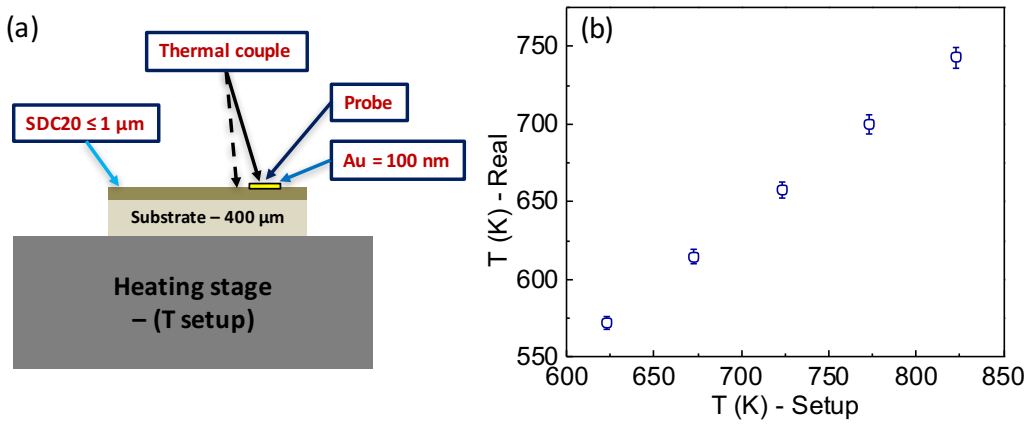

Figure 3.2 Temperature calibration of the heating stage. (a) Schematic of the experiment setup. (b) The relationship between the setup temperature and film surface temperature.

Electrochemical impedance spectroscopy (EIS) was performed on a semi-automatic probe station (Lucas Signatone Corporation) with the aid of a Solartron 1260 impedance analyzer as shown in Figure 3.1 (d). Before the EIS measurements, one multilayer device sample was used to calibrate the temperature between the setup temperature of heating stage and the film surface temperature measured by a K-type thermocouple as shown in Figure 3.2. (The temperature gradient across SDC20 layer is negligible due to the very small thickness (≤1 µm)). The sample was heated by a heating stage in ambient air and an AC voltage with an amplitude of 20 mV and a frequency range of 1 Hz to 10 MHz were used in the EIS measurements. Two gold plated probe tips are controlled by two individual micro-positioners to contact a top microelectrode and the bottom electrode easily. The heating stage can be controlled to move 3-dimensionally with micron resolution by entering the appropriate coordinates

in the control software. In this way, we were able to contact each microelectrode accurately and perform the EIS measurement in the temperature range of 623 K to 823 K at a 50 K interval. The AC impedance data were measured after a waiting period of 30 minutes for temperature stabilization. The obtained data were simulated with ZView Software (3.4c version, Scribner Associates, Inc.) to extract the appropriate equivalent circuit for the cell. Temperature dependence of the electrical transport properties of SRO and BLSO were investigated using a standard 4-wire method in a physical property measurement system (PPMS, Quantum Design Inc.). I-V curves were measured with a precise current meter (Picometer, Voltage source model Keithley 2400) through two successive contacts at a temperature range of 300 K to 823 K in air.

3.4 Results and discussion

3.4.1 High crystalline and heteroepitaxial SDC20 thin film

We use $Sm_{0.2}Ce_{0.8}O_{2-\delta}$ (SDC20) as the electrolyte for epitaxial growth. SDC20 has a cubic fluorite structure with a lattice constant of 0.543 nm (JCPDS 34-0394). SDC20 is an ideal electrolyte material because of its high ionic conductivity in an intermediate temperature range and well-known bulk transport properties. [77,78]

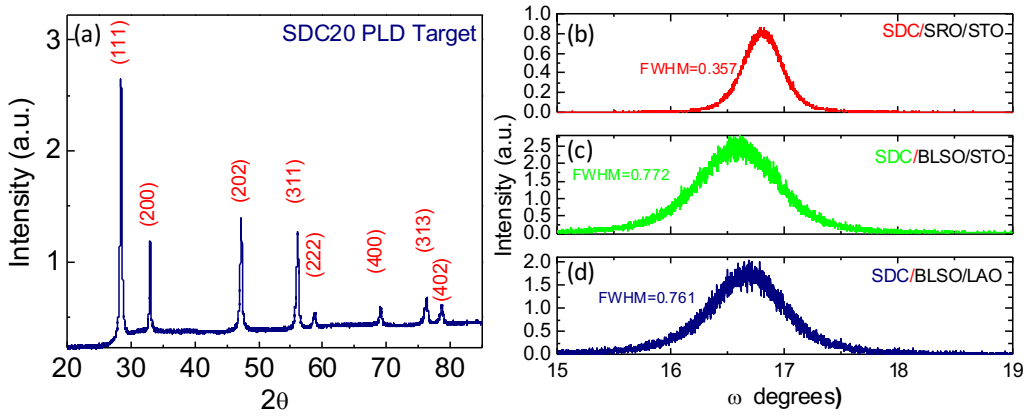

Figure 3.3 (a) The XRD spectrum of the SDC20 PLD target. The rocking curves of SDC20 (200) peak, (b) on SRO/STO (001), (c) on BLSO/STO(001), and (d) on BLSO/LAO(001) after EIS measurements.

Pulsed laser deposition (PLD) was used to grow a 100 to 200 nm thick SRO or BLSO bottom layer on STO (001) substrates. Following the deposition of the bottom layer, a 1 μm thick SDC20 electrolyte layer was fabricated on top by PLD. Figure 3.4a and 3.4b show X-ray diffraction (XRD) patterns of SDC20 films grown on STO (001) substrates with bottom electrode layers of SRO and BLSO, respectively. Only the (002) reflections (45.3° for SRO in Fig. 3.4a and 43.8° for BLSO in Fig. 3.4b) are observed from the bottom electrode layers. The peak positions of SDC20 thin films correspond to the (00l) reflections of the bulk SDC20 with a lattice constant of 0.543 nm (Figure 3.3a). [78] The in-plane 4-fold symmetry of SDC20 thin films on SRO and BLSO is observed in the Ø scans as shown in the Figure 3.4c and 3.4d, respectively. The result indicates an in-plane rotation of 45° of the SDC20 [100] direction with respect to the STO [100] direction. The peaks in Figure 3.4d are broader compared to those in Figure 3.4c, indicating the presence of an in-plane mosaicity in the SDC20 film grown on

BLSO. [79] The FWHM values of rocking curves for (002) peaks of SDC20 films grown on SRO and BLSO are 0.36 ° and 0.77 ° (Figure 3.3b), respectively.

Figure 3.4e to 3.4g show the cross-sectional HAADF-STEM images of a SDC20/SRO/STO (001) sample. As seen in the lower-magnification image (Figure 3.4e), both SRO and SDC20 layers are smooth and uniform in thickness. It can be seen in a high magnification image (Figure 3.4f) that the SRO-SDC20 interface is flat and atomically sharp, indicating that SDC20 has grown coherently with the [110] direction of SDC20 parallel to the [100] direction of SRO. The in-plane epitaxial relationship is STO (100)‖SRO (100) ‖SDC20 (110). Similarly high quality epitaxial microstructure was also confirmed with transmission electron microscopy (TEM) for SDC20/BLSO/STO(001) structures. The AFM images as shown in Figure 3.5 indicate that SDC20 films are rather flat with the root mean square surface roughness of 4.9 nm (5 μm × 5 μm) for SDC20/SRO/STO(001) and 5.3 nm (5 μm × 5 μm) for SDC20/BLSO/STO(001). The root mean square surface roughness of SDC20/SRO and SDC20/BLSO is 0.69 nm and 1.46 nm (5 μm × 5 μm, Figure 3.5), respectively. The dense and smooth surface of bottom electrode films is very important to the epitaxial growth of electrolyte layer.

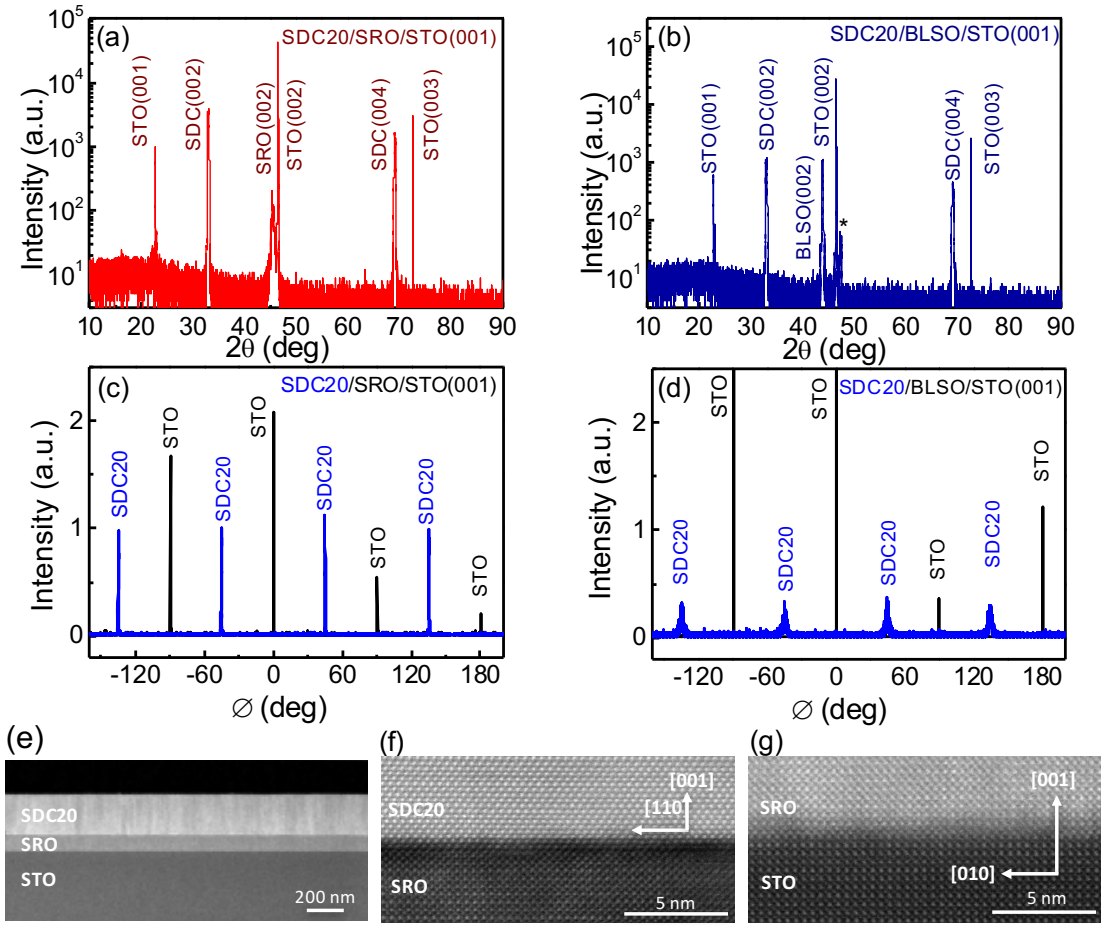

Figure 3.4 XRD θ-2θ-scans of a SDC20/SRO/STO (001) multilayer, and (b) a SDC20/BLSO/STO (001) multilayer. Asterisk mark (*) indicates the (202) peak of SDC20. (c) XRD Ø scans of the (202) plane reflections of STO and SDC20 on SRO/STO (001), and (d) on BLSO/STO (001). (e) Low-magnification cross-sectional HAADF-STEM image of the SDC20/SRO/STO (001) sample. (f) The atomically resolved HAADF-STEM images at the SDC20/SRO interface, and (g) at the SRO/STO (001) interface.

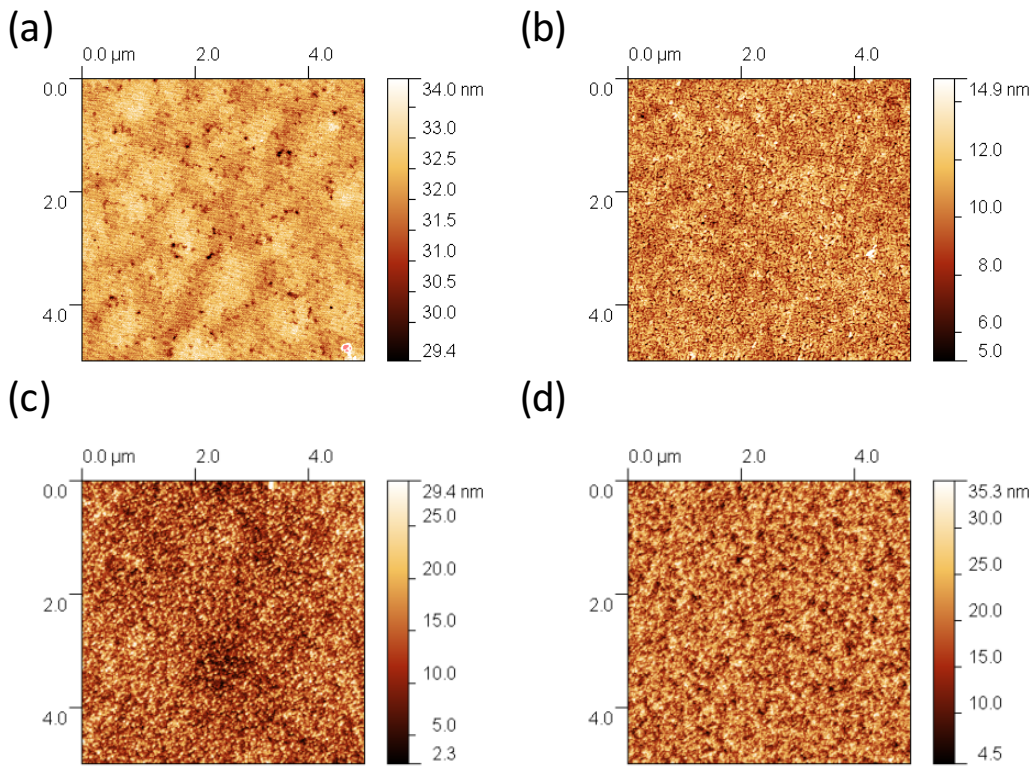

Figure 3.5 Atomic force microscopy (AFM) topography images. (a) The SRO film grown on STO(001) with a RMS 0.69 nm at 5×5 μm^2; (b) The BLSO film grown on STO(001) with a RMS 1.46 nm at 5×5 μm^2; (c) The SDC20 film grown on SRO/STO(001) with a RMS 4.9 nm 5×5 μm^2; (d) The SDC20 film grown on BLSO/LAO with a RMS 5.3 nm 5×5 μm^2.

3.4.2 Cox and Strack geometry for impedance measurements

To complete the device structure, a top metal electrode layer consisting of Cr (5 nm) and Au (95 nm) was deposited on the surface of SDC20 by thermal evaporation, and it was patterned into an array of microelectrodes using photolithography and ion milling. The fabricated device structure is schematically illustrated in Figure 3.6a. Figure 3.6b shows an overview SEM image of the microelectrodes with different diameters grown on the surface of SDC20 electrolyte. Figure 3.6c and 3.6d show the

dense surface and sharp edge of Au microelectrodes, respectively. The SEM images indicate that the top microelectrodes with diameters ranging from 30 μm to 500 μm formed on the electrolyte film are well-defined and stable even after annealing for 2 hours at 823 K in air.

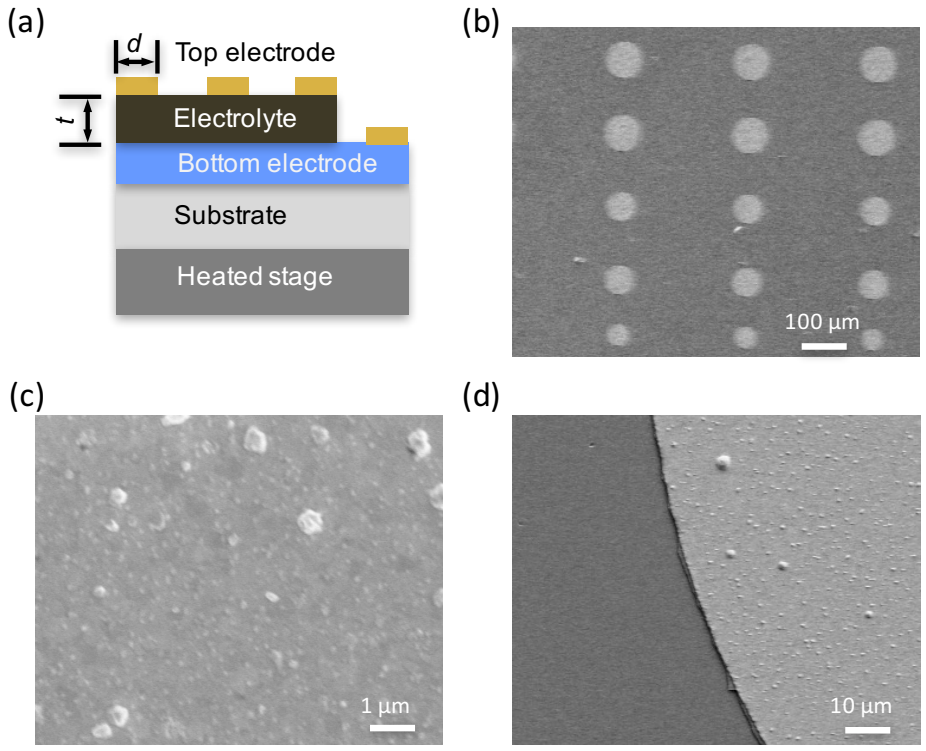

Figure 3.6 (a) Schematic of the measurement geometry for the fabricated thin-film electrochemical device. (b) The overview of the microelectrode array at the surface of SDC20 electrolyte, (c) A magnification of the Au surface, and (d) The edge of a microelectrode.

We have used a Cox and Strack geometry[80] for analysis of the electrochemical impedance spectroscopy (EIS) measurements. The method of Cox and Strack utilizes the structure of Figure 3.6a, where the resistance of a circular contact on a conducting or semiconducting epitaxial or bulk layer is to be measured. The top Au microelectrodes serve as electrolyte boundary, and only the area covered by

microelectrode is stimulated and recorded during the EIS measurement. In this configuration, the spreading resistance of the electrolyte layer, $\boldsymbol{R_s}$, between a top circular microelectrode and a bottom electrode is given by:

$$\boldsymbol{R_S = \frac{\rho}{\pi d} tan^{-1}\left(\frac{4t}{d}\right)} \qquad (1)$$

where $\boldsymbol{\rho}$ is the resistivity of the electrolyte, $\boldsymbol{d}$ is the diameter of the circular microelectrode, and $\boldsymbol{t}$ is the thickness of the electrolyte. The Newman's formula ($\boldsymbol{R_s = \frac{\rho}{2d}}$) which is usually used to estimate the conductivity of the specimen in SOFC studies can give accurate approximations only when $\boldsymbol{t}$ is substantially larger than $\boldsymbol{d}$, as in typical bulk devices. [81-83] When the thickness of the electrolyte is less than the diameter of the circular microelectrode ($\boldsymbol{t/d}$ < 0.25), Equation (1) was found to give the spreading resistance with an accuracy better than 0.1% based on Finite Element Analysis and experimental results.[80,84] In the present work, Equation (1) was used to calculate the conductivities of electrolytes based on $\boldsymbol{R_s}$ values measured by EIS in the $\boldsymbol{t/d}$ ratio range (<0.01).

Compared to standard bulk devices, one measurement challenge in thin-film devices grown by PLD is the limited thickness of the electrolyte (≈ 1μm). While 1 μm is substantially thinner compared to a typical bulk device, for PLD 1 μm is considered a thick film, where it becomes nontrivial to grow smooth films while maintaining the high-quality epitaxial integrity of the material. [48] When the thickness is limited, the out-of-plane resistance of electrolyte in thin film structures becomes comparable to the electrode resistance at high temperatures because the resistivity of an electrolyte such as SDC20 decreases with increasing temperature.[85] For instance, for typical thin film device dimensions ($\pi \times (150\ \mu m)^2$ for area and thickness 1 μm), the resistance of SDC20

would decrease from 7.86×10^{3} Ω at 523 K to 67 Ω at 723 K as estimated using the bulk conductivity of SDC20 (8.55×10^{-4} S/cm at 673 K). [86] The electrode resistance then is of the same order of magnitude at 723 K (≈15 Ω, 200 nm SRO at 723 K in this study). In order to ensure that we are properly probing the impedance through the electrolyte, an array of microelectrodes with varying diameters (30 µm to 500 µm) is employed, so that based on Equation (1), we can monitor the change in the resistance of the electrolyte as a function of the diameter of the circular microelectrode. A number of individual microelectrodes placed on each sample also enables statistical averaging and ensures data reproducibility.[87]

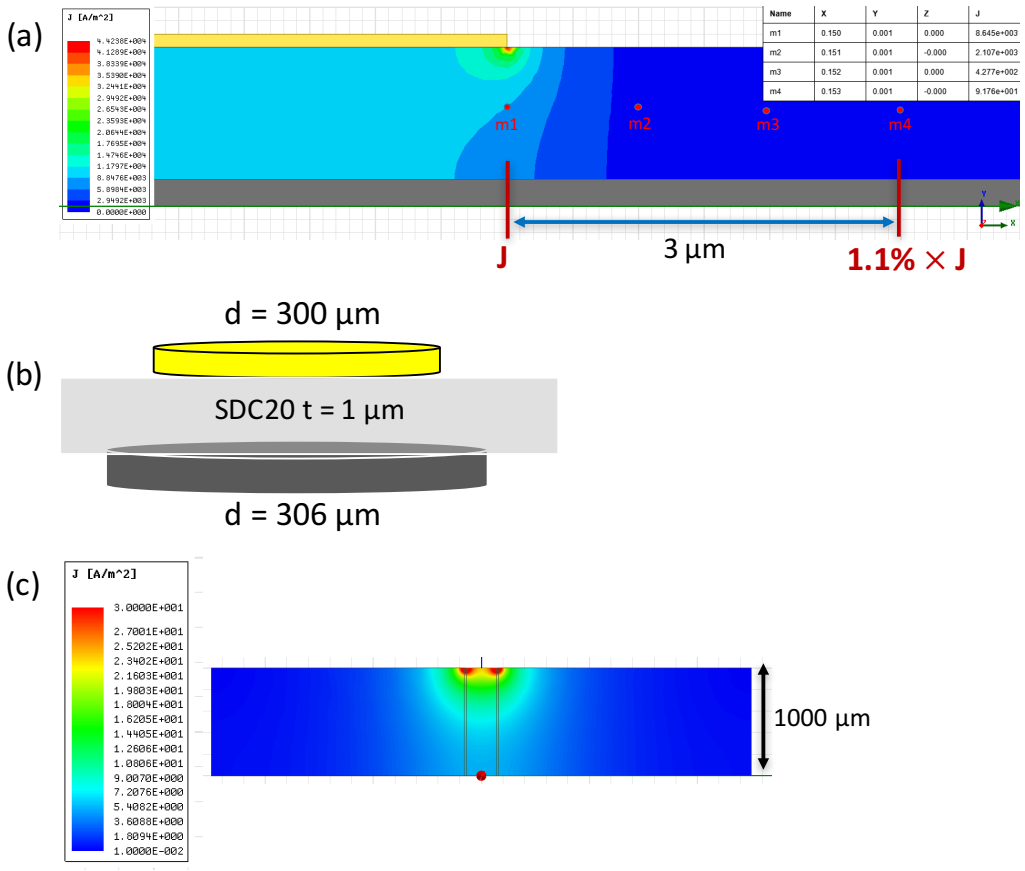

Figure 3.7 ANSYS Maxwell 2D Simulations. (a) The modeling of current spreading through the SDC20 electrolyte film with 1 µm thickness. (b) The schematic device

structure of Au/SDC20/SRO. (c) The modeling of current spreading through the SDC20 electrolyte film with 1000 μm thickness.

The current-flow pattern is axial, through the layer to the bottom electrode. The current distribution through the SDC20 electrolyte thin film ($\leq$ 1 μm) is pretty well localized by the top Au microelectrode based on ANSYS Maxwell 2D simulations as shown in Figure 3.7. For ANSYS Maxwell 2D Simulations, an excitation voltage (20 – 100 mV) was applied on Au electrode (d = 300 μm, 100 nm thick) with a frequency range of 1kHz to 100 MHz as shown in Figure 3.7b. SRO is grounded and its conductivity is 3×10^5 S/m with a thickness of 200 nm. The electrolyte conductivity and thickness are in a range of 10^{-2} to 10^{-1} S/m and 600 nm to 1000 μm, respectively.

When the thickness of SDC20 is 1 μm, the current density at the position of m4 (3 μm away the position of m1) is only about 1% of the current density of m1 (Figure 3.7a) and the area is enlarged by ~4% on SRO layer compared to the area of top Au electrode (Figure 3.7b). The current distribution is pretty well localized and the factor that the area is increased by ~4% is still taken into account in our experiments. When the thickness of SDC20 is 1000 μm, the current distribution is clearly illustrated in Figure 3.7c. That is also why Newman's formula works only when $\boldsymbol{t}$ is substantially larger than $\boldsymbol{d}$.

3.4.3 Electrical properties of bottom electrodes

This Cox and Strack structure requires metallization of both the top and the back electrodes for a successful operation of the device. In this work, the top microelectrode is 100 nm Au, which has been used extensively due to its low resistivity

and high stability. Therefore, the bottom electrode is critical to the success of the device. Ideally, a bottom electrode has a low resistivity and a stable Ohmic contact in the measurement temperature range. Thus, we first investigated the temperature dependence of the electrical transport properties of SRO and BLSO thin films on STO (001) substrates (Figure 3.8). The conductivity of SRO and BLSO goes from 2.1×10^3 s/cm and 3.3×10^3 s/cm at 300K to 1.4×10^3 s/cm and 1.5×10^3 s/cm at 743 K, respectively. The results are consistent with their conductivity values obtained on bulk single crystals, [68,88] and are about one order of magnitude higher than that of 0.7% wt Nb:STO (1.43×10^2 s/cm at 300 K, MTI Corporation). The Mott-Ioffe-Regel (MIR) limit behavior was observed in Figure 2b (red line), implying that the resistivity of a SRO thin film saturates at around 720 μΩ·cm at high temperatures.[89] The current (I) and the voltage (V) relationships of the Au/SRO and Au/BLSO structures at different temperatures were obtained using a two-point probe method. The linear I-V curves as shown in Figure 3.8c and 3.8d in the whole bias range from -50 mV to 50 mV suggest that all the contacts are Ohmic in the temperature range of 300 K to 800 K and there is no Schottky barrier formed at the interface between Au and the metal oxide.

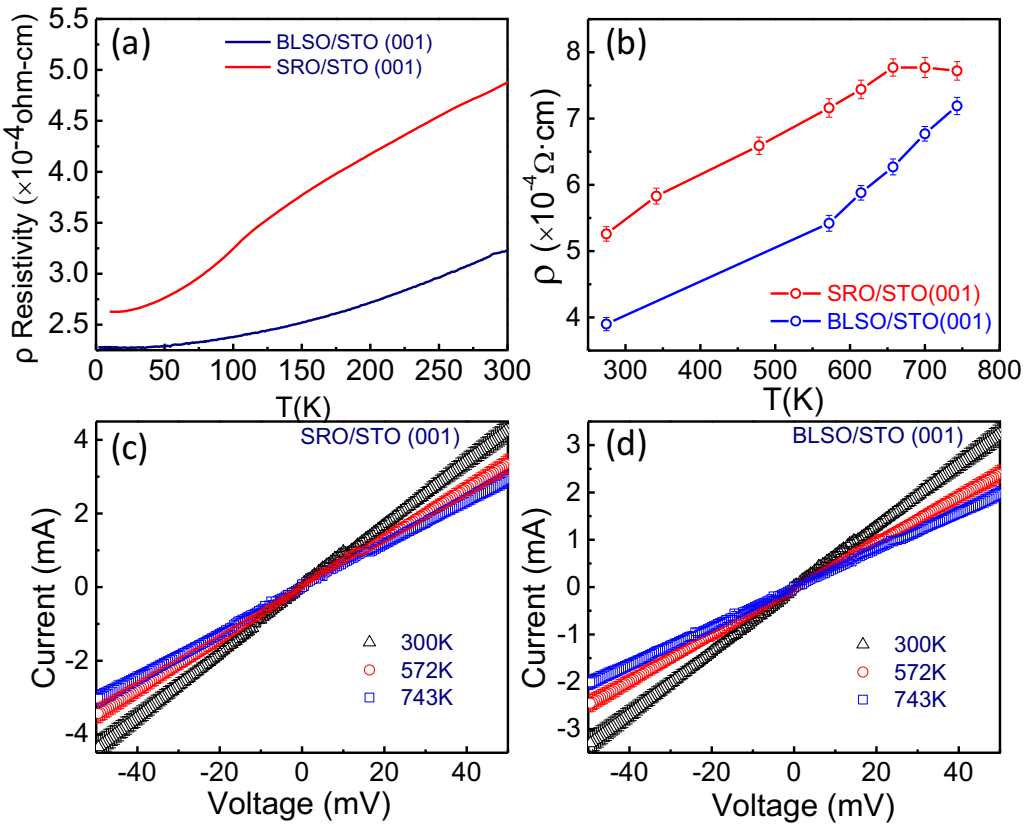

Figure 3.8 (a) The temperature dependence of the electrical resistivity of SRO and BLSO films on STO (001). (b) The temperature dependence of the electrical resistivity of SRO film on STO (001) and BLSO film on STO (001). The error bars represent multiple measurements. (c) Current-voltage curves between the Au contact and SRO bottom electrode, and (d) between the Au contact and BLSO bottom electrode.

While both SRO and BLSO show low resistivity, their contribution to the measurement can still be substracted by making an identical device without SDC20 electrolyte layer as shown in the inset of Figure 3.9. As we discussed in the part of 3.4.2, the current flow is well localized by the top circular Au microelectrode, therefore, the resistance from electrodes in the device of Au/SRO(BLSO)/STO is about the same as that in the device of Au/SDC20/SRO(BLSO)/STO. From the plots of frequency-dependent real part impedance in Au/SRO and Au/BLSO bilayer devices in the

temperature range of 300 K to 800 K as shown Figure 3.9, the background resistance (from top and bottom electrodes) can be obtained. The plots in Figure 3.9 also reveal the pure electronic conducting properties of SRO and BLSO based on the linear curves with zero slope in the whole frequency range of 1Hz to 1MHz.

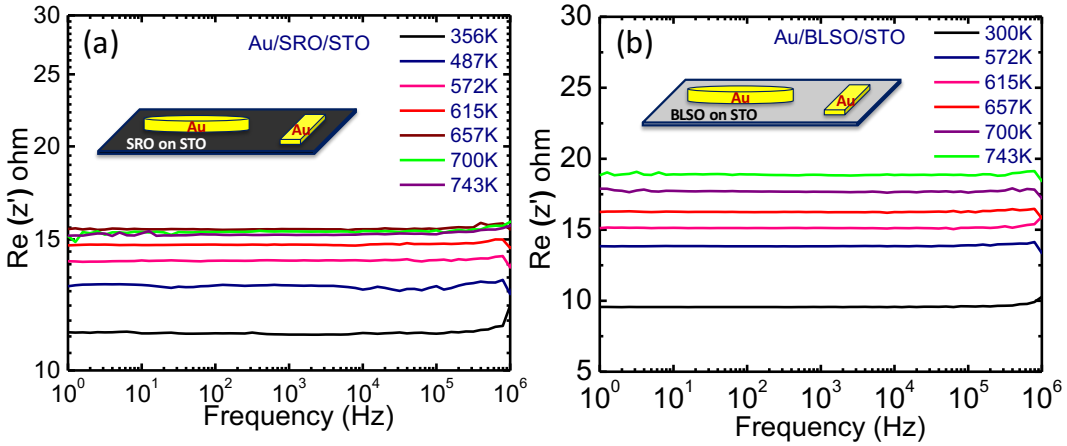

Figure 3.9 (a) Frequency dependence of the real part of impedance measured on Au(100nm)/SRO(200nm)/STO(001). The inset shows the measurement geometry. (b) Frequency dependence of the real part of impedance measured on Au(100nm)/BLSO (100nm)/STO(001). The inset shows the measurement geometry.

3.4.4 EIS results of the electrochemical devices

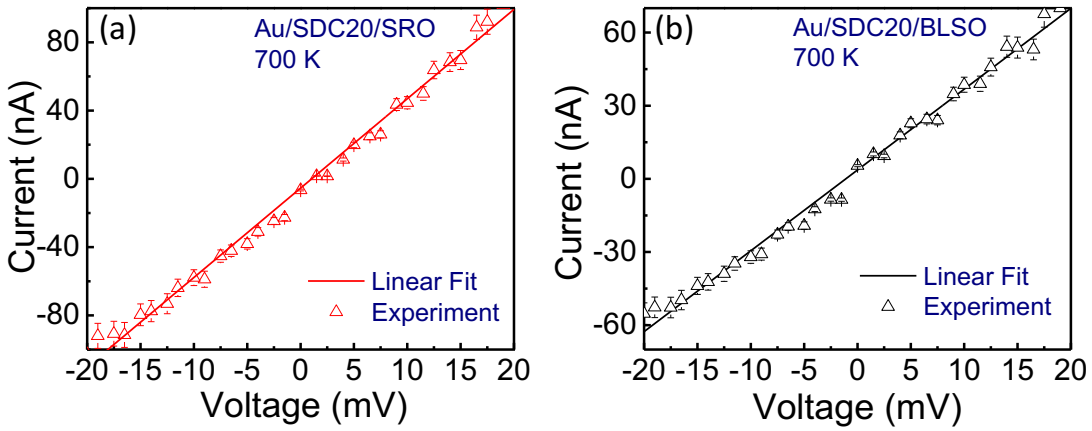

Figure 3.10 (a) Current-voltage curves between the SRO bottom electrode and SDC20 electrolyte at 700 K, and (b) between the BLSO bottom electrode and SDC20 electrolyte at 700 K. The error bars represent multiple measurements.

We first measured the I-V curves of Au/SDC20/SRO(BLSO) to check the DC resistance. As both Au and SRO(BLSO) are ionic insulating, the DC resistance represents the electronic conducting property of SDC20. As shown in Figure 3.10, the total DC resistance is around 10^5 Ω at 700 K. The resistances from bottom electrodes (SRO or BLSO) and the top Au electrode are negligible, and thus, the total DC resistance is dominated by the SDC20 thin film and their interfaces with electrodes (SRO or BLSO and Au).[90] The DC conductivity values agree well with previous results and is several orders of magnitude smaller than the ionic conductivity of SDC20 under similar experimental conditions. [61]

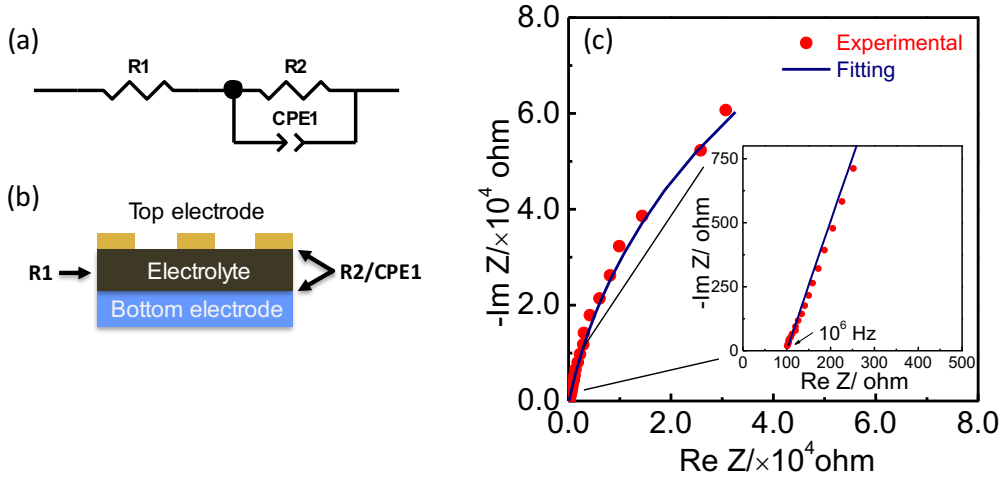

Figure 3.11 (a) The equivalent circuit used in this work. (b) The main origins of R1 and R2/CPE1 based on the device geometry in this work. (c) A representative Nyquist plot measured at 700 K on Au($d = 300\mu m$)/SDC20/SRO/STO structure. The inset shows an enlargement of the indicated region.

Two-probe EIS measurements were performed to investigate the transport properties of the thin-film electrolyte/bottom electrode structures in a temperature range of 623 K to 823 K in air using a semi-automatic probe station. A simplified Randles circuit[66] as shown in the inset of Figure 3.11a was used to fit the impedance data with the ZView Software (3.4c version)[1]. The model circuit includes the charge transfer resistance (R2) in parallel with a constant phase element (CPE1) that describes the double layer capacitance between electrode and electrolyte, in series with the total ohmic resistance R1. A representative impedance spectrum (Figure 3.11c) shows the typical features of an electrochemical device comprising the oxygen ion blocking and

[1] Certain commercial equipment and materials are identified in this paper in order to specify adequately the experimental procedure. In no case does such identification imply recommendations by the National Institute of Standards and Technology nor does it imply that the material or equipment identified is necessarily the best available for this purpose.

inert electrodes[61]: an intercept to the real part axis at high frequency corresponding to R1 as shown in the inset of Figure 3.11c, and a very large and depressed arc in the medium to low frequency range is attributed to the electrode response. Our focus in this study is the transport properties of electrolytes, so we only focus on the high frequency axis intercept (R1) by simulating every impedance spectrum using a complex non-linear least squares (CNLS) fitting routine. The total ohmic resistance R1 includes the background resistance mainly from both electrodes and a spreading resistance from the SDC20 electrolyte. The spreading resistance ($\boldsymbol{R_s}$) of electrolyte SDC20 was extracted by measuring the background resistance separately from an identical device structure, but were made without the SDC20 layer as discussed in the part of 3.4.3.

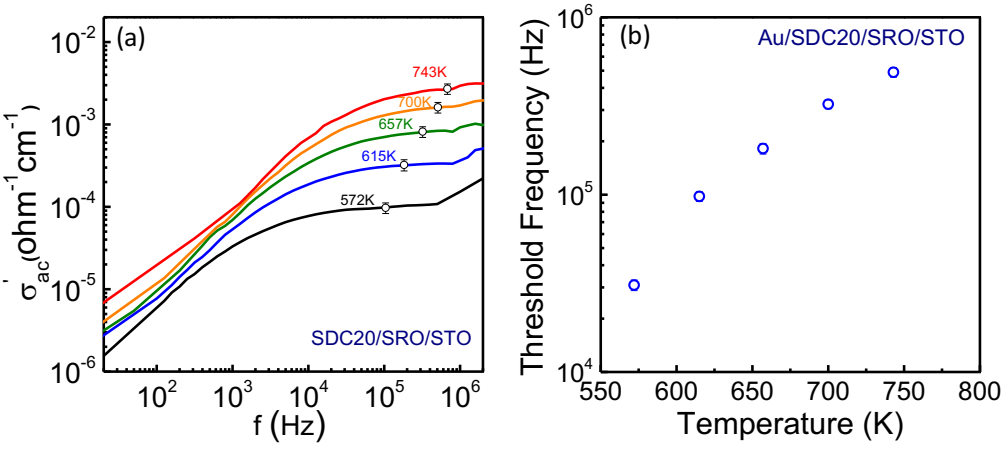

Figure 3.12 (a) Frequency dependence of the real part of ac conductivity σ'_{ac} measured on Au($d = 200\mu m$)/SDC20/SRO/STO structure at different temperatures. The error bars represent the spread in plateau positions. (b) Temperature dependence of the threshold frequency marking the onset of ac conductivity in (a).

Figure 3.12a shows the plots of frequency dependence of the real part of the ac conductivity σ'_{ac} in a temperature range of 500 K to 800 K. The relationship between σ'_{ac} and f exhibits the characteristic electrical response of this model system where the

ion conduction layer sandwiched with ion-blocking electrodes.[61] As Figure 3.12a shows, the σ'_{ac} decreases with decreasing frequency at the high-frequency parts since ac conductivity is governed by ion movements in this region.[91] At intermediate frequency, σ'_{ac} is not a strong function of *f* and the distinct plateaus appear due to long-range ion transport. At low frequency, σ'ac decreases again with decreasing *f* since the ions are blocked by the electrodes and accumulated there.[92,93] The distinct plateaus at intermediate frequencies were determined by the local minima of the derivative curves and represented by the solid circles as shown in Figure 3.12a. The plateaus can be used to define the ionic conductivity σ'_{ac}, [91,93,94], which are also in good agreement with the fitting results. The ionic conductivity increases with increase in temperature and the frequency leading to the onset of ac conductivity to also increase as observed in Figure 3.12b. [61,92] These features confirm the ionic conducting nature of SDC20 films and represent the characteristic electrical response of the multilayer system where the ion conduction layer is sandwiched by two ion-blocking electrodes.[92] Our thin-film heteroepitaxial devices, thus, accurately capture the main feature of the electrolyte, indicating that SRO and BLSO can both be used as bottom electrodes for investigating the thin-film electrolytes for SOFCs applications.

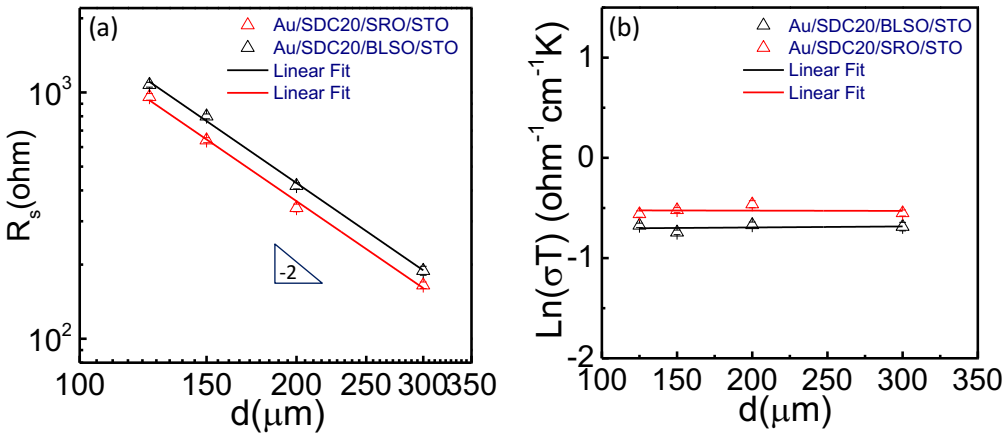

Figure 3.13 (a) SDC20 spreading resistance ($\boldsymbol{R_s}$) as a function of the microelectrode diameter at 657 K. (b) Diameter dependence of SDC20 ionic conductivity calculated based on Equation (1) at 657 K.

The effect of the diameter of microelectrodes on the impedance response was explored by extracting the spreading resistance from microelectrodes with diameters ranging from 100 μm to 350 μm as shown in Figure 3.13a. Applying which spreading resistance equation to do experimental data analysis is critical for a reasonable evaluation of the ionic conductivity of electrolytes. Here, R_s is dominated by the resistance of a very thin electrolyte (≤ 1 μm) after the subtraction of background resistance. If Newman equation ($\boldsymbol{R_s} = \frac{\boldsymbol{\rho}}{\boldsymbol{2d}}$) is used when the $\boldsymbol{t/d}$ ratio is large enough, the slope will be -1 in the double-logarithmic plot.[87] If the $\boldsymbol{t/d}$ ratio is approaching zero, we can use the equation of $\boldsymbol{R_S} = \frac{\boldsymbol{4\rho t}}{\boldsymbol{\pi d^2}}$, a slope of -2 will be expected. As for the diameter ($\boldsymbol{d}$) dependence of spreading resistance ($\boldsymbol{R_s}$) in this work, the power-law relation of (1) with a slope of around 2 is expected due to the small $\boldsymbol{t/d}$ ratio. This is confirmed by our experimental results as shown in Figure 3.13a, where the slopes of -

1.99 and -1.98 were obtained. The conductivity of SDC20 determined from Equation (1) is approximately constant and independent of the diameter of microelectrodes at 657 K as seen in Figure 3.13b, indicating that Equation (1) can provide a reasonable evaluation of the ionic conductivity of electrolytes in our model system.

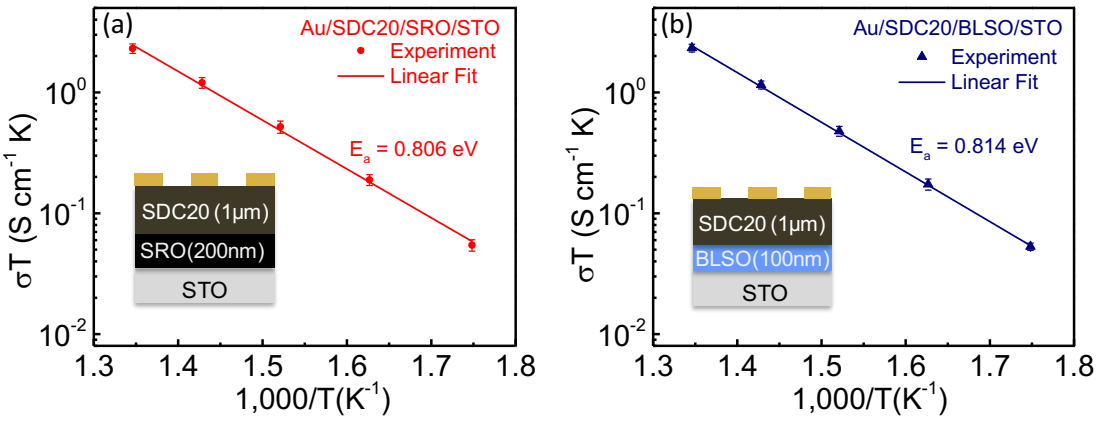

Figure 3.14 Temperature dependence of ionic conductivity and the Arrhenius plots of the Au/SDC20/SRO/STO structure (a) and the Au/SDC20/BLSO/STO structure. The error bars represent the spread of conductivities based on different diameters of microelectrodes.

Figure 3.14 shows the temperature dependence of the conductivity of SDC20. It follows the Arrhenius behavior for both multilayer thin-film structures. The average oxygen ion conductivity of SDC20 obtained in Figure 3.14 is around 9.8×10^{-4} S/cm at 673 K, which is very close to the bulk conductivity of polycrystalline SDC20 pellets ($\approx 8.55 \times 10^{-4}$ S/cm at 673 K).[86] The activation energies (E_a) for the oxygen ionic conductivity in SDC20/SRO/STO and SDC20/BLSO/STO were determined to be 0.806 eV and 0.814 eV from Figure 3.14a and 3.14b, respectively. The results are in good agreement with the bulk E_a values reported in literatures. [58,86] The transport

properties of electrolytes in this study reflect exclusively the bulk properties, and thus avoiding the effects of grain boundaries on the transport is possible. This is one obvious advantage in SOFCs field, as we know that, at higher temperatures, only the single crystals, sintered pellets with very large average grain size or highly ordered thin films allow a direct measurement of the bulk oxygen ion conductivity.[95] Single crystals are expensive and sintered pellets with micro-meter grain size are difficult to be fabricated. In this out-of-plane thin-film device, even though there is trace amount of impurity phases, the contribution of grain boundaries to the impedance is neglected due to their large resistance with respect to the bulk phase under the out-of-plane geometry (be parallel to the electric field) based on the brick-layer mode.[96] Therefore, the measurement of epitaxial out-of-plane thin film devices is a valuable alternative for direct measurements of the intrinsic bulk ionic transport properties. The above results indicate that our all epitaxial systems are suitable for probing the bulk ionic transport properties directly at high temperatures.

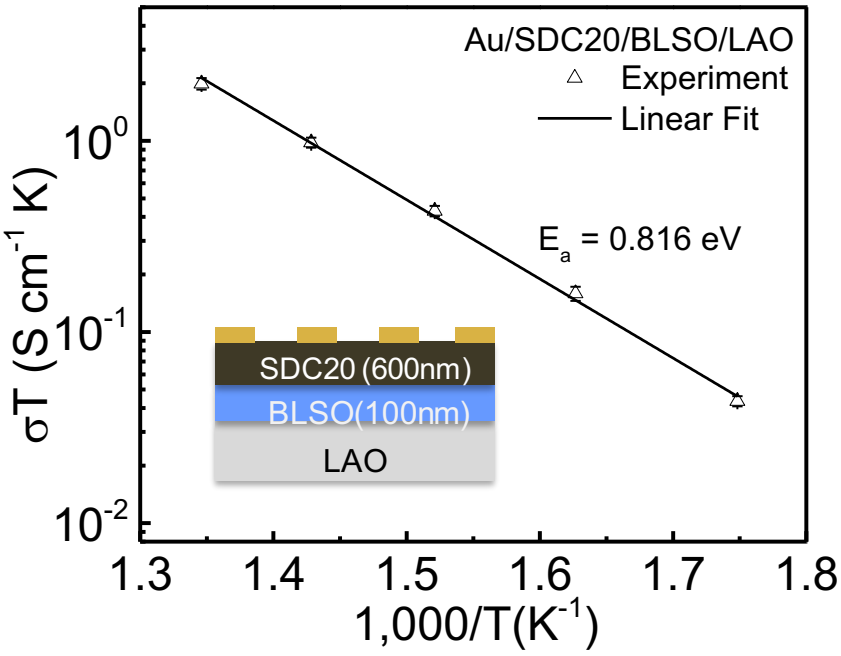

Figure 3.15 (a) Temperature dependence of ionic conductivity and the Arrhenius plots of the Au/SDC20/BLSO/LAO structure. The error bars represent the spread of conductivities based on different diameters of microelectrodes.

Finally, the flexibility of the epitaxial platform and the reproducibility of the out-of-plane device design were demonstrated by fabricating the same SDC20/BLSO structure on LAO(001) using the same growth and characterization methods discussed above. The devices on LAO(001) substrates were found to be thermally stable, and EIS results similar to devices on STO(001) were obtained as shown in Figure 3.15a.

3.5 Conclusions

In summary, we have successfully demonstrated a PLD-based fabrication approach for out-of-plane heteroepitaxial thin-film electrochemical devices and the feasibility of using the devices to evaluate single-crystal-like properties of electrolytes

for SOFC applications. The electrically conducting SRO and BLSO are promising bottom electrode materials for thin-film SOFC structures, both exhibiting very low equivalent series resistance in the relevant temperature range for SOFCs. Despite their limited thickness compared to conventional bulk devices, the present devices accurately capture the bulk ionic transport properties of thin-film electrolytes at different temperatures and circumvent undesired influence from the substrates. The model system is also a practical device geometry for miniaturization of electrochemical devices. This work may also open up new avenues for investigating the intrinsic/bulk properties of electrochemical materials at the nanoscale level. Because growth of epitaxial buffer layers of STO on Si is a well-established technique,[97] an exciting possibility for the future is to directly integrate all epitaxial SOFC microdevices on Si-based platforms.

Chapter 4: Thin Film Cathode Materials for Intermediate Temperature SOFCs

4.1 Abstract

The development of cathode materials with high catalytic activity for the oxygen reduction reaction plays an important role in determining the performance of solid oxide fuel cells (SOFCs) at relatively low temperatures. The mixed ionic-electronic perovskite-type oxide $La_{0.6}Sr_{0.4}Co_{1-x}Fe_xO_{3-\delta}$ is a state-of-the-art cathode material for intermediate temperature SOFCs. However, there is no consensus on the mechanisms of oxygen reduction reactions (ORR) at the surface of mixed conducting cathode materials, which is possibly due to the different and complex geometries and microstructures of the samples prepared by various research groups. In this work, we have used the high-throughput thin film formalism to develop a fundamental understanding of surface ORR mechanisms in mixed-conducting cathode materials by fabricating thin-film microelectrode arrays of $La_{0.6}Sr_{0.4}Co_{1-x}Fe_xO_{3-\delta}$ ($0 \leq x \leq 1$) on a YSZ(100) substrate. The electrochemical properties of these microelectrode stacks are investigated via scanning impedance spectroscopy, and reveal that electrochemical resistance is dominated by surface oxygen exchange reactions on the electrode through a two-phase boundary electrochemical pathway. A monotonic increase in electrochemical resistance is observed in $La_{0.6}Sr_{0.4}Co_{1-x}Fe_xO_{3-\delta}$ from x =0 to x =1 along with a decrease in chemical capacitance corresponding to a decrease in oxygen vacancy concentration. A power law dependence of R_s and k^q on pO_2 with the value of the power law exponent in a range of 0.5 to 0.75 for the whole spread film is observed,

indicating that the oxygen vacancy transport to surface-adsorbed oxygen intermediates is the rate determining step for mixed conducting cathodes. This study demonstrates the rich insights obtained via high-throughput methodologies and the promise of applying such techniques to discover highly active solid-state cathode materials.

4.2 Introduction

Solid oxide fuel cells (SOFCs) are promising candidates for the use in future clean energy generation applications due to their high efficiency, fuel flexibility, and environmentally benign fabrication and operation.[46] SOFCs efficiently convert chemical energy into electrical energy at high temperatures (>800 ˚C). Usually, in order to achieve desired performance, SOFCs need to be operated at high temperatures to assure the high ionic conductivity for the electrolytes and the high catalytic activity for the electrodes.[46] However, the high operating temperatures may lead to various issues such as limited materials selection, sealing problems, thermal mismatch between components, and accelerated coarsening of electrodes.[19] These problems are the major hurdles on the road to commercialize a wide range of applications of SOFCs. Therefore, there remains a strong motivation for the development of intermediate temperature SOFCs (<800˚C).

In recent years, intermediate temperature SOFCs have attracted significant interest due to their long-term stability, cost reduction, and a wide range of applications.[98] However, such reduction in the operating temperature remains a challenge because of the high resistance of the electrolyte and the degraded cathode performance at low temperatures. While reducing the thickness of thin-film electrolytes, developing high ionic conducting materials, or using proton conducting

electrolytes have been proposed to compensate for the high ohmic resistance at low operating temperatures, the sluggish kinetics of the oxygen reduction reaction (ORR) at the cathode becomes a key limitation in improving the performance of intermediate temperature SOFCs.[3] Therefore, the development of cathode materials with high catalytic activity for ORR at intermediate temperatures becomes an essential aspect in the field of SOFC research.

In SOFCs, the primary function of the cathode is to facilitate an electrochemical reduction of oxygen. The cathode materials are expected to have a variety of features and properties, including high catalytic activity for the dissociation and reduction of oxygen molecules, high electronic and oxygen ion conductivities, chemical and dimensional stability, desired thermal expansion to match with other cell components, good compatibility and minimum reactivity with the electrolyte and the interconnection. [99] The overall oxygen reduction reaction at the cathode of an SOFC can be represented using the Kröger-Vink notation as shown in Equation (1):[99]

$$\frac{1}{2}O_{2(g)} + 2e' + V_o^{\cdot\cdot} \rightarrow O_o^{\times} \quad (1)$$

where $V_o^{\cdot\cdot}$ is an oxygen vacancy with double positive charge, $O_o^{\times}$ is an oxygen ion sitting on an oxygen lattice site with neutral charge.

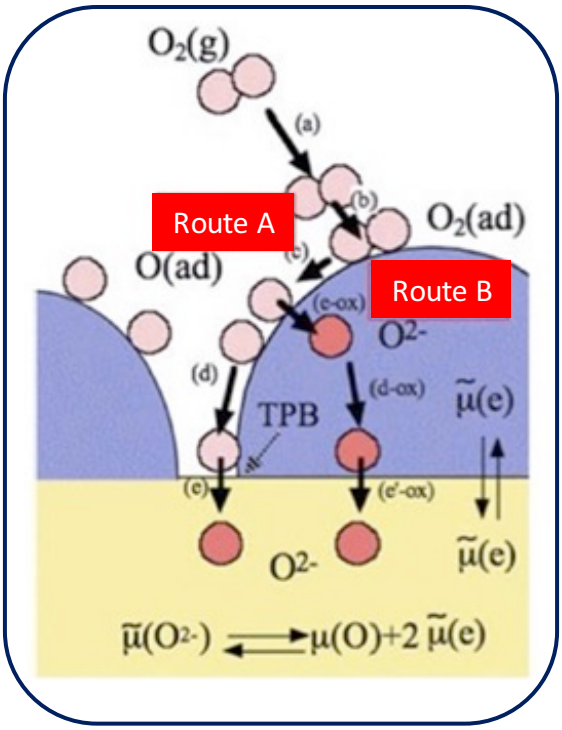

Figure 4.1 A schematic illustration of cathodic reaction.[100]

A triple phase boundary (TPB) is a region of contact between three different phases (an electrolyte, an electrode, and a gaseous fuel). A TPB plays a central role in determining the performance of an SOFC cathode, because the oxygen reduction reaction usually proceeds at the interface of electrode/electrolyte/gas as shown in Figure 4.1.[100] The oxygen reduction reaction involves diffusion, adsorption, electronic conduction, charge transfer reaction, and ionic conduction processes.[101] As shown in Figure 4.1, two reaction routes have been proposed: Route A is through a surface path, and Route B is through a bulk path. In general, the reaction occurs almost exclusively in the vicinity of TPBs, therefore, gaseous, electronic, and ionic species are simultaneously necessary for a reaction to proceed efficiently. In the case of a mixed ionic and electronic conducting (MIEC) cathode, the two-phase boundary could also

contribute to the ORR as Route B illustrated in Figure 4.1. Many efforts have been made to study the kinetics of the surface and the bulk paths in order to identify the rate-determining steps,[26,39,102] but so far there is no general agreement on which path is more important. In addition, the crystallinity, the microstructure, and the surface morphology of cathode materials can strongly affect the overall rate of oxygen reduction reaction.[103] Therefore, a systematic understanding of the reaction mechanism of SOFC cathodes is still very much in need.

The perovskite $La_{1-x}Sr_xMnO_{3-\delta}$ (LSM) is one of the most promising cathode materials for high temperature SOFCs.[101] However, its application in intermediate temperature SOFCs is seriously limited due to its low ionic conductivity and poor electro-catalytic activity in the lower temperature range. [101] The perovskite oxide of $La_{1-x}Sr_xCoO_{3-\delta}$ (LSC) has a very high electronic conductivity and high oxide ion conductivity over a wide temperature range, and thus it is a promising candidate cathode material for intermediate temperature SOFCs. However, LSC has a large thermal expansion coefficient (TEC) and an active chemical interface reaction with YSZ electrolyte at temperatures above 900 °C, thus hindering its practical applications in SOFCs.[104] While doping the Co-site with Fe^{3+} to synthesize $La_xSr_{1-x}Co_yFe_{1-y}O_{3-\delta}$ (LSCF) can reduce the TEC of LSC, the ionic conductivity and long-term stability of LSC will also be decreased by Fe^{3+} doping.[105] It has been reported that using a composite cathode of LSCF-electrolyte can enhance the cathode performance at low temperatures. However, the improved cathodic performance of composite cathodes is found to decrease during the cell lifetime. [106] It is also very difficult to experimentally study the oxygen reaction mechanism at the composite cathodes due to their relatively

complex geometry and morphology. More importantly, which elementary step is rate limiting during the oxygen incorporation (adsorption, dissociation, charge transfer) is still under debate for LSCF and most other MIEC cathode materials.

A better understanding of the ORR processes at the cathode can help predict cathode performance and guide future electrode designs. To this end, we propose to fabricate geometrically well-defined microelectrodes to probe ORR processes using heteroepitaxial or highly textured multilayer thin films. Our approach eliminates the complexity of composite cathodes. In particular, we fabricate the composition-spread cathode films on YSZ single crystal substrates through a high-throughput pulsed laser deposition approach in order to systematically investigate the effects of dopants on the ORR performance.

The good performance and the well-known properties of $La_{0.6}Sr_{0.4}Co_{0.2}Fe_{0.8}O_{3-\delta}$(LSCF6428) make $La_{0.6}Sr_{0.4}Co_xFe_{1-x}O_{3-\delta}$ (LSCF, $0 \leq x \leq 1$) a perfect candidate to study the effects of Co/Fe ratio on its performance. ORR is very sensitive to the microstructure of SOFC cathodes, making it very difficult to separate the influence of the electrode morphology from intrinsic properties of the material. In this work, we optimized the parameters (oxygen pressure and substrate temperature) of PLD to fabricate a dense LSC-LSF spread film, and then patterned it into a library of micro-electrodes using photolithography and ion milling techniques. Thus, a high quality and well-defined thin-film cathode was fabricated for developing the mechanistic understanding of the oxygen reduction reaction. Combining the high-throughput PLD fabrication method with unique electrochemical characterization tools, the thin-film cathodes of $La_{0.6}Sr_{0.4}CoO_{3-\delta}$(LSC) - $La_{0.6}Sr_{0.4}FeO_{3-\delta}$(LSF) were studied at the

temperature range of 700-775 °C with an oxygen partial pressure of 10^{-3} to 1 atm. Our aim was to obtain systematic electrochemical information about the LSC-LSF cathodes on YSZ electrolytes. The goal of the project was to develop knowledge which will contribute to the development of high electrochemical activity and structural compatible cathode materials for IT SOFCs.

4.3 Experimental

4.3.1 Materials and characterization methods

To fabricate PLD targets of LSCF6428, LSC, LSF, and BZY20, oxide powders were synthesized by the Pechini process.[107] Specifically, metal nitrate precursors were dissolved in water, to which citric acid (CA) and ethylenediaminetetraacetic acid (EDTA) were added as chelating agents in a 1:1.5:1.5 molar ratio of metal cations:CA:EDTA. This solution was heated and aged overnight to produce a viscous gel, which was then dried between 250 °C and 600 °C to produce a very fine powder. For SDC20, commercial $Sm_{0.2}Ce_{0.8}O_{2-\delta}$ (SDC20) powders were purchased from NexTech Materials. From this point, powders obtained by either method were calcined at 950 °C for 5 hours to achieve the correct cubic structure confirmed by X-ray powder diffraction (XRD). To improve the strength of the pellets, ~1 wt% polyvinylpyrrolidone (PVP) was added as a binder. The powders were mechanically pressed into discs and sintered at 1450-1600 °C for 12-24 hours to yield pellets with ~ 24 mm in diameter, 3-5 mm in thickness and 93-97% of theoretical densities, as determined by the Archimedes method. Commercially available (100) oriented yttria stabilized zirconia

(YSZ, 8 mol% Y_2O_3, MTI Co.) single crystals with a thickness of 0.3 mm and a size of 5×10 mm^2 were used as deposition substrates. A custom-designed PLD/Laser-MBE System (Pascal Co., Ltd.) equipped with a loadlock chamber and a reflection high energy electron diffraction (RHEED) was used to fabricate the thin film samples. A KrF (λ=248nm) excimer laser (Lambda COMPexPro) was used to ablate the targets at a pulse repetition rate of 5 Hz, a laser fluence of 0.8 J/cm^2 and a target-substrate distance of ~55mm.

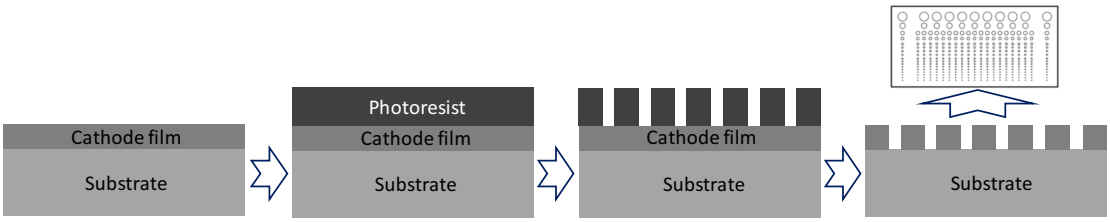

Figure 4.2 A schematic sketch of the photolithography and ion milling process for the microelectrodes.

Each cathode thin film was patterned into a library of microelectrodes using photolithography and ion milling process as shown in Figure 4.2. Specifically, each sample was coated with a photoresist (Shipley 1813) by a regular spin coating method (4000 rpm for 50 s). After spin coating, the photoresist was baked at 100 °C for 2 min to drive off solvents and to solidify the film, following an exposure to UV radiation for 12 s through a photomask, and then developed in Shipley 352 developer for 40 s. The samples then underwent ion milling for 45 min, resulting in a milling depth of 250 nm. In the final step, the residual photoresist was stripped using acetone. After the patterning, the LSCF cathode film was converted into a circular microelectrode array with diameters of 30-500 μm on the top of YSZ.

X-ray diffraction (XRD) was performed on a Bruker D8 Discover with 4 bounce monochromator (40 kV, 40 mA, Cu Kα) in a θ-2θ scan geometry. Atomic force microscopy (AFM, Digital Instruments Nanoscope III and Dimension 5000) was used to map the topography by lightly tapping the surface of films with an oscillating probe tip. Features observed in AFM images were quantified by image analysis using the software program Gwyddion. Scanning electron microscopy (SEM) was performed using a Hitachi SU-70 with field emission gun equipped with a Bruker XFlash silicon drift EDS detector. Electrochemical impedance spectroscopy (EIS) was performed on a custom-made automated impedance microprobe at Northwestern University (Prof. Sossina Haile's group).

4.3.2 Optimization of deposition conditions

PLD is a relatively simple experimental deposition technique, but the deposition process is in fact complex, and in order to make high quality thin films, the process parameters must be optimized first. In this study, we mainly optimized the deposition oxygen pressure and substrate temperature by studying their influence on the structure and morphology of the grown films.

In the deposition chamber, the presence of gas has a strong influence on the kinetic energy and the spatial distribution of the ejected species present in the laser-produced plasma.[30] Thus, it may induce the compositional change as compared to the target composition, as well different morphologies in the deposited films. [30] To get stoichiometric (as dictated by the target composition) and dense oxide thin films, we optimized the deposition pressure by growing LSCF6428 thin films on YSZ (100) substrates under different oxygen pressures. Keeping the laser fluence (0.8 J/cm^2), the

repetition rate (5 Hz), and the substrate temperature (~600 °C) the same, oxygen pressures of 10 mTorr and 100 mTorr were used to grow two LSCF6428 films on YSZ(100) substrates. X-ray diffraction (XRD) patterns only show (110) peaks of LSCF6428 at almost the same 2θ angle for both deposition pressures as shown in Figure 4.3a, indicating that the films have a strong preference for the (110) orientation with a pseudocubic lattice constant of ~ 3.90 Å and that the deposition pressures (10 mTorr, and 100 mTorr) have no obvious effect on the crystal structure. However, the film deposited at 10 mTorr oxygen shows a lower surface roughness with a root-mean-square (RMS) value of 0.38 nm (Figure 4.3b) than the one at 100 mTorr oxygen with a RMS value of 0.51 nm (Figure 4.3c). The different surface roughness is due to the slight difference of grain size under different background pressures (10 mTorr: 64 nm; 100 mTorr: 81 nm). This is consistent with the effect of background pressure on gas-phase nucleation during PLD process: Higher background pressure induces more gas-phase collisions, and then leading to big size of nanoparticles.[108] Based on the results of XRD and AFM, we used the deposition pressure of 10 mTorr for the growth of LSCF6428 thin films.

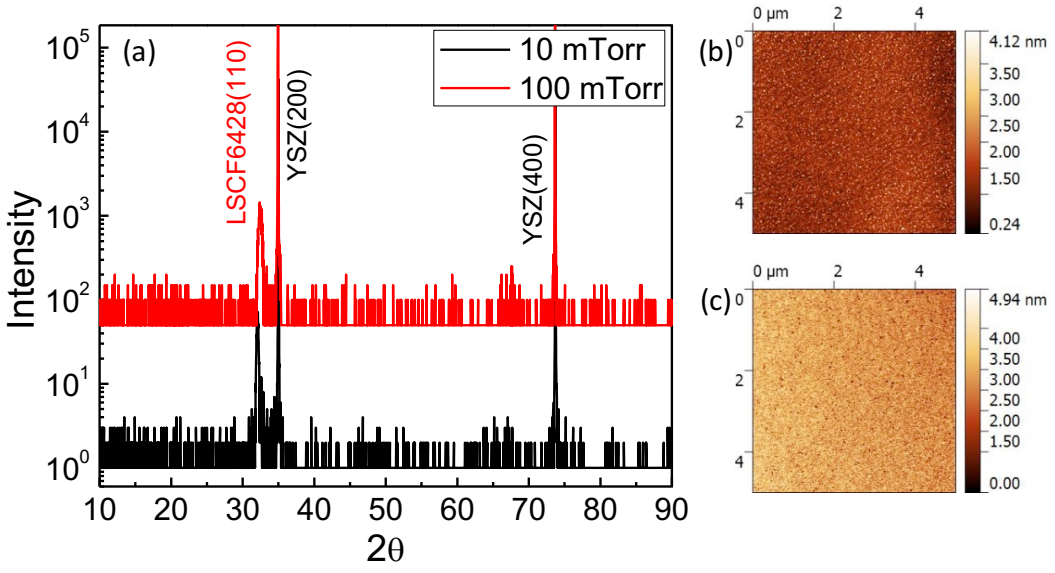

Figure 4.3 (a) The X-ray diffraction (XRD) patterns of θ-2θ-scans of LSCF6428 on YSZ(100) at different deposition pressures. (b) The atomic force microscopy (AFM) image of LSCF6428 film deposited under 10 mTorr oxygen pressure showing a root-mean-square (RMS) roughness 0.38 nm. (c) The AFM image of LSCF6428 film deposited under 100 mTorr oxygen pressure showing a RMS roughness 0.51 nm.

Another important deposition parameter is the substrate temperature, which plays an important role in determining the structural and morphological properties of thin films.[30] The deposition temperature was optimized by growing a LSCF6428 thin film on YSZ (100) with a temperature range of 566 °C to 683 °C as shown in Figure 4.4a. XRD and AFM were performed at each position to investigate the effect of substrate temperature on the structural and morphological properties of LSCF6428 film. Figure 4.4c shows that the (110) peak splitting becomes more pronounced at lower substrate temperatures, indicating impurity phases appear at lower substrate temperatures. As shown in Figure 4.5, a high temperature benefits for the growth of dense and smooth film, however, if the temperature is too high, some big particles of

the target material will be produced on the surface of the film. Considering the XRD and AFM results shown in Figure 4.4 and 4.5, a substrate temperature of ~600 °C is suitable for the growth of LSCF6428 films with a relatively high crystallinity and a good surface roughness. Using the similar processes, we identified the optimal deposition oxygen pressure and substrate temperature for all other targets.

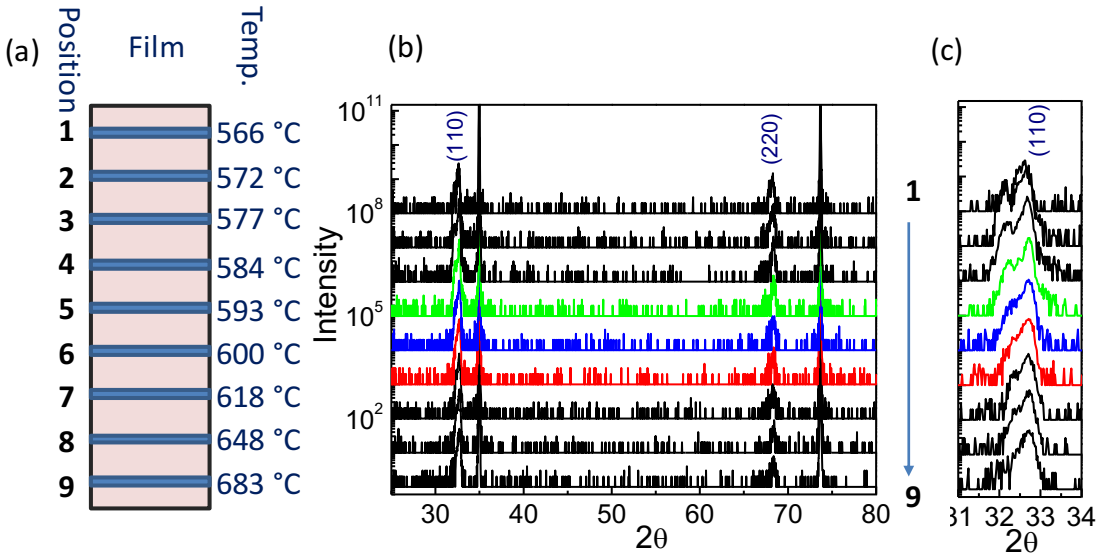

Figure 4.4 (a) The schematic sketch of a temperature gradient film sample. (b) The XRD patterns at different temperatures of the LSCF6428/YSZ(100) temperature gradient sample. (c) The enlarged (110) peak from (b).

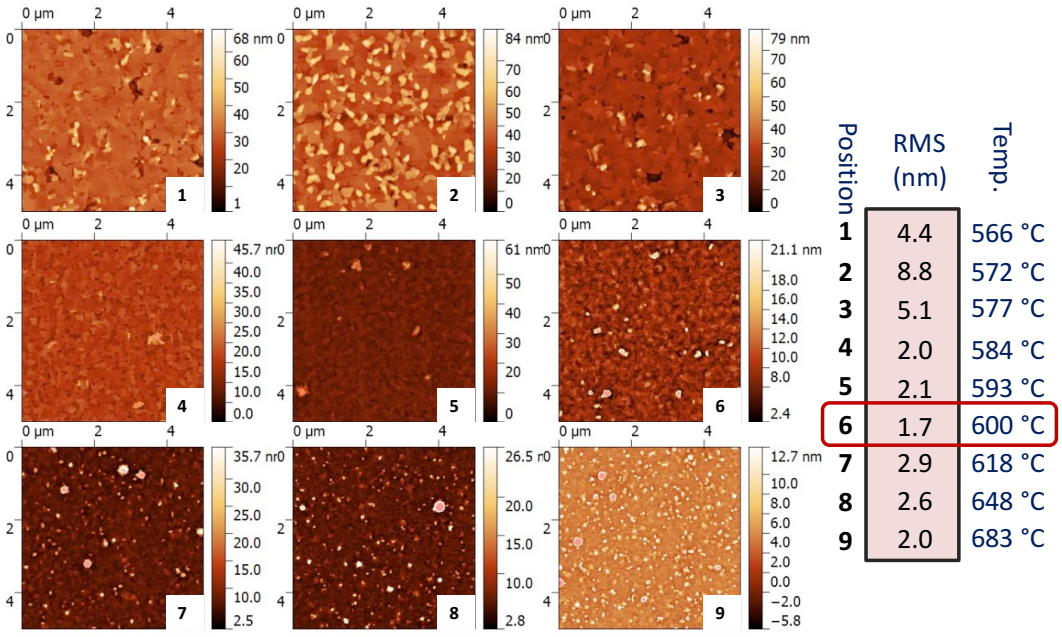

Figure 4.5 5μm×5μm AFM scan images of the LSCF6428/YSZ(100) temperature gradient sample. Position 1 to 9 means the substrate temperature is from 566 °C to 683 °C. The red frame highlights the substrate temperature with the lowest RMS.

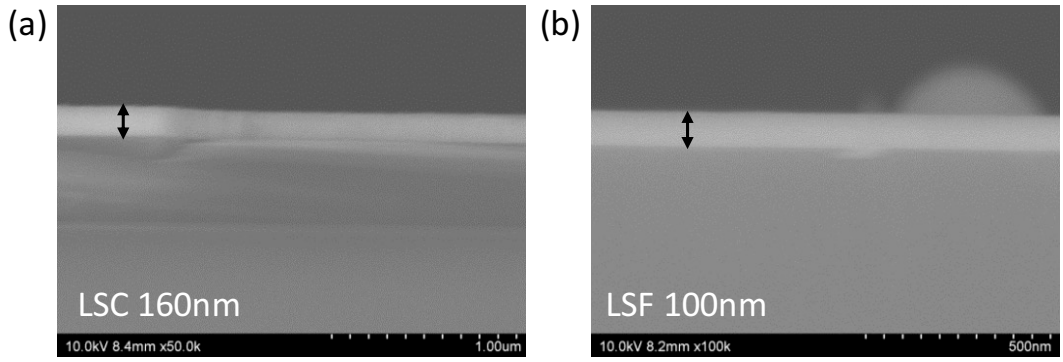

Figure 4.6 (a) The cross-sectional scanning electron microscopy (SEM) image of LSC on Si(100). (b) The cross-sectional SEM image of LSF on Si(100). (Deposition conditions: The laser fluence 0.8 J/cm^2, 5 Hz repetition, substrate temperature 600~620°C, and 30 mTorr O_2)

A few methods can be used to determine the deposition rates, such as X-Ray Reflectometry (XRR), a stylus profilometry tool (Dektak), AFM, or scanning electron microscopy (SEM). Figure 4.6 shows how the cross-sectional SEM is used to determine the thickness. It is straightforward to measure the film thickness from the cross-sectional SEM images of LSC and LSF samples, and thus the deposition rates can be calculated from the total deposition pulses. The deposition rates were determined to be 0.3 Å/s (LSCF6428), 0.4 Å/s (LSC), 0.25 Å/s (LSF), 0.5 Å/s (SDC20) and 0.3 Å/s (BZY20) with a laser fluence of 0.8 J/cm^2 and 5 Hz repetition. Following the depositions, the samples were left in the PLD chamber with the same deposition oxygen pressure during the cool-down period (5 °C/min).

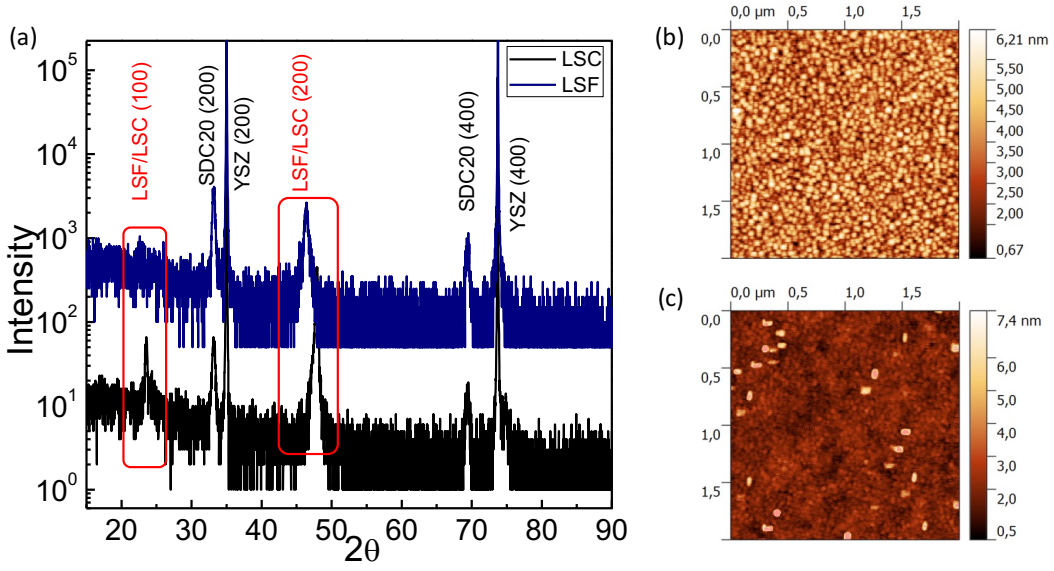

Figure 4.7 (a) XRD patterns ($2\theta - \theta$ scan) of LSC and LSF thin films grown on SDC20/YSZ (100), respectively. (b) The AFM image of a LSC thin film grown on SDC20/YSZ with a RMS value of 0.96 nm on 2μm×2μm scan area and an average grain size of ~60 nm. (c) The AFM image of a LSF thin film grown on SDC20/YSZ with a RMS value of 0.59 nm on 2μm×2μm scan area and an average grain size of ~25 nm.

4.4 Results and discussion

4.4.1 Structural properties of composition-spread films

LSC (~220nm) and LSF (~220nm) thin films were fabricated on YSZ (100) single crystals with a ~20 nm SDC20 buffer layer, respectively. A SDC20 buffer layer was used to avoid the undesired solid-state reaction between the cathode and the YSZ electrolyte. Figure 4.7a shows the XRD patterns of LSC and LSF films grown on SDC20/YSZ(100). Their peaks were indexed with respect to the pseudo-cubic structure because the small rhombohedral distortion of the crystal lattices could not be measured with the given resolution.[109] As shown in Figure 4.7a, only the $(h00)$ reflections are observed, corresponding to the lattice constants of ~3.82 Å and ~3.89 Å for LSC and LSF, respectively. This indicates that both LSC and LSF films are grown preferentially along the (100) orientation on the SDC20/YSZ substrate. The SDC20 buffer layer is grown only in the [100] direction due to the good lattice match between SDC20 (~5.41Å) and YSZ (~5.12Å).[11] AFM was used to characterize the surface morphology of the films as shown in Figure 4.7b and 4.7c (2μm×2μm). Both films show very similar denseness and smoothness of the surface, which is expected for the PLD growth conditions applied. The LSF thin film shows a lower RMS roughness (0.59 nm) and relatively smaller grain size (d = ~20nm) as compared to LSC thin film (RMS: 0.96 nm; d = ~70nm).

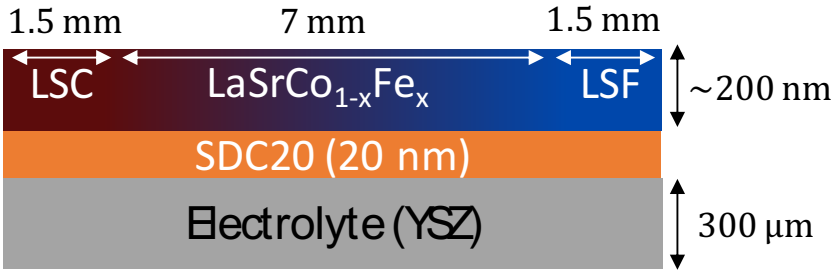

Figure 4.8 A schematic sketch of the LSC-LSF composition spread sample.

Using the high-throughput PLD methodology (Details discussed in Chapter 2), the compositional gradients of LSC-LSF (~220nm) were fabricated on YSZ substrates with or without the SDC20 (~20nm) buffer layer. Figure 4.8 shows the schematic sketch of the compositional-spread films: The x in $La_{0.6}Sr_{0.4}Co_{1-x}Fe_xO_{3-\delta}$ increases from 0 to 1 over a length of ~7 mm, and two ends (~1.5mm) are individual LSC and LSF.

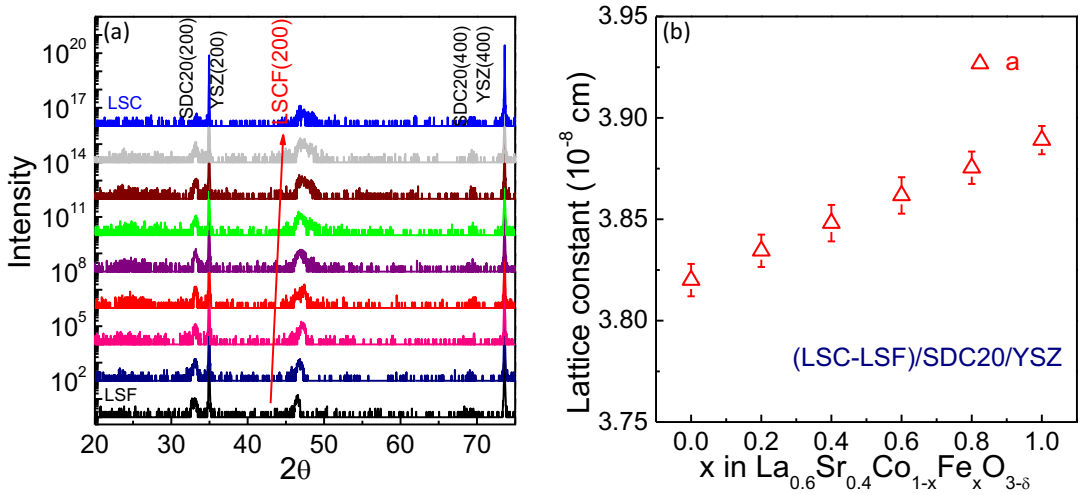

Figure 4.9 (a) The XRD diffraction patterns of a LSC-LSF composition spread film on SDC20/YSZ(100) substrate. (b) The lattice parameters of the pseudo-cubic $La_{0.6}Sr_{0.4}Co_{1-x}Fe_xO_{3-\delta}$ on SDC20/YSZ.

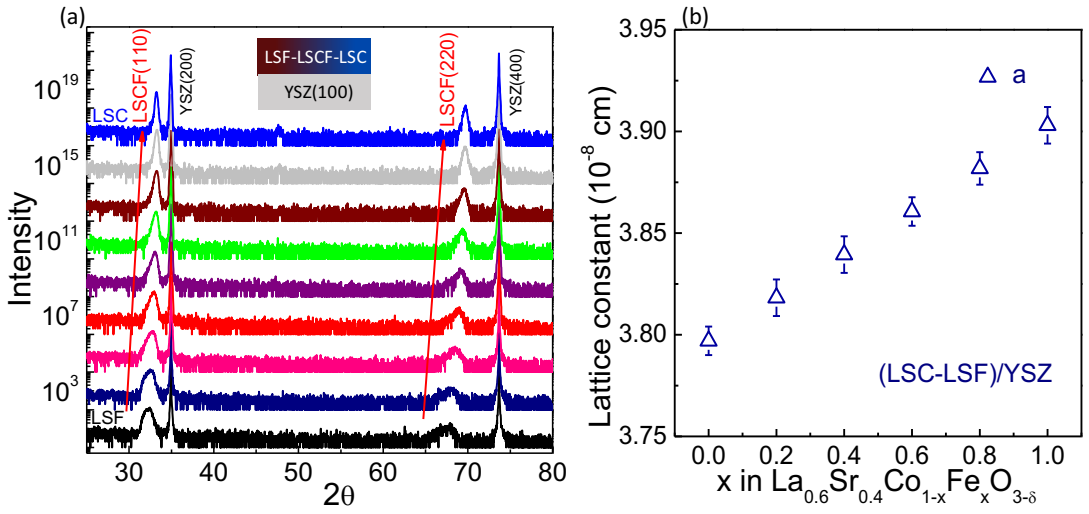

Figure 4.10 (a) The XRD diffraction patterns of a LSC-LSF composition spread film on YSZ (100) substrate. (b) The lattice parameters of the pseudo-cubic $La_{0.6}Sr_{0.4}Co_{1-x}Fe_xO_{3-\delta}$ on YSZ.

Figure 4.9a shows the XRD patterns of (LSC-LSF)/SDC20/YSZ measured on a Bruker D8 ADVANCE X-Ray Diffractometer. The dominated (200) peaks of $La_{0.6}Sr_{0.4}Co_{1-x}Fe_xO_{3-\delta}$ (LSCF) observed in Figure 4.9a indicate that the whole spread film has a pseudo-cubic structure and grows with a (h00) preferred orientation. The lattice parameters of the pseudo-cubic LSCF were calculated from the positions of (200) peaks in the XRD patterns (Figure 4.9a) according the following relation:[86]

$$a = \frac{\lambda\sqrt{(h^2 + k^2 + l^2)}}{2\sin\theta}$$

where a is the lattice parameter, λ is the wavelength of X-ray beam (1.5406 Å, $Cu - k_{\alpha 1}$ in this study), h, k, and l ae the miller indices of the diffraction peaks, and θ is the angle of incidence. As shown in Figure 9a, the angle positions of (200) peaks shift to large 2θ angles with the doping concentration of Fe decreasing (Bottom to Top) since

the ionic radius of Co^{3+} (0.75Å) is slightly smaller than that of Fe^{3+} (0.79Å). Figure 4.9b shows the composition dependence of *a* determined from the (200) peaks of LSCF film. The lattice constant of the pseudo-cubic LSCF film is in a range of 3.8 Å - 3.9 Å, which matches well with the lattice constant of SDC20 buffer layer (a = ~5.41 Å) by an in-plane rotation of 45°. Without the SDC20 buffer layer, the LSC-LSF spread film grown on YSZ (100) shows dominated peaks at (110) and (220) reflections as shown in Figure 10a. (110) peaks were used to calculate the lattice constants as shown in Figure 4.10b. XRD results show both films are crystalline and single phase. The use of the SDC20 buffer layer not only provides better thermal expansion match and prevents interaction between the cathode (e.g. LSCF) and electrolyte (e.g. YSZ), but also facilitates the growth of highly textured spread film along (100) direction.

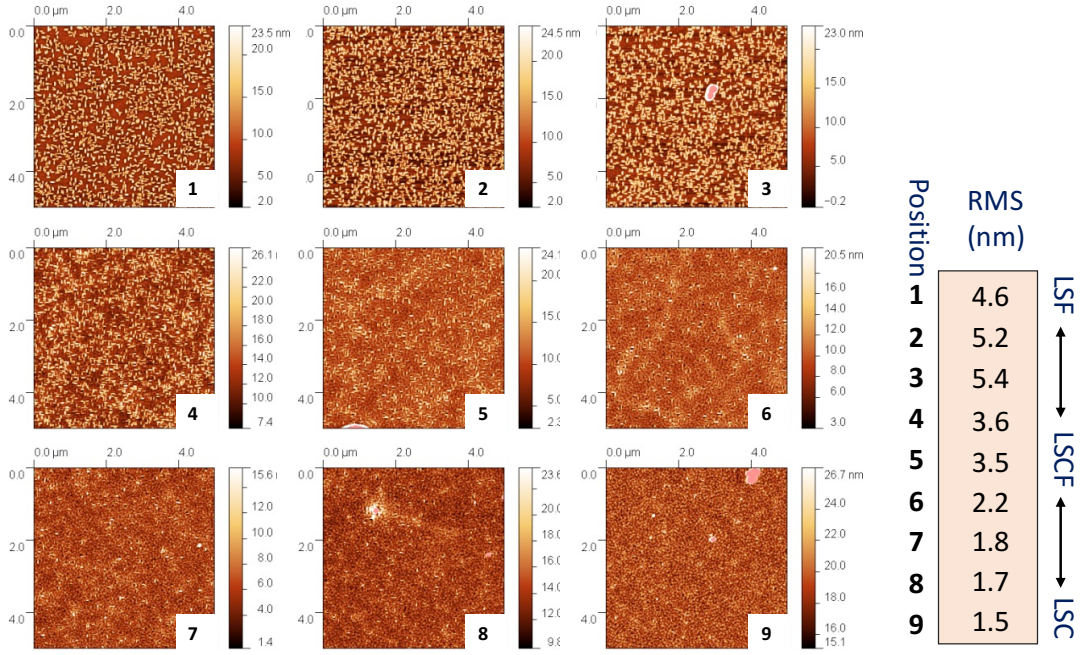

Figure 4.11 5μm×5μm AFM scan images of a LSF-LSC composition spread film on SDC20/YSZ (100) substrate. Position 1 to 9 means the x in $La_{0.6}Sr_{0.4}Co_{1-x}Fe_xO_{3-\delta}$ is from 1 to 0.

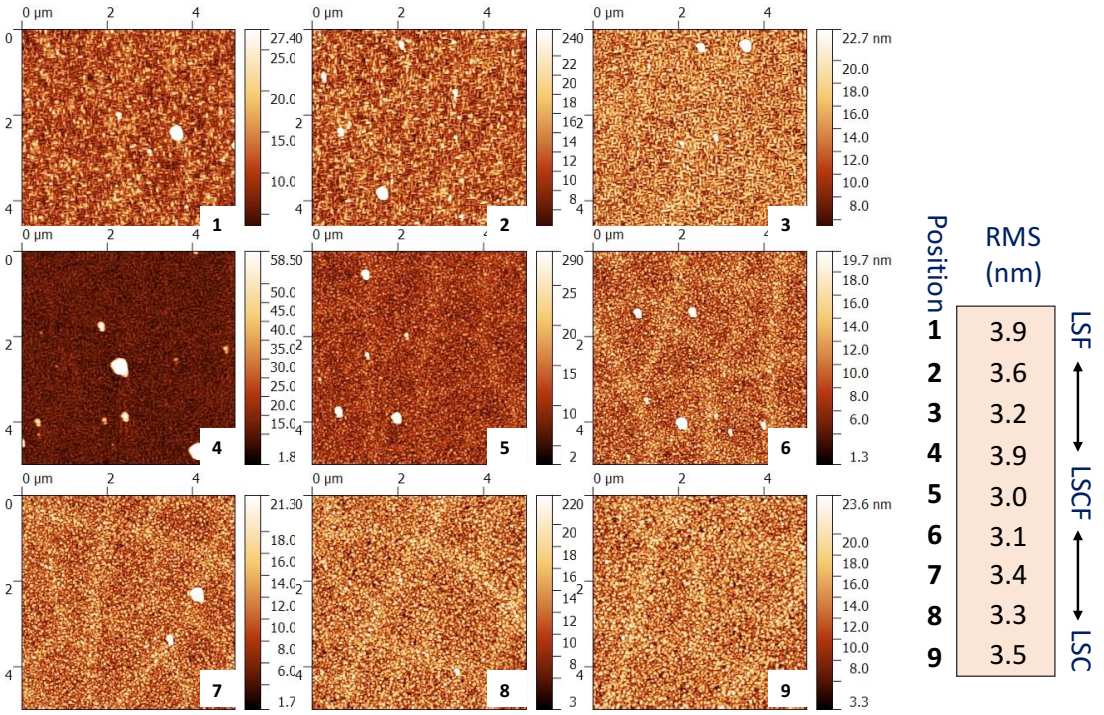

Figure 4.12 5μm×5μm AFM scan images of a LSF-LSC composition spread film on YSZ (100) substrate. Position 1 to 9 means the x in $La_{0.6}Sr_{0.4}Co_{1-x}Fe_xO_{3-\delta}$ is from 1 to 0.

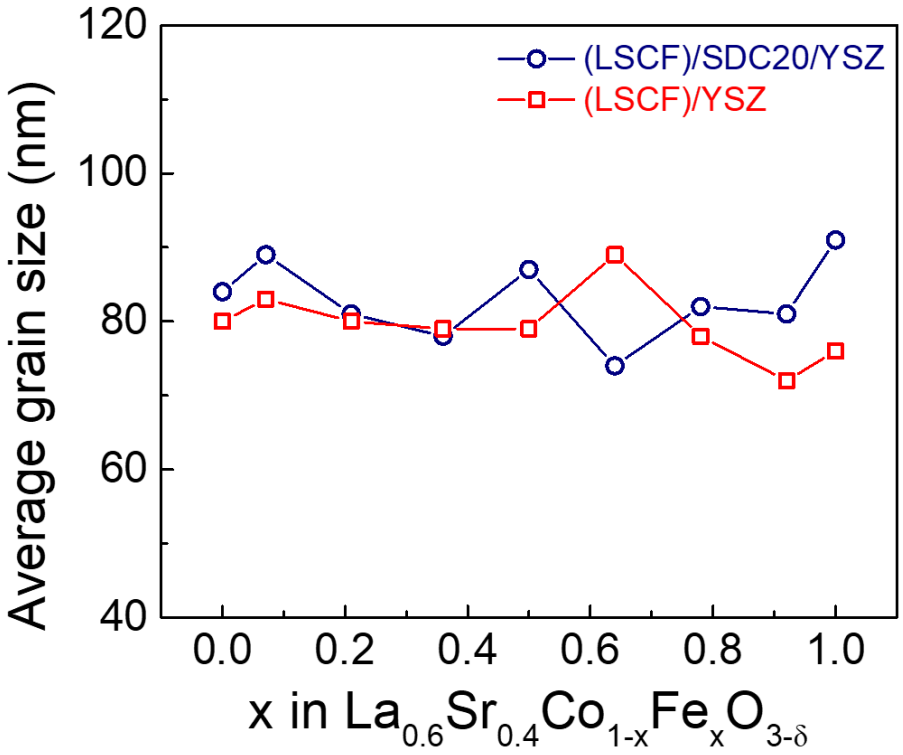

Figure 4.13 The composition dependence of the average grain size of LSCF spread film on SDC20/YSZ(blue line) and YSZ(red line).

AFM analysis revealed relatively smooth film surfaces with RMS surface roughness of a few nanometers for both samples, as shown in Figure 4.11 and 4.12. Interestingly, some patterns occur near LSC end (more Co than Fe) as shown in Figure 4.12, which is due to the large mismatch in the thermal expansion coefficient (TEC) of LSC (~16×10^{-6}/K) vs. YSZ(~11×10^{-6}/K).[110] This also suggests that the dopant Fe in LSC is important to real applications due to the relatively small TEC of LSF (13.4×10^{-6}/K). Comparing the AFM images in Figure 11 and 12, SDC20 buffer layer with a TEC of ~13×10^{-6}/K also helps to alleviate the TEC mismatch between LSCF and YSZ. The average surface grain size was observed to be pretty consistent across the whole spread

film for both samples as shown in Figure 4.13, indicating that the variation of surface morphology in the composition spread sample can be excluded. Therefore, the dense and smooth (LSC-LSF)/SDC20/YSZ spread film is a good candidate for investigating the effect of intrinsic properties of LSCF on ORR performance.

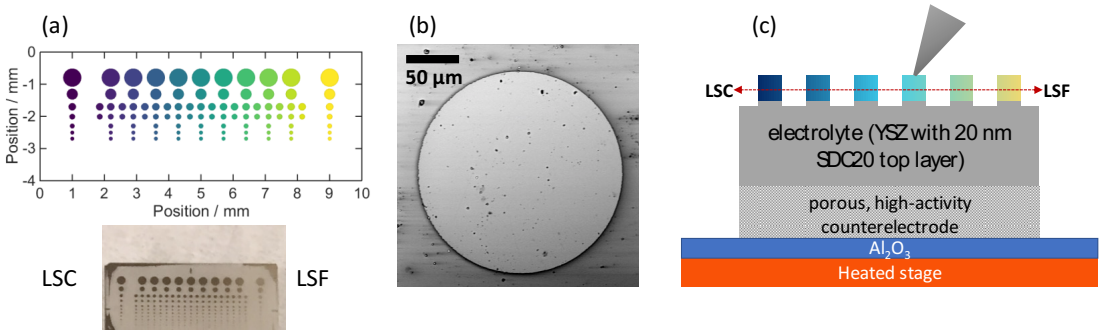

Figure 4.14 (a) Top colored image is the layout of a library of LSC-LSF microelectrodes with diameters ranging from 100 to 500 µm, and different colors represent different compositions. The bottom image is the photograph of a library of LSC-LSF microelectrodes on a 5×10 mm SDC20/YSZ(100) substrate. (b) A top view SEM image of the LSC-LSF microelectrode with a diameter of 200 µm. (c) A schematic sketch of the cross-sectional configuration in the automated scanning impedance microprobe (not drawn to scale).

4.4.2 Electrochemical measurements

Using photolithography and ion milling, each cathode film was patterned into a library of microelectrodes with diameters ranging from 100 to 500 µm as shown in Figure 4.14a. In the layout image (Figure 4.14a: top), the sizes and colors of microdots indicate the diameters of microelectrodes from top to bottom and the composition gradient from left to right, respectively. A real sample picture (Figure 4.14a: bottom)

of the (LSC-LSF)/SDC20/YSZ chip shows the well-defined patterns. Figure 4.14b shows the in-plane view SEM image of a microelectrode with a diameter of 200 μm, indicating that the microelectrodes are dense and crack-free before EIS testing.

Figure 4.14c shows the schematic configuration of the samples for EIS measurements. Each patterned sample was adhered to a ~10×20×0.6 mm alumina sheet by applying silver (or Pt) paste to the back side of the YSZ substrate to form a porous, low-impedance counter-electrode. The samples were then installed on the heated stage of the automated impedance microprobe for EIS measurements under different environments (substrate temperature, oxygen pressure, humidity, etc.). Each microelectrode was contacted by the probe tip of a Pt/Ir alloy with a tip radius of 20 μm. The probe tip could be positioned accurately by micromanipulators. An impedance analyzer (Solartron 1260) was used to acquire the impedance spectra. An a.c. voltage of 30 mV, without d.c. voltage, and a typical frequency range of 10^4 Hz to 3.2×10^{-2} Hz were used in the measurements.

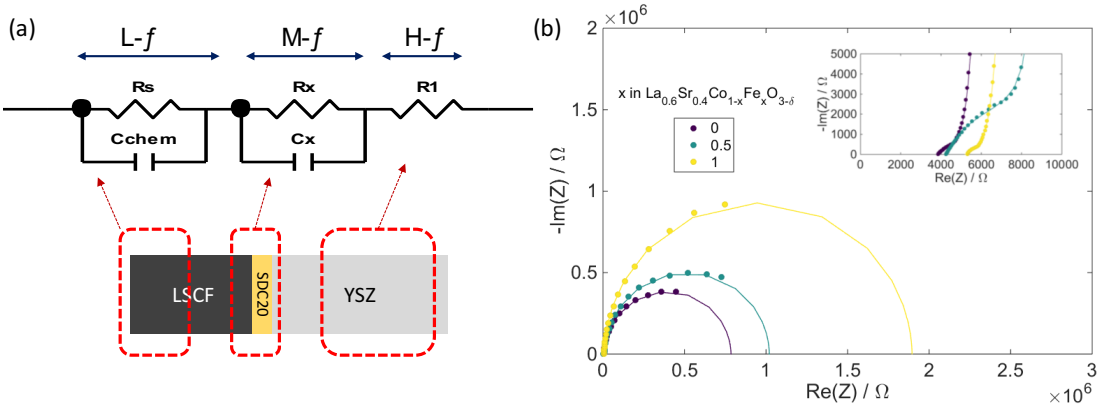

Figure 4.15 (a) The equivalent circuit model used for the evaluation of the experimental impedance data presented in this paper. H-*f*, M-*f* and L-*f* indicate the high, medium, and low frequency feature in the impedance spectra, which correspond to the respective parts of the circuit. (b) Representative impedance spectra acquired on

the electrodes (d = 500 μm) with different x values (Fe concentration) at 700 °C under 1 atm oxygen pressure.

The equivalent circuit shown in Figure 4.15a was adopted to fit impedance spectra in this work. This equivalent circuit is based on the models proposed by Baumann *et al.*[111] and Rupp *et al.*[112] for MIEC perovskite (ABO_3) cathode materials on ionic conducting electrolytes. The H-f resistance ($R1$) originating from the electrolyte was determined by the intercept of the real axis at high frequency. The M-f resistance (Rx) corresponds to the interfacial impedance resulting from the transferring of oxide ions (O^{2-}) across the interfaces of LSCF/SDC20/YSZ. The M-f capacitance (Cx) includes both the interface property of electrolyte/electrode (double layer capacitance) and stoichiometric changes (chemical capacitance) at the interface because the capacitance values (C_x) derived from the medium frequency are larger than the traditional double layer capacitance (~100 μF/cm^2). [112] The exact mechanisms for $Rx||Cx$ are still unknown, and it is very difficult to get a perfect equivalent circuit to model this regime.[112] The L-f resistance (R_s) associates with the oxygen exchange at the surface of the electrode, corresponding to big semicircles in Figure 4.15b. The large capacitance (C_{chem}) is called chemical capacitance related to oxygen stoichiometry changes in the bulk of the electrode. The L-f-arc contains information on both the surface (R_s) and the bulk (C_{chem}) of the electrode materials. Besides the low resistivity of the porous back-contact electrode (Ag or Pt), its area (10mm×5mm) is about 2 orders of magnitude larger than that of the biggest circular LSCF cathode ($d = 500\ \mu m$), so the effect of the counter-electrode on the measurement results is negligible. Therefore,

the overall electrode impedance is dominated by the large L-f-arc (Figure 4.15b), which represents the oxygen exchange reaction at the surface of the LSCF micro-electrodes.

EIS data were acquired at a temperature range of 700 °C to 775 °C over an oxygen partial pressure range of 10^{-3} to 1 atm. All the Nyquist plots show the similar typical features to that shown in Figure 4.15b. ZView software (Scribner Associates, USA) was used to perform complex least-square-fitting to extract the fitting parameters to describe the system. Considering the complexity of M-f regime and our purpose in this study, we focus on the low frequency part of the impedance spectrum. The equivalent circuit model shows a good correspondence between experimental data and fitted curves, especially for the low frequency part. This indicates that the proposed model can provide a good interpretation to the (LSC-LSF)/SDC20/YSZ system in this study.

The electrochemical reactions of oxygen species at a mixed conducting electrode is a complex process, and mainly includes two steps: 1) The surface exchange step: the oxygen molecules are absorbed on the surface of cathode, dissociated into oxygen ions, and then the oxygen anions are incorporated into the surface oxygen vacancies; 2) The diffusion step of the oxygen ions in the bulk of cathode layer.[101] Therefore, the major resistance for oxygen permeation is from the surface exchange and bulk diffusion, and they are affected by two key parameters of the cathode materials: the oxygen diffusion coefficient D and the corresponding surface exchange coefficient k. The ratio of D to k is defined as the critical thickness L_c, which is used to estimate the relative importance of surface exchange and bulk diffusion.[113] The

values of D^* and k^* can be obtained from the isotope exchange experiment by fitting $\frac{^{18}O}{(^{16}O+^{18}O)}$depth profiles to the appropriate diffusion equation.[114]

When the thickness of the cathode layer, t, is equal to L_c, the surface exchange and bulk diffusion are equally important to the resistance; $t > L_c$, the bulk diffusion will be more important; $t < L_c$, the surface exchange will dominate the resistance. [114] For the LSCF materials, L_c values have been studied extensively by different researchers.[113] Based on the results from Niedrig *et al.*[115], L_c of LSCF is estimated to be around 300 μm at 800 °C, which is about three orders of magnitude larger than the thickness of the LSC-LSF spread film (~220 nm) in this study. In addition, it can be expected that the L_c will increase at lower temperatures for LSCF family material because the parameters, D^* and k^*, follow the Arrhenius relation and it has been reported that k^* has much higher activation energy than that of D^*.[116] Therefore, considering the thickness (~220 nm) of our thin film microelectrodes and the EIS measurement temperatures (700 °C - 775 °C), the electrochemical resistance (R_s, the low frequency feature of the EIS spectra) is dominated by the surface exchange reaction rather than by the ionic conduction through the electrode bulk in our case.

EIS data obtained on geometrically well-defined thin film microelectrodes were used to determine the surface resistance (R_s), the chemical capacitance (C_{chem}), and the surface oxygen exchange coefficient (k^q) as a function of the composition of Fe, the temperature, the size of micro-electrodes, and the oxygen partial pressure. Thus, the oxygen surface exchange kinetics of the LSC-LSF spread thin film was systematically investigated by analyzing the extracted parameters.

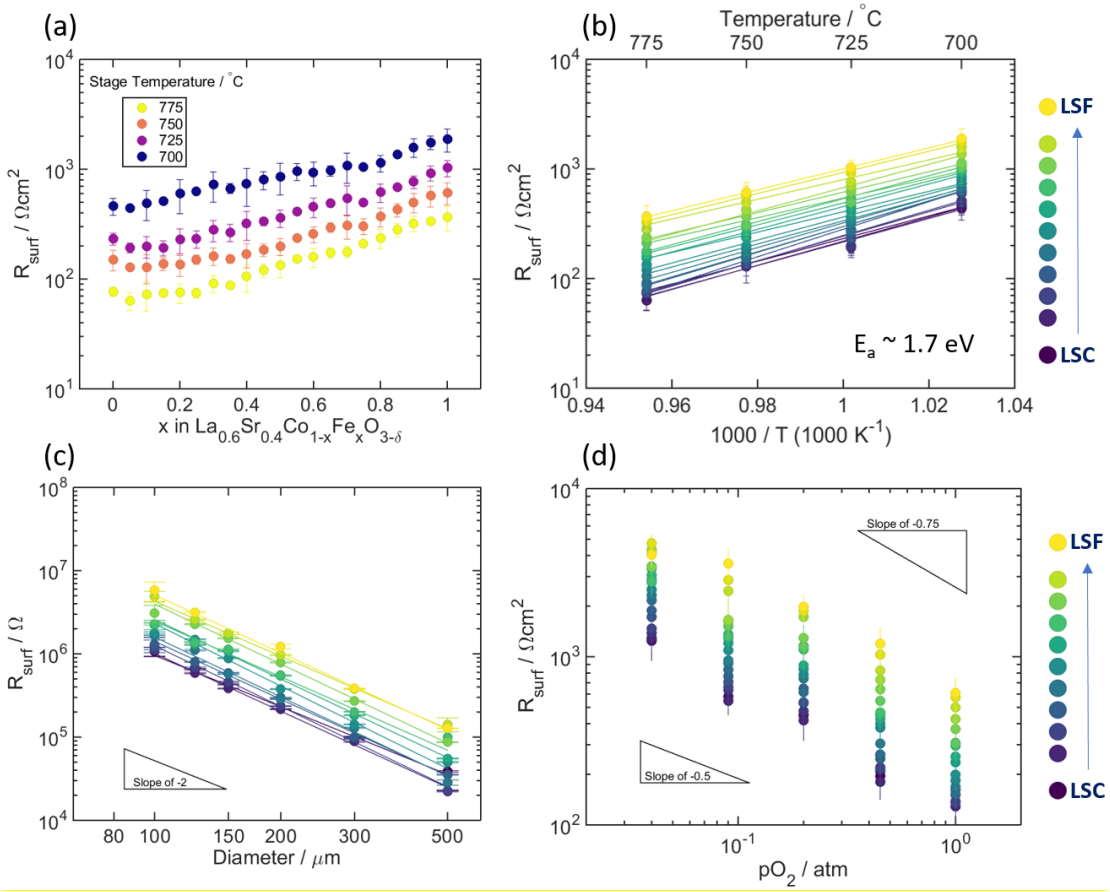

Figure 4.16 (a) Temperature dependence of the surface resistance measured on micro-electrodes ($d = 500\mu m$) as a function of the composition of Fe in $La_{0.6}Sr_{0.4}Co_{1-x}Fe_xO_{3-\delta}$. (b) Arrhenius plots of the surface resistance of the $La_{0.6}Sr_{0.4}Co_{1-x}Fe_xO_{3-\delta}$ film. (c) Electrode diameter dependence of the resistance measured at 775 °C with a pO_2 of 0.2 atm. (d) Oxygen partial pressure dependence of the surface resistance measured on micro-electrodes ($d = 500\ \mu m$) at 750 °C.

4.4.3 The resistance of oxygen surface exchange (R_s)

The area specific resistance (ASR), referred to the entire electrode surface, is in a range of ~100 to ~1000 Ω cm^2 for the whole spread film. The values of ASR in this study are relatively larger as compared to those of previous results, [113,117] however, all the values are still in a reasonable range considering the highly dense thin film property

in this study and the differences from thermal history, surface segregation and contamination.[101]

Figure 4.16a shows a clear dependence of ASR on the concentration of B-site Fe. The ASR values increase by a factor of ~4 when x changes from 0 to 1 in $La_{0.6}Sr_{0.4}Co_{1-x}Fe_xO_{3-\delta}$. This trend agrees well with the electrical property of LSCF, which shows a decrease in the electrical conductivity with the concentration of Fe increasing.[118] An approximately linear relationship was found for each of the compositions between the logarithm of the ASR and the inverse temperature from Figure 4.16b, indicating an Arrhenius-type behavior. Using the Arrhenius Equation, $R_s \propto \exp(-{}^{E'_a}/_{RT})$, the activation energy (E_a = - E'_a), was calculated to be in a range of ~1.4 eV to ~1.9 eV (the average E_a is ~1.7 eV), which are close to that reported by Baumann *et al.*[111] and Rupp *et al.*[112] However, there is no clear trend between the activation energy and the concentration of Fe in LSCF as shown in Figure 4.16b.

Geometry dependence of the microelectrode impedance has also been investigated by carrying out the EIS measurements on microelectrodes with various diameters. Figure 4.16c shows that R_s is inversely proportional to the microelectrode area as indicated by a slope of ~ -2 in the log-log plot for the whole LSCF spread film. A slope of -2 is expected for a MIEC cathode because the entire surface area is active towards the oxygen exchange reaction. LSCF is a mixed conducting material, and the slope of ~-2 supports the hypothesis that the electrochemical reaction occurs over the entire surface of the LSCF microelectrodes through a bulk path.

Figure 4.16d shows the pO_2 dependence of the surface resistances from LSC end to LSF end on a microelectrode with a diameter of 500 μm at 750 ºC. A linear

relationship was observed between the logarithm of the surface resistance and the logarithm of the pO_2 for the whole spread film. The ORR impedance was found to decrease with increasing pO_2 from 10^{-3} to 1 atm, as shown in Fig. 4.16d, suggesting that the kinetics of ORR on the whole LSCF spread film (~200nm) was limited by surface oxygen exchange. This is also in good agreement with the reported critical thickness of LSCF family materials (~300 μm at 800 °C).[118]

The oxygen surface exchange resistance, R_s, is oxygen partial pressure dependent. And thus, the power law, $R_s \propto P_{O2}^{-m}$ was used to extract the exponent *m* from the slope of the log-log plot. As shown in Figure 4.16d, the exponents *m* for the surface resistance is in a range of 0.5 to 0.75. Considering the following three processes of ORR,[113] where

$$m = 1 \quad O_{2,gas} \leftrightarrow O_{2,ads} \qquad (2)$$

$$m = \frac{1}{2} \quad O_{2,ads} \leftrightarrow 2O_{ads} \qquad (3)$$

$$m = \frac{1}{4} \quad O_{ads} + 2e^- + V_O^{\cdot\cdot} \leftrightarrow O_O^{\times} \qquad (4)$$

From this simple model, the reaction order of *m* with a range of 0.5 to 0.75 implies that molecular oxygen species and atomic oxygen species are involved in the rate-determining step (rds).[113] So a dissociative adsorption step was proposed to be the rate-limiting step in this study. This result is in good agreement with that of LSC reported by Adler *et al.*[119]

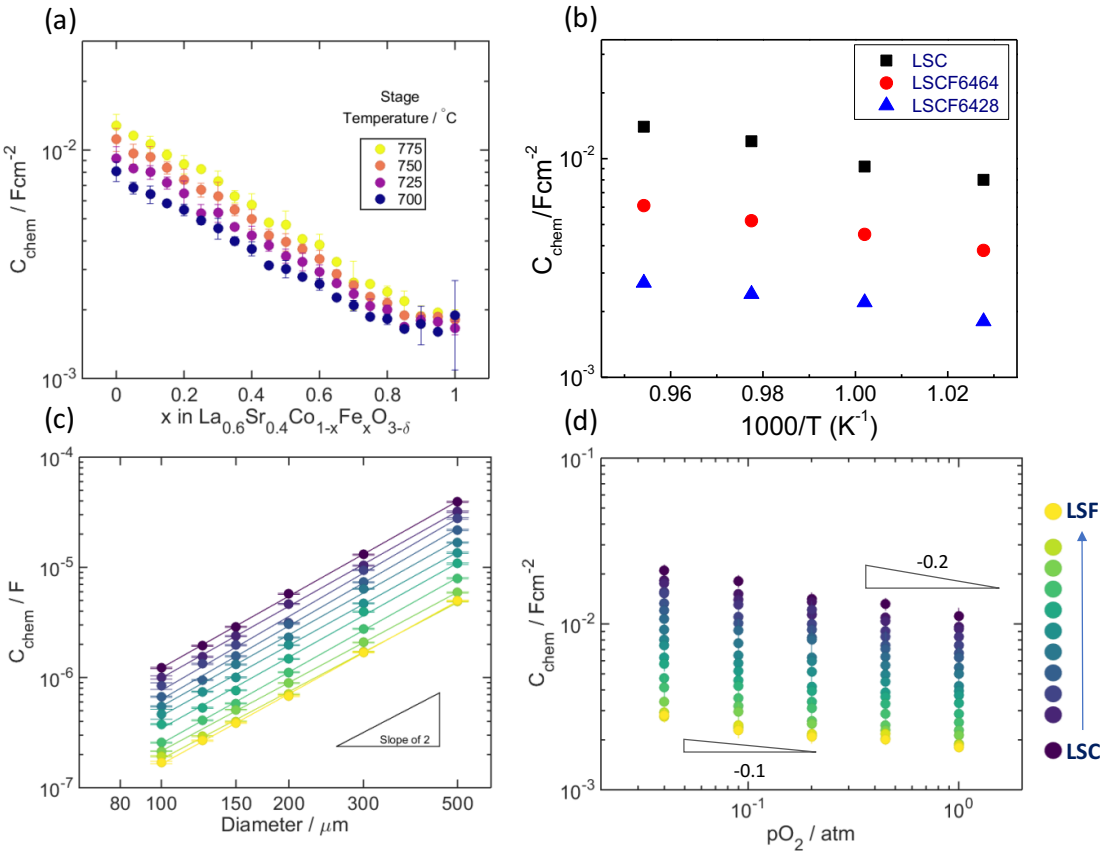

Figure 4.17 (a) Temperature dependence of the chemical capacitances measured on micro-electrodes ($d = 500\mu m$) as a function of the composition of Fe in $La_{0.6}Sr_{0.4}Co_{1-x}Fe_xO_{3-\delta}$. (b) Arrhenius plots of the chemical bulk capacitance of the $La_{0.6}Sr_{0.4}Co_{1-x}Fe_xO_{3-\delta}$ film. (x=0, 0.4, and 0.8) (c) Electrode diameter dependence of the chemical capacitance measured at 775 °C with a pO_2 0.2 atm. (d) Oxygen partial pressure dependency of the chemical capacitance measured on micro-electrodes ($d = 500\mu m$) at 750 °C.

4.4.4 Chemical bulk capacitance (C_{chem})

Fitting the EIS data to calculate the capacitance using the following Equation:[111]

$$C = (R^{1-n} \cdot Q)^{-n} \quad (5)$$

where Q is a constant phase element, R is the resistance, and n is the non-ideality factor. All the parameters can be extracted by fitting the EIS data. If n is 1, Q is an ideal capacitor. In this study, the value of n is close to 1 for the low frequency region ($R_s \parallel C_{chem}$), so the value of R_s will have a minor contribution to C_{chem}. Therefore, the parameter of C_{chem} will give complementary information about the oxygen surface exchange kinetics on LSCF micro-electrodes.[111]

The chemical capacitance, C_{chem}, is caused by stoichiometric changes in the electrode bulk and proportional to the inverse of the derivative of the chemical potential of oxygen vacancies with respect to their concentration $[(\frac{\partial \mu_{Vo}}{\partial c_{Vo}})^{-1}]$.[111] The oxygen nonstoichiometric parameter δ in the mixed conducting perovskite-type $La_{0.6}Sr_{0.4}Co_{1-x}Fe_xO_{3-\delta}$ depends on the concentration of B-site dopant, temperature, and oxygen partial pressure. In general, δ in $La_{0.6}Sr_{0.4}Co_{1-x}Fe_xO_{3-\delta}$ is proportional to the concentration of cobalt (Co) and the temperature, but is inversely proportional to the oxygen partial pressure.[120] Therefore, the chemical capacitance increases with increasing the temperature and the Co content as observed in Figure 4.17a. This indicates a higher oxygen vacancy concentration at a higher temperature or a higher concentration of Co in $La_{0.6}Sr_{0.4}Co_{1-x}Fe_xO_{3-\delta}$. The values of area-specific capacitances are in the range of 1.2×10^{-2} F/cm^2 to 2×10^{-3} F/cm^2 at 750 °C in 1 atm pO_2, which are comparable to the values reported by Baumann *et al.*[111] under the same conditions. The chemical capacitance shows a weak temperature dependence behavior, especially for LSF end, as shown in Figure 4.17a. The similar behavior was also observed from the Arrhenius plots (Figure 4.17b) as the activation energies of C_{chem} decrease from ~0.68 eV to ~0.46 eV with x increased to 0.8 in $La_{0.6}Sr_{0.4}Co_{1-x}Fe_xO_{3-\delta}$. This is consistent with the

results that both δ and $\Delta\delta/\Delta p(O_2)$ of LSC increase much more than those of LSF with temperature increasing from 600 ºC to 800 ºC.[120]

Figure 4.17c shows that the chemical capacitance scales with a slope of ≈2 in relation to the diameter of microelectrodes in the log-log plots. This is expected because the chemical capacitance reflects the bulk property of the materials.[105] Figure 4.17d shows that the chemical capacitance decreases with increasing oxygen partial pressure, however, C_{chem} shows a very weak pO_2 dependence at 750°C in the pO_2 range of 10^{-3} to 1 atm. This result is consistent with the low pO_2 dependence of the chemical capacitance observed by thermogravimetry on the bulk materials.[120]

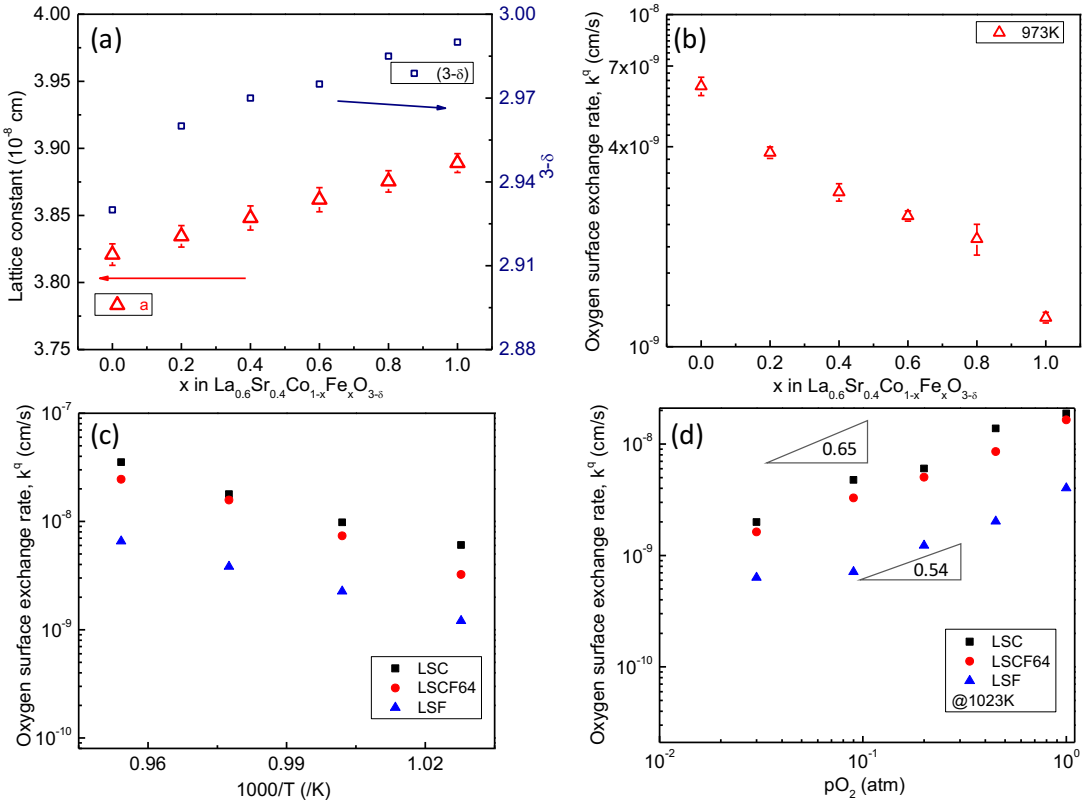

Figure 4.18 (a) The lattice constant of the pseudo-cubic LSCF and the oxygen nonstoichiometry (3-δ), as a function of the composition of Fe in $La_{0.6}Sr_{0.4}Co_{1-x}Fe_xO_{3-\delta}$ at 700 °C. (b) Composition dependency of the surface exchange coefficients (k^q) of the LSC-LSF micro-electrodes ($d = 500\ \mu m$) at 700 °C with pO_2 1 atm. (c) Arrhenius-

type plot of the surface exchange coefficient (k^q) of the LSC-LSF micro-electrodes ($d = 500\ \mu m$). (d) Oxygen partial pressure dependency of the surface exchange coefficients (k^q) of the LSC-LSF micro-electrodes ($d = 500\ \mu m$) at 750 °C.

4.4.5 Oxygen surface exchange coefficients (k^q)

The oxygen surface exchange coefficient was investigated to identify the rate-determining step (rds) for the oxygen incorporation reaction at the surface of mixed conducting cathode. There are three different exchange coefficients based on different experimental techniques: k^q is from the electrical measurement, k^δ is from the chemical experiment, and k^* is from isotope exchange experiment.[39] In this work, we only investigated k^q obtained from the EIS data as a function of composition, $p(O_2)$, and temperature.

The ORR area specific resistance was used to calculate surface exchange coefficient, k^q from the following equation:[113]

$$k^q = k_B T / 4e^2 R_s A_{electrode} c_0 \quad (6)$$

Where k_B is the Boltzmann's constant, T is the absolute temperature, e is the elementary charge, R_s is the oxygen surface exchange resistance, $A_{electrode}$ is the microelectrode surface area, and c_0 is the total lattice oxygen concentration in $La_{0.6}Sr_{0.4}Co_{1-x}Fe_xO_{3-\delta}$. Oxygen nonstoichiometry was determined based on the previous work from Hashimoto *et al.*[120] The lattice constant of the pseudo-cubic $La_{0.6}Sr_{0.4}Co_{1-x}Fe_xO_{3-\delta}$ film was estimated based on the XRD data and the thermal expansion coefficients of LSC and LSC at 700 °C. Both the nonstoichiometry parameter (3- δ) and the lattice constant are

shown in Figure 4.18a as a function of Fe composition. Thus, c_0 was calculated to be in the range of 8.72×10^{-2} mol/cm^3 to 8.44×10^{-2} mol/cm^3 from LSC-end to LSF-end.

The oxygen exchange rate constant (k^q) decreases gradually with the doping of Fe in LSC as shown in Figure 4.18b. The k^q is in the range of 6.1×10^{-9} cm/s to 1.2×10^{-9} cm/s from LSC to LSF at 700 °C with pO_2 1 atm. A particularly strong increase in k^q by about a factor of 5 is achieved upon introduction of Co on the B site of the perovskite. It has been reported that the correlation between the oxygen exchange rate constant and ionic conductivity is nearly perfectly linear and the oxygen exchange rate constant can be increased by increasing the oxygen vacancy concentration and mobility for mixed conducting cathode materials.[99] This trend is in good agreement with the changes of k^q in Figure 4.18b. The decrease in ionic conductivity from LSC to LSF can be attributed to the decreased concentration of the oxygen vacancy.[99]

The temperature dependence of k^q was investigated in the range of 700 °C to 775 °C under 1 atm pO_2 as shown in Figure 4.18c. A fair linearity is observed in the plots, showing that k^q describes a thermally activated process as expected. The activation energy for k^q was in a range of 199 KJ/mol to 241 KJ/mol between 700 °C and 775 °C at 1 atm pO_2. These activation energy values are comparable to those of LSCF family thin-film microelectrodes reported previously. [39,121,122]

Figure 4.18d shows oxygen partial pressure dependence of surface oxygen exchange coefficients (k^q) at 750 °C. The values of k^q increase with increasing pO_2 following $k^q \propto P_{O2}^m$ in the pO_2 range of 10^{-3} to 1 atm as shown in Figure 4.18d. The dependence of m was determined to be in a range of 0.54 to 0.65, which is consistent with the pO_2 dependence of oxygen surface exchange resistance. The pO_2 dependence

of k^q further supports the result that a dissociative adsorption step was proposed as the rate-limiting step in this study. In addition, the observed pO_2 dependence of LSCF in this study is in good agreement with those expected for metallic and p-type mixed conducting cathodes, such as LSC with *m* in the range from ~0.43 to ~0.92 reported by Adler *et al.*[123] and LSF with *m* in the range of ~0.75 to ~0.95 reported by ten Elshof *et al.*[124]

4.4.6 Evaluation of the possible reaction mechanisms

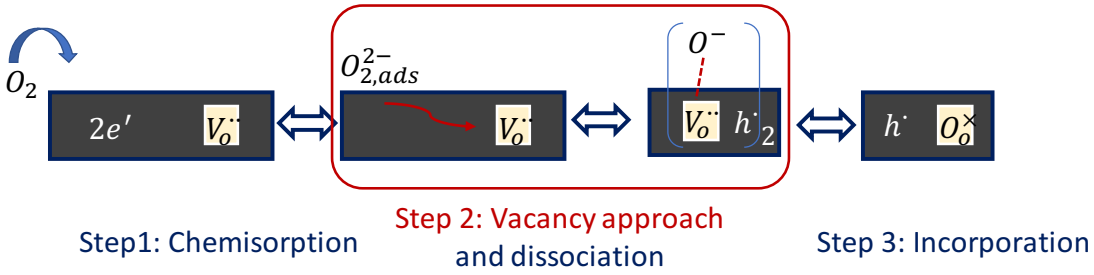

Figure 4.19 The scheme of the proposed oxygen surface exchange reaction mechanism for a $La_{0.6}Sr_{0.4}Co_{1-x}Fe_xO_{3-\delta}$ thin-film cathode on the YSZ electrolyte.

There are a number of different possibilities for the reaction mechanism that gives rise to a slope of $\log(k^q)$ vs. $\log(pO_2)$ in the range of 0.5 to 1, however, a dissociative adsorption step has been identified as the rate-determining step for $La_{0.6}Sr_{0.4}Co_{1-x}Fe_xO_{3-\delta}$ thin-film cathode in this study. As Wang *et al.*[99] reported that high oxygen vacancy concentration is a key factor for the surface oxygen exchange rate, the surface concentration of $V_o^{\cdot\cdot}$ determines the performance of LSCF thin-film cathode. Considering the high electronic conductivity (>100 s/cm),[99] the high $V_o^{\cdot\cdot}$ concentration for LSCF, and our experimental results, it might be the approach of an

oxygen vacancy to $O_{2,ads}^{2-}$ to determine the overall oxygen exchange rate as shown in Figure 4.19. These species of $(O_2 \cdots V_O^{\cdot\cdot})$ and $(O \cdots V_O^{\cdot\cdot})$ are involved in the rds for surface oxygen exchange in this study. This result will provide some insights into the reaction mechanisms underlying the ORR.

4.5 Conclusions

The most studied cathode materials for SOFCs include lanthanum and strontium manganites (LSM), cobaltites (LSC), and ferrites (LSF). However, none of them can meet all the requirements for cathodic materials due to issues such as low ionic conductivity, low stability, and incompatibility with other components in SOFC system. One promising approach is to fabricate new compositions by the combination among them to obtain enhanced performance in IT-SOFCs. In this study, we used the high-throughput pulsed laser deposition approach to fabricate a $La_{0.6}Sr_{0.4}Co_{1-x}Fe_xO_{3-\delta}$ ($0 \leq x \leq 1$) composition gradient thin film on YSZ single crystal substrate, and the geometrically well-defined thin-film microelectrodes were used as a model system to obtain mechanistic information on the oxygen reduction reaction at the surface of SOFC cathodes. The PLD thin film with well-defined geometry can minimize the complexity arising from the morphology of cathode materials used in traditional preparation procedures. A systematic investigation of the influence of the B-site dopant, microelectrode diameter, temperature, and oxygen partial pressure on the oxygen surface exchange resistance (R_s), chemical capacitance (C_{chem}), and the electrical surface oxygen exchange coefficient (k^q) has been performed. The results for $La_{0.6}Sr_{0.4}Co_{1-x}Fe_xO_{3-\delta}$ thin-film microelectrodes have led to elucidating their

behavior as a cathode for intermediate temperature SOFCs. For the mixed conducting LSCF, the oxygen reduction reaction follows a bulk path in this work, and the oxygen ionic conductivity ($[V_o^{\cdot\cdot}]$) is an important factor in determining the performance of oxygen surface exchange reaction. The pO_2 dependence of R_s and k^q of the entire LSC-LSF spread film shows consistent results with a value of m (slope of a log–log plot) in a range of ~0.5 to ~0.75 for R_s and ~0.54 to ~0.65 for k^q. As a result, the oxygen vacancy transport to surface-adsorbed oxygen intermediates is proposed to be the rate-determining step for mixed conducting cathodes. This study also showed the potential of increasing the surface oxygen vacancies (such as surface modification or surface nano-engineering) to develop highly active surface oxygen exchange materials for applications in the field of solid oxide fuel cells and electrolysis cells. A better understanding of the influence of the surface chemical composition on the ORR is needed because surface exchange reactions are highly sensitive to the surface chemistry. For this purpose, more work focused on surface characterizations are in order.

Chapter 5: High Performance Cathode Materials for Proton Conducting SOFCs

5.1 Abstract

Proton conducting SOFCs have been demonstrated to be the highly efficient, environmentally sustainable, and cost-effective energy conversion devices at intermediate temperatures (400-600 °C). However, the power output from these devices has lagged behind predictions based on electrolyte conductivity due to the poor performance of the traditionally used cathode materials and the stability challenge of proton conductors under H_2O/CO_2 atmosphere. Here we identify a double perovskite (PBSCF) that possesses the combined conduction of e^-, O^{2-}, and H^+ by investigating the geometrically well-defined microelectrodes. Combining with a chemically stable electrolyte, $BaZr_{0.4}Ce_{0.4}Y_{0.1}Yb_{0.1}O_3$ (BZCYYb4411) and a thin dense PLD PBSCF interface layer between the cathode material and the electrolyte, we achieved a peak power density of 548 mW/cm^2 at 500 °C and an unprecedented stability under CO_2.

5.2 Introduction

SOFCs are promising candidates for the use in future clean energy generation applications due to their high efficiency, fuel flexibility, and environmentally benign properties.[46] However, their high operating temperatures have delayed the commercialization of SOFCs in a wide range of applications. In lowering the high operating temperatures (>800 °C) of solid-oxide fuel cells, proton conducting SOFCs (p-SOFCs) have attracted much attention from both the academia and industry due to

the high ionic conductivity of the proton conducting electrolyte materials at intermediate temperatures (400-600 °C).[125] However, the state-of-the-art power densities of p-SOFCs are just exceeding 200 mW/cm^2 at 500 °C,[126-129] whereas such performance is routine for cells based on oxygen ion conductors.[130-132] Besides the reactivity of many protonic ceramics with H_2O or CO_2, another big challenge limiting the power densities to date is the poor state of electrode development for p-SOFCs.[125]

The ideal cathode materials for p-SOFCs should have high electronic, protonic, and oxide ionic conductivity, high catalytic activity for the dissociation and reduction of oxygen molecules, chemical and dimensional stability in oxidizing humid atmospheres, thermal expansion match with other cell components.[125] The overall cathode reaction of p-SOFCs can be represented using the Equation (1):

$$\frac{1}{2}O_2\ (gas) + 2e^-\ (cathode) + 2H^+(electrolyte) \rightarrow\ H_2O\ (gas)\ \ (1)$$

The cathode reaction as shown in (1) is different to that of a traditional SOFC. For the traditional SOFCs, as we discussed in Chapter 4, the primary function of the cathode material is to facilitate the electrochemical reduction of oxygen molecules and to accelerate the transport of formed oxygen ions into the electrolyte. We have learned that the best cathode materials for traditional SOFCs are those mixed oxygen ion and electron conductors, such as $La_{0.6}Sr_{0.4}Co_{1-x}Fe_xO_{3-d}$ (LSCF), which extends the reaction sites to the entire surface of the cathode material beyond the triple phase boundaries as we discussed in Chapter 4. In a p-SOFC, while the cathode reaction follows the regular ORR, the water evolution reaction shifts from anode to cathode, making the cathode reactions more complicated.[133,134] As shown by Equation (1), proton conduction, instead of oxygen ion conduction, plays an important role in determining the cathode

reactions for a p-SOFC. However, most of the demonstrations of p-SOFCs to date are just based on the ideal cathode materials for traditional SOFCs, the mixed oxygen ion and electron conductors.[135] This is the likely reason for poor power densities of p-SOFCs.

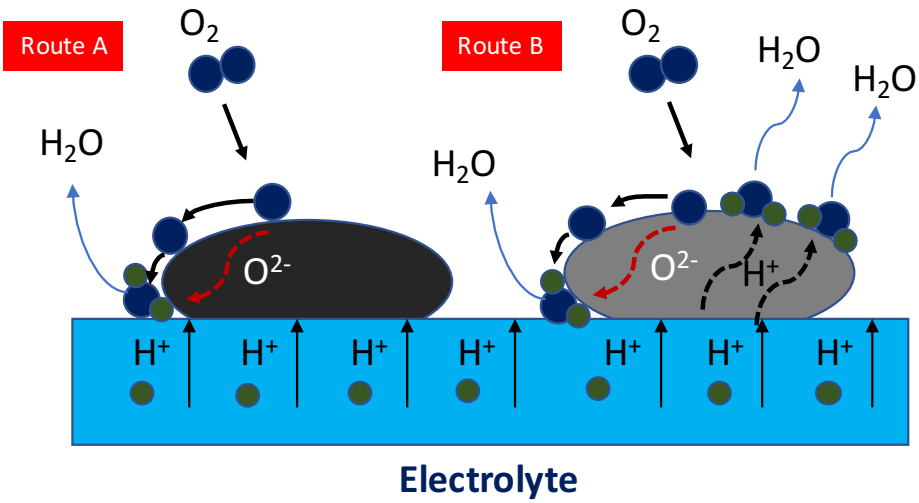

Figure 5.1 A schematic illustration of cathodic reaction in a p-SOFC.

As shown in Figure 5.1, two reaction routes have been proposed based on different kinds of cathode materials. Most cathode materials for p-SOFCs are oxygen ion-electronic mixed conductors, the reduced oxygen ion may only meet the proton transported from the anode through electrolyte at the TPB sites as shown in Route A (surface path), and the TPB sites are also the places for the water evolution. The insufficient reaction sites limit the performance of this kind of cathode materials in p-SOFCs. When the proton-electronic mixed conducting cathode material is applied, the two phase boundary could also contribute to the cathodic reaction as Route B (bulk path) illustrated in Figure 5.1. Thus, the reaction sites would be extended to the entire surface, and the cathode polarization resistance can be reduced. Therefore, the most

promising cathode materials for p-SOFCs should have simultaneous electronic, oxygen ionic, and protonic conduction properties.[136-138]

In general, there are two main advantages for the 'triple-conducting oxides'. First, protons can transport through the cathode bulk and this enhances the electrochemical reaction active area from the TPB to the whole cathode specific surface. Second, water generation is not limited at the TPB site, but it can be produced from the whole cathode surface and this helps the evaporation of produced water.[139] However, the deliberate creation of this kind of 'triple-conducting oxides' has met with limited success. [133,134] The efficacy of the traditional mixed oxygen ionic and electronic cathodes (MIECs) for oxygen electro-reduction in p-SOFCs has led some authors to conclude that some conventional MIECs can, in fact, absorb H_2O and thereby become good proton conductors (in addition to conducting oxygen ions and electrons).[136-138] Such materials have been termed 'triple conducting oxides' and the evident proton uptake justifies an examination of conventional MIECs for further p-SOFC development.[135] In this thesis work we demonstrate exceptional proton solubility and transport through PBSCF, rendering it ideal for oxygen electro-reduction in p-SOFCs.

The cathode, PBSCF, was selected on the basis of the high activity of the related material $NdBa_{0.5}Sr_{0.5}Co_{1.5}Fe_{0.5}O_{5+\delta}$ (NBSCF), from which p-SOFC cells with peak power density of 690 mW/cm^2 at 600 °C have been obtained.[140] This is amongst the highest values in the open literature at 600 °C, approaching results achieved using $Sm_{0.5}Sr_{0.5}CoO_{3-\delta}$ (SSC)[128] and $La_{0.6}Sr_{0.4}CoO_{3-\delta}$ (LSC)[129] and exceeding those obtained using the designer mixed proton-electron (and oxide ion) conductor $BaCo_{0.4}Fe_{0.4}Zr_{0.1}Y_{0.1}O_{3-\delta}$[127]as cathodes. The Pr analog offers potential advantages as a

result of its slightly higher electronic conductivity; its activity in conventional SOFCs is also slightly higher.[132]

Both PBSCF and NBSCF are double-perovskites of general composition $LnA'B_2O_{5+\delta}$ (Ln = La, Pr, Nd, Sm, Gd; A' = Ba, Sr; and B = Co, Fe, Mn), in which the A cation of the architype ABO_3 perovskite is replaced in alternating fashion with Ln and A' cations. The result is a layered structure with stacking sequence …[A'O]–[BO_2]–[LnO_δ]–[BO_2]… along the c-axis.[141,142] Kim et al. showed that the bulk oxygen diffusivity and surface reaction constant of the representative double perovskite $PrBaCo_2O_{5+\delta}$ are much higher than those of standard perovskite MIEC cathode materials,[142] spawning a surge in efforts to exploit these materials for conventional SOFCs.[132,141,143-148] The diffusivity is particularly high in the *ab* plane, where has the high oxygen vacancy concentration.[149] Exploration of double-perovskites in p-SOFC systems is at a nascent stage. Furthermore, at least in the case of $PrBaCo_2O_{5+\delta}$, the capacity for H_2O uptake, a prerequisite for oxygen reduction in p-SOFC systems via a double-phase boundary pathway, is in some dispute.[137,138,150] These factors drive our evaluation of PBSCF from both performance and mechanistic perspectives.

The potential use of PBSCF for p-SOFCs calls for a deeper understanding of the fundamental mechanisms behind their high performance. As dense thin-film electrodes behaved as "pure bulk", we fabricated a library of high quality PBSCF microelectrodes with various diameters on proton conducting electrolytes by PLD to investigate the oxygen electrochemical reduction pathway on PBSCF. The goals of this work were to get a deep understanding about the triple conducting properties of PBSCF

and to establish structure-property relations for these cathodes in order to further improve their properties and design new structures.

5.3 Experimental methods

Cathode materials and electrolytes. To fabricate PLD targets/pellets of PBSCF, $PrBa_{0.5}Sr_{0.5}Co_2O_{5+\delta}$ (PBSC), $PrBa_{0.5}Sr_{0.5}Fe_2O_{5+\delta}$ (PBSF), $BaZr_{0.8}Y_{0.2}O_3$ (BZY20), $BaZr_{0.4}Ce_{0.4}Y_{0.1}Yb_{0.1}O_3$ (BZCYYb4411), and $BaZr_{0.4}Ce_{0.4}Y_{0.1}Yb_{0.1}O_3$ (BZCYYb1711), oxide powders were synthesized by the Pechini process.[107] Specifically, metal nitrate precursors were dissolved in water, to which citric acid (CA) and ethylenediaminetetraacetic acid (EDTA) were added as chelating agents in a 1:1.5:1.5 molar ratio of metal cations:CA:EDTA. This solution was heated and aged overnight to produce a viscous gel, which was then dried between 250 °C and 600 °C to produce a very fine powder. To improve the strength of the pellets, ~1 wt% polyvinylpyrrolidone (PVP) was added as a binder. The powders were mechanically pressed into discs and sintered at 1450-1600 °C for 12-24 hours to yield pellets with ~ 24 mm in diameter, 3-5 mm in thickness and 93-97% of theoretical densities, as determined by the Archimedes method.

Microelectrode preparation and characterization. Electrochemical characterizations were performed on an array of microdots of the PBSC-PBSF composition spread film and the PBSCF film supported on a (100) oriented YSZ (8 mol% Y_2O_3, MTI Co.) single crystal and a proton-conducting electrolyte substrate, respectively. Initial experiments in this work began with the electrolyte BZCYYb1711 and thus this material served as the substrate. A dense compact of BZCYYb1711 ~1.5 mm in thickness was prepared by the methods described above (solid state synthesis,

final sintering at 1600 °C for 18 h). To provide a smooth surface for electrode deposition, a thin (~250 nm) buffer layer of $BaZr_{0.8}Y_{0.2}O_3$ was applied by a custom-made PLD/Laser-MBE System (Pascal Co., Ltd.) equipped with a loadlock chamber using a target prepared by chemical solution method which is described in detail elsewhere. A KrF (λ=248nm) excimer laser (Lambda COMPexPro) was used to ablate the targets at a pulse repetition rate of 5 Hz, a laser fluence of 0.51 J/cm^2 and a target-substrate distance ~55mm. Following the deposition of buffer layer, a thin film (~600 nm) of PBSCF was deposited on top using a target identical to the type used for PLD-modification of fuel cells. The growth rate of PBSC, PBSF, BZY and PBSCF was determined to be 3 nm/min, 2.2 nm/min, 2 nm/min, and 2.6 nm/min, respectively, for the following growth conditions: oxygen pressure: 30 mTorr for BZY, 100 mTorr for PBSC, PBSF, and PBSCF; laser fluence on target:0.51 J cm^{-2}; laser power: 25 mJ; repeat rate: 5 Hz; substrate temperature: ~680 °C for BZY, ~640 °C for PBSC, PBSF, and PBSCF. The grown film was then characterized by XRD (Bruker D8 Discover with 4 bounce monochromator, Cu Kα radiation), optical microscopy (Keyence VW-9000), and atomic force microscopy (AFM, Digital Instruments Nanoscope Ⅲand Dimension 5000). For electrochemical characterization the film was patterned, using photolithography and ion milling, into a library of microelectrodes with diameters spanning from 125 to 500 μm. Specifically, each sample was coated with a photoresist (Shipley 1813) by a regular spin coating method (4000 rpm for 50 s). After spin coating, the photoresist was baked at 100 °C for 2 min to drive off solvents and to solidify the film, following an exposure to UV radiation for 12 s through a photomask, and then developed in Shipley 352 developer for 40 s. The sample then underwent ion milling

for 90 min, resulting in a milling depth of 650 nm. In the final step, the residual photoresist was stripped using acetone. After the patterning, a circular microelectrode array with diameters of 125-500 μm was well defined on the top of BZCYYb1711. Impedance data were collected at a film temperature of 500 oC (pO_2 = 0.2 atm and pH_2O = 0.016 atm) over the frequency range 1 MHz to 32 mHz using a voltage amplitude of 30 mV under zero-bias conditions (Solartron 1260). The data acquisition in an automated impedance microprobe instrument is described in detail elsewhere.[87]

Proton uptake measurement. To evaluate proton uptake in PBSCF, thermogravimetric analysis (TGA) was carried out using a Netzsch STA 449 C on powder samples in dry and wet air. 200 sccm of synthetic air and 20 sccm Ar were supplied to the measurement chamber to obtain an oxygen partial pressure (pO_2) of 0.19 atm. For the wet air condition, the gas mixture was bubbled through a distilled water bubbler held at 18 °C to obtain a water partial pressure (pH_2O) of 0.020. Under both conditions, the sample temperature was first increased from 100 to 800 °C at 5 °C min-1 and weight data then recorded upon cooling to 100 °C.

Fuel cell fabrication. Anode-supported full cells with a configuration of NiO-BZCYYb4411/BZCYYb4411/PBSCF was fabricated using a drop-coating method to conduct fuel cell measurements. The anode was formed from in-house synthesized NiO and the electrolyte powder. For NiO synthesis, nickel nitrate was dissolved in distilled water and glycine was added in the solution in a 1:1 molar ratio. The solution was heated on a hot plate set at 350 °C to evaporate water, yielding a viscous liquid. Fine NiO powders were obtained via a subsequent combustion reaction. The resulting NiO powder was calcined at 800 °C for 4h in air. The NiO-BZCYYb4411 composite anode

was prepared by ball milling NiO powder, BZCYYb4411 powder, and starch in a weight ratio of 65:35:0.5 in ethanol for 24 h. After a drying step, the composite powders were mechanically pressed into a disc and lightly sintered at 800 °C for 4 h. For the fuel cell with the PLD layer, the PBSCF film was first deposited on the electrolyte side of NiO+BZCYYb4411/BZCYYb4411 bi-layer cells using a conventional PLD system. After the PLD PBSCF layer, a slurry of PBSCF was then brush-painted onto the PBSCF thin film and the complete cell was sintered at 950 °C for 4 hours in air.

Fuel cell electrochemical characterization. Ag wires (GoodFellow) were attached at both electrodes of single cell using an Ag paste (SPI supplies) as a current collector. An alumina tube and a ceramic adhesive (Ceramabond 552, Aremco) were employed to fix and seal the single cell. Humidified hydrogen (3% H_2O) was applied as fuel to the anode through a water bubbler with a flow rate of 60 sccm and air was supplied to cathode with a flow rate of 200 sccm during single cell tests. Impedance spectra were recorded under open circuit voltage (OCV) in a frequency range of 100 kHz to 0.1 Hz with AC perturbation of 20 mV. I-V curves were collected using a BioLogic SP-300 Potentiostat at operating temperature from 500 to 650 °C in intervals of 50 °C. The current stability was measured under a fixed voltage of 0.5V at 550 °C. The open circuit stability was measured for BZCYYb4411 and BZCYYb1711 electrolyte-based fuel cells with humidified (3% H2O) 10 % CO_2 and 90 % H_2 mixture at 500 °C supplied to the anode and air to the cathode.

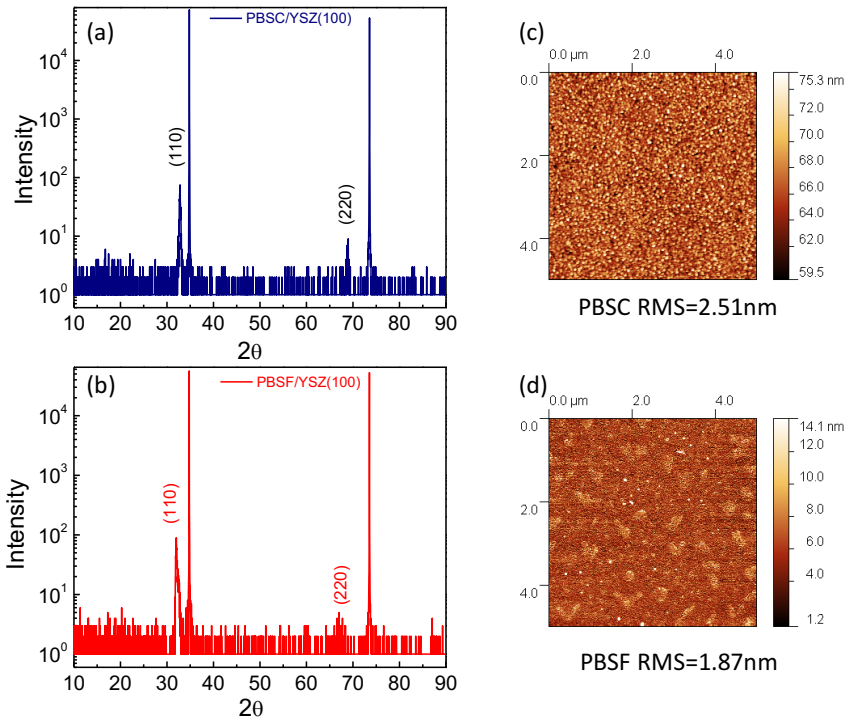

Figure 5.2 (a) (b) XRD patterns ($2\theta - \theta$ scan) of PBSC and PBSF thin films grown on YSZ (100), respectively. (c) (d) The AFM images of PBSC and PBSF thin films grown on YSZ (100), respectively. A RMS value of 2.51 nm on 5μm×5μm scan area for PBSC and 1.87 nm for PBSF.

5.4 Results and discussion

5.4.1 PLD cathode thin films

Figure 5.2a shows the XRD patterns of PBSC and PBSF films grown on YSZ(100) using the optimized deposition conditions. Their peaks were indexed with respect to the tetragonal structure (P4/mmm).[151] Only the (110) reflections are observed as shown in Figure 5.2, indicating that both PBSC and PBSF films are grown preferentially along (110) orientation on the YSZ substrate. The PBSCF has the lattice constant of a = b = 3.87 Å and c = 7.76 Å[151], and YSZ has the lattice constant of 5.12Å.

The good lattice match between the (110) orientation of PBSCF and the (100) orientation drives the growth of PBSCF along the [110] direction. AFM results (Figure 5.2 c and d) indicate the dense and smooth features of both films.

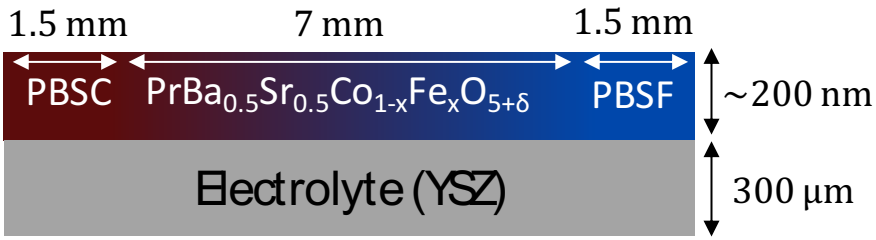

Figure 5.3 A schematic sketch of the PBSC-PBSF composition spread sample.

Using the high-throughput PLD methodology (Details discussed in Chapter 2), the compositional gradients of PBSC-PBSF (~200nm) was fabricated on YSZ substrates. Figure 5.3 shows the schematic of the compositional-spread films: The x in $PrBa_{0.5}Sr_{0.5}Co_{2-x}Fe_xO_{5+\delta}$ increases from 0 to 1 over a length of ~7 mm, and two ends (~1.5mm) are individual PBSC and PBSF.

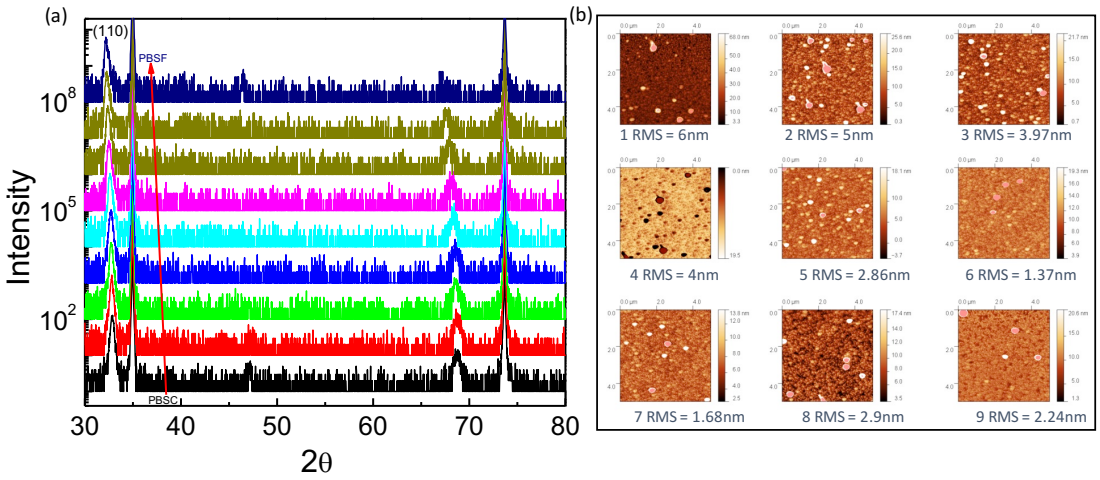

Figure 5.4 (a) The XRD diffraction patterns of a PBSC-PBSF composition spread film on YSZ (100) substrate. (b) 5μm×5μm AFM scan images of a PBSC-PBSF

composition spread film on YSZ (100). Position 1 to 9 means the x in $PrBa_{0.5}Sr_{0.5}Co_{2-x}Fe_xO_{5+\delta}$ is from 0 to 1.

The dominated (110) peaks of the PBSC-PBSF film observed in Figure 5.4 indicate that the whole spread film has a tetragonal structure and grows with a (110) preferred orientation. As shown in Figure 5.4a, the angle positions of (110) peaks shift to small 2θ angles with the doping concentration of Fe increasing (Bottom to up) since the ionic radius of Co^{3+} (0.545Å) is smaller than that of Fe^{3+} (0.645Å). XRD patterns show the high crystallinity of the single-phase PBSC-PBSF film. AFM analysis revealed relatively smooth film surfaces with RMS surface roughness of a few nanometers for the whole spread film, as shown in Figure 5.4b. As demonstrated by the XRD and AFM results, the dense and smooth (PBSC-PBSF)/YSZ spread film is a good candidate for investigating the effect of intrinsic properties of PBSCF on ORR performance.

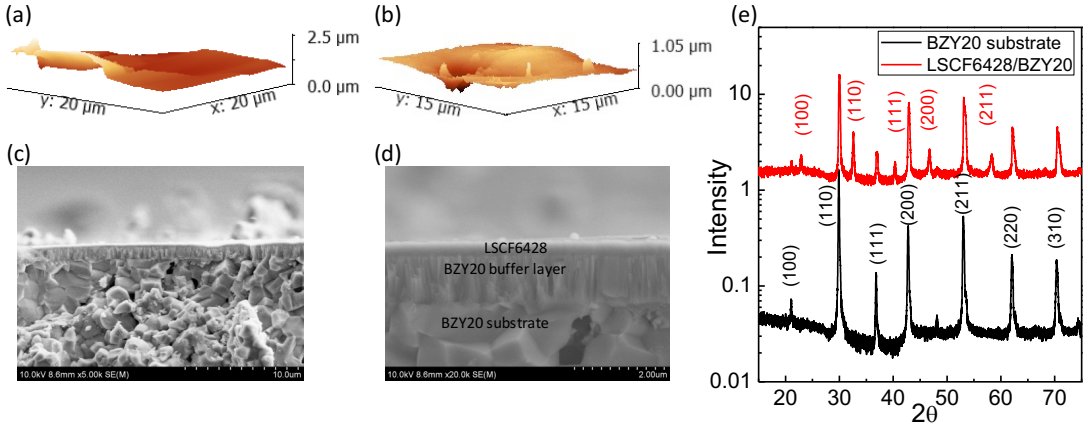

Figure 5.5 (a) The 3D AFM image of BZY20 substrate with a RMS roughness of 0.36 μm. (b) The 3D AFM image of the LSCF648 cathode film grown on a BZY20 substrate with a RMS roughness of 107 nm. The cross-sectional images of an as prepared

LSCF6428/BZY20/BZY20 structure: (c) Low-magnification SEM image and (d) high-magnification SEM image. (e) The XRD diffraction patterns of a LSCF6428/BZY20 sample.

One big challenge for the PLD cathode thin film on proton conducting electrolytes is the large surface roughness of in-house made electrolytes, such as BZY20 electrolytes. The surface RMS roughness of a BZY20 substrate is around 360 nm as shown in Figure 5.5a, indicating a rough surface as expected from the in-house made BZY20 substrates (90% theoretical density). To get a smooth PLD cathode thin film, we proposed to deposit 200-1000 nm BZY20 buffer layer on the top of BZY20 pellet first, and then deposit 200-800 nm cathode film on the top of buffer layer. As demonstrated with a ~300 nm LSCF6428 cathode film, the surface RMS roughness of LSCF6428 is 107 nm as shown in Figure 5.5b. A uniform and dense buffer layer was clearly shown in the cross-sectional images (Figure 5.5c and 5.5d), thus, the BZY20 buffer layer helps to provide a smooth surface for cathode deposition. Figure 5.5e shows the XRD patterns of LSCF6428/BZY20 and BZY20 substrate, respectively. The patterns of the LSCF6428 layer were indexed to the pseudo cubic perovskite structure and no impurity phase was detected, indicating a single phase and well-crystallized cathode thin film prepared on top of proton conducting BZY20 substrate. The same methodology was used to provide a smooth surface for PBSCF deposition on BZCYYb1171 by using a thin (~250 nm) buffer layer of BZY20 as shown in Figure 5.6. X-ray diffraction analysis confirmed the absence of reactivity between these components (Figure 5.6a), and atomic force microscopy revealed the PBSCF surface to have a rms roughness of 43.8 nm, reflecting the roughness of the underlying

polycrystalline substrate (Figure 5.6b). We patterned the PBSCF film by ion milling to create sharply-defined microelectrodes ranging in diameter from 125 to 500 μm, with over ten duplicates of each diameter as shown in Figure 5.6d.

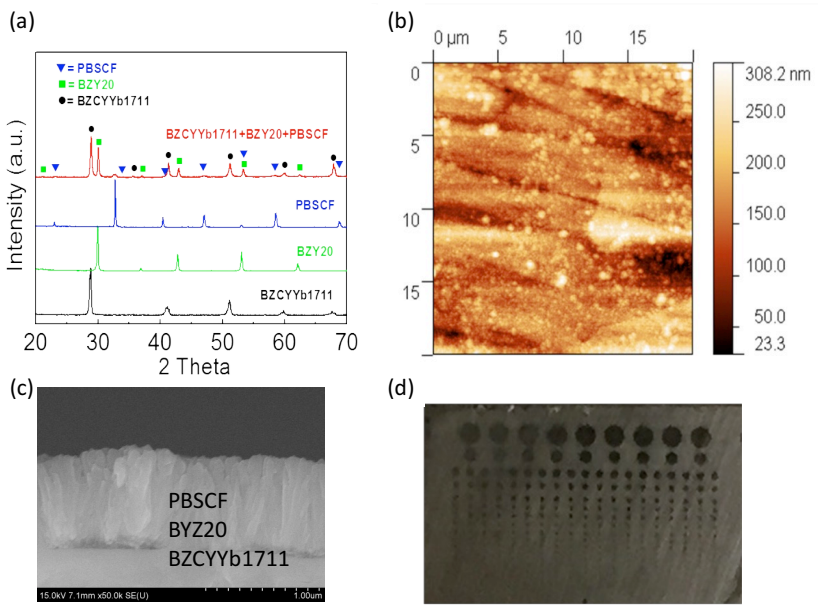

Figure 5.6 (a) Diffraction patterns for BZCYYb1711(substrate), BZY20 (buffer layer), and PBSCF cathode. (b) AFM image of microdot electrode with a RMS roughness of 43.8 nm. (c) The cross-sectional SEM image of the BZCYYb1711/ BZY20/PBSCF structure. (d) The optical microscope image showing microdots with various diameters.

5.4.2 Electrochemical properties of the (PBSC-PBSF)/YSZ sample

Using photolithography and ion milling, PBSC-PBSF cathode film was patterned into a library of microelectrodes ranging in diameters from 100 to 500 μm. The sample was then installed on the heated stage of the automated impedance microprobe for EIS measurements. An a.c. voltage of 30 mV, without d.c. voltage, and a typical frequency range of 10^4 Hz to 3.2×10^{-2} Hz were used in the measurements.

EIS data were acquired at a temperature range of 700 °C to 775 °C in 1 atm oxygen pressure. All the Nyquist plots show the similar typical features to that of the (LSC-LSF)/SDC20/YSZ sample as discussed in Chapter 4. We used the similar fitting method to do the EIS data analysis and focused on the low frequency part of the impedance spectrum. The overall electrode impedance is dominated by the large L-*f*-arc, which contains information on both the surface (R1) and the bulk (C1) of the electrode materials. The L-*f* resistance (R1) associates with the oxygen exchange at the surface of the electrode, corresponding to big semicircles in Figure 5.7a. The large capacitance (C1) is called chemical capacitance related to oxygen stoichiometry changes in the bulk of the electrode.

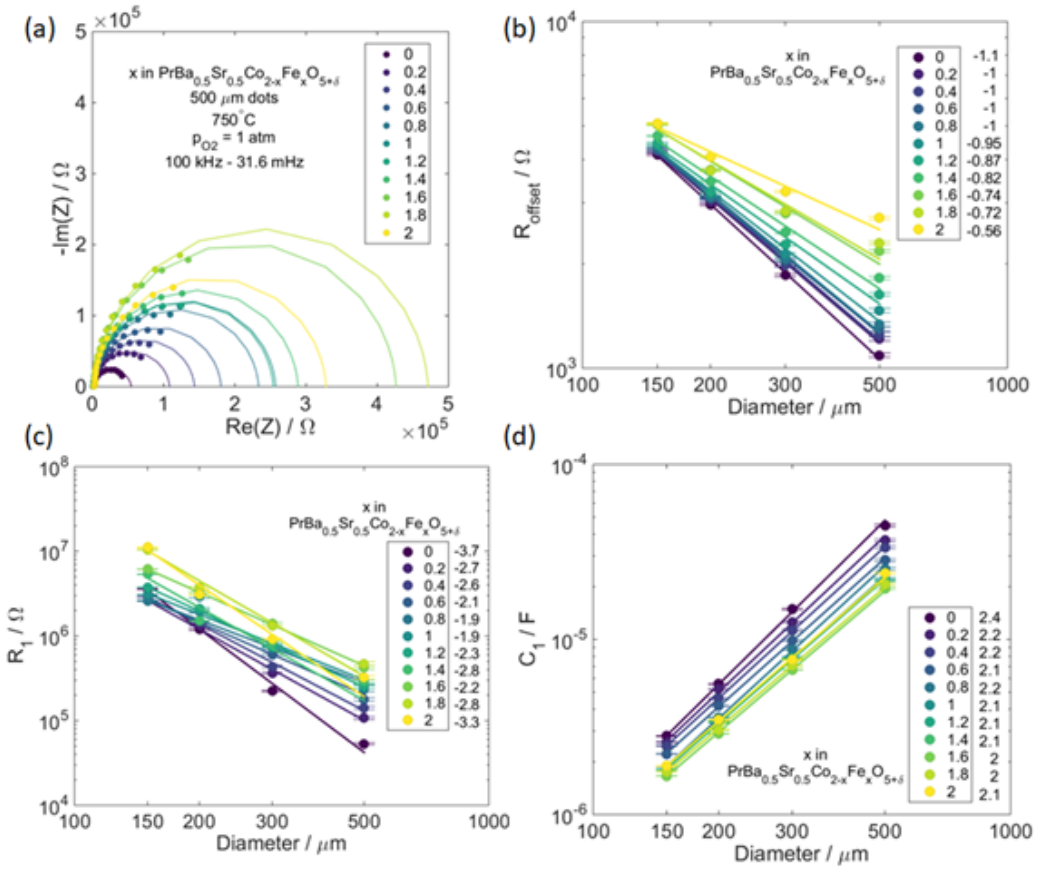

Figure 5.7 (a) Representative impedance spectra acquired on the electrodes (d = 500 μm) with different x values (Fe concentration) at 750 °C under 1 atm oxygen pressure.

(b) Electrode diameter dependence of the offset resistance measured at 750 °C with 1 atm oxygen pressure. (c) Electrode diameter dependence of the surface resistance measured at 750 °C with 1 atm oxygen pressure. (d) Electrode diameter dependence of the chemical capacitance measured at 750 °C with 1 atm oxygen pressure.

The offset resistance, R_{offset}, mainly includes the resistance of the electrolyte and the sheet resistance of the cathode film. Geometry dependence of the microelectrode impedance has also been investigated by carrying out the EIS measurements on microelectrodes with various diameters. The offset resistance is expected to be dominated by the resistance of the underlying electrolyte, with a scaling with diameter according to the Newman equation $R_{offset} = 1/(2\sigma d)$,[81] where σ and d are the electrolyte conductivity and the microelectrode diameter, respectively. In accord with this expression, R1 is inversely proportional to the microelectrode diameter as indicated by a slope of ~ -1 in the log-log plot for the whole PBSCF spread film is expected. The sheet resistance of $PrBa_{0.5}Sr_{0.5}Co_{2-x}Fe_xO_{5+\delta}$ was found to increase with increasing of Fe concentration, which results in the discrepancy with -1 when x is larger than 1 as shown in Figure 5.7b. R1 is inversely proportional to the microelectrode area as indicated by a slope of ~-2 in the log-log plot when x is between 0.4 and 1.2 as shown in Figure 5.7c. A slope of -2 is expected for a MIEC cathode because the entire surface area is active towards the oxygen exchange reaction.[87] PBSCF is a mixed conducting material, and the slope of ~-2 supports that the electrochemical reaction occurs over the entire surface of the $PrBa_{0.5}Sr_{0.5}Co_{2-x}Fe_xO_{5+\delta}$ ($0.4<x<1.2$) microelectrodes through a bulk path. The chemical capacitance, C1, is caused by stoichiometric changes in the electrode bulk.[111] The oxygen nonstoichiometric

parameter in the mixed conducting double perovskite $PrBa_{0.5}Sr_{0.5}Co_{2-x}Fe_xO_{5+\delta}$ depends on the concentration of B-site dopant, temperature, and oxygen partial pressure. In general, the chemical capacitance increases with increasing the Co content and scales with a slope ~2 in relation to the diameter of microelectrodes in the log-log plots as observed in Figure 5.7d. This is expected because the chemical capacitance reflects the bulk property of the materials.

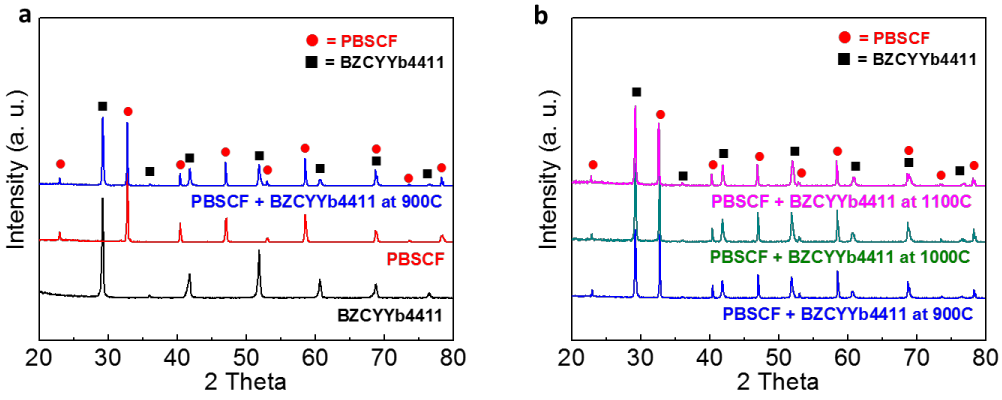

Figure 5.8 Chemical compatibility between PBSCF cathode and BZCYYb electrolyte. (a) X-ray diffraction patterns for sintered BZCYYb4411 and PBSCF pellets are shown as references for the diffraction pattern of a mixture of the two materials annealed at 900 °C. No secondary peaks occur, indicating the absence of a reaction between these phases. (b) X-ray diffraction patterns for the mixture annealed at 900, 1000, and 1100 °C also show no secondary phases.

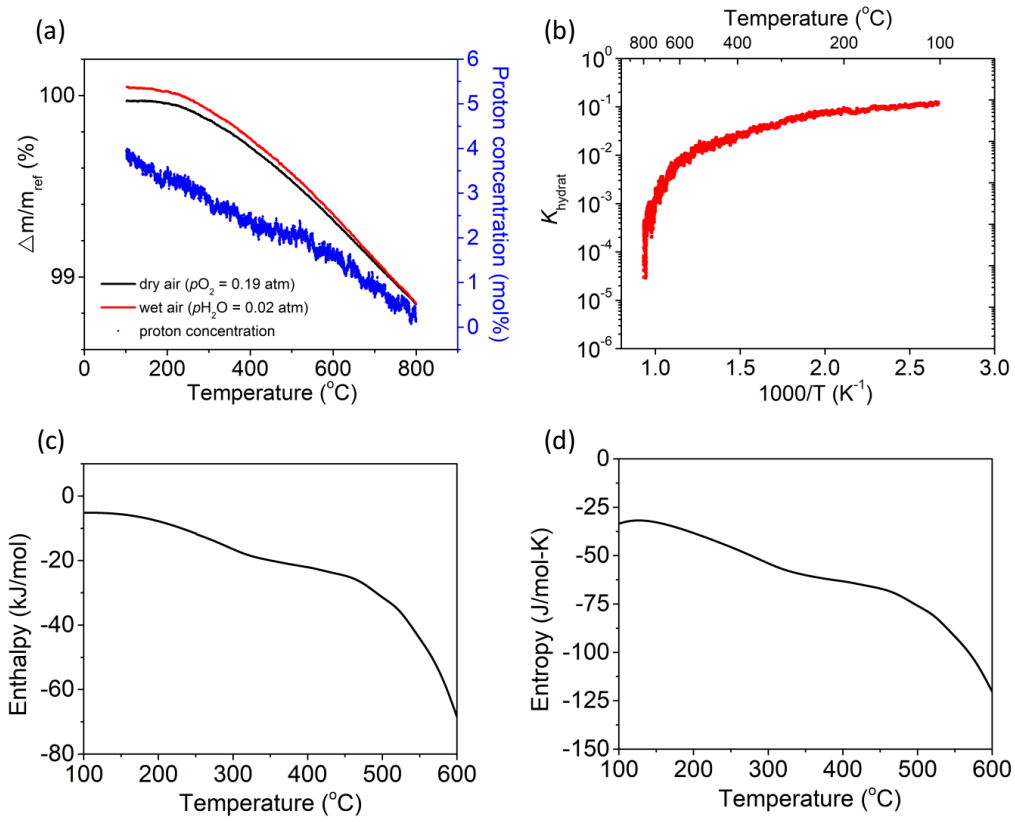

Figure 5.9 H_2O uptake behavior of PBSCF. (a) Thermogravimetric profiles on cooling in dry and wet air and implied proton concentration. (b) Equilibrium constant for the hydration reaction. (c) Enthalpy of hydration and (d) entropy of hydration. Thermodynamic properties obtained from analysis of the van't Hoff plot given in (b) after smoothing to remove spurious effects resulting from the subtraction of mass values given in (a).

5.4.3 Compatibility and H_2O uptake characteristics of PBSCF

Based on the results in the previous part and previous published results, the composition of $PrBa_{0.5}Sr_{0.5}Co_{1.5}Fe_{0.5}O_{5+\delta}$ (PBSCF) has been demonstrated to be the highly efficient and robust electrode for the traditional SOFCs, so we used this composition to investigate its application for p-SOFCs. We first checked for chemical compatibility between the electrolyte and PBSCF. Powders of the cathode and electrolyte materials were combined in a 1:1 weight ratio, milled, compacted together, then heat treated at 900, 1000 and 1100 °C for 24 h under static air. The diffraction patterns obtained subsequent to these treatments are fully described by a superposition of the two individual components, Figure 5.8. We then evaluated the extent of H_2O uptake into PBSCF by thermogravimetric analysis (TGA). The mass of the material (in loose powder form) was recorded as a function of temperature under humidified (pH_2O = 0.020 atm) and under dry synthetic air (pO_2 = 0.19 atm, balance N_2) between 800 and 100 °C. A clear difference in mass under the two atmospheres is evident at all temperatures below 800 °C as shown in Figure 5.9a. Attributing this difference to H_2O uptake into the bulk implies a proton concentration that ranges from 3.5 mol % at 200 °C to 1.7 mol % at 600 °C.

These proton uptake results enable evaluation of the thermodynamics of the hydration reaction:

$$H_2O + V_O^{\bullet\bullet} + O_O^{\times} \leftrightarrow 2OH_O^{\bullet} \quad K_W = \frac{[OH_O^{\bullet}]^2}{pH_2O[V_O^{\bullet\bullet}][O_O^{\times}]} = \exp\left(\frac{\Delta S_W}{R}\right)\exp\left(-\frac{\Delta H_W}{RT}\right) \quad (2)$$

where $[OH_O^{\bullet}]$, $[V_O^{\bullet\bullet}]$, and $[O_O^{\times}]$ are, respectively, the proton (hydroxyl), oxygen vacancy, and oxygen concentrations in the hydrated state; ΔH_W and ΔS_W are the enthalpy and entropy, respectively, of the hydration reaction; and R and T are,

respectively, the universal gas constant and temperature. The TGA results under synthetic air were used to determine the oxygen vacancy concentration under dry conditions using an oxygen stoichiometry of 5.88 at 100 °C as a reference.[147] The site concentrations under wet conditions, Figure 5.10, were then obtained according to

$$[\mathrm{O}_{\mathrm{O}}^{\times}]^{wet} = [\mathrm{O}_{\mathrm{O}}^{\times}]^{dry} - \frac{1}{2}[\mathrm{OH}_{\mathrm{O}}^{\bullet}] \quad (3)$$

$$[\mathrm{V}_{\mathrm{O}}^{\bullet\bullet}]^{wet} = [\mathrm{V}_{\mathrm{O}}^{\bullet\bullet}]^{dry} - \frac{1}{2}[\mathrm{OH}_{\mathrm{O}}^{\bullet}] \quad (4)$$

A negligible change in electronic defect concentration in response to reaction with steam is implicitly assumed.

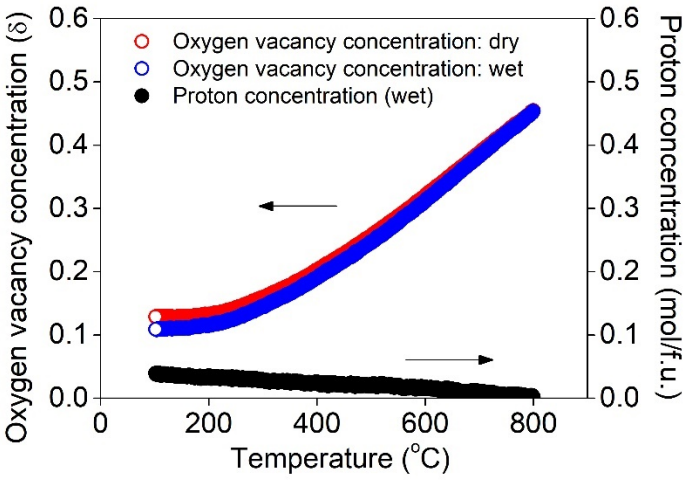

Figure 5.10 PBSCF defect concentrations as a function of temperature under both dry and wet conditions, as determined from thermogravimetric analysis. Concentrations are given in units of moles of species per mole of double-perovskite formula unit.

From an evaluation of the temperature dependence of K_{W}, shown in the van't Hoff plot in Fig. 5.9b, we extract enthalpy and entropy values of -22 kJ mol^{-1} and -63 J mol^{-1} K^{-1}, respectively, at 400 °C. In principle, a van't Hoff analysis should be performed at fixed stoichiometry (rather than fixed chemical potential) and the

significant non-linearity in the present van't Hoff plot may be a result of the changing hydration state with temperature. In addition, electronic defects can become important at high temperature[139,152,153] and contribute to non-linearity. Nevertheless, the thermodynamics values can be compared to those reported for other oxides considered for either electrolyte or cathode applications, for which analogous analysis methodologies are employed. In this context, both the enthalpy and entropy obtained here are small in magnitude, where typical values range from -20 to -170 kJ mol^{-1} and -90 to -180 J mol^{-1} K^{-1}, respectively.[139] The entropy is particularly far from the range of observed values and is much smaller in magnitude than has been reported for $Ba_{0.5}Sr_{0.5}Fe_{0.8}Zn_{0.2}O_{3-\delta}$ and $BaCo_{0.4}Fe_{0.4}Zr_{0.2}O_{3-\delta}$ (respectively, -145 ± 30 and -103 ± 5 J mol^{-1} K^{-1}), the only other 'triple conducting oxides' for which the thermodynamics have been determined.[139,154] Thus, the entropic penalty of hydrating the double-perovskite is small in comparison to other materials and correlates with the much higher proton content. For example, the proton concentration in $BaCo_{0.4}Fe_{0.4}Zr_{0.2}O_{3-\delta}$ is just 0.5 mol% (equivalent to 1.0 mol% for comparison to the double perovskite) at 400 ^{o}C in 0.065 atm pH_2O.[154] Whether this is a universal difference between standard and double-perovskite materials, resulting from the different configurations available to dissolved hydroxyl groups, remains to be addressed. Significant also is the extremely rapid mass response to the imposed temperature steps, with mass increasing almost entirely in synchronization with the temperature during each cooling step. Such fast mass changes imply rapid migration of all the relevant ionic defects of Eq. (2).

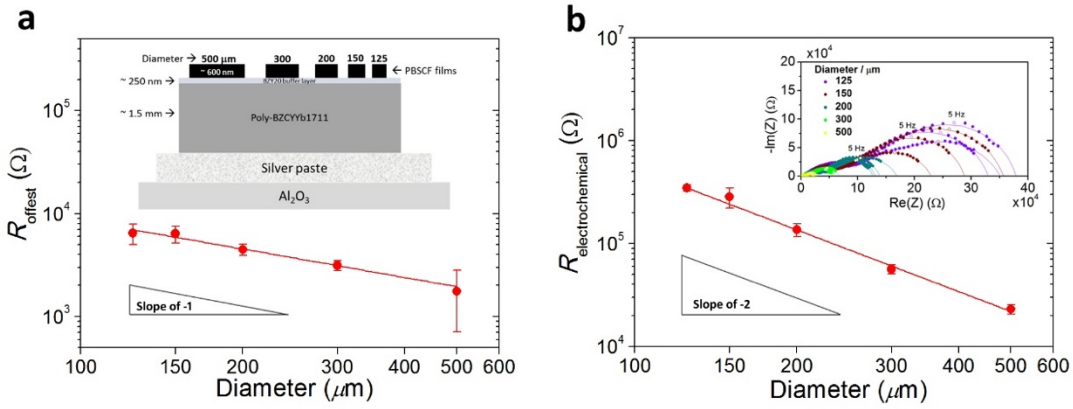

Figure 5.11 Electrochemical behavior of microdot PBSCF at 500 °C under lightly humidified synthetic air as determined from a.c. impedance spectroscopy. (a) The offset resistance (mainly from the electrolyte). (b) The electrochemical reaction resistance.

5.4.4 Oxygen electrochemical reduction pathway on PBSCF

The high performance and the high H_2O uptake into PBSCF suggest that the oxygen electrochemical reaction occurs by a bulk rather than surface pathway, with protons migrating through the bulk of the PBSCF and reacting with oxygen at the cathode/gas interface. Such a pathway is strongly indicated by the observation that a dense PBSCF layer on the cathode side of the electrolyte enhances rather than diminishes cell performance. We directly examined the possibility of reaction via a double-phase boundary pathway by measuring the electrochemical properties of PBSCF thin film (~600 nm) microdot electrodes, deposited onto the surface of dense, polycrystalline BZCYYb1711 ~ 1.5 mm in thickness as shown in the inset of Figure 5.11a. X-ray diffraction analysis confirmed the absence of reactivity between these components (Figure 5.6a), and atomic force microscopy revealed the PBSCF surface to have a rms roughness of 43.8 nm (Figure 5.6b), reflecting the roughness of the

underlying polycrystalline substrate. We patterned the PBSCF film by ion milling to create sharply-defined microelectrodes ranging in diameter from 125 to 500 μm, with over ten duplicates of each diameter. We then measured the A.C. electrical impedance at each microelectrode, using an automated probe station described previously.[87] Data were recorded under 0.2 atm O_2 (balance Ar) at 500 °C after a 24 h stabilization period. Under these conditions, BZCYYb1711, like BZCYYb4411, is predominantly a proton conductor, ensuring that the electrochemical response measured here is that associated with reaction (1) as catalyzed by PBSCF.

All impedance spectra could be adequately described by an equivalent circuit composed of a resistor (R_{offset}) in series with two subcircuits, each composed of a resistor in parallel with a constant phase element. For this initial study, the sum of these two resistances is taken to be the electrochemical reaction resistance. For the geometry considered (a semi-infinite conductor), the offset resistance is expected to be dominated by the resistance of the underlying electrolyte, with a scaling with diameter according to the Newman equation[81] $R_{offset} = 1/(2\sigma d)$, where σ and d are the electrolyte conductivity and the microelectrode diameter, respectively. Therefore, a double-logarithmic plot of R_{offset} vs d shows the linear feature with a slope close to -1 is expected (Fig. 5.11a), and a conductivity of 5.6×10^{-3} S cm^{-1} (in reasonable agreement with the properties of BZCYYb1711) was observed using the Newman Equation. The electrochemical resistance is expected to be dominated by the properties of the microelectrode. Here, the double-logarithmic plot yields a slope of -2, which would result from a process occurring via a double-phase boundary pathway, Figure 5.11b. That is, the data reveal that resistance scales inversely with area, implying that the

entire surface of the microelectrode is electrochemically active. This feature, enabled in part by the high solubility of H_2O into the oxide, undoubtedly contributes to the very activity of PBSCF for the oxygen reduction reaction in p-SOFCs.

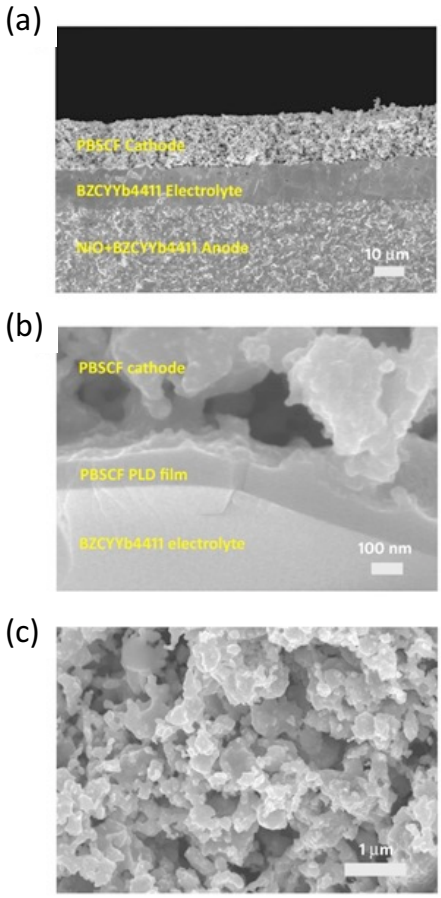

Figure 5.12 SEM images of PBSCF/BZCYYb4411/cermet anode fuel cell. (a) The cross-sectional image. (b) The expanded view of cross-section showing PLD layer at the cathode of electrolyte-cathode interface. (c) PBSCF cathode microstructure after sintering at 950 °C.

5.4.5 High performance p-SOFCs based on PBSCF cathode materials

We then prepared anode-supported cells incorporating neat PBSCF as the cathode and Ni + BZCYYb4411 as the anode. With the aim of addressing the apparently poor cathode-electrolyte contact in a typical SOFC fabrication, we applied the cathode layer by two different approaches. In one case, we followed a typical procedure in which a slurry of PBSCF was directly painted onto the electrolyte surface. In the second case, we first applied a thin (~100 nm) layer of PBSCF byPLD, on top of which the standard slurry was brush-painted. The final sintering step was carried out at 950 °C in air for 4 h. For both cells, the electrolyte was ~ 15 μm thick and the cathode ~ 20 μm thick, Figure 5.12a, with the PLD cathode layer forming a conformal coating onto the electrolyte, Figure 5.12b, and the cathode retaining good porosity after the final sintering step, Figure 5.12c. Ag wires were attached to both electrodes and electrical behavior was measured in a pseudo-four probe configuration (eliminating the resistance of the lead wires).

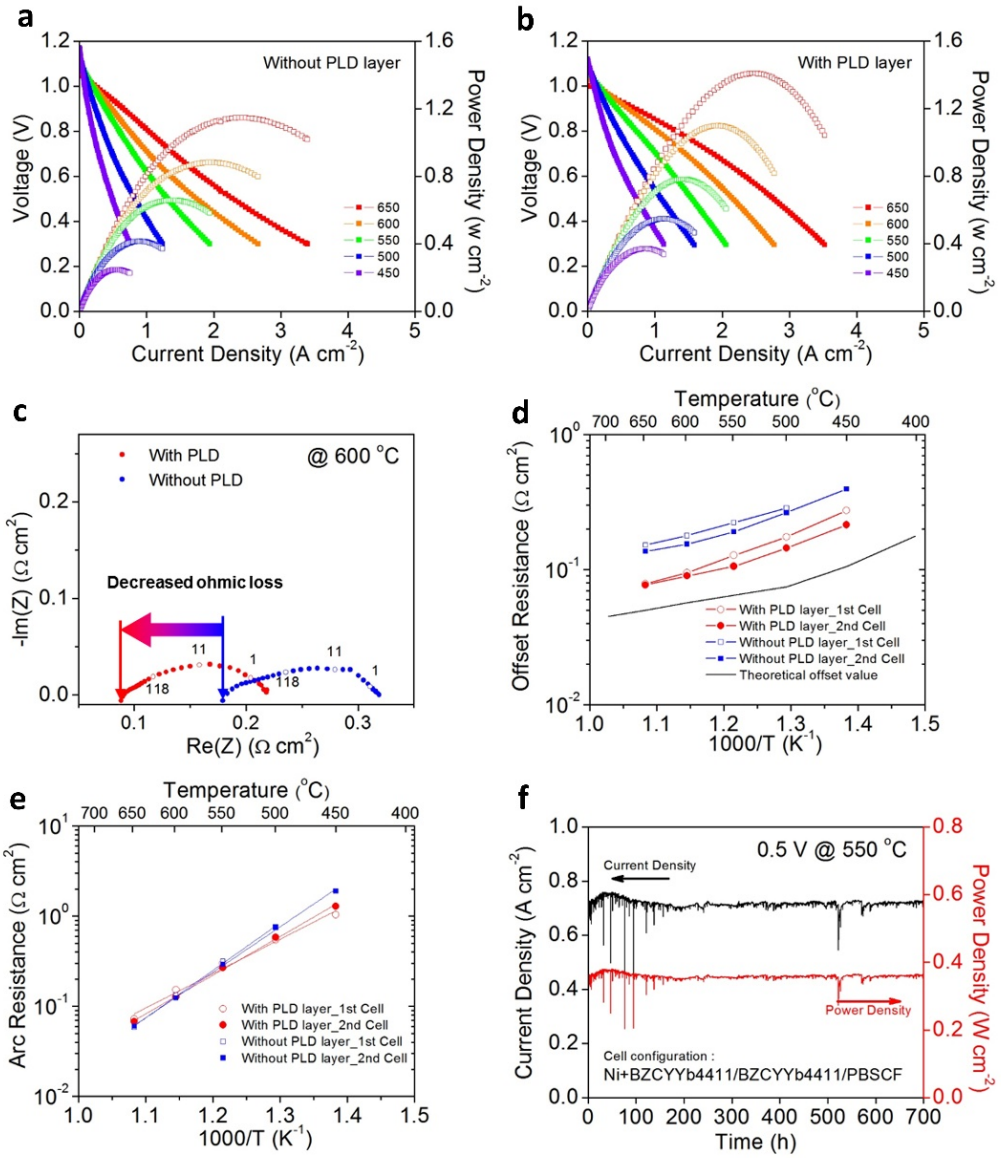

Figure 5.13 Electrochemical properties the PBSCF cathode based on BZCYYb4411 proton conducting electrolyte using humidified (3% H_2O) H_2 as fuel and dry air as oxidant at various temperatures. (a) polarization and power density curves of a representative cell without a PLD layer. (b) polarization and power density curves of a representative cell with a PLD layer. (c) impedance spectra collected at 600 °C, showing dramatic decrease in offset resistance on introduction of the cathode PLD layer. (d) offset (ohmic) resistance under OCV, (e) electrochemical reaction (arc) resistance under OCV. (f) temporal evolution of the cell current density and power density under a constant voltage load of 0.5 V at 550 °C in humidified H_2.

The polarization behavior (Figure 5.13), collected with humidified H_2 supplied to the anode and synthetic air to the cathode, reveals exceptionally high activity for the PBSCF cathode. Even for the conventionally prepared cell, the peak power density at 600 °C exceeds 800 mW/cm^2. Application of the PLD layer resulted in a marked increase in power output. The peak power density at 600 °C becomes 1098 mW/cm^2, surpassing all previous records, including that obtained using dry O_2 as the oxidant in conjunction with the cathode SSC[128] (747 mW/cm^2). At 500 °C, the peak power density of 548 mW/cm^2 exceeds the value of 455 mW/cm^2 obtained using $BaCo_{0.4}Fe_{0.4}Zr_{0.1}Y_{0.1}O_{3-\delta}$,[127] a material explicitly designed to display protonic conductivity, in addition to electronic and oxygen ion conductivity. The power density of p-SOFCs based on the PBSCF cathode reported here competes with that of the high performance SOFCs based on oxide ion conductors.

To elucidate the role of the cathode PLD layer, we measured the A.C. electrical impedance under open circuit conditions, enabling deconvolution of the various contributions to the overall cell resistance. Plotted in the complex plane, each impedance spectrum showed a single, depressed arc, attributed to the electrochemical reaction resistance, with a finite offset from the origin, representing the ohmic losses (Figure 5.13c). Application of the PLD layer dramatically decreased the offset resistance as shown in Figure 5.13d. In contrast, it had only a slight impact on the electrochemical resistance, slightly decreasing the activation energy such that this resistance contribution was decreased marginally in the lower temperature regime as shown in Figure 5.13e. Indeed, while application of similar PLD-derived dense films

to improve contact between electrolyte and cathode in conventional SOFCs has been suggested, [155] success relies on the ion permeability of the cathode material. Thus, the high performance of the p-SOFC based on PLD-PBSCF layer further confirms the protonic conducting property of the PBSCF film.

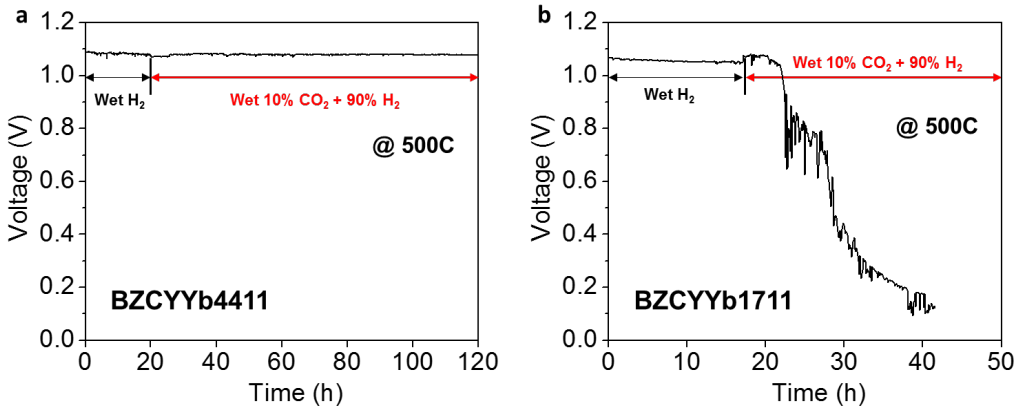

Figure 5.14 Temporal evolution of fuel cell OCV at 500 °C with humidified (3% H_2O) 10% CO_2 and 90% H_2 supplied to the anode and air to the cathode using cells of two different electrolytes: (a) BZCYYb4411 and (b) BZCYYb1711. The OCV from the BZCYYb4411-based cell is extremely stable for a 100 h period of measurement, deviating from the initial value by no more than 1 %. In contrast, the OCV of the BZCYYb1711-based falls by 86% OCV in just 20 h, clearly reflecting the chemical instability of BZCYYb1711.

We then examined the stability of our cell components by evaluating two (different) cells for prolonged periods. In one case we measured the open circuit voltage (OCV) upon exposure of the anode to a humidified mixture of CO_2 and H_2, and in the second we measured the current upon exposure to humidified hydrogen at a constant cell voltage. Under both conditions, the cells display excellent stability. As measured over a 100 h period, the OCV deviates from the initial value by no more than 1 % as shown in Figure 5.14a. In contrast, an analogous BZCYYb1711 based-cell shows an

86 % OCV loss after just 20 h of measurement as shown in Figure 5.14b. In addition, the cell based on BZCYYb4411 shows excellent stability under constant voltage over a 700-hour period as shown in Figure 5.13f.

5.5 Conclusions

In this work, we demonstrated that exceptional power densities and excellent long-term stability can be achieved in intermediate temperature p-SOFCs by combining the double-perovskite cathode PBSCF and the new electrolyte BZCYYb4411. The double-perovskite PBSCF provides the unique electronic, protonic, and oxygen ionic transporting properties ("triple conducting oxides") under humidified atmosphere. The high capacity of PBSCF to adsorb H_2O at high temperature (Proton concentration: 1.7 mol% at 600 °C) and the excellent ORR performance facilitate the cathodic electrochemical reaction in p-SOFCs. Integrating with the CO_2/H_2O tolerable BZCYYb4411 proton conductor, a maximum peak power density of 1098 mW/cm^2 was achieved at 600 °C. Furthermore, great cell stability has been demonstrated over 700 hours of testing under a constant voltage at 550 °C in humidified H_2. The demonstrated excellent performance of PBSCF based p-SOFCs can pave the way for incorporating fuel cells into a sustainable energy future.

Chapter 6: Tungsten Doped Vanadium Dioxide

6.1 Abstract

Vanadium dioxide (VO_2) has been extensively studied due to its fully reversible first-order metal-insulator transition (MIT) associated with a structural phase transition at a critical temperature of about 340 K. One major challenge in VO_2 research on thin films is to fabricate phase pure thin films because of the complicated phase diagram of vanadium oxides where there are many polymorphs of VO_2. Moreover, in order to pursue room-temperature applications, many efforts have been focused on uniformly introducing chemical dopants into VO_2 to effectively tune the metal-insulator transition.

In this work, a high-throughput pulsed laser deposition approach was developed to grow high-quality and phase pure $V_{1-x}W_xO_2$ ($0 \leq x < 4\%$) thin films on different substrates. In particular, the concentration of W ions had a directional variation from 0% to 4% across each film. It is widely reported that tungsten dopants are able to effectively reduce the phase transition temperature. However, the underlying mechanism, especially how the tungsten dopants affect the hysteresis of the phase transition, is poorly understood. Based on our experimental results, we found that the 'cofactor conditions', which are strongest lattice-structure compatibility conditions (of high temperature and low temperature phases) proposed based on the geometric nonlinear theory of first order phase transition recently, can be used to explain the relation between the doping concentration of tungsten ions and the hysteresis characteristics of the structural transition of $V_{1-x}W_xO_2$ films. Specifically, the cofactor

condition was found to be satisfied in $V_{1-x}W_xO_2$ when x is around 2.4%. A minimum transition hysteresis width consistently observed in both epitaxial and polycrystalline $V_{1-x}W_xO_2$ films at the same tungsten concentration (x ~2.4%) showed for the first time that the geometric nonlinear theory (previously applied to shape memory alloys) is also applicable to oxide materials. The potential application of $V_{1-x}W_xO_2$ thin films in rechargeable lithium batteries were systematically studied based on the tungsten concentration dependence of electrical properties of $V_{1-x}W_xO_2$. Their potential use as dual functional cathode materials (host of lithium ions and conductor of electron) for rechargeable lithium batteries has been demonstrated in proof-of-concept experiments.

6.2 Introduction to vanadium dioxide

Vanadium dioxide (VO_2) has been an archetypical $3d^1$ correlated oxide since it was first discovered by Morin in 1959.[156] Bulk VO_2 shows a first-order metal-insulator transition (MIT) at a critical temperature (Tc) of ~340 K.[157-160] Across the critical temperature, VO_2 undergoes a crystal structure transition from a low temperature monoclinic structure (M1) to a high temperature rutile-type tetragonal structure (T), which is accompanied by dramatic changes in both electrical resistance and optical transmittance.[161] Moreover, the phase transition in VO_2 can be driven by a variety of parameters, such as temperature, chemical doping, electrical field, light irradiation, external pressure, etc. [157-160,162] The above unique properties make VO_2 a promising candidate for various applications, including smart-window coatings, ultrafast sensors, and switching devices.[163] It is very important to fabricate high-quality pure phase VO_2 films because the MIT characteristics strongly depend on the nature of the crystal structure and the defects (stoichiometry, strain, oxygen deficiency, etc.). However, it is

difficult to get single-phase films with desired MIT properties due to the rich oxidation states of vanadium (e.g. V_2O_5, VO_2, V_2O_3, V_3O_7, V_4O_9, V_6O_{13}, etc.) as shown in Figure 6.1.[164,165] In addition, vanadium dioxides have different polymorphs, such as VO_2(M1), VO_2(T), VO_2(B), VO_2(A), etc. Among the VO_2 polymorphs, VO_2(M1/T) and VO_2(B) attract more attention due to their first-order phase transition close to room temperature and potential lithium-ion battery applications, respectively. [166,167] Figure 6.2 shows the lattice structures of VO_2(M1/T) and VO_2(B). The low-temperature insulating phase has a monoclinic structure (space group $P2_1/c$) with alternating V-V distances of 2.62 Å and 3.17 Å[166] as shown in Figure 6.2a. The high-temperature metallic phase, as shown in Figure 6.2b, has a rutile crystal structure (space group $P4_2/mnm$) with a uniform V-V distance of 2.87 Å. [166] The bronze phase of VO_2(B) has a low-symmetry monoclinic structure (space group of C2/m)[168] and is a promising cathode material for Li-ion batteries due to its layered structure as shown in Figure 6.2c.

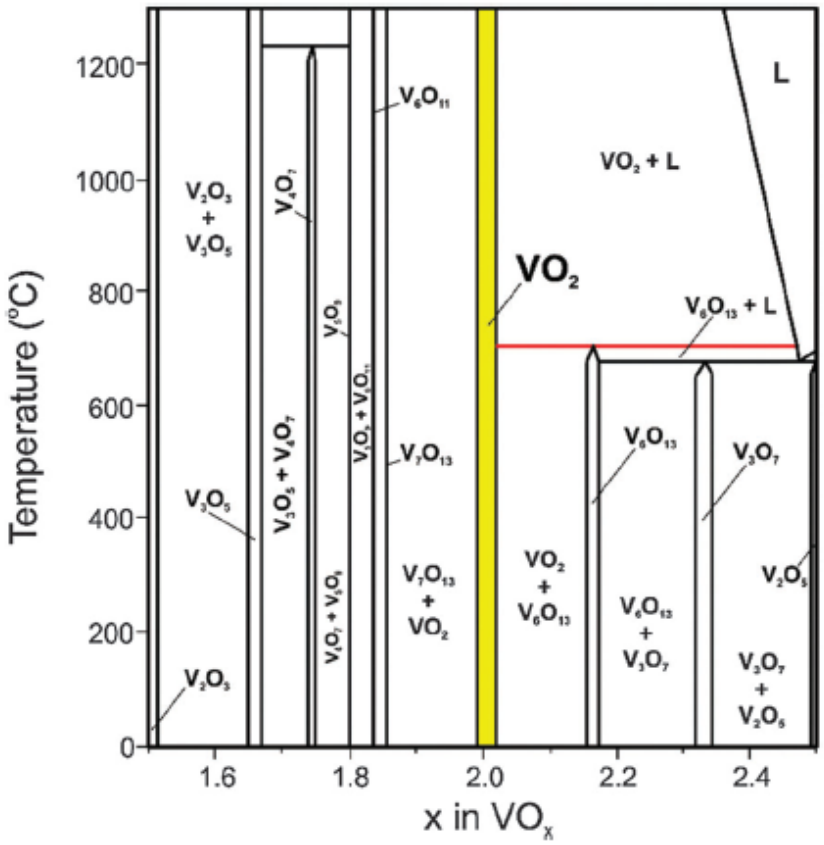

Figure 6.1 The phase diagram of $VO_{1.5}$-$VO_{2.5}$.[164]

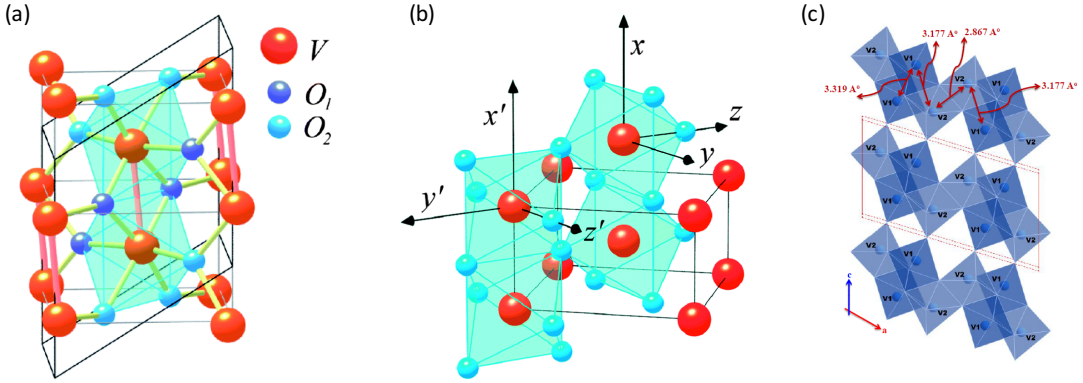

Figure 6.2 (a) The monoclinic lattice structure of VO_2 (M1) in the low temperature insulating phase.[166] (b) The rutile lattice structure of VO_2 (T) at a temperature above the critical temperature. (Red and orange circles represent V^{4+} and blue circles represent O^{2-}.)[166] (c) The bronze lattice structure of VO_2 (B).[168]

Although there have been intensive theoretical and experimental efforts, the underlying mechanisms for the first order phase transition between the tetragonal metal phase VO_2 (T) and the monoclinic insulating phase VO_2 (M1) are still under debate. The great controversy for this coupled structural and electronic transition is focused on whether the transition is driven by structural distortion (Peierls mechanism), electronic correlation (Mott mechanism), or their combination (Mott-Peierls transition mechanism).[169] During the phase transition, the changes of the electronic band structure near the Fermi level (E_F) is associated with the octahedral environment and the *p*-*d* hybridization (O 2*p*, V 3*d*) based on the crystal-field model as shown in Figure 6.3. In the high-temperature metallic state (Figure 6.3a), the density of states of E_F (dashed line) is formed from a mixture of the half-filled $3d_{\parallel}$ band which is parallel to the tetragonal *c* axis (c_T) and antibonding π^* orbital. Across the MIT, the pairing between V ions along the c_T and the tilting of the VO_6 octahedral split the $d_{\parallel}$ bands into a bonding $d_{\parallel}$ and an antibonding combination of $d_{\parallel}$* and π* as shown in Figure 6.3b. Thus, the orbital polarization between the bonding $d_{\parallel}$ band being fully occupied and the $d_{\parallel}$* and π* being empty results in an opening of a small band gap.[170-172] However, whether the splitting of the $3d_{\parallel}$ band is due to the V-V paring (dimerization) or due to the presence of strong electron-electron correlations in the $3d_{\parallel}$ band is always a focus of the debate. To get better understanding about the MIT mechanisms, various thin film deposition techniques, such as chemical vapor deposition, sputtering deposition, and pulsed laser deposition, have been used to grow pure-phase VO_2 thin films.[166] Among

these methods, pulsed laser deposition has been demonstrated to be an excellent method, especially for the growth of oxide thin films as discussed in Chapter 2. In this chapter, I will focus on the PLD method for the fabrication of VO_2 based thin films.

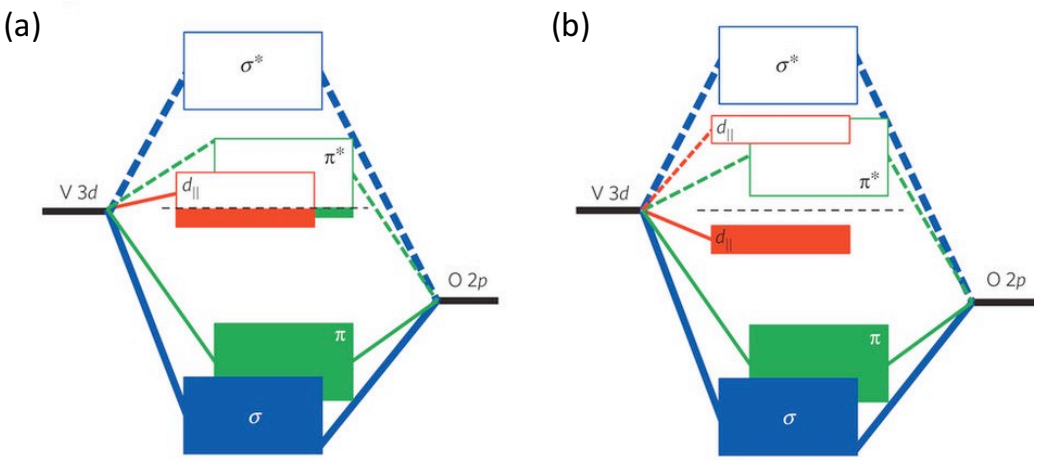

Figure 6.1 Schematic of the VO_2 band structures. (a) The metallic state of VO_2 at above T_c. (b) The insulating state of VO_2 below T_c.[170]

Another challenge for pristine VO_2 is that its phase transition temperature (~340K) is still relatively high for practical applications. In addition, the width of the hysteresis loop associated with the transition may also cause reliability issues in VO_2 devices for ultrafast optical or electrical switching applications.

In order to explore practical room-temperature applications, many solutions have been developed to optimize the transition characteristics of VO_2. Among these solutions, chemical substitution is widely viewed as one of the most promising strategies and has been extensively studied.[173-176] It has been reported that the transition temperature can be reduced by substitution of V^{4+} ions with metal ions that have higher oxidation states, such as W^{6+}, Nb^{5+}, Mo^{6+}, etc., and be increased by replacing V^{4+} ions with metal-ion dopants with lower oxidation states, such as Cr^{3+}, Al^{3+}, Fe^{3+}, etc.[177] The

dependence of the phase transition temperature on a single substituent is usually linear, so it is simple to use a certain amount of substituent ions to reduce the T_c to a temperature desirable for applications. In particular, tungsten (W) has been shown to reduce the transition temperature by 21 – 28 K for each atomic percentage of W dopant introduced into bulk VO_2.[176] Although the W dopant would effectively reduce the value of the T_c, the magnitudes of the changes in resistance and optical transmittance are known to be significantly deteriorated at high doping levels.[176] Moreover, the mechanism for the change in the hysteresis width due to introducing the W dopant is still not well understood.[178] From a material synthesis point of view, a particular challenge is that successful growth of high-quality VO_2 films is very difficult due to various oxidation states of vanadium and many polymorphs of VO_2 as discussed above.[179] In addition, the transition characteristics are easily affected by the crystallinity, morphology, and synthesis method. As such, it is difficult to make meaningful comparisons across various available reports due to potential artificial complications during the fabrication of the materials.[180] From a theoretical understanding point of view, a critical challenge is the lack of suitable theory for guiding the development of low hysteresis VO_2-based materials. Therefore, in order to satisfy the requirements for further practical applications, it is highly desired to find an elaborate fabrication approach to ensure the formation of pure $V_{1-x}W_xO_2$ and explore an effective and convenient approach to modulate the MIT properties of $V_{1-x}W_xO_2$.

The MIT of VO_2 could be described by a martensitic transformation model, in which the coexistence of two phases over a narrow temperature range leads to the hysteretic behavior of the first-order transition. A recently developed theory of general

non-linear theory of martensite (GNLTM) supports the dependence of the hysteresis with λ2 (λ2 is the middle eigenvalue of the 3 × 3 'transformation stretch matrix' U, obtained from X-ray measurements of lattice parameters and knowledge of the space groups of the two phases). [181-183] λ2 is an indicator of the compatibility between the austenite and martensite phases.[182] A sharp drop in the hysteresis width when λ2 approaches 1 has been observed in both thin-film and bulk alloys. The result demonstrates a universal relation between the hysteresis width and λ2. When λ2 is 1, it is called the 'cofactor conditions' (CC), which represents the conditions for super compatibility of the two phases (low temperature and high temperature phases) in a martensitic transformation. With the CC satisfied, the material exhibits tremendous reversibility. Interestingly, it has been suggested that the CC may also be applicable for phase transitions in oxide systems; however, no direct experimental evidence has been reported since the CC theory was proposed.[182]

In this work, by taking advantage of the high-throughput methodology, we have systematically fabricated and studied composition-spread $V_{1-x}W_xO_2$ thin films. The W concentration in our samples was controlled in a relatively narrow range ($0 \leq x < 4\%$) to prevent potential phase separation and indistinguishable transition as reported in samples with higher W concentrations.[184] The crystal structures, microstructures, electrical properties, and phase transition characteristics of the thin films were systemically studied. We mainly investigated the effect of W dopant on the structural properties and the phase transition characteristics (T_c and hysteresis width (ΔT)) of $V_{1-x}W_xO_2$ films grown on different substrates (*c*-Al_2O_3 and Si/SiO_2).

A much larger resistance change, a smaller thermal hysteresis width, and a sharper phase transition were observed for the $V_{1-x}W_xO_2$ thin film grown on the *c*-Al_2O_3 in comparison with a counterpart at a same doping level (x) that was grown directly on silicon. We systematically tuned the lattice parameters of VO_2 through W-doping to satisfy the CC ($\lambda 2 = 1$) and also measured the hysteresis behavior based on the temperature dependence of the resistance (R-T curves). The hysteresis width changes in a predicted manner as the W concentration varies, that is, a minimum value of hysteresis width is observed when $\lambda 2$ approaches 1. We experimentally demonstrate that the CC theory, for the first time, is applicable to a prototypical oxide system, namely, W doped VO_2. Furthermore, the application of the $V_{1-x}W_xO_2$ thin film as a dual functional thin-film cathode in LIBs was investigated.

6.3 Experimental

6.3.1 Film fabrication

As one of the most promising oxide thin film growth techniques, PLD has probably become the most popular technique for VO_2 thin film. In 1993, PLD was first used for VO_2 deposition (Singh et al.)[185] by ablating a metallic vanadium target in a PLD deposition chamber under the atmosphere of 100-200 mTorr Ar/O_2 (10:1). Later, successful growth of high quality VO_2 films on sapphire substrates by PLD at a high temperature without post-annealing was reported in 1994.[186] Because the substrate plays an important role in the quality of the epitaxial films and their microstructures, a variety of substrates, such as silicon, glass, sapphire, quartz, etc. have been used for

successful PLD deposition of VO_2 thin films. In this work, we mainly investigated the substrates of silicon, quartz, $SrTiO_3$, and *c*-Al_2O_3.

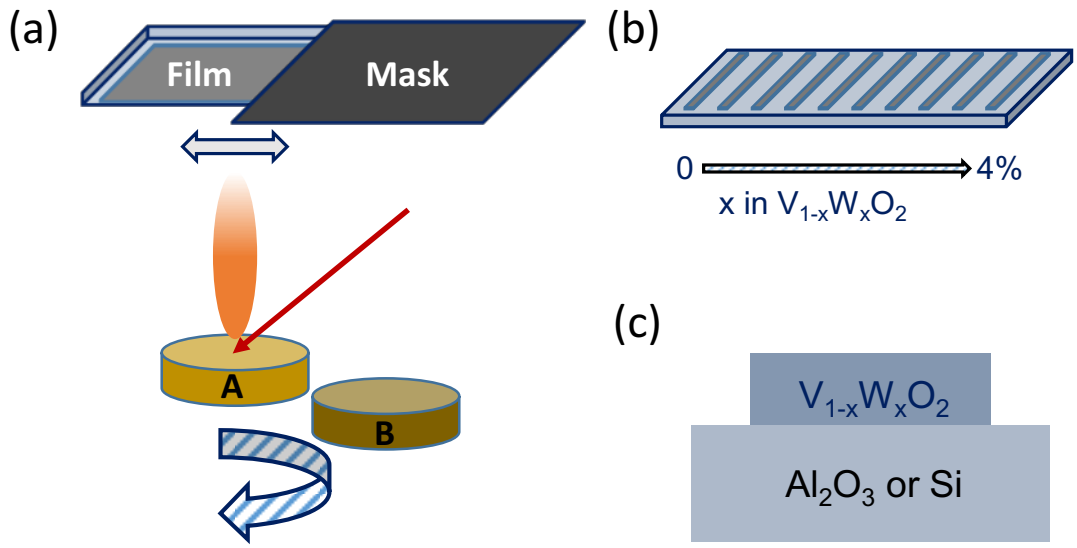

Figure 6.4 Fabrication of the continuous composition-spread film of $V_{1-x}W_xO_2$. (a) A schematic view of the set-up for film growth; (b) A schematic view of a patterned spread film. (c) A schematic cross-section view of a completed $V_{1-x}W_xO_2$ device.

A V_2O_5 pellet (1.0" Dia. x 0.250" Thick) used as the PLD target A shown in Figure 6.4a was obtained from Kurt J. Lesker Company. A $V_{1.92}W_{0.08}O_5$ pellet used as the PLD target B shown in Figure 6.4a was prepared by cold compaction of a mixture of VO_2 and WO_3 powder at ambient conditions and was then sintered at 823 K in air for 5 hours. Vanadium dioxide (VO_2) and tungsten trioxide (WO_3) were obtained from Sigma-Aldrich. The deposition oxygen pressure has been found to be critical for the preparation of the pure VO_2 phase due to the multiple oxidation states of vanadium and the existence of many polymorphs of VO_2 as discussed above. Therefore, we first optimized the background oxygen pressure and laser energy for the successful growth of VO_2 thin films in our PLD system, their optimal conditions are 3-5 mTorr and 22

mJ@5Hz, respectively, and then we studied the effects of the substrate type and the deposition temperature on the formed phases of VO_2.

Figure 6.5a shows the XRD results of VO_2/SiO_2 samples deposited at different temperatures in a range of 326 °C to 460 °C. The crystal structure of VO2 changes from a monoclinic phase for samples deposited at temperatures above 400 °C to a bronze phase for samples deposited at temperatures below 400 °C. As the deposition temperature further decreases to be lower than 350 °C, the crystal structure of VO_2 becomes amorphous. The representative AFM images shown in Figure 6.5b indicate that all the films are relatively smooth and the monoclinic phase obtained at a deposition temperature of ~450 °C shows a bigger average grain size as compared to the bronze phase obtained at a deposition temperature of ~390 °C. Based on the results described above, we selected a substrate temperature of ~450 °C as the growth condition for monoclinic phase and a substrate temperature of ~390 °C as the growth condition for bronze phase. It has been reported that the use of STO(001) substrates benefits the epitaxial growth of the bronze-phase VO_2 because of the well-matched lattice constants.[187] Here, we also optimized the deposition temperature for growing high quality VO_2(B) on STO(001). As shown in the XRD patterns (Figure 6.6), the pure bronze-phase VO_2 was formed at deposition temperatures above 394 °C, and the unknown impurity phase (marked with asterisk) was observed in samples at lower deposition temperatures. Considering the XRD (Figure 6.6) and AFM (Figure 6.7) results, a substrate temperature of ~440 °C is suitable for the growth of VO_2(B) on STO(001). Using the similar processes, we optimized the deposition temperature on *c*-Al_2O_3. The optimization parameters and sample information are summarized in Table

6.1. All films reported in this work were grown by PLD with a KrF excimer laser (wavelength: 248 nm, fluence: 0.8 J/cm^2, distance between target and substrate: ~55mm, repetition rate: 5 Hz) at a substrate temperature of ~723 K under an oxygen pressure of 3~5 mTorr. Prior to deposition, the STO, sapphire, quartz, and silicon substrates were ultrasonicated in acetone and methanol, respectively, and then rinsed with isopropanol.

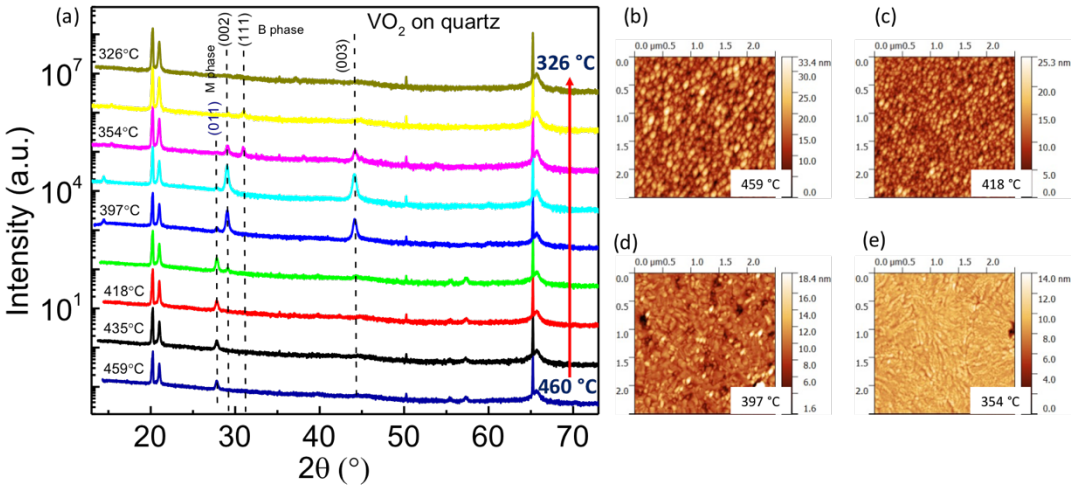

Figure 6.5 (a) The X-ray diffraction (XRD) pattern of θ-2θ-scans of VO_2 grown on quartz (001) substrate at different temperatures. (b) The atomic force microscopy (AFM) image of VO_2 film at 459 °C, showing a root-mean-square (RMS) roughness of 4.49 nm with an average grain size of 107 nm. (c) The AFM image of VO_2 film at 418 °C, showing a RMS roughness of 2.59 nm with an average grain size of 69 nm. (d) The AFM image of VO_2 film at 397 °C, showing a RMS roughness of 1.85 nm. (e) The AFM image of VO2 film at 354 °C, showing a RMS roughness of 0.91 nm.

Several tools including an X-Ray Reflectometry (XRR), a stylus profilometry tool (Dektak), and atomic force microscopy (AFM) were used to determine the deposition rates of target A and target B. For example, Figure 6.8 shows how the AFM

method is used to determine the deposition rates. Corresponding to the deposition conditions described above, the deposition rates of target A and target B were confirmed to be 0.11 Å/s, 0.064 Å/s, respectively. The composition-spread $V_{1-x}W_xO_2$ films were grown on $SrTiO_3$ (001) (400 μm thick, MTI), *c*-Al_2O_3 (0001) (400 μm thick, MTI), and Si (400 μm thick with 400 nm SiO2 layer, MTI) substrates by alternately ablating target A and target B in coordination with moving a mask as shown in Figure 6.4a. More details of the composition-spread system can be found in our previous work.[6] Following the deposition process, the samples were left in the PLD chamber with an oxygen background pressure of 3~5 mTorr during cooling. During the cooling period, the cooling rate was approximately 5 K/min. All films reported in this work had a thickness of ~150 nm in order to minimize substrate-induced strain effects. Finally, the spread films were patterned into stripes (5 mm Length × 0.2 mm Width) as shown in Figure 6.4b using ion milling.

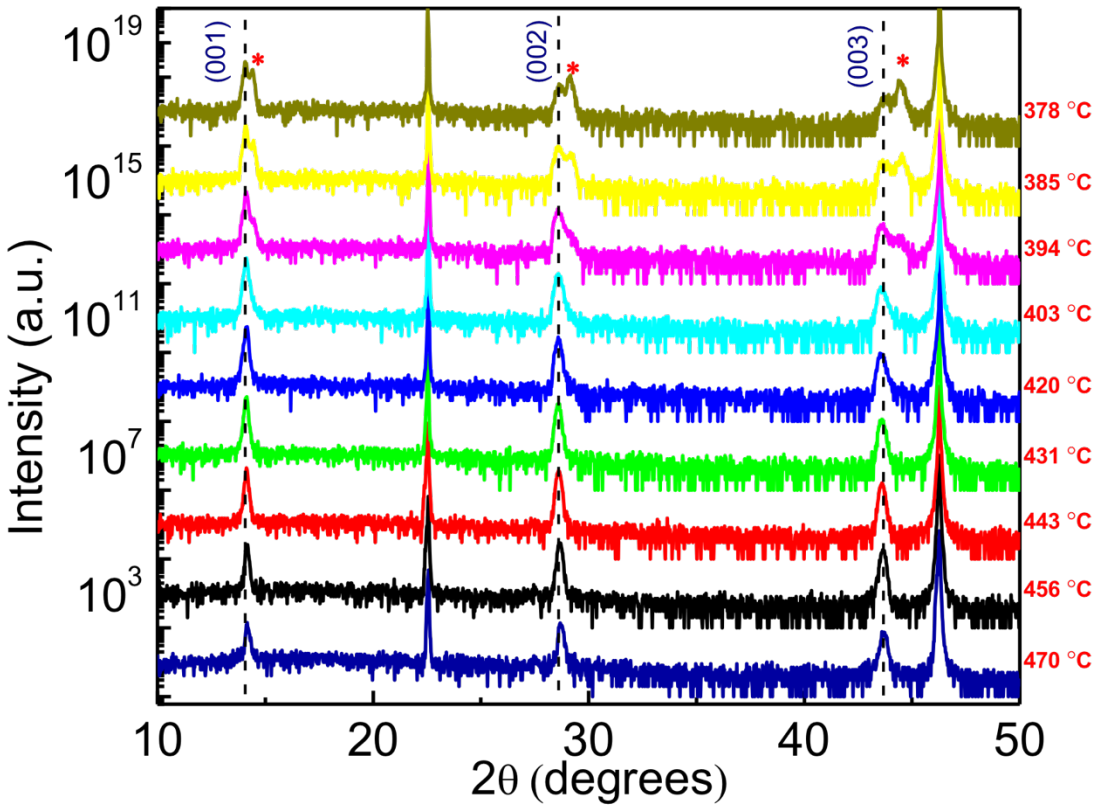

Figure 6.6 The results of θ-2θ-scans measured on a VO_2 film grown on a STO (001) substrate at different temperatures.

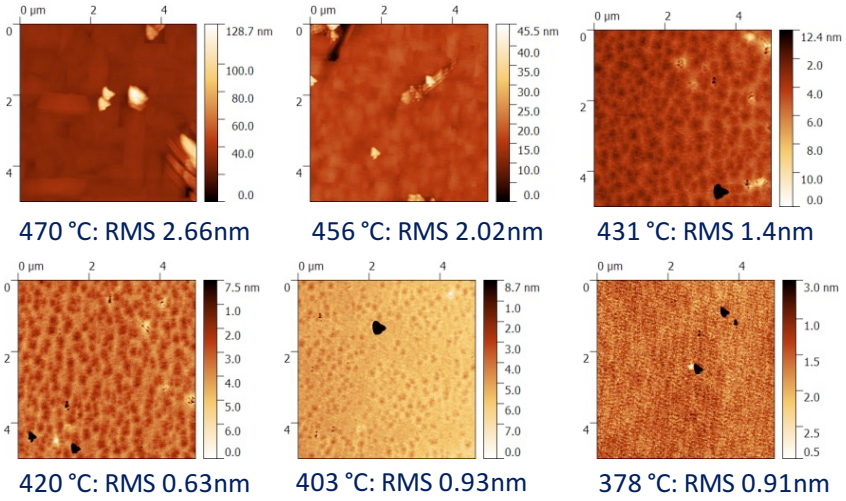

Figure 6.7 5μm×5μm AFM scan images of the VO_2/STO(001) temperature gradient sample.

Substrate	Substrate Temperature	W dopant	polymorphs
c-Al_2O_3	450 – 500 °C	0% to ~3.7%	M to T **Epitaxial film**
Si/SiO_2(100)	T > 400 °C (450 – 500 °C) 350 °C < T < 400 °C (~380 °C) T < 250 °C	0% to ~3.7% 0% to ~3.7% 0%	M to T, **Polycrystalline film** B, or M/T and B Amorphous film
STO(100)	400 °C < T < 470 °C (~430 °C) T > 480 °C T < 400 °C	0% to ~3.7%	B, **Epitaxial film** M B, polycrystalline film

Table 6.1 Optimized deposition conditions and sample information. (M is the monoclinic phase, T is the tetragonal phase, and B is the bronze phase).

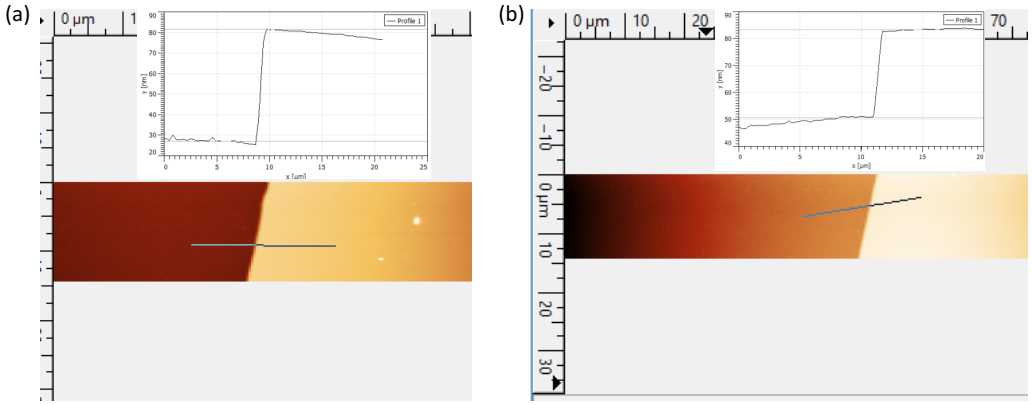

Figure 6.8 Deposition rate calibration using AFM. (a) The AFM scan image of the VO_2 film on silicon substrate. (b) The AFM scan image of the $V_{0.963}W_{0.037}O_2$ film on silicon substrate.

6.3.2 Structure determination and microstructure characterization

Crystalline phase structure was characterized by X-ray diffraction in a Bruker D8 Discover with an X-ray source of Cu Kα radiation. The instrument was equipped with an area detector, and a sample stage that allowed 80 mm translation in two directions for automated data collection. θ-2θ spectra were collected at different temperatures (270 K – 358 K) using an in-situ heating stage or a cold bath. Based on

the XRD data, the phase composition and Rietveld refinement were completed by using the Topas-5 software from Bruker as shown in Table 6.2.

x% in $V_{1-x}W_xO_2$	T (K)	% Phases		Lattice constant-Monoclinic Phase					Lattice constant-Tetragonal phase		
		%Mono	%Tetra	a (Å)	b (Å)	c (Å)	beta (deg.)	volume (Å^3)	a (Å)	c (Å)	volume (Å^3)
0	**300**	100	0	5.8751(0.0073)	4.5217(0.0021)	5.4861(0.0022)	124.359(0.016)	120.313(0.082)			
0.1(0.1)	**300**	100	0	5.8763(0.0015)	4.5221(0.0021)	5.4920(0.0022)	124.279(0.016)	120.591(0.083)			
0.3(0.1)	**300**	100	0	5.8999(0.0014)	4.5225(0.0020)	5.5037(0.0021)	124.535(0.015)	120.973(0.079)			
0.9(0.1)	**300**	65.6(0.15)	34.4(0.15)	5.9201(0.0016)	4.5208(0.0019)	5.5105(0.0023)	124.634(0.019)	121.347(0.084)	4.5424(0.0011)	2.86391(0.00070)	59.091(0.033)
1.5(0.1)	**300**	62.3(0.14)	37.7(0.14)	5.9356(0.0016)	4.5254(0.0020)	5.5367(0.0023)	125.029(0.019)	121.783(0.087)	4.5488(0.0012)	2.86120(0.00070)	59.203(0.034)
2.1(0.1)	**300**	63.50(0.1)	36.5(0.1)	6.0801(0.0019)	4.5311(0.0024)	5.5918(0.0025)	125.944(0.023)	124.72(0.10)	4.5457(0.0011)	2.85593(0.00057)	59.014(0.031)
2.4(0.1)	**300**	62.53(0.9)	37.47(0.9)	6.0652(0.0014)	4.5514(0.0017)	5.5878(0.0018)	125.748(0.017)	125.193(0.073)	4.55138(0.00090)	2.85959(0.00053)	59.237(0.026)
2.8(0.1)	**270**	65.90(0.79)	34.10(0.79)	6.1421(0.0015)	4.5784(0.0019)	5.6338(0.0020)	126.873(0.017)	126.736(0.080)	4.54883(0.00096)	2.85830(0.00060)	59.144(0.028)
3.4(0.1)	**270**	64.83(0.83)	35.17(0.83)	6.1607(0.0014)	4.5853(0.0018)	5.6325(0.0019)	126.798(0.015)	127.409(0.076)	4.5505(0.0010)	2.86554(0.00065)	59.336(0.029)
3.5(0.1)	**270**	48.78(0.97)	51.22(0.97)	6.2953(0.0015)	4.6135(0.0021)	5.7095(0.0020)	128.311(0.018)	130.114(0.087)	4.54333(0.00090)	2.86259(0.00059)	59.089(0.026)

Table 6.2 Phase Fraction Atomic Percent Determined by Rietveld Refinement. Data analysis was carried out by Rietveld refinement using the TOPAS software. (Monoclinic phase: ICSD #15889; Tetragonal phase: ICSD #4110)

The W concentration of each strip segment in the spread film of $V_{1-x}W_xO_2$ was determined by wavelength dispersive X-ray spectroscopy (WDS) measurements. The WDS measurement function is integrated into a scanning electron microscope with an automated xyz stage offering the programmable automation needed to easily measure the multiple samples on a substrate. With a good calibration standard, the WDS measurement can offer composition accuracy of a fraction of a percent. The composition is averaged over a range characterized by a beam size of about 30 μm. Depending on the elements in the spread, it takes about 1 minute to measure a single position. A JEOL JXA-8900 electron microprobe was used in this thesis.

The surface topography of the as-grown films was characterized by an atomic force microscopy (AFM, Digital Instruments Nanoscope III and Dimension 5000) using the tapping mode. All AFM images were taken in air at room temperature.

High angle annular dark field (HAADF)-STEM images were acquired from the prepared lamellas using a probe corrected FEI Titan 80−300 microscope operated at

300 kV. The probe is typically corrected to 20 mrad, providing a spatial resolution of 0.1 nm. The probe convergence angle is 24 mrad, and the HAADF inner and outer collection angles are 70 and 400 mrad, respectively.

6.3.3 Transport measurement

To investigate the dc transport properties, a wire bonder was used to wire each strip segment into a four-probe geometry as shown in Figure 6.9 and a physical property measurement system (Quantum Design Inc.) was used to measure the electronic transport. The temperature sweep rate was set to be 1K/min with a step of 0.2K.

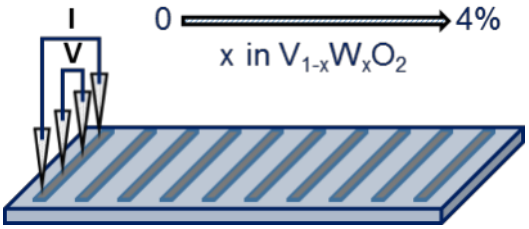

Figure 6.9 A schematic view of the four-probe resistance measurement geometry.

6.4 Results and discussion

6.4.1 The crystalline structures as a function of W concentration

High quality $V_{1-x}W_xO_2$ (B) epitaxial or highly-textured film was grown on (001) -oriented STO in our high throughput PLD system under well-optimized growth conditions as described above. As shown in Figure 6.10a, only the (00*l*) peaks of $V_{1-x}W_xO_2$ are observed, indicating the film is (00*l*) orientation preferred grown on STO(001). The (00*l*) peaks shift to lower 2θ angles with increasing the W concentration because W^{6+} ions are slightly larger than V^{4+} ions. The result demonstrates the

homogenous distribution of W ions in the $V_{1-x}W_xO_2$(B) film. The whole spread film shows a relatively low RMS roughness (< 1 nm) and an average grain size in a range of 337 nm to 530 nm (Figure 6.10b). High W concentration benefits the grain growth and leads to the bigger grain size. To our knowledge, this is the first time to grow high quality $V_{1-x}W_xO_2$ (B) composition spread films on STO(001); therefore, the successful demonstration of growing high-quality $V_{1-x}W_xO_2$ (B) films on STO (001) substrates can potentially help get the fundamental insights into the applications of $V_{1-x}W_xO_2$ (B) for LIBs.

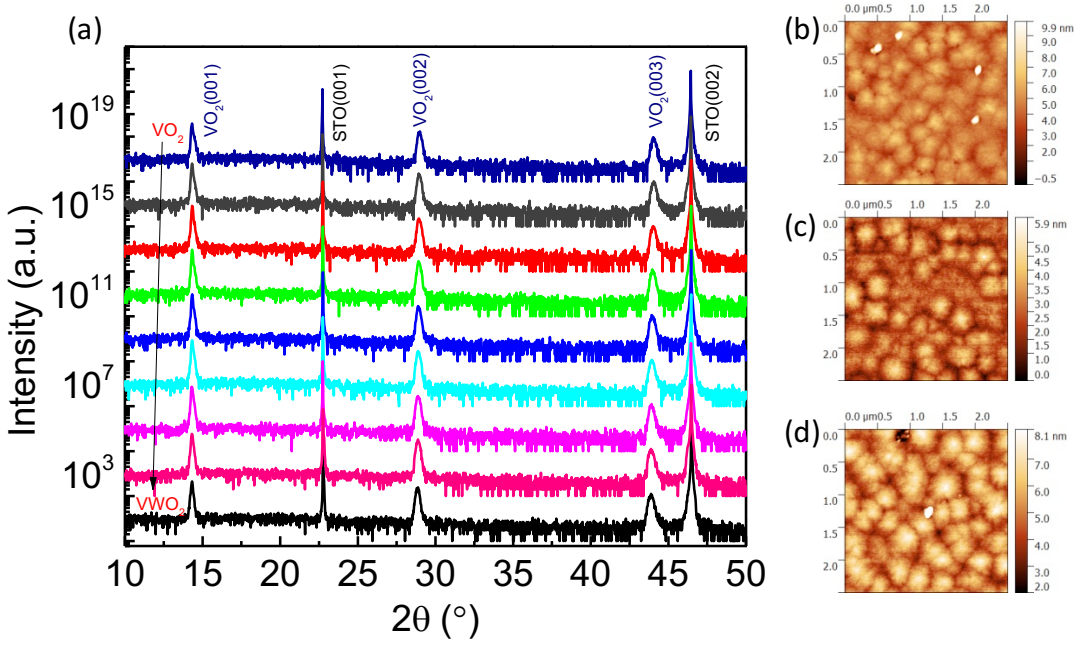

Figure 6.10 (a) The θ-2θ results of a VO_2-VWO_2 composition spread film formed on a STO (001) substrate; 2.5 μm × 2.5 μm AFM scan images of the $V_{1-x}W_xO_2$/STO (001). (b) x = 0, showing a RMS roughness 0.95 nm with an average grain size of 337 nm. (c) x = 1.8%, showing a RMS roughness 0.74 nm with an average grain size of 405 nm. (d) x = 3.4%, showing a RMS roughness 0.95 nm with an average grain size of 530 nm.

In this thesis work, we primarily focus on the monoclinic (M1) and tetragonal (T) phases of $V_{1-x}W_xO_2$ films grown on *c*-Al_2O_3 and silicon substrates. The *c*-Al_2O_3 substrate leads to high-quality epitaxial $V_{1-x}W_xO_2$ films because its lattice constants match well with the lattice constants of VO_2. The large crystal lattice mismatch between the silicon (SiO_2) substrates and VO_2 makes the $V_{1-x}W_xO_2$ films fabricated on silicon substrates polycrystalline. Despite the polycrystalline texture of the $V_{1-x}W_xO_2$ films fabricated on silicon substrates, VO_2 films still show a change around three orders of magnitude in the resistance.

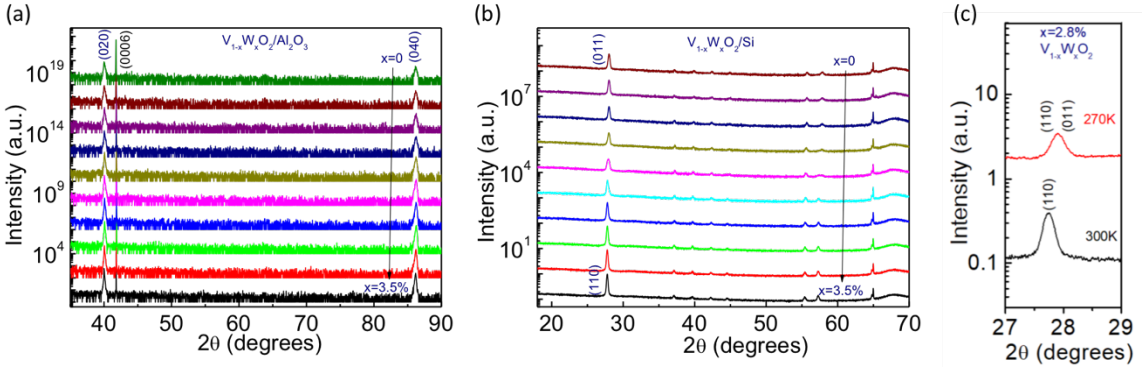

Figure 6.11 (a) XRD patterns of $V_{1-x}W_xO_2$ on c-Al_2O_3 at room temperature. (b) XRD patterns of $V_{1-x}W_xO_2$ on Si/SiO_2 at room temperature. (c) The temperature dependence of representative XRD patterns for $V_{1-x}W_xO_2$ on Si/SiO_2. (011) Reflections of VO_2(M1) (ICSD #15889) and (110) reflections of VO_2 (T) (ICSD #4110) are indicated.

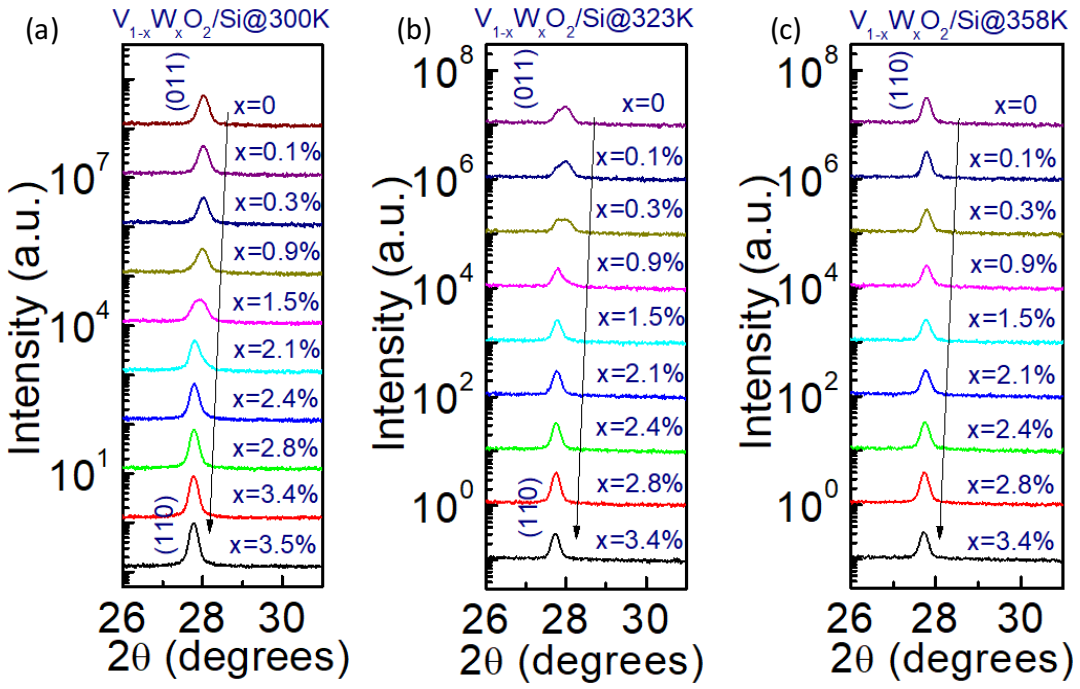

Figure 6.12 XRD 2θ-ω spectra obtained from the $V_{1-x}W_xO_2$ films grown on the Si/SiO_2 substrates at 300K (a), 323 K (b), and 358 K (c), respectively.

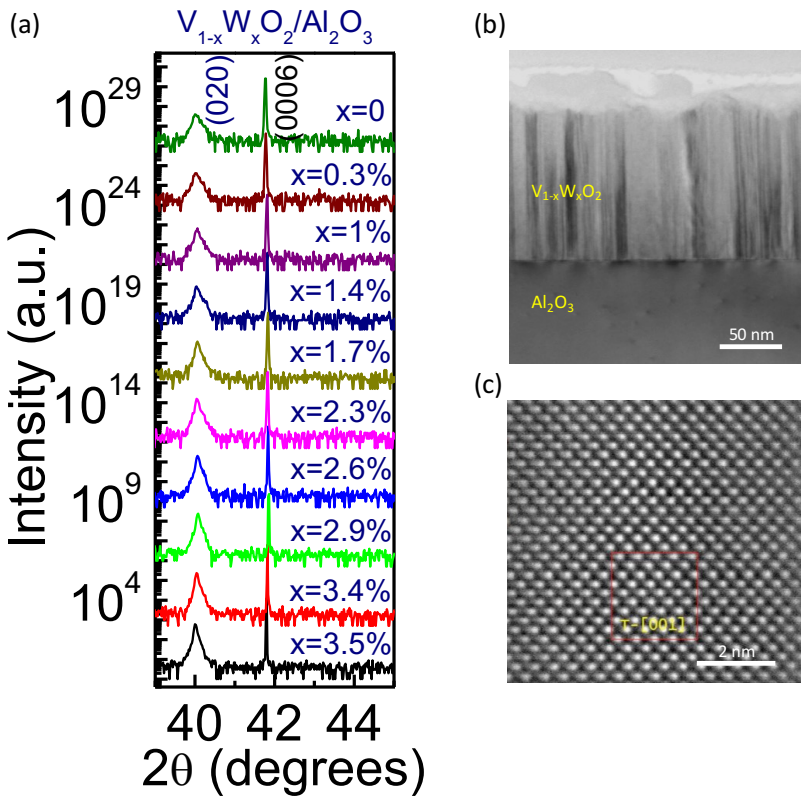

Figure 6.13 (a) XRD 2θ-ω spectra obtained from the a $V_{1-x}W_xO_2$ film grown on the *c*-Al_2O_3 (0001) substrate at room temperature. (b) Low-magnification cross-sectional HAADF-STEM image, and (c) the atomically resolved HAADF-STEM image of the $V_{1-x}W_xO_2$/*c*-Al_2O_3 (x = 3.44%).

The crystallinity and the lattice constant of the films were evaluated at different temperatures by X-ray diffraction (XRD) measurements (Figure 6.11) and confirmed by Rietveld refinement of XRD data (Table 6.2). The high purity of the $V_{1-x}W_xO_2$ monoclinic and tetragonal phases in all the films were confirmed as there are no obvious peaks corresponding to other phases of vanadium oxides and tungsten oxides. Figure 6.12 shows enlarged XRD spectra of a $V_{1-x}W_xO_2$/Si sample in a 2θ range of 26° to 31° measured at different temperatures. As shown in Figure 6.12a, the strong peak between 27 ° and 28° for each sample specimen of the composition-spread film of V_{1-}

$_xW_xO_2$ may have two origins: the (011) diffractions of the monoclinic phase when x is close to 0, and the (110) diffractions of the tetragonal phase when x is close to 4%. With increasing doping, the peak shifts towards a smaller 2θ, suggesting an increase in the lattice constant. The increase in the lattice constant is attributed to the difference in the ionic radius of V^{4+} (0.58 Å) and W^{6+} (0.60 Å) in an octahedral coordination. [178,188,189] At 300 K, an M1 phase and a T phase coexist at an intermediate doping level around 1.5% (x = 1.5%) where the doping-induced MIT starts at 300 K. As temperature is increased to 323 K (Figure 6.12b), the M1 phase and the T phase coexist in sample segments at a lower W concentration, but shown in Figure 6.12c, only the reflections of T phase (110) of $V_{1-x}W_xO_2$ were observed at 358 K, indicating the completion of the phase transition at 358 K. Thus, the above results demonstrate that the W dopant can facilitate the phase transition from M1 to T in the $V_{1-x}W_xO_2$ system and the transition temperature decreases with increasing the W concentration.

As displayed in Figure 6.11a, the $V_{1-x}W_xO_2$ film grown on *c*-Al_2O_3 shows reflections only from the (020) and (040) planes of the M1 phase, indicating that an epitaxial $V_{1-x}W_xO_2$ thin film in the M1 phase was successfully grown on *c*-Al_2O_3 (0001), and the out-of-plane epitaxial relationship between $V_{1-x}W_xO_2$ and the sapphire substrate is $(020)_{M1}\|(006)_S$.[190] The cross-sectional HAADF-STEM image of the $V_{1-x}WxO_2$/*c*-Al_2O_3 heterostructure (Figure 6.13b) shows a uniform $V_{1-x}W_xO_2$ thin film layer with a thickness of 150 nm and comprising parallel column-like grains. Figure 6.13c is a high-resolution STEM image taken from the $V_{1-x}W_xO_2$ (x = 3.44%) film in a zone along the [001] direction. The image indicates the tetragonal phase stabilized by W dopants.

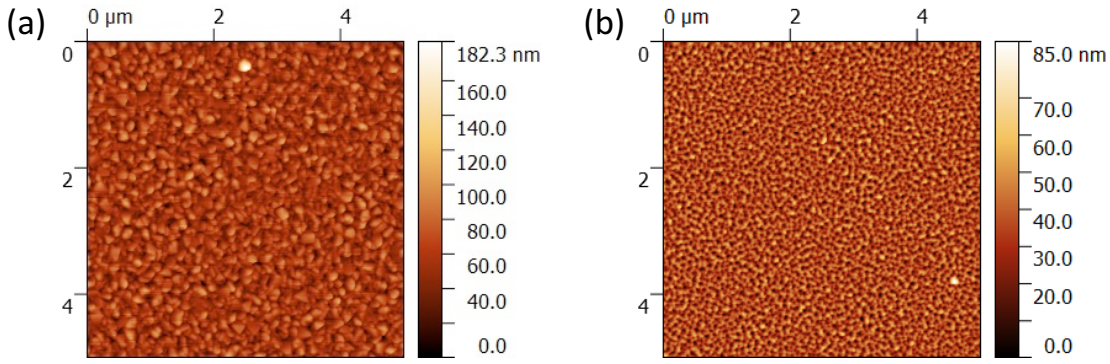

Figure 6.14 Representative AFM images of $V_{1-x}W_xO_2$ (x~1%) on Si/SiO_2 substrate with a surface roughness of RMS ~15 nm and an average grain size of ~220 nm (a), and on *c*-Al_2O_3 substrate with a surface roughness of RMS 9.6 nm and an average grain size of ~130 nm.

The microstructure of the W-doped polycrystalline VO_2 thin film grown on Si/SiO_2 is independent of the W concentration. Specifically, as shown in Figure 6.14a, continuous and compact nanoparticles with an average grain size of ~220 nm, consistent with previous reports[191], were consistently observed in all the samples grown on Si/SiO_2 substrates. On *c*-Al_2O_3 substrates, the overall microstructure is also independent of the W concentration, but the film surface was found to be smooth and dominated by small irregularly shaped islands separated by corrugations as shown in Figure 6.14b, similar characteristics are commonly observed for VO_2 films grown on sapphire substrates.[190] Therefore, the composition-spread film of $V_{1-x}W_xO_2$ with a uniform surface morphology within the W concentration range has been fabricated on a specific substrate (*c*-Al_2O_3 or Si/SiO_2) successfully, thus the effect of film morphology on the phase transition characteristics can be potentially eliminated.

6.4.2 Structural 'cofactor conditions' for the phase-transition

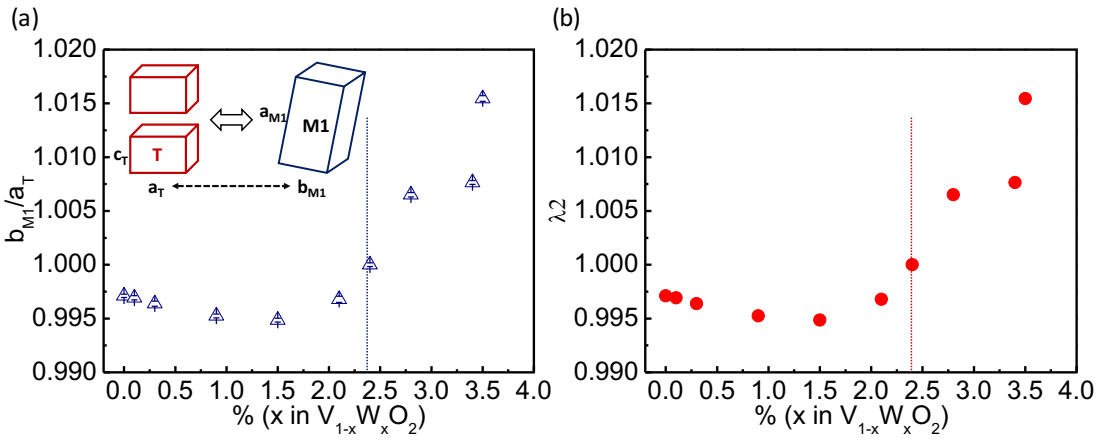

Figure 6.15 (a) W concentration (x) dependence of b_{M1}/a_T (b_{M1}: b axis of the Monoclinic phase; a_T: a axis of the Tetragonal phase). (b) W concentration (x) dependence of the value of λ2.

A thermal hysteresis loop is induced by elastic and interfacial energy stored due to the coexistence of the two phases during the first order transition.[192] Thus, the compatibility between the tetragonal phase and the monoclinic phase of VO_2-based materials is a key factor to determine the hysteresis width through the MIT. In the high-temperature tetragonal phase (T), the V^{4+} ions have a linear periodic arrangement along the c_T-axis. As the material goes from the high-temperature phase to the low-temperature phase, the V^{4+} ions are distorted into dimerized zigzag chains along the crystallographic a_{M1}-axis in the monoclinic phase (M1) as shown in the inset of Figure 6.15a. During the phase transition, b_{M1} of the monoclinic phase corresponds to a_T of the tetragonal phase, so we hypothesize that when the ratio of b_{M1}/a_T is closer to 1, the transition barrier between the two phases is less. Accordingly, we first investigated the relation between the W concentration and the ratio of b_{M1}/a_T across the MIT, and the

results are shown in Figure 6.15a. Interestingly, it is observed that the ratio of b_{M1}/a_T approaches to 1 when the x is around 2.4% based on the semi-empirical relationship.

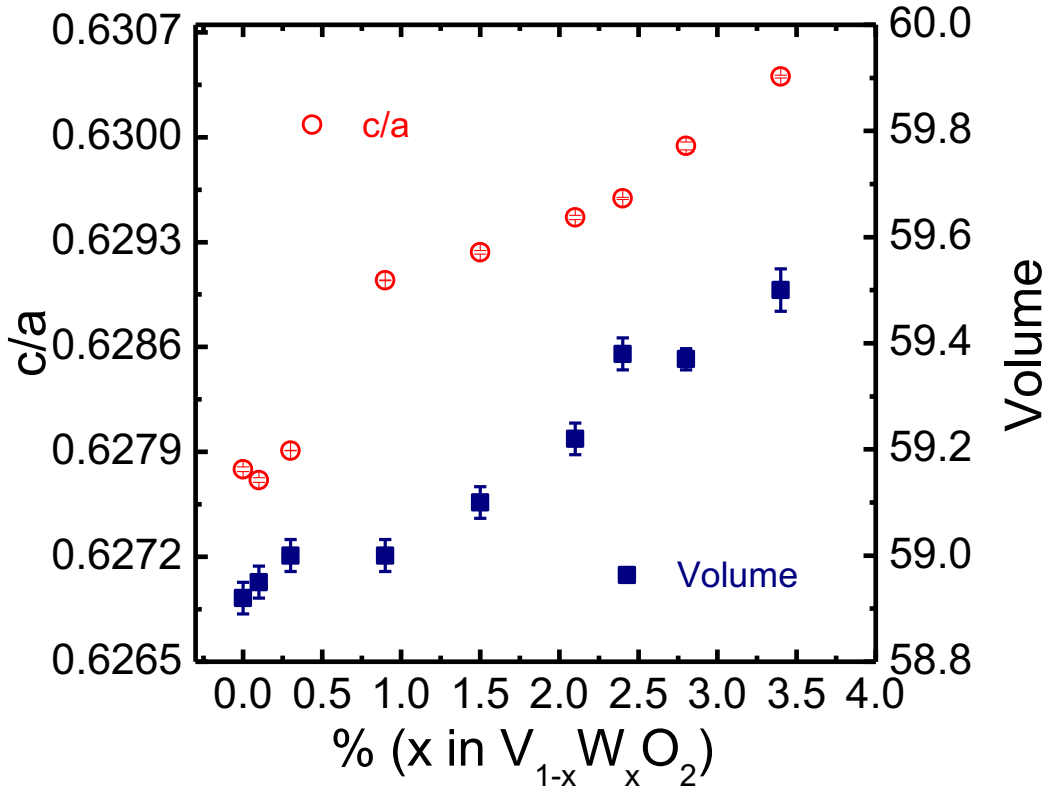

Figure 6.16 W concentration dependence of the c/a ratio and the unit volume of $V_{1-x}W_xO_2$/Silicon based on the XRD results at 358 K.

At 358 K, the whole spread film of $V_{1-x}W_xO_2$/Silicon shows uniform tetragonal phase (Figure 6.12c). To understand the effect of W dopants on combination of both *a* and *c* parameters and lattice volume, as shown in Figure 6.16, we plotted the variation of the *c*/*a* ratio and the unit cell volume as a function of W concentration. Figure 6.16 shows that the unit volume increases linearly with increasing the W content, similar to the variation of the lattice parameter ratio of *c*/*a*. These results further confirm the homogenous distribution of W in the $V_{1-x}W_xO_2$ film.

Introducing structural defects into VO_2 films through chemical doping has been reported to be an effective method to reduce the hysteresis width, and their MIT transitions could be described by a martensitic transformation model.[183] Recently, stronger compatibility conditions called the 'cofactor conditions'[181-183] have been theoretically proposed based on the general non-linear theory of martensite (GNLTM) to represent the conditions that allow better reversibility. A sharp drop in the hysteresis width has been observed for shape memory alloys when the 'cofactor condition' is satisfied, i.e. $\lambda 2 = 1$, where $\lambda 2$ is the middle eigenvalue of the 3×3 'transformation stretch matrix' U. [181-183] $\lambda 2$ can be obtained based on the lattice parameters and the space groups of the two phases.[181-183]Thus, systematically tuning the composition of the alloy to make $\lambda 2$ approach 1 is a promising strategy for narrowing the hysteresis width. In the present study, this strategy was used to extract the values of $\lambda 2$ by investigating the lattice parameters of $V_{1-x}W_xO_2$ as the W concentration varies. A clear correlation between the W concentration and $\lambda 2$ is observed as shown in Figure 6.15b. The value of $\lambda 2$ is 1 when the concentration of W is about 2.4%. That is, CC is satisfied when W concentration in $V_{1-x}W_xO_2$ is 2.4% (x% = ~2.4), which suggests that x = 2.4% is the optimal composition in $V_{1-x}W_xO_2$ for a minimum hysteresis width. Surprisingly, the optimal composition that satisfies $\lambda 2 = 1$ is consistent with the experimental result. As shown in Figure 6.15a, the b_{M1}/a_T ratio is close to 1 when W concentration is around 2.4% indicates that $V_{1-x}W_xO_2$ should show minimum hysteresis width when x is around 2.4%.

6.4.3 The phase-transition characteristics (Tc and ΔT) as functions of W concentration

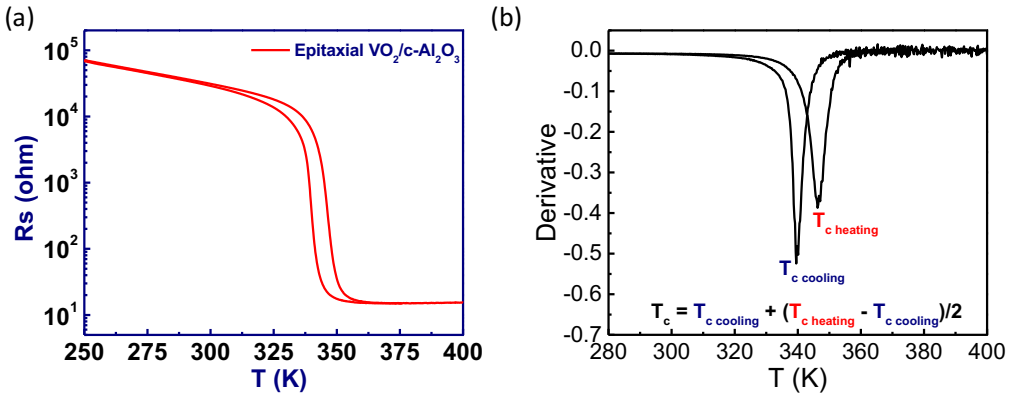

Figure 6.17 (a) A representative R-T curve of a pure VO_2 on *c*-Al_2O_3. (b) The first derivative of log(Rs) as a function of temperature.

W-concentration dependence of phase-transition characteristics was investigated through resistance measurements performed on both epitaxial and polycrystalline films. As shown in Figure 6.17a, the sheet resistance-temperature (Rs-T) curve of VO_2/*c*-Al_2O_3 showed a resistance change of nearly 4 orders of magnitude across the transition, and the phase transition temperature was found to be 342 K, consistent with that obtained from VO_2 single crystals.[161] In this work, all the films had a thickness above 150 nm such that the substrate-induced strain effect is expected to be negligible. The phase transition characteristics (T_c and ΔT) of each strip segment were extracted from the temperature dependence of the first derivative of log(Rs)[187] as shown in Figure 6.17b, from the derivative plot, the critical transition temperatures ($T_{c\ heating}$, $T_{c\ cooling}$, and T_c) and the transition hysteresis width ($\Delta T = T_{c\ heating} - T_{c\ cooling}$) were determined.

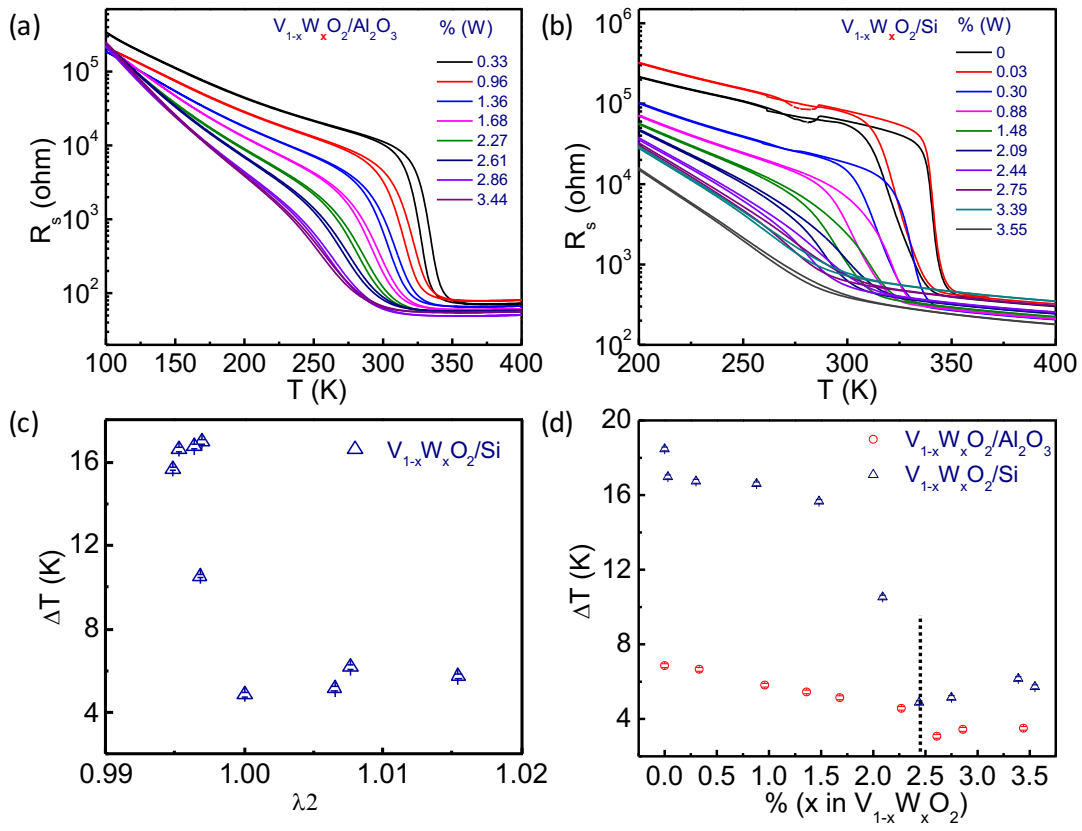

Figure 6.18 (a), (b) The temperature dependence of the sheet resistance (Rs) of two $V_{1-x}W_xO_2$ films grown on *c*-Al_2O_3 (a) and on Si/SiO_2 (b), respectively. (c) Hysteresis width as a function of λ2 for $V_{1-x}W_xO_2$/Si. (d) The W concentration (%) dependence of hysteresis width (ΔT) for both $V_{1-x}W_xO_2/Al_2O_3$ and $V_{1-x}W_xO_2$/Si films.

Figures 6.18a and 6.18b show the thermal hysteresis of the Rs–T characteristics as expected for first-order phase transitions. Moreover, increasing the W concentration in both spread films can effectively reduce the transition temperature. The phase transition temperature almost decreases linearly with increasing the W concentration for both spread films as shown in Figure 6.19. The linear fits shown in Figure 6.19 further suggest that corresponding to each atomic percentage of W increased, the Tc in the epitaxial film and the polycrystalline film is reduced by 26 K and 21 K, respectively.

The results agree well with the previous reports,[169] indicating that tuning the W concentration is able to adjust the switching temperature precisely and efficiently.

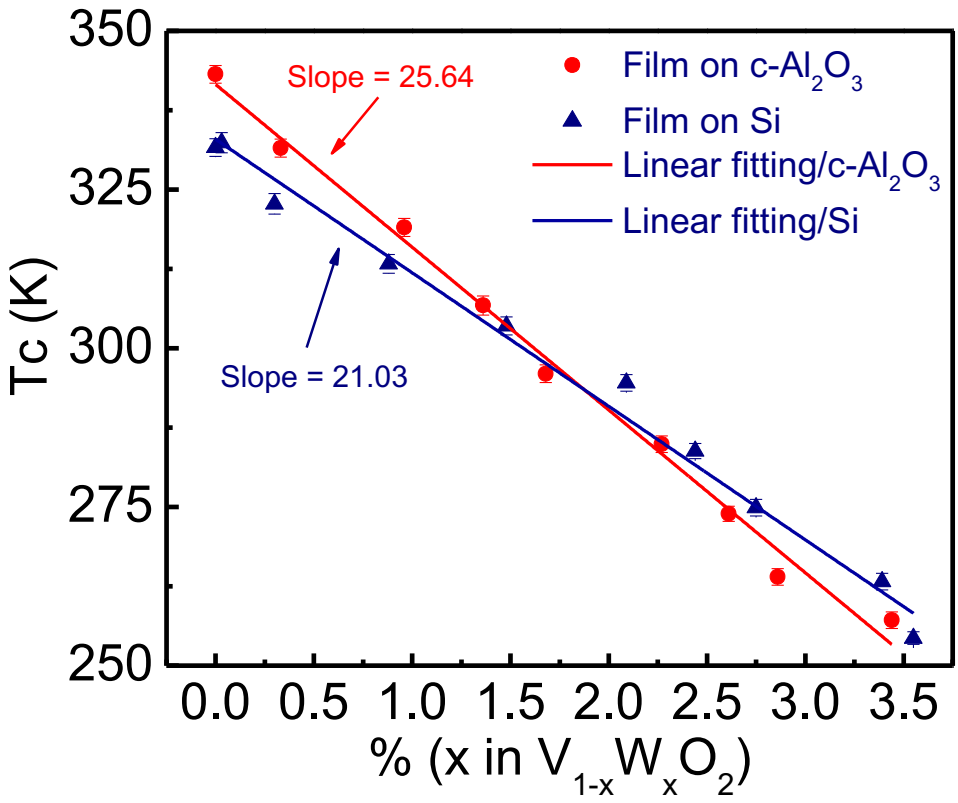

Figure 6.19 W content (%) dependence of critical phase transition temperature (T_c) for both samples.

To verify that the 'cofactor condition' corresponds to a minimum hysteresis width (ΔT), we plot the measured ΔT as a function of $\lambda 2$ in Figure 6.18c. It is expected that the ΔT decreases as the value of $\lambda 2$ approaches 1 and a minimum value of ΔT is obtained at $\lambda 2 = 1$. Further, we also plot the measured ΔT as a function of W concentration for both films shown in Figure 6.18d. The width and the shape of the hysteresis cycle are determined by the film microstructure, the film-substrate interface, and localized strain. Epitaxial films are generally expected to show phase transition

behavior close to that of bulk crystals.[166] This is the reason that the overall hysteresis in the sample of $V_{1-x}W_xO_2$/Si is larger than that in the sample of $V_{1-x}W_xO_2$/*c*-Al_2O_3. The difference in the hysteresis width may be attributed to the polycrystallinity of the film grown on Si/SiO_2 substrate, which may result in a highly defective microstructure.[193] Regardless of such a difference in the determined hysteresis width, both spread films share a common feature, namely, a dip consistently appearing at a W concentration of ~2.4% in the plots of ΔT versus W concentration (Figure 6.18d). The result strongly indicates a likely intrinsic origin for the 'cofactor condition'. Therefore, as evident in the spread films of $V_{1-x}W_xO_2$ grown on different substrates, the theoretical prediction of 'cofactor condition' is likely applicable to correlated oxide systems.

6.4.4 The possible mechanism of MIT in W-doped VO_2

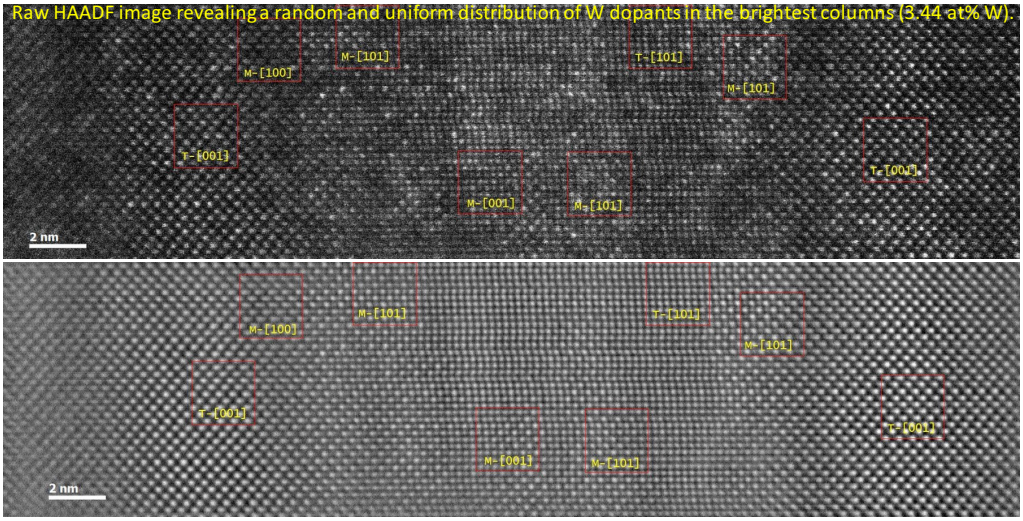

Figure 6.20 An atomic resolution HAADF-STEM image of $V_{1-x}W_xO_2$ (x = 3.44%) grown on *c*-Al_2O_3.

A small amount of W dopants can effectively change the MIT of VO_2, but it still remains unclear how the W dopants manipulate the phase transition in VO_2. The

main controversy focuses on the role of the W dopants. In particular, whether the W dopants introduce extra electrons into the system or cause internal structural effects is still under debate.[176] It has been demonstrated that each W doping ions are in a 6+ valence state, and thus each W ion donates 2 electrons. Therefore, introducing W doping ions is equivalent to reducing the valence of the V ions. [176] In addition, as shown in Figure 6.18, the resistance of the insulating state changes dramatically with changing the W doping concentration, underlining the importance of the electronic properties of the insulating state in governing the metal–insulator transition. Furthermore, our HAADF results (Figure 6.20) indicate that W ions are randomly and uniformly distributed into the film and form localized tetragonal-like centers, which can reduce the structural distortion effect and make the phase transition occur smoothly and easily.[176] There may be a balance between the W concentration and the structural distortion for a high-quality phase transition, because it has been reported that increasing the doping concentration will adversely affect the phase transition characteristics due to an increase in the carrier density for the low temperature phase.[176] Structural defects due to the introduction of W doping ions may act as nucleation sites for the phase transition, and thus reduce the activation energy of the phase transition. However, an overly large doping level of W ions will induce structural disorders, which further affect the hysteresis behavior. In addition, it is difficult to study the effects of isolated W ion on the phase transition due to the strong coupling effect between W ions in the heavily-doped samples. The values of $\lambda 2$, derived from the lattice parameters of the M1 and the T phases of $V_{1-x}W_xO_2$, are spread on both sides of $\lambda 2 = 1$ with increasing the W concentration, suggesting the existence of an optimal W concentration to

maintain a desired lattice structure for a phase transition with a minimum energy barrier according to the theory GNLTM. Therefore, besides the extra electrons introduced by the W ions, the structure effect associated with W dopants contributes significantly to the hysteresis behavior across the MIT. This critical correlation between the structural effect and the hysteresis width may have important implications for the understanding of the nature of the MIT in the $V_{1-x}W_xO_2$ system.

6.4.5 The application of W-doped VO2 for cathode materials in LIBs

In a lithium-ion battery, the cathode material is a key component that determines the performance of LIBs.[194] To improve the performance of LIBs and reduce the cost of LIBs, the potential cathode materials should satisfy a series of requirements such as structural stability during insertion and extraction of lithium-ions, high capacity, low cost, environmentally benign, and good electronic conduction.[195] In particular, highly electronic conducting cathode materials attract much attention because such materials allow for easy addition or removal of electrons during the electrochemical reaction and minimize the need for inactive conductive diluents (e.g. carbon black, binders), which take away from the overall energy density. More importantly, the high electronic- conduction active materials potentially offer more possibilities to gain a fundamental understanding of the electrochemical behaviors of cathode materials by eliminating the effects from the conductive additives/binders in the traditional LIBs. [195]

For Li-ion intercalation applications, both V_2O_5 and VO_2 (B) offer the essential advantages such as low cost, high safety, high specific capacity, and energy density. The state-of-the art V_2O_5 and VO_2 (B) cathode materials have large theoretical

capacities of 294 mAh/g and 323 mAh/g, respectively. [196,197] Both values are rather higher than those of commonly used cathode materials, e.g., $LiCoO_2$ (140 mA h/g), $LiMn_2O_4$ (148 mA h/g) and $LiFePO_4$ (170 mA h/g).[195] However, a major drawback of both V_2O_5 and VO_2 (B) based cathode materials is the high resistivity. Thus, current collectors and conductive dopants (carbon black) are necessary for increasing the conductivity in a conventional Li-ion cell as shown in Figure 6.21a. According to our studies on W doped VO_2, the electrical conductivity of the $V_{1-x}W_xO_2$ is high even at a relatively low temperature (e.g. $x > 3\%$, $\sigma > 10^2$ s/cm at 253K). Therefore, it is expected that the tungsten doped vanadium dioxide thin film could be used as a dual functional thin film cathode in lithium ion batteries.

For example, as shown in Figure 6.21b, the cathode part in our coin cell may include only one active cathode-layer (the $V_{1-x}W_xO_2$ film), which has the ability to accommodate Li-ions (host for Li-ions) and conduct electrons (high electronic conductivity) without the conductive carbon black and binders. The $V_{1-x}W_xO_2$ film does not have a layered structure, but the lithium ions can go in and out along the *c* direction due to the anisotropic feature of the tetragonal crystal structure as shown in Figure 6.21c.

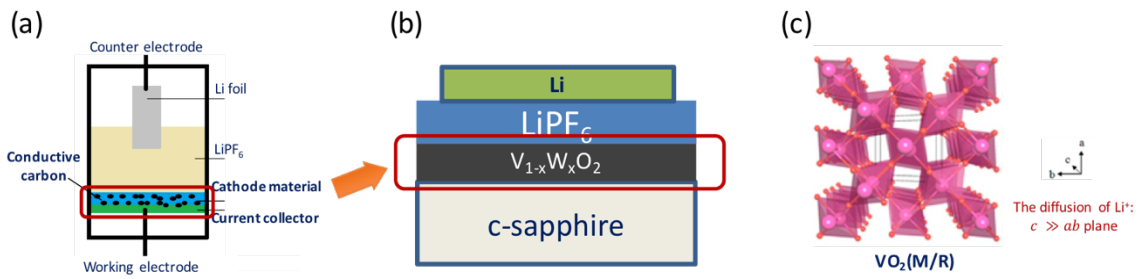

Figure 6.21 (a) A schematic view of the configuration of a conventional lithium ion cell. (b) A schematic view of the configuration of a lithium ion cell proposed in this thesis. (c) A schematic view of a tunnel structure of the tetragonal-phase VO_2.[198]

To carry out proof-of-concept experiments, a PVDF−HFP-Based Gel Electrolyte was synthesized, and a coin cell was then fabricated in glovebox. The details of the fabrication and test process are described as the following.

PVDF−HFP-based gel electrolyte was made by first dissolving 0.25 g of PVDF−HFP (Sigma-Aldrich) into a mixture of 4.5 g of acetone and 0.25 g of ethanol under mechanical stirring for 1 h to get a homogeneous solution. The solution was then cast onto a flat aluminum foil, and the solvent was evaporated in a constant 80% humidity chamber at 25 °C. The samples were dried under vacuum at 60 °C for 5 h, after which a homogeneous freestanding membrane was obtained. The thickness of the PVDF−HFP membrane is around 40μm. The as-prepared porous PVDF−HFP membrane was cut into small round films with an area of 0.2 cm^2 and immersed into 1 M $LiPF_6$ in 1:1 ethylene carbonate (EC):diethyl carbonate (DEC) liquid electrolyte for 1 min to be fully soaked by electrolyte, and the excess liquid on the surface of the membrane was moved away by wipers.

Further, battery assembly and electrochemical tests were done in an argon filled glove box. The lithium-metal electrodes were pressed and punched from a Li belt (Sigma-Aldrich) into round disks with an area of 0.2 cm^2 and a thickness 0.5 mm. The VO_2 electrodes, gel membranes, and lithium metal were pressed together in sequence by clips, with one stainless steel disk on anode side in a CR2016 coin cell and sealing by epoxy. The electrochemical performances of the cells were tested by an Arbin tester. The cell was cycled with a constant current of 50 $\mu A/cm^2$ in the voltage range of 1.5−3.5 V.

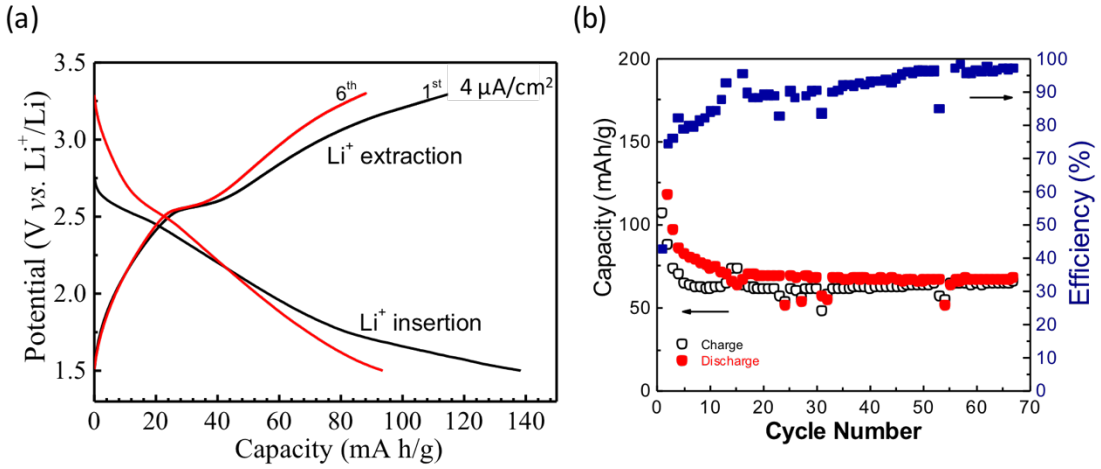

Figure 6.22 (a) The galvanostatic charge-discharge profile of a $V_{1-x}W_xO_2$ (x = 2.4%) thin-film cathode material. (b) The cyclic performance of the $V_{1-x}W_xO_2$ (x = 2.4%) thin-film cathode material.

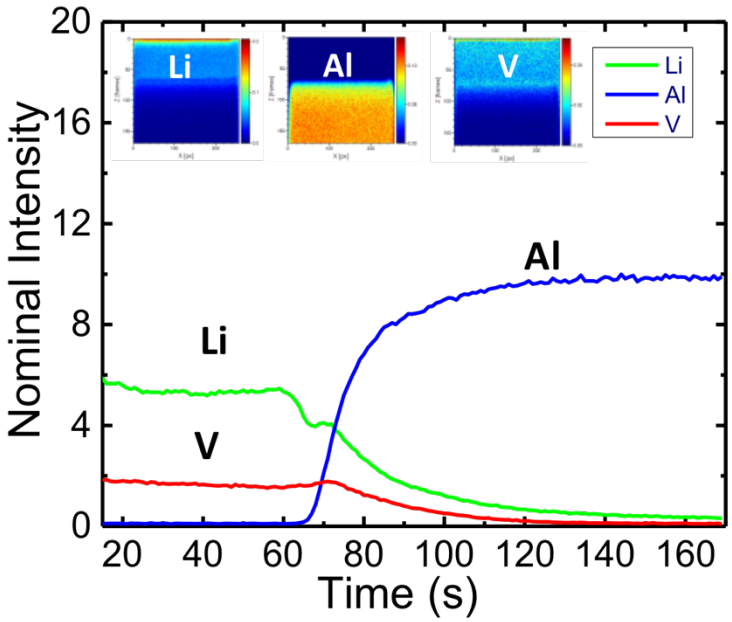

Figure 6.23 The Time-of-Flight Secondary Ion Mass Spectrometry (TOF-SIMS) depth profile for a $V_{1-x}W_xO_2/Al_2O_3$ (x = 2.4%) sample after lithiation. The inset images show the cross-sectional distribution of Li, Al, and V, respectively.

As shown in the charge-discharge profile (Figure 6.22a), the discharging voltage plateau is around 2.5 V, which is consistent with the reported value. From the cycling performance (Figure 6.22b), the capacity is initially high, but then decreases to be less than 100 mAh/g accompanied with a stable and high coulombic efficiency. To check the lithiation efficiency, we have done the ToF-SIMS study and the results ae shown in Figure 6.23. The depth profile shows the lithiation is complete and lithium ions are homogeneously distributed into the film.

Based on our preliminary experiments, we have proved the concept of $V_{1-x}W_xO_2$ thin-film cathode for LIB application and obtained high capacity. For our future work, we are analyzing the possible reasons for the rapid capacity decay and doing further optimizations, such as optimizing the device design, using solid electrolytes,

and studying the structural stability of $V_{1-x}W_xO_2$ after lithiation, and cooperating with NIST to study the lithium ion adsorption sites and diffusion pathways by using STEM.

6.5 Conclusions

In summary, a highly reliable fabrication method has been developed for high quality composition-spread $V_{1-x}W_xO_2$ films based on the high-throughput pulsed laser deposition approach. The high-throughput method makes it possible to systematically investigate the role of W dopants on the MIT of VO_2 by eliminating various factors arising from different fabrication methods. The lattice-constant cofactor condition was satisfied by tuning the lattice parameters of VO_2 via W doping, verified by a minimum hysteresis width at 2.4% W for both polycrystalline and epitaxial films. This is the first time the cofactor condition was satisfied experimentally in an oxide system. These findings not only emphasize the impact of crystal structures on the MIT of VO_2 but also guide us to control and optimize the hysteresis behavior of various physical properties in functional materials.

VO_2 (B) has been demonstrated to be a promising cathode material in Li-ion batteries, however, fabrication of the material using the traditional synthesis methods may be difficult. Using the high-throughput pulsed laser deposition approach, we successfully fabricated composition spread films of $V_{1-x}W_xO_2$ (B) on STO (001) substrates. With W ions doped into VO_2, the materials were found to show properties similar to VO_2 (B) in the metastable bronze phase. Furthermore, we have demonstrated that the rutile $V_{1-x}W_xO_2$ thin film can be used as a dual functional thin-film cathode in LIBs with a high capacity of ~140 mAh/g using a $V_{0.976}W_{0.024}O_2$ thin-film cathode. We

are developing a screening methodology for rapid discovery of cathode materials in LIBs.

Chapter 7: Fabrication of Organic-inorganic Perovskite Thin Films for Planar Solar Cells via Pulsed Laser Deposition

7.1 Abstract

We report on fabrication of organic-inorganic perovskite thin films using a hybrid method consisting of pulsed laser deposition (PLD) of lead iodide and spin-coating of methylammonium iodide. Smooth and highly crystalline $CH_3NH_3PbI_3$ thin films have been fabricated on silicon and glass coated substrates with fluorine doped tin oxide using this PLD-based hybrid method. Planar perovskite solar cells with an inverted structure have been successfully fabricated using the perovskite films. Because of its versatility, the PLD-based hybrid fabrication method not only provides an easy and precise control of the thickness of the perovskite thin films, but also offers a straightforward platform for studying the potential feasibility in using other metal halides and organic salts for formation of the organic-inorganic perovskite structure.

7.2 Introduction

Organic-inorganic perovskite solar cells (PSCs) have recently emerged as one of the most promising alternatives to silicon based solar cells due to their high efficiency, relatively low cost, and flexibility in materials growth and architecture.[199-204] Many breakthroughs have been made since PSCs were first unveiled in 2009,[199] and a power conversion efficiency (PCE) as high as 20.3% has been reported.[204]

The superior performance of PSCs is based on the unique characteristics of the organic-inorganic perovskite, namely, its relatively high absorption coefficient, tunable bandgap,[205-207] low binding energy of photo-generated electron-hole pairs,[208] high charge-carrier mobilities, and long charge carrier diffusion lengths.[209,210] These factors are of great benefit to the simple planar heterojunction architecture and can lead to low-cost manufacturing with robust device performance.[211]

The high efficiency of PSCs is generally associated with specific synthesis procedures, where controlling the morphology and the grain size of perovskite materials in the device is of utmost importance.[212] Various fabrication methods of the perovskite thin films have been reported to date.[193,213-215] The synthesis methods can be categorized into the one-step method (e.g. one-step precursor deposition and dual-source vapor deposition) and the two-step method (e.g. the sequential deposition method and vapor-assisted solution process). Compared to the one-step method, the two-step deposition is known to provide better control of the composition, the thickness, and the morphology of the organic-inorganic perovskite films, thus resulting in higher performance PSCs.[216,217] In particular, low-temperature all solution-based processes have attracted considerable attention due to their ease of synthesis and low-cost. However, the low solubility of metal halide precursors in organic solvents has been identified as a limiting factor for possible further improvement. [218-220] Thermal evaporation methods have been reported as successful in overcoming this issue and synthesizing high quality perovskite thin films.[202,221] Atomic layer deposition (ALD) has also been introduced for growth of halide compounds which are subsequently converted to perovskite thin films by dipping them into a methylammonium iodide

(MAI) solution.[222] The typical substrate temperatures of the thermal evaporation method and the ALD method are 325 °C and 150 °C, respectively. Based on these methods, the organic-inorganic perovskite thin films with high purity and crystallinity have been synthesized, they have been used in high-performance devices.[223]

Here, we used pulsed laser deposition (PLD) to fabricate organic-inorganic perovskite thin films, where the substrate temperature is held at room temperature. PLD is a versatile method for fabricating high-quality films of a variety of materials. The main advantages of PLD include its operational simplicity and its non-equilibrium nature which allows stoichiometric mass transfer of materials from the target to the substrate.[224] In PLD, only a few parameters such as the laser energy density, the pulse repetition rate, the substrate temperature, and the deposition pressure need to be adjusted.[224] It is straightforward to apply PLD to the fabrication of multi-layered or composition-spread films by sequential ablation of multiple targets.[225] There have been only a few reports of the use of PLD for deposition of metal halides.[226] Very recently, Bansode et al.[227] prepared perovskite films and solar cells by an off-axis PLD method. In this work, we take advantage of the flexibility of PLD to explore a hybrid method for the fabrication of organic-inorganic perovskites thin films. We show that a PLD-based approach can provide good control of the morphology and the thickness of the perovskite films at room temperature.

7.3 Experimental setup

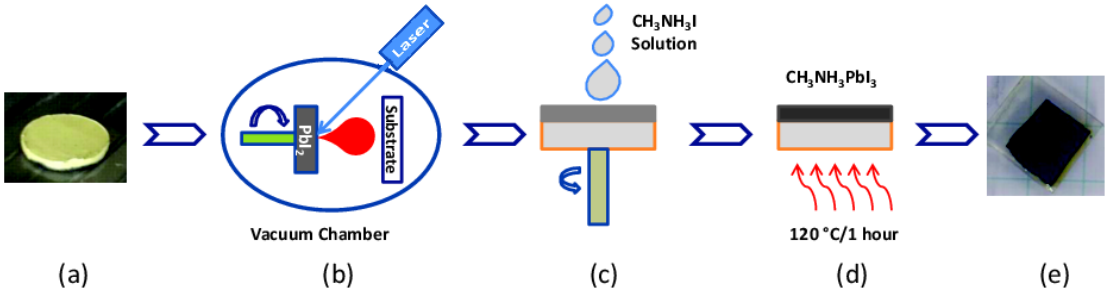

Figure 7.1 The schematic representation of the organic-inorganic perovskite thin film formation via pulsed laser deposition. (a) The PbI_2 target used in this work; (b) PbI_2 thin film is deposited on Si or FTO coated glass substrates by the PLD method in a vacuum chamber; (c) The 2-propanol-based CH_3NH_3I solution is spin-coated onto the PbI_2 thin film; (d) The film is heated at 120 ° for 1 hour to form $CH_3NH_3PbI_3$; (e) The dark $CH_3NH_3PbI_3$ film after annealing.

The fabrication procedure of organic-inorganic perovskite thin films based on our PLD-based hybrid two-step process is schematically shown in Fig. 7.1. It starts with PLD of PbI_2 at room temperature (Step 1) followed by spin coating of MAI with a subsequent annealing (Step 2). Both Si and glass substrates coated with fluorine doped tin oxide (FTO) are used.

To prepare a PLD target, PbI_2 powders were ground in isopropanol (IPA), baked at 100 °C, pressed as a pellet, and then sintered at 120°C under a nitrogen atmosphere for 8 hours. Fig. 7.1(a) shows the finished yellow PbI_2 target used in our work. We optimized the laser energy, the repetition rate, and the distance between the substrate and the target to fabricate a smooth PbI_2 film with a relatively low deposition rate. During the PLD of the PbI_2 target, the distance between the substrate and the target was kept at 5.0 cm and a pulsed excimer laser (KrF; λ = 248 nm) was used with an

energy density of 0.25 J/cm^2 and a repetition rate of 2 Hz. PbI_2 films were deposited on the substrates in vacuum (~3.0×10^{-6} Torr) at room temperature with the deposition rate of ~0.33 nm/pulse. Step 2 (Fig. 7.1(c) and (d)) consisted of spin-coating of MAI and a subsequent thermal annealing process. Here, we use a conventional spin coating method for the MAI deposition following a procedure described in literature.[228] After optimizing the concentration (MAI in isopropanol), the spin speed, and the drying temperature, a 150 µl MAI solution (40 mg/ml) was spin-coated onto a dried PbI_2 film at 1000 rpm, and the film was then dried at 120 °C for 1 hour to form the $CH_3NH_3PbI_3$ as shown in Fig. 7.1(e).

7.4 Results and discussion

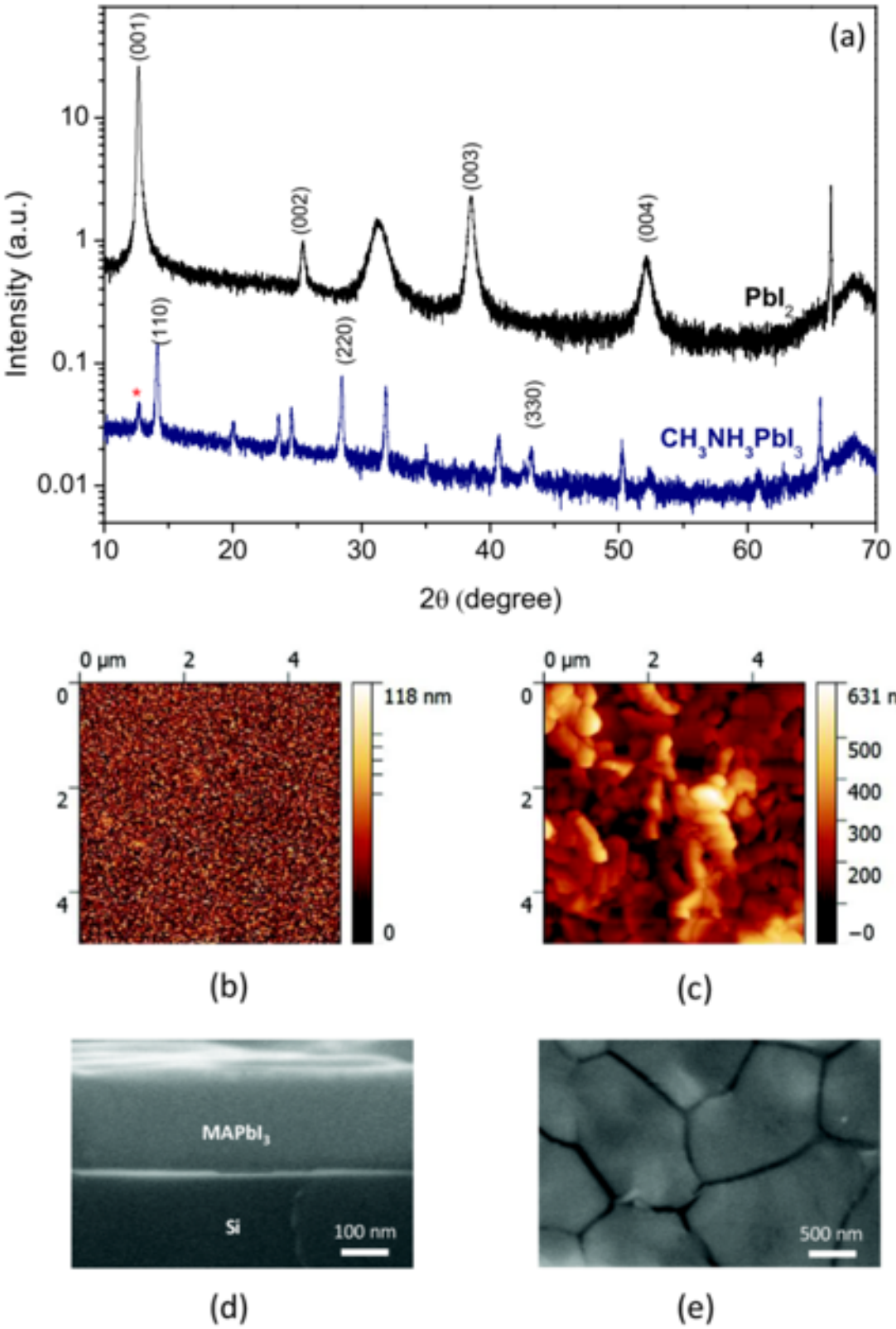

Figure 7.2 X-ray diffraction patterns, AFM and SEM images of PbI_2 and $CH_3NH_3PbI_3$ layers. (a) XRD patterns of PbI_2/Si (top), $CH_3NH_3PbI_3$/Si (bottom); (b) AFM image of PLD PbI_2 film on Si; (c) AFM image of $CH_3NH_3PbI_3$ on Si; (d) and (e) Cross-sectional and top view SEM images of $MAPbI_3$ fabricated on Si via PLD method.

Fig. 7.2(a) shows the X-ray diffraction (XRD) patterns of a PbI_2 film (after PLD) and a $MAPbI_3$ film (after Step 2) on Si substrates. Polycrystalline and highly oriented nature of the PbI_2 films is evident in Fig. 7.2(a) (top), where (00l) peaks of PbI_2 are seen,[229] confirming that the (00l) orientated hexagonal lattice of the PbI_2 crystal [space group: P-3m1(164)] has been generated by the PLD method.

For the perovskite phase formed after Step 2, the main XRD peaks of the film indicate that the tetragonal $CH_3NH_3PbI_3$ film is predominantly (110) oriented (Fig. 7.2(a) (bottom)).[219] A small XRD peak indicated by an asterisk corresponds to the (001) peak of PbI_2, which is possibly due to the decomposition of $CH_3NH_3PbI_3$ in air or due to residual unreacted PbI_2.[206]

We performed atomic force microscopy (AFM) to examine the morphology of our films. A 5 μm × 5 μm AFM image of a PbI_2 film prior to spin-coating of a MAI layer is shown in Fig. 7.2(b). The root mean square (RMS) roughness is 7.74 nm, indicating that relatively smooth PbI_2 thin films can be prepared by PLD at room temperature. The surface morphology of a completed $CH_3NH_3PbI_3$ film (≈220 nm) was found to show significantly larger RMS roughness of 89 nm (Fig. 7.2(c)). This enhanced roughness is due to the volume expansion when the perovskite phase is formed during the intercalation of MAI into the PbI_2 layer.[219] This in-situ growth

process of organic-inorganic perovskite crystal also leads to a substantial increase in the grain size as shown in Fig. 7.2(c).

We further characterized the morphology of our perovskite films by scanning electron microscopy (SEM) (Fig. 7.2(d),(e)). The cross-sectional SEM image of $CH_3NH_3PbI_3$ on Si in Fig. 7.2(d) shows a smooth and a uniform film (220 nm) indicating highly crystalline nature of the organic-inorganic perovskite film. The top-view SEM image shown in Fig. 7.2(e) indicates complete coverage by the film on the Si substrate surface. The typical grain size ranges from ≈800 nm to ≈1,500 nm. Obtaining large grains is very important for the fabrication of high performance devices because large grains can reduce bulk defects and increase the mobility of charge carriers.[230]

The perovskite films were also fabricated on FTO coated glasses using the same method. Following a procedure described in literatrue,[231] a 50 nm poly(3,4-ethylenedioxythiophene):poly(styrenesulphonate) (PEDOT:PSS) layer was first spin-coated onto FTO coated glasses as the hole transport layer in the device. Following the hybrid PLD process illustrated in Fig. 7.1, the perovskite phase was formed on the FTO-glass/PEDOT:PSS.

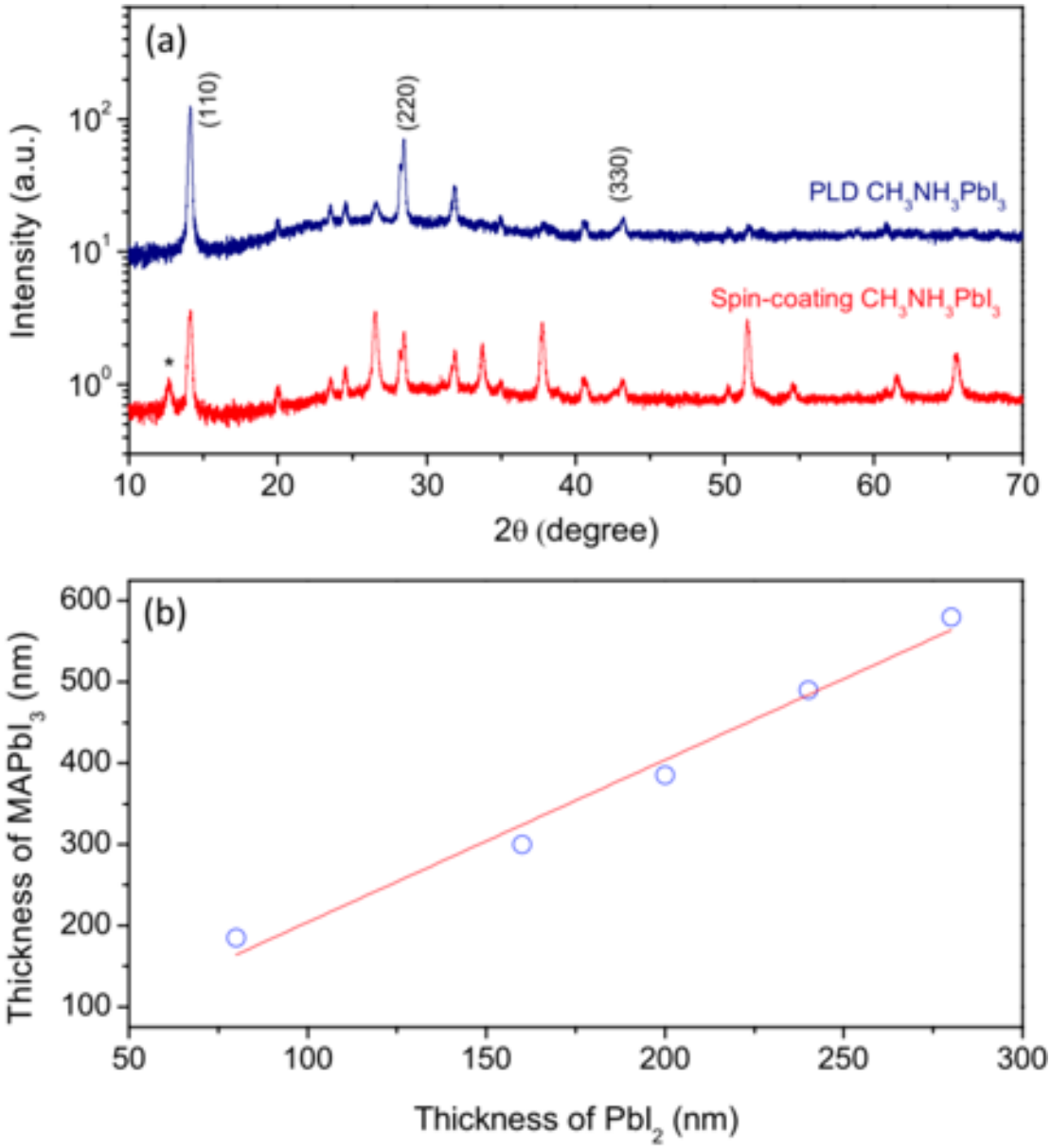

Figure 7.3 X-ray diffraction patterns of (a) $CH_3NH_3PbI_3$ films made by the PLD hybrid method (top) and by standard spin-coating-only method (bottom); (b) Perovskite film thickness as a function of the thickness of the PLD PbI_2 film.

The XRD pattern of a $MAPbI_3$ film (300 nm) fabricated by the PLD-based hybrid method on a FTO coated glass substrate is shown in Fig. 7.3(a) (top). To perform side-by-side comparison of films made by our hybrid method vs. the conventional

method, a $CH_3NH_3PbI_3$ thin film (295 nm) has also been prepared via the standard spin coating of PbI_2 from a dimethylformamide (DMF) solution.[231] The XRD pattern of the latter film is shown in Fig. 7.3(a) (bottom). The comparison shows that the film made by the PLD-based hybrid method is preferentially (110) oriented, whereas the film made by the conventional spin-coating method shows a relatively weak intensity of (110) peaks. Haruyama et al.[232] reported flat terminations on the (110) and the (001) surfaces are important for the PSC performance. Here, the strongly (110) preferred orientation of $CH_3NH_3PbI_3$ made by the hybrid method is attributed to the high quality of the PbI_2 thin film deposited by PLD.

In perovskite thin-film solar cells, a $CH_3NH_3PbI_3$ thin film is used as an absorbing layer. Therefore, the thickness of the $CH_3NH_3PbI_3$ layer is an important device design parameter. To demonstrate precise control of the thickness of the $CH_3NH_3PbI_3$ thin film using the PLD-based hybrid method, we deposited PbI_2 films with different thicknesses and compared them to the thicknesses and the composition of the final $CH_3NH_3PbI_3$ films. When the thickness of the starting PbI_2 thin films is in the range of 80 - 280 nm, the thickness of the final $CH_3NH_3PbI_3$ thin films is found to be in the range of 185 - 580 nm, as determined by profilometry. Interestingly, in all the films synthesized here, the average ratio between the thickness of the $MAPbI_3$ film and the thickness of the starting PbI_2 layer was consistently found to be around 2 (Fig. 7.3(b)). This agrees well with a recent report[219] and suggests that the excess amount of MAI evaporates during the annealing process. Thus, the PLD of PbI_2 precursor allows the fabrication of organic-inorganic perovskite films with a precisely tailored thickness. In addition, we found that we always see a minor XRD peak at 12.6° ((001) peak of

PbI_2) when the thickness of PbI_2 is around 240 nm (and the final $MAPbI_3$ is 490 nm). The intensity of this peak increases with increasing thickness of PbI_2 in Step 1. This is due to the fact that there is not enough MAI solution to convert all the PbI_2 into the perovskite under our current recipe (Step 2). We expect that a further optimized MAI spin-coating step may help achieve a complete conversion.

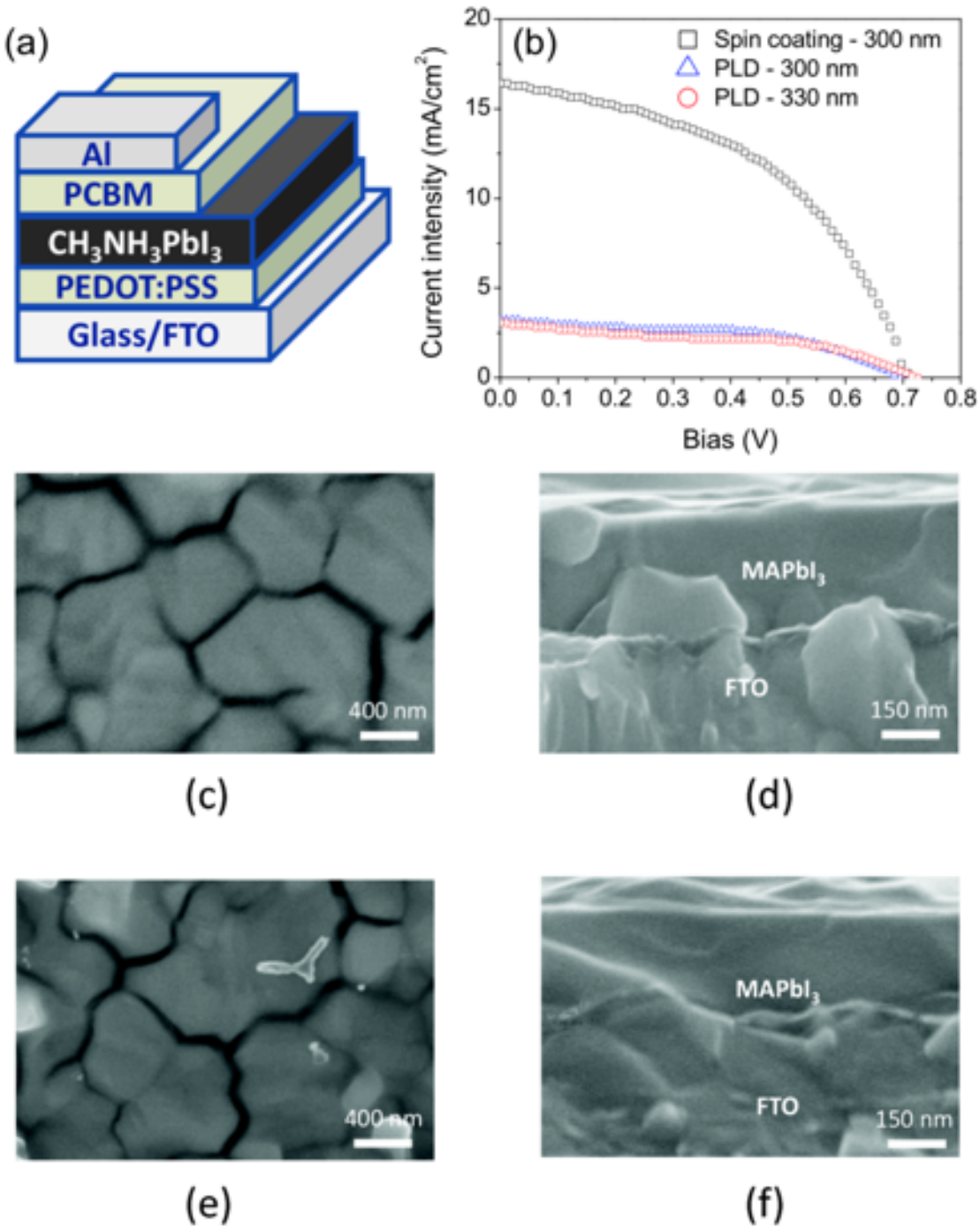

Figure 7.4 Planar devices and their performance (a) Device schematic configuration used for this study; (b) J-V curves obtained from the perovskite solar cells fabricated by PLD method ($MAPbI_3$ layer thicknesses: 300 nm and 330 nm) and conventional spin-coating-only method (300 nm $MAPbI_3$ layer); (c) and (d) Top view and cross sectional SEM images of $MAPbI_3$ in a complete solar cell device fabricated via the

PLD-based method; (e) and (f) Top view and cross sectional view SEM images of $MAPbI_3$ in a complete solar cell device fabricated via conventional spin-coating-only method.

We have fabricated complete cell structures using $MAPbI_3$ films made with our PLD-based hybrid method and also, for comparison, using $MAPbI_3$ films deposited by the conventional spin coating method. In such structures, after the synthesis of a $MAPbI_3$ thin film on PEDOT:PSS coated FTO glasses, an electron transport layer of phenyl-C-butyric acid methyl ester (PCBM) was spin-coated on the surface of $MAPbI_3$, and then a contact electrode of Al was thermally evaporated on the surface of PCBM[231] completing an inverted planar FTO/PEDOT:PSS/$MAPbI_3$/PCBM/Al device structure. A schematic architecture of the device is illustrated in Fig. 7.4(a). The photovoltaic performance was measured at illumination (AM 1.5G, 100 mA/cm^2). The J-V curves are shown in Fig. 7.4(b). PCEs of 1.12% and 1.03% were obtained for two cells made by the PLD method with a $MAPbI_3$ layer of 300 nm and 330 nm, respectively. On the other hand, a relatively high PCE (5.45%) was achieved in a cell fabricated through the conventional spin coating method with a 300 nm $MAPbI_3$.

We show the cross-sectional views and the top-view SEM images of $MAPbI_3$ thin films in the two types of cells (one with PLD-based $MAPbI_3$, and another with standard spin-coating $MAPbI_3$). Both films in top-view images (Fig. 7.4(c)(e)) display closely-packed grains with full coverage on the surface of PEDOT:PSS, and there is little difference in the crystallite shape and size between the two. The cross-sectional SEM images (Fig. 7.4(d), (f)) also show that both films are similar in texture and relatively smooth. Based on the XRD and SEM results, we therefore conclude that

$MAPbI_3$ thin films fabricated by the PLD method are similar in phase purity and crystallinity compared to those fabricated by the standard spin-coating method, despite the difference in the PCE of the devices. From the J-V curves (Fig. 7.4(b)), we found that cells made with PLD have similar V_{oc} and the fill factor as the spin-coating cells. This is suggestive of the fact that the films are uniform and pin-hole free[230-233], and this is consistent with the SEM images. The low PCE is likely due to a dramatically low J_{sc}: a possible reason is that the PEDOT:PSS layer may have deteriorated in the vacuum chamber during the PLD process, reducing the conductivity and resulting in a low J_{sc} and a low V_{oc}. We believe that by further optimizing device parameters and developing materials, achieving higher efficiency values is possible for the PLD-based hybrid deposition process.

7.5 Conclusions

In summary, we have demonstrated a novel hybrid fabrication process that combines PLD of PbI_2 with subsequent spin coating of MAI to prepare continuous, crystalline, uniform, and compact lead iodide perovskite films with a large grain size. We have demonstrated the versatility of the PLD-based hybrid process in synthesizing $CH_3NH_3PbI_3$ thin films with well-controlled thicknesses. A device based on the PLD process showed a PCE of 1.12%. The hybrid technique described in this work provides a new route for low-temperature fabrication of organic-inorganic perovskite thin films for PSCs with rapid crystallization and good film-thickness control.

Chapter 8: Summary and future work

8.1 Summary of results

The work presented in this dissertation focuses on rapid discovery and optimization of novel functional metal oxides in the broad field of energy conversion technologies. In particular, a high-throughput pulsed laser deposition was used to develop functional thin films for a range of applications with an emphasis on their electrochemical properties.

We have successfully demonstrated a PLD-based fabrication of out-of-plane heteroepitaxial thin-film electrochemical devices and the feasibility of using the devices to evaluate single-crystal-like properties of electrolytes for SOFC applications in **Chapter 3**. The electrically conducting SRO and BLSO are promising bottom electrode materials for thin-film SOFC structures, both exhibiting very low equivalent series resistance in the temperature range relevant for SOFCs. Despite their limited thickness compared to conventional bulk devices, the present devices accurately capture the bulk ionic transport properties of thin-film electrolytes at different temperatures and circumvent undesirable influence from the substrates. The model system is also a practical device geometry for miniaturization of electrochemical devices. This part of work may also open up new avenues for investigating the intrinsic/bulk properties of electrochemical materials at the nanoscale level. Because growth of epitaxial buffer layers of $SrTiO_3$ on Si is a well-established technique, an exciting possibility for the future is to directly integrate all epitaxial SOFC micro devices on Si-based platforms.

While thin-film electrolytes have increasingly employed to lower the operating temperatures of SOFCs, the cathode materials become the key factor limiting the overall performance of SOFCs at low operating temperatures. Mixed ionic and electronic conductive perovskites, particularly LSCF materials, have been extensively studied as the most promising cathode materials for SOFCs. However, the mechanisms and rate laws governing exchange of oxygen with the bulk at the surface of LSCF are still poorly understood. In **Chapter 4**, we used the high-throughput pulsed laser deposition approach to fabricate a $La_{0.6}Sr_{0.4}Co_{1-x}Fe_xO_{3-\delta}$ ($0 \leq x \leq 1$) composition gradient thin film on YSZ single crystal substrate, and the geometrically well-defined thin-film microelectrodes were used as a model system to obtain mechanistic information on the oxygen reduction reaction at the surface of SOFC cathodes. The PLD thin film with well-defined geometry can minimize the complexity arising from the morphology of cathode materials used in traditional preparation procedures. A systematic investigation of the influence of the B-site dopant, microelectrode diameter, temperature, and oxygen partial pressure on the oxygen surface exchange resistance (R_s), chemical capacitance (C_{chem}), and the electrical surface oxygen exchange coefficient (k^q) has been performed. The results for $La_{0.6}Sr_{0.4}Co_{1-x}Fe_xO_{3-\delta}$ thin-film microelectrodes have led to elucidating their behavior as a cathode for intermediate temperature SOFCs. For the mixed conducting LSCF, the oxygen reduction reaction follows a bulk path in this work, and the oxygen ionic conductivity ($[V_o^{\cdot\cdot}]$) is an important factor in determining the performance of oxygen surface exchange reaction. The pO_2 dependence of R_s and k^q of the entire LSC-LSF spread film shows consistent results with a m (slope of a log–log plot) in a range of ~0.5 to ~0.75 for R_s and ~0.54

to ~0.65 for k^q. As a result, the oxygen vacancy transport to surface-adsorbed oxygen intermediates is proposed to be the rate-determining step for mixed conducting cathodes. This study also showed the potential of increasing the surface oxygen vacancies (such as surface modification or surface nano-engineering) to develop highly active surface oxygen exchange materials for applications in the field of solid oxide fuel cells and electrolysis cells. A better understanding of the influence of the surface chemical composition on the ORR is needed because surface exchange reactions are highly sensitive to the surface chemistry. For this purpose, more work focused on surface characterizations are in order.

In **Chapter 5**, we demonstrated that exceptional power densities and excellent long-term stability can be achieved in intermediate temperature p-SOFCs by combining the double-perovskite cathode PBSCF and the new electrolyte BZCYYb4411. The double-perovskite PBSCF provides the unique electronic, protonic, and oxygen ionic transporting properties ("triple conducting oxides") under humidified atmosphere. The high capacity of PBSCF to adsorb H_2O at high temperature (Proton concentration: 1.7 mol% at 600 °C) and the excellent ORR performance facilitate the cathodic electrochemical reaction in p-SOFCs. Integrating with the CO_2/H_2O tolerable BZCYYb4411 proton conductor, a maximum peak power density of 1098 mW/cm^2 was achieved at 600 °C. Furthermore, great cell stability has been demonstrated over 700 hours of testing under a constant voltage at 550 °C in humidified H_2. The demonstrated excellent performance of PBSCF based p-SOFCs can pave the way for incorporating fuel cells into a sustainable energy future.

We also used the high-throughput PLD methodology to investigate the phase transition characteristics of VO_2 based materials and demonstrated their potential applications in lithium-ion batteries as discussed in **Chapter 6**. The high-throughput method makes it possible to systematically investigate the role of W dopants on the MIT of VO_2 by eliminating various factors arising from different fabrication methods. The lattice-constant cofactor condition was satisfied by tuning the lattice parameters of VO_2 via W doping, verified by a minimum hysteresis width at 2.4 W% for both polycrystalline and epitaxial films. This is the first time the cofactor condition was satisfied experimentally in an oxide system. These findings not only emphasize the impact of crystal structures on the MIT of VO_2 but also guide us to control and optimize the hysteresis behavior of various physical properties in functional materials. We have demonstrated that the rutile $V_{1-x}W_xO_2$ thin film can be used as a dual functional thin-film cathode in LIBs with a high capacity of ~140 mA h/g using a $V_{0.976}W_{0.024}O_2$ thin-film cathode. We are developing a screening methodology for rapid discovery of cathode materials in LIBs.

As another application of PLD for energy materials, we have demonstrated a novel hybrid fabrication process that combines PLD of PbI_2 with subsequent spin coating of MAI to prepare continuous, crystalline, uniform, and compact lead iodide perovskite films with a large grain size as shown in **Chapter 7**. We have demonstrated the versatility of the PLD-based hybrid process in synthesizing $CH_3NH_3PbI_3$ thin films with well-controlled thicknesses. A device based on the PLD process showed a PCE of 1.12%. The hybrid technique described in this work provides a new route for low-

temperature fabrication of organic-inorganic perovskite thin films for PSCs with rapid crystallization and good film-thickness control.

8.2 Future work

8.2.1 Proton conducting electrolytes

One promising approach to reduce the operation temperatures of SOFCs is to develop proton conductors which show higher conductivity than oxide ion conductors especially at intermediate temperatures. High proton transport in doped barium zirconate has been known for over a decade, but this material had showed low performance within the intermediate temperature range due to the high impedance of its grain boundaries.[234] Based on our thin-film electrolyte evaluation method developed in **Chapter 3**, we propose to investigate the proton conductivities of $BaREZr_{1-x}Ce_xO_3$-$BaZr_{1-x}Ce_xO_3$ (RE=Y, Yb, and Ho) libraries in the intermediate temperature range. The rare earth elements, such as Y, Yb, and Ho, are chosen because of their multivalent oxidation states that can promote electronic conduction, low third ionization potential, and an ionic radius comparable with that of zirconium/cerium.

The goal is to improve the proton conductivity and stability of the materials and predict new materials by understanding how the dopants affect the conductivity and stability of $BaZrO_3$ and $BaCeO_3$ based materials.

Appendices

A1. Supplementary information for Chapter 7

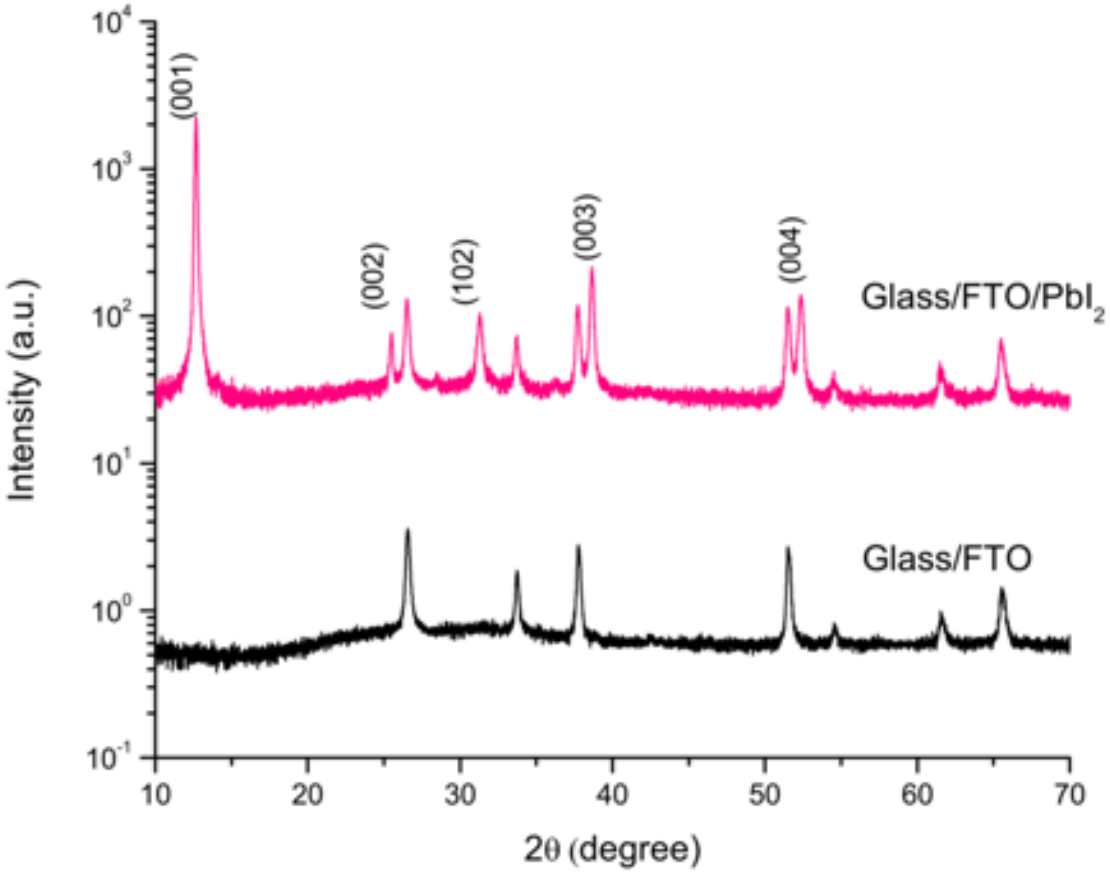

Figure S1. XRD patterns of bare FTO coated glass and PbI_2 on FTO coated glass.

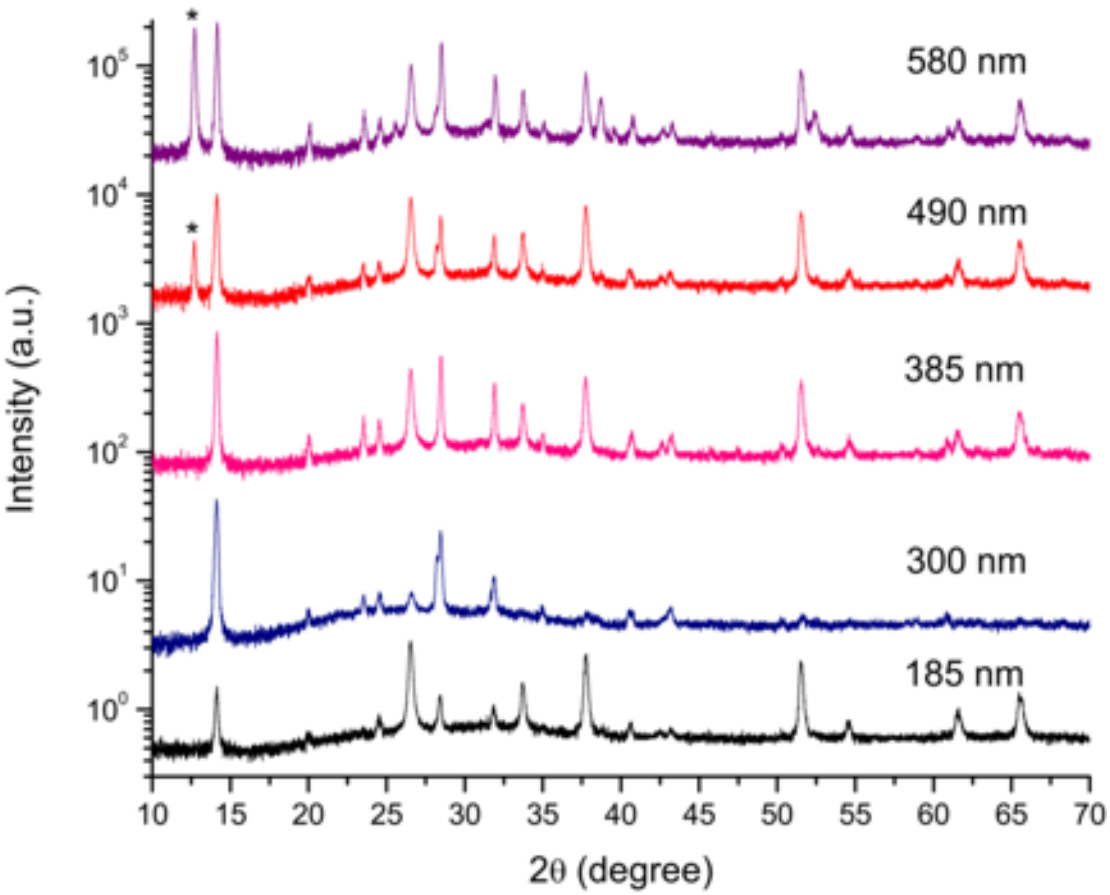

Figure S2. XRD patterns of the $CH_3NH_3PbI_3$ films with varying thickness on FTO coated glasses.

Device	V_{oc} (v)	J_{sc}(mA/cm²)	FF	PCE(%)
PLD-300	0.69	3.22	0.50	1.12
PLD-330	0.72	3.06	0.47	1.03
Spin coating	0.71	16.29	0.47	5.45

Table S1. The photovoltaic parameters of PLD perovskite solar cells and conventional spin-coating perovskite solar cell. Device configuration: glass/FTO/PEDOT:PSS/$CH_3NH_3PbI_3$/PCBM/Al.

A2. Publications Related to This Dissertation

1. **Y. Liang**; Y. Yao; X. Zhang; W-L Hsu *et al.* "Fabrication of organic-inorganic perovskite thin films for planar solar cells via pulsed laser deposition," *AIP ADVANCES*, 2016, 6, 015001.
2. S. Lee; X. Zhang; **Y. Liang**; S. Fackler *et al.* "Observation of the superconducting proximity effect in the surface state of SmB_6 thin films," *PHYSICAL REVIEW X*, 2016, 6, 031031.
3. S. Choi; C. Kucharczyk; **Y. Liang**; X. Zhang *et al.* "Exceptional power density and stability at intermediate temperatures in protonic ceramic fuel cells," *NATURE ENERGY,* 2018, 3, 202-210.
4. **Y. Liang**; X. Zhang; C. Kucharczyk; R. Huang *et al.* "Out-of-plane electrochemical transport in all-thin-film heteroepitaxial solid oxide fuel cell structures," manuscript almost completed, will be submitted to *ACS Applied Materials & Interfaces*.
5. **Y. Liang**; S. Lee; X. Zhang; I. Takeuchi *et al.* "Discovery of the ultra-compatible phase transition in $V_{1-x}W_xO_2$," manuscript in preparation.
6. C. Kucharczyk; **Y. Liang**; S. Choi *et al.* "Electrochemical characterization of complete $La_{0.6}Sr_{0.4}Co_{1-x}Fe_xO_{3-\delta}$ composition phase space by microelectrode impedance spectroscopy," manuscript in preparation.

Bibliography

[1] U.S.E.I. Administration, *Annual Energy Outlook 2017 with Projections to 2050* (Createspace Independent Publishing Platform, 2017).
[2] G.P.A. Bongaerts and R. De Abreu, Innovative Energy Policies **2**, 1 (2012).
[3] E.D. Wachsman and S.C. Singhal, *Solid Oxide Fuel Cell Commercialization, Research, and Challenges* (The Electrochemical Society Interface, 2009).
[4] E.M. Erickson, F. Schipper, T.R. Penki, J.-Y. Shin, C. Erk, F.-F. Chesneau, B. Markovsky, and D. Aurbach, J. Electrochem. Soc. **164**, A6341 (2017).
[5] Z. Yang, C. Ko, and S. Ramanathan, Annu. Rev. Mater. Res. **41**, 337 (2011).
[6] H. Koinuma and I. Takeuchi, Nature Materials **3**, 429 (2004).
[7] K.S. Chang, M.A. Aronova, C.L. Lin, M. Murakami, M.H. Yu, J. Hattrick-Simpers, O.O. Famodu, S.Y. Lee, R. Ramesh, M. Wuttig, I. Takeuchi, C. Gao, and L.A. Bendersky, Appl. Phys. Lett. **84**, 3091 (2004).
[8] Y. Liang, Y. Yao, X. Zhang, W.-L. Hsu, Y. Gong, J. Shin, E.D. Wachsman, M. Dagenais, and I. Takeuchi, AIP Advances **6**, 015001 (2016).
[9] X. Yu, T.J. Marks, and A. Facchetti, Nature Materials **15**, 383 (2016).
[10] J. García-Barriocanal, A. Rivera-Calzada, M. Varela, Z. Sefrioui, E. Iborra, C. León, S.J. Pennycook, and J. Santamaria, Science **321**, 676 (2008).
[11] S. Sanna, V. Esposito, D. Pergolesi, A. Orsini, A. Tebano, S. Licoccia, G. Balestrino, and E. Traversa, Adv. Funct. Mater. **19**, 1713 (2009).
[12] M. Lorenz and M.S.R. Rao, Journal of Physics D: Applied Physics **47**, (2014).
[13] D.J.L. Brett, A. Atkinson, N.P. Brandon, and S.J. Skinner, Chem. Soc. Rev. **37**, 1568 (2008).
[14] M. Irshad, K. Siraj, R. Raza, A. Ali, P. Tiwari, B. Zhu, A. Rafique, A. Ali, M. Kaleem Ullah, and A. Usman, Applied Sciences **6**, 75 (2016).
[15] Z. Gao, L.V. Mogni, E.C. Miller, J.G. Railsback, and S.A. Barnett, Energy & Environmental Science **9**, 1602 (2016).
[16] L. Malavasi, C.A.J. Fisher, and M.S. Islam, Chem. Soc. Rev. **39**, 4370 (2010).
[17] N. Mahato, A. Banerjee, A. Gupta, S. Omar, and K. Balani, Progress in Materials Science **72**, 141 (2015).
[18] S.A. Hajimolana and M. Soroush, Industrial & Engineering Chemistry Research **48**, 6112 (2009).
[19] E.D. Wachsman and K.T. Lee, Science **334**, 935 (2011).
[20] E. Fabbri, L. Bi, D. Pergolesi, and E. Traversa, Adv. Mater. **24**, 195 (2011).
[21] M. Tsuchiya, B.-K. Lai, and S. Ramanathan, Nature Nanotechnology **6**, 282 (2011).
[22] K. Kerman, A. Luntz, V. Viswanathan, Y.-M. Chiang, and Z. Chen, J. Electrochem. Soc. **164**, A1731 (2017).
[23] E.C.C. de Souza and R. Muccillo, Materials Research **13**, 385 (2010).
[24] A. Evans, A. Bieberle-Hütter, J.L.M. Rupp, and L.J. Gauckler, Journal of Power Sources **194**, 119 (2009).
[25] X. Chen, N.J. Wu, L. Smith, and A. Ignatiev, Appl. Phys. Lett. **84**, 2700 (2004).
[26] G.M. Rupp, A.K. Opitz, A. Nenning, A. Limbeck, and J. Fleig, Nature Materials **16**, 640 (2017).
[27] H.M. Christen and G. Eres, J. Phys.: Condens. Matter **20**, 264005 (2008).

[28] H.M. Christen and G. Eres, J. Phys.: Condens. Matter **20**, 264005 (2008).
[29] D. Dijkkamp, T. Venkatesan, X.D. Wu, S.A. Shaheen, N. Jisrawi, Y.H. Min Lee, W.L. McLean, and M. Croft, Appl. Phys. Lett. **51**, 619 (1987).
[30] C. Ma and C. Chen, *Pulsed Laser Deposition for Complex Oxide Thin Film and Nanostructure* (Wiley-VCH Verlag GmbH & Co. KGaA, Weinheim, Germany, 2016), pp. 1–31.
[31] H. Koinuma, H.N. Aiyer, and Y. Matsumoto, Science and Technology of Advanced Materials **1**, 1 (2008).
[32] X.D. Xiang, X. Sun, G. Briceno, Y. Lou, K.A. Wang, H. Chang, W.G. Wallace-Freedman, S.W. Chen, and P.G. Schultz, Science **268**, 1738 (1995).
[33] J.H.N.F.A.D.C. Technical1996, Pdfs.Semanticscholar.org (n.d.).
[34] J.M. Gregoire, D.G. Van Campen, C.E. Miller, R.J.R. Jones, S.K. Suram, and A. Mehta, J Synchrotron Radiat **21**, 1262 (2014).
[35] D. Chateigner, J Appl Crystallogr **39**, 925 (2006).
[36] P. Eaton and P. West, *Atomic Force Microscopy* (Oxford University Press, 2010).
[37] M.E. Orazem and B. Tribollet, *Electrochemical Impedance Spectroscopy* (John Wiley & Sons, 2017).
[38] W. Lai and S.M. Haile, J American Ceramic Society **88**, 2979 (2005).
[39] M. Kubicek, T.M. Huber, A. Welzl, A. Penn, G.M. Rupp, J. Bernardi, M. Stöger-Pollach, H. Hutter, and J. Fleig, Solid State Ionics **256**, 38 (2014).
[40] B.E. McNealy, J. Jiang, and J.L. Hertz, J. Electrochem. Soc. **162**, F537 (2015).
[41] S. Ji, G.Y. Cho, W. Yu, P.-C. Su, M.H. Lee, and S.W. Cha, ACS Appl. Mater. Interfaces **7**, 2998 (2015).
[42] K. Kerman, B.-K. Lai, and S. Ramanathan, Adv. Energy Mater. **2**, 656 (2012).
[43] P.-C. Su, C.-C. Chao, J.H. Shim, R. Fasching, and F.B. Prinz, Nano Lett. **8**, 2289 (2008).
[44] J.H. Shim, C.-C. Chao, H. Huang, and F.B. Prinz, Chem. Mater. **19**, 3850 (2007).
[45] D. Beckel, A. Bieberle-Hütter, A. Harvey, A. Infortuna, U.P. Muecke, M. Prestat, J.L.M. Rupp, and L.J. Gauckler, Journal of Power Sources **173**, 325 (2007).
[46] R.M. Ormerod, Chem. Soc. Rev. **32**, 17 (2002).
[47] Y. Shi, A.H. Bork, S. Schweiger, and J.L.M. Rupp, Nature Materials **14**, 721 (2015).
[48] J. Santiso and M. Burriel, J Solid State Electrochem **15**, 985 (2010).
[49] R.A. De Souza and A.H.H. Ramadan, Physical Chemistry Chemical Physics **15**, 4505 (2013).
[50] X. Guo, Science **324**, 465 (2009).
[51] E.M. Mills, M. Kleine-Boymann, J. Janek, H. Yang, N.D. Browning, Y. Takamura, and S. Kim, Physical Chemistry Chemical Physics **18**, 10486 (2016).
[52] M. Gerstl, E. Navickas, G. Friedbacher, F. Kubel, M. Ahrens, and J. Fleig, Solid State Ionics **185**, 32 (2011).
[53] D. Roehrens, U. Packbier, Q. Fang, L. Blum, D. Sebold, M. Bram, and N. Menzler, Materials **9**, 762 (2016).
[54] U.P. Muecke, D. Beckel, A. Bernard, A. Bieberle-Hütter, S. Graf, A. Infortuna, P. Müller, J.L.M. Rupp, J. Schneider, and L.J. Gauckler, Adv. Funct. Mater. **18**, 3158 (2008).

[55] K. van de Ruit, I. Katsouras, D. Bollen, T. van Mol, R.A.J. Janssen, D.M. de Leeuw, and M. Kemerink, Adv. Funct. Mater. **23**, 5787 (2013).
[56] G. Baure, R.M. Kasse, N.G. Rudawski, and J.C. Nino, Physical Chemistry Chemical Physics **17**, 12259 (2015).
[57] E. Navickas, M. Gerstl, G. Friedbacher, F. Kubel, and J. Fleig, Solid State Ionics **211**, 58 (2012).
[58] V. Esposito, D. Pergolesi, S. Sanna, A. Tebano, P.G. Medaglia, S. Licoccia, G. Balestrino, and E. Traversa, in *10th International Symposium on Solid Oxide Fuel Cells (SOFC-X)* (ECS, 2007), pp. 891–898.
[59] S.H. Choi, C.S. Hwang, and M.H. Lee, ECS Electrochemistry Letters **3**, F57 (2014).
[60] P. Blennow, K.K. Hansen, L.R. Wallenberg, and M. Mogensen, Solid State Ionics **180**, 63 (2009).
[61] S.M. Yang, S. Lee, J. Jian, W. Zhang, P. Lu, Q. Jia, H. Wang, T.W. Noh, S.V. Kalinin, and J.L. MacManus-Driscoll, Nature Communications **6**, 8588 (2015).
[62] S. Cho, C. Yun, S. Tappertzhofen, A. Kursumovic, S. Lee, P. Lu, Q. Jia, M. Fan, J. Jian, H. Wang, S. Hofmann, and J.L. MacManus-Driscoll, Nature Communications **7**, 1 (2016).
[63] Y. Hikita, Y. Kozuka, T. Susaki, H. Takagi, and H.Y. Hwang, Appl. Phys. Lett. **90**, 143507 (2007).
[64] A. Ruotolo, C.Y. Lam, W.F. Cheng, K.H. Wong, and C.W. Leung, Phys. Rev. B **76**, 075122 (2007).
[65] F. Borgatti, C. Park, A. Herpers, F. Offi, R. Egoavil, Y. Yamashita, A. Yang, M. Kobata, K. Kobayashi, J. Verbeeck, G. Panaccione, and R. Dittmann, Nanoscale **5**, 3954 (2013).
[66] S. Takeuchi, H. Tan, K.K. Bharathi, G.R. Stafford, J. Shin, S. Yasui, I. Takeuchi, and L.A. Bendersky, ACS Appl. Mater. Interfaces **7**, 7901 (2015).
[67] M. Abuwasib, H. Lee, A. Gruverman, C.-B. Eom, and U. Singisetti, Appl. Phys. Lett. **107**, 242905 (2015).
[68] A. Ito, H. Masumoto, and T. Goto, Materials Transactions **48**, 227 (2007).
[69] E. Vasco, R. Dittmann, S. Karthäuser, and R. Waser, Appl. Phys. Lett. **82**, 2497 (2003).
[70] D. Rubi, A.H.G. Vlooswijk, and B. Noheda, Thin Solid Films **517**, 1904 (2009).
[71] A.S. Daryapurkar, J.T. Kolte, and P. Gopalan, J Mater Sci: Mater Electron **24**, 4698 (2013).
[72] H.N. Lee, H.M. Christen, M.F. Chisholm, C.M. Rouleau, and D.H. Lowndes, Appl. Phys. Lett. **84**, 4107 (2004).
[73] B. Hadjarab, A. Bouguelia, A. Benchettara, and M. Trari, Journal of Alloys and Compounds **461**, 360 (2008).
[74] L. Zhu, J. Ye, X. Zhang, H. Zheng, G. Liu, X. Pan, and S. Dai, Journal of Materials Chemistry a: Materials for Energy and Sustainability **5**, 3675 (2017).
[75] P.V. Wadekar, J. Alaria, M. O'Sullivan, N.L.O. Flack, T.D. Manning, L.J. Phillips, K. Durose, O. Lozano, S. Lucas, J.B. Claridge, and M.J. Rosseinsky, arXiv **cond-mat.mtrl-sci**, (2014).
[76] A.M. Hussain, K.-J. Pan, I.A. Robinson, T. Hays, and E.D. Wachsman, J. Electrochem. Soc. **163**, F1198 (2016).

[77] W.C. Chueh and S.M. Haile, Physical Chemistry Chemical Physics **11**, 8144 (2009).
[78] Y.-P. Fu, S.-B. Wen, and C.-H. Lu, J American Ceramic Society **91**, 127 (2007).
[79] R. Sayers, N.L.O. Flack, J. Alaria, P.A. Chater, R.G. Palgrave, S.R.C. McMitchell, S. Romani, Q.M. Ramasse, T.J. Pennycook, and M.J. Rosseinsky, Chem. Sci. **4**, 2403 (2013).
[80] M.W. Denhoff, Journal of Physics D: Applied Physics **39**, 1761 (2006).
[81] J. Newman, J. Electrochem. Soc. **113**, 501 (1966).
[82] H.L. Frandsen, P.V. Hendriksen, S. Koch, and K.K. Hansen, J. Electrochem. Soc. **164**, E3035 (2017).
[83] W. Franks, I. Schenker, P. Schmutz, and A. Hierlemann, IEEE Transactions on Biomedical Engineering **52**, 1295 (2005).
[84] M. Ahmad, T. Ganguli, S. Patil, S. Major, Y.G.K. Patro, and B.M. Arora, Solid-State Electronics **38**, 1437 (1995).
[85] B.C.H. Steele and A. Heinzel, Nature **414**, 345 (2001).
[86] F. Giannici, G. Gregori, C. Aliotta, A. Longo, J. Maier, and A. Martorana, Chem. Mater. **26**, 5994 (2014).
[87] R.E. Usiskin, S. Maruyama, C.J. Kucharczyk, I. Takeuchi, and S.M. Haile, Journal of Materials Chemistry a: Materials for Energy and Sustainability **3**, 19330 (2015).
[88]J. Appl. Phys. **117**, 103107 (2015).
[89] P.L. Bach, S.R. Saha, K. Kirshenbaum, J. Paglione, and R.L. Greene, Phys. Rev. B **83**, 237 (2011).
[90] X. Guo, J. Fleig, and J. Maier, J. Electrochem. Soc. **148**, J50 (2001).
[91] J.C. Dyre, P. Maass, B. Roling, and D.L. Sidebottom, Reports on Progress in Physics **72**, (2009).
[92] S. Lee, W. Zhang, F. Khatkhatay, Q. Jia, H. Wang, and J.L. MacManus-Driscoll, Adv. Funct. Mater. **25**, 4328 (2015).
[93] A. Dunst, V. Epp, I. Hanzu, S.A. Freunberger, and M. Wilkening, Energy Environ. Sci. **7**, 2739 (2014).
[94] K.J. Moreno, G. Mendoza-Suárez, A.F. Fuentes, J. García-Barriocanal, C. León, and J. Santamaria, Phys. Rev. B **71**, 470 (2005).
[95] D. Pergolesi, V. Roddatis, E. Fabbri, C.W. Schneider, T. Lippert, E. Traversa, and J.A. Kilner, Science and Technology of Advanced Materials **16**, 1 (2015).
[96] S. Kim and J. Maier, J. Electrochem. Soc. **149**, J73 (2002).
[97] S.R. Singamaneni, J.T. Prater, and J. Narayan, Applied Physics Reviews **3**, 031301 (2016).
[98] Z. Gao, L.V. Mogni, E.C. Miller, J.G. Railsback, and S.A. Barnett, Energy & Environmental Science **9**, 1602 (2016).
[99] L. Wang, R. Merkle, Y.A. Mastrikov, E.A. Kotomin, and J. Maier, J. Mater. Res. **27**, 2000 (2012).
[100] T. Ishihara, J. Korean Ceram. Soc **53**, 469 (2016).
[101] S.B. Adler, Chem. Rev. **104**, 4791 (2004).
[102] C. Fu, K. Sun, N. Zhang, X. Chen, and D. Zhou, Electrochimica Acta **52**, 4589 (2007).
[103] Y. Orikasa, T. Nakao, M. Oishi, T. Ina, A. Mineshige, K. Amezawa, H. Arai, Z. Ogumi, and Y. Uchimoto, J. Mater. Chem. **21**, 14013 (2011).

[104] M. Liu, D. Ding, K. Blinn, X. Li, L. Nie, and M. Liu, International Journal of Hydrogen Energy **37**, 8613 (2020).
[105] E. Mostafavi, A. Babaei, and A. Ataie, Iranian Journal of Hydrogen & Fuel Cell **1**, 239 (2015).
[106] G.-H. Zhou, X.-Z. Fu, J.-L. Luo, K.T. Chuang, and A.R. Sanger, Materials Technology **28**, 3 (2013).
[107] 3.6. US Patent 31967, Google Patents
(n.d.).
[108] R. Eason, *Pulsed Laser Deposition of Thin Films* (John Wiley & Sons, 2007).
[109] J.B. Yang, W.B. Yelon, W.J. James, Z. Chu, M. Kornecki, Y.X. Xie, X.D. Zhou, H.U. Anderson, A.G. Joshi, and S.K. Malik, Phys. Rev. B **66**, 583 (2002).
[110] M. Irshad, K. Siraj, R. Raza, A. Ali, P. Tiwari, B. Zhu, A. Rafique, A. Ali, M. Kaleem Ullah, and A. Usman, Applied Sciences **6**, 75 (2016).
[111] F. BAUMANN, J. Fleig, H. HABERMEIER, and J. Maier, Solid State Ionics **177**, 1071 (2006).
[112] G.M. Rupp, A. Schmid, A. Nenning, and J. Fleig, J. Electrochem. Soc. **163**, F564 (2016).
[113] M. Mosleh, M. Sogaard, and P.V. Hendriksen, J. Electrochem. Soc. **156**, B441 (2009).
[114] E.N. Armstrong, K.L. Duncan, and E.D. Wachsman, Physical Chemistry Chemical Physics **15**, 2298 (2013).
[115] A. Giuliano, M.P. Carpanese, D. Clematis, M. Boaro, A. Pappacena, F. Deganello, L.F. Liotta, and A. Barbucci, J. Electrochem. Soc. **164**, F3114 (2017).
[116] D. Lee, Y.-L. Lee, A. Grimaud, W.T. Hong, M.D. Biegalski, D. Morgan, and Y. Shao-Horn, J. Phys. Chem. C **118**, 14326 (2014).
[117] G.J. la O, S.-J. Ahn, E. Crumlin, Y. Orikasa, M.D. Biegalski, H.M. Christen, and Y. Shao-Horn, Angew. Chem. Int. Ed. **49**, 5344 (2010).
[118] H. Chiba, K. Yashiro, S.-I. Hashimoto, and T. Kawada, ECS Transactions **75**, 69 (2017).
[119] G.J. la O and Y. Shao-Horn, J. Electrochem. Soc. **156**, B816 (2009).
[120] Y. Fukuda, S.-I. Hashimoto, K. Sato, K. Yashiro, and J. Mizusaki, in *216th ECS Meeting* (ECS, 2009), pp. 2375–2380.
[121] E.J. Crumlin, E. Mutoro, S.-J. Ahn, G.J. la O, D.N. Leonard, A. Borisevich, M.D. Biegalski, H.M. Christen, and Y. Shao-Horn, J. Phys. Chem. Lett. **1**, 3149 (2010).
[122] M. Krauz, M. Radecka, and M. Rękas, Materiały Ceramiczne (2011).
[123] S. ADLER, X. Chen, and J. WILSON, Journal of Catalysis **245**, 91 (2007).
[124] J.E. ten Elshof, M.H.R. Lankhorst, and H.J.M. Bouwmeester, J. Electrochem. Soc. **144**, 1060 (1997).
[125] E. Fabbri, D. Pergolesi, and E. Traversa, Chem. Soc. Rev. **39**, 4355 (2010).
[126] N.T.Q. Nguyen and H.H. Yoon, Journal of Power Sources **231**, 213 (2013).
[127] C. Duan, J. Tong, M. Shang, S. Nikodemski, M. Sanders, S. Ricote, A. Almansoori, and R. O'Hayre, Science **349**, 1321 (2015).
[128] S.H. Nien, C.S. Hsu, C.L. Chang, and B.H. Hwang, Fuel Cells **11**, 178 (2011).
[129] K. Bae, D.Y. Jang, H.J. Choi, D. Kim, J. Hong, B.-K. Kim, J.-H. Lee, J.-W. Son, and J.H. Shim, Nature Communications **8**, 1 (1AD).
[130] Q.L. Liu, K.A. Khor, and S.H. Chan, Journal of Power Sources **161**, 123 (2006).

[131] W. Sun, Z. Shi, S. Fang, L. Yan, Z. Zhu, and W. Liu, International Journal of Hydrogen Energy **35**, 7925 (2010).
[132] S. Choi, S. Yoo, J. Kim, S. Park, A. Jun, S. Sengodan, J. Kim, J. Shin, H.Y. Jeong, Y. Choi, G. Kim, and M. Liu, Nature Publishing Group **3**, 305 (2013).
[133] E. Fabbri, I. Markus, L. Bi, D. Pergolesi, and E. Traversa, Solid State Ionics **202**, 30 (2011).
[134] D. Han, Y. Okumura, Y. Nose, and T. Uda, Solid State Ionics **181**, 1601 (2010).
[135] Z. Wang, M. Liu, W. Sun, D. Ding, Z. Lü, and M. Liu, Electrochemistry Communications **27**, 19 (2013).
[136] A. Grimaud, F. Mauvy, J. Marc Bassat, S. Fourcade, M. Marrony, and J. Claude Grenier, J. Mater. Chem. **22**, 16017 (2012).
[137] A. Grimaud, F. Mauvy, J.M. Bassat, S. Fourcade, L. Rocheron, M. Marrony, and J.C. Grenier, J. Electrochem. Soc. **159**, B683 (2012).
[138] R. Strandbakke, V.A. Cherepanov, A.Y. Zuev, D.S. Tsvetkov, C. Argirusis, G. Sourkouni, S. Prünte, and T. Norby, Solid State Ionics **278**, 120 (2015).
[139] D. Poetzsch, R. Merkle, and J. Maier, Faraday Discussions **182**, 129 (2015).
[140] J. Kim, S. Sengodan, G. Kwon, D. Ding, J. Shin, M. Liu, and G. Kim, ChemSusChem **7**, 2811 (2014).
[141] S. Choi, J. Shin, and G. Kim, Journal of Power Sources **201**, 10 (2012).
[142] G. Kim, S. Wang, A.J. Jacobson, L. Reimus, P. Brodersen, and C.A. Mims, J. Mater. Chem. **17**, 2500 (2007).
[143] S. Yoo, S. Choi, J. Kim, J. Shin, and G. Kim, Electrochimica Acta **100**, 44 (2013).
[144] J.-H. Kim, M. Cassidy, J.T.S. Irvine, and J. Bae, Chem. Mater. **22**, 883 (2010).
[145] A. Jun, S. Yoo, Y.-W. Ju, J. Hyodo, S. Choi, H.Y. Jeong, J. Shin, T. Ishihara, T.-H. Lim, and G. Kim, Journal of Materials Chemistry a: Materials for Energy and Sustainability **3**, 15082 (2015).
[146] J.-H. Kim and A. Manthiram, Journal of Materials Chemistry a: Materials for Energy and Sustainability **3**, 24195 (2015).
[147] D. Jeong, A. Jun, Y.-W. Ju, J. Hyodo, J. Shin, T. Ishihara, T.-H. Lim, and G. Kim, Energy Technol. **5**, 1337 (2017).
[148] J.H. Kim, F. Prado, and A. Manthiram, J. Electrochem. Soc. **155**, B1023 (2008).
[149] M. Burriel, J. Peña-Martínez, R.J. Chater, S. Fearn, A.V. Berenov, S.J. Skinner, and J.A. Kilner, Chem. Mater. **24**, 613 (2011).
[150] D. Hashimoto, D. Han, and T. Uda, Solid State Ionics **262**, 687 (2014).
[151] S. Choi, S. Yoo, J. Kim, S. Park, A. Jun, S. Sengodan, J. Kim, J. Shin, H.Y. Jeong, Y. Choi, G. Kim, and M. Liu, Nature Publishing Group **3**, 305 (2013).
[152] Y. Yamazaki, P. Babilo, and S.M. Haile, Chem. Mater. **20**, 6352 (2008).
[153] Y. Yamazaki, C.-K. Yang, and S.M. Haile, Scripta Materialia **65**, 102 (2011).
[154] R. Zohourian, R. Merkle, and J. Maier, Solid State Ionics **299**, 64 (2017).
[155] N. Hildenbrand, B.A. Boukamp, P. Nammensma, and D.H.A. Blank, Solid State Ionics **192**, 12 (2011).
[156] F.J. Morin, Physical Review Letters **3**, 34 (1959).
[157] J.D. Budai, J. Hong, M.E. Manley, E.D. Specht, C.W. Li, J.Z. Tischler, D.L. Abernathy, A.H. Said, B.M. Leu, L.A. Boatner, R.J. McQueeney, and O. Delaire, Nature **515**, 535 (2014).
[158] J.G. Ramírez, A. Sharoni, Y. Dubi, M.E. Gómez, and I.K. Schuller, Phys. Rev. B

79, 277 (2009).
[159] M. Nakano, K. Shibuya, D. Okuyama, T. Hatano, S. Ono, M. Kawasaki, Y. Iwasa, and Y. Tokura, Nature **487**, 459 (2012).
[160] J.H. Park, J.M. Coy, T.S. Kasirga, C. Huang, Z. Fei, S. Hunter, and D.H. Cobden, Nature **500**, 431 (2013).
[161] B.G. Chae, D.H. Youn, H.T. Kim, S.L. Maeng, and K.Y. Kang, Journal of the Korean Physical Society **44**, 884 (2004).
[162] S. Lee, I.N. Ivanov, J.K. Keum, and H.N. Lee, Sci Rep **6**, 19621 (2016).
[163] T. Wang, D. Torres, F.E. Fernández, A.J. Green, C. Wang, and N. Sepúlveda, ACS Nano **9**, 4371 (2015).
[164] A.M. Makarevich, I.I. Sadykov, D.I. Sharovarov, V.A. Amelichev, A.A. Adamenkov, D.M. Tsymbarenko, A.V. Plokhih, M.N. Esaulkov, P.M. Solyankin, and A.R. Kaul, Journal of Materials Chemistry C **3**, 9197 (2015).
[165] Y.-B. Kang, Journal of the European Ceramic Society **32**, 3187 (2012).
[166] M.E.A. Warwick and R. Binions, J. Mater. Chem. A **2**, 3275 (2014).
[167] N.I. Zheludev and Y.S. Kivshar, Nature Materials **11**, 917 (2012).
[168] E. Baudrin, G. Sudant, D. Larcher, B. Dunn, and J.-M. Tarascon, Chem. Mater. **18**, 4369 (2006).
[169] Z. Li, J. Wu, Z. Hu, Y. Lin, Q. Chen, Y. Guo, Y. Liu, Y. Zhao, J. Peng, W. Chu, Y. Xie, and C. Wu, Nature Communications **8**, 1 (2017).
[170] N.B. Aetukuri, Nature Physics **9**, 661 (2013).
[171] W.-K. Hong, S. Cha, J.I. Sohn, and J.M. Kim, Journal of Nanomaterials **2015**, 1 (2015).
[172] Y. Wu, L. Fan, W. Huang, S. Chen, S. Chen, F. Chen, C. Zou, and Z. Wu, Physical Chemistry Chemical Physics **16**, 17705 (2014).
[173] H. Asayesh-Ardakani, A. Nie, P.M. Marley, Y. Zhu, P.J. Phillips, S. Singh, F. Mashayek, G. Sambandamurthy, K.-B. Low, R.F. Klie, S. Banerjee, G.M. Odegard, and R. Shahbazian-Yassar, Nano Lett. **15**, 7179 (2015).
[174] C. Castellani, C.R. Natoli, and J. Ranninger, Phys. Rev. B **18**, 5001 (1978).
[175] K. Shibuya, M. Kawasaki, and Y. Tokura, Appl. Phys. Lett. **96**, 022102 (2010).
[176] X. Li, A. Gloter, A. Zobelli, H. Gu, X. Cao, P. Jin, and C. Colliex, Acta Materialia **80**, 16 (2014).
[177] Y. Wu, L. Fan, W. Huang, S. Chen, S. Chen, F. Chen, C. Zou, and Z. Wu, Physical Chemistry Chemical Physics **16**, 17705 (2014).
[178] M. NISHIKAWA, T. NAKAJIMA, T. KUMAGAI, T. OKUTANI, and T. TSUCHIYA, Journal of the Ceramic Society of Japan **119**, 577 (2011).
[179] X. Li, A. Gloter, H. Gu, X. Cao, P. Jin, and C. Colliex, Acta Materialia **61**, 6443 (2013).
[180] S. Lee, I.N. Ivanov, J.K. Keum, and H.N. Lee, Sci Rep **6**, 19621 (2016).
[181] J. Cui, Y.S. Chu, O.O. Famodu, Y. Furuya, J. Hattrick-Simpers, R.D. James, A. Ludwig, S. Thienhaus, M. Wuttig, Z. Zhang, and I. Takeuchi, Nature Materials **5**, 286 (2006).
[182] X. Chen, V. Srivastava, V. Dabade, and R.D. James, Journal of the Mechanics and Physics of Solids **61**, 2566 (2013).
[183] Y. Song, X. Chen, V. Dabade, T.W. Shield, and R.D. James, Nature **502**, 85 (2017).

[184] M. Netsianda, P.E. Ngoepe, C.R.A. Catlow, and S.M. Woodley, Chem. Mater. **20**, 1764 (2008).
[185] D. Singh, J Pers Soc Psychol **65**, 293 (1993).
[186] D.H. Kim and H.S. Kwok, Appl. Phys. Lett. **65**, 3188 (1994).
[187] A. Chen, Z. Bi, W. Zhang, J. Jian, Q. Jia, and H. Wang, Appl. Phys. Lett. **104**, (2014).
[188] M. Soltani, M. Chaker, E. Haddad, R.V. Kruzelecky, and J. Margot, Appl. Phys. Lett. **85**, 1958 (2004).
[189] D. Vernardou, M.E. Pemble, and D.W. Sheel, Chem. Vap. Deposition **13**, 158 (2007).
[190] T.-H. Yang, C. Jin, R. Aggarwal, R.J. Narayan, and J. Narayan, J. Mater. Res. **25**, 422 (2010).
[191] H.-T. Zhang, L. Zhang, D. Mukherjee, Y.-X. Zheng, R.C. Haislmaier, N. Alem, and R. Engel-Herbert, Nature Communications **6**, 1 (2017).
[192] M. Gurvitch, S. Luryi, A. Polyakov, and A. Shabalov, J. Appl. Phys. **106**, 104504 (2009).
[193] A.H. Ip, L.N. Quan, M.M. Adachi, J.J. McDowell, J. Xu, D.H. Kim, and E.H. Sargent, Appl. Phys. Lett. **106**, 143902 (2015).
[194] J. Xu, S. Dou, H. Liu, and L. Dai, Nano Energy **2**, 439 (2013).
[195] M.S. Whittingham, Chem. Rev. **104**, 4271 (2004).
[196] F. Sediri and N. Gharbi, Journal of Physics and Chemistry of Solids **68**, 1821 (2007).
[197] Q. Wang, J. Pan, M. Li, Y. Luo, H. Wu, L. Zhong, and G. Li, Journal of Materials Science & Technology **31**, 630 (2015).
[198] S. Park, C.W. Lee, J.-C. Kim, H.J. Song, H.-W. Shim, S. Lee, and D.-W. Kim, ACS Energy Lett. **1**, 216 (2016).
[199] A. Kojima, K. Teshima, Y. Shirai, and T. Miyasaka, J. Am. Chem. Soc. **131**, 6050 (2009).
[200] J.-H. Im, C.-R. Lee, J.-W. Lee, S.-W. Park, and N.-G. Park, Nanoscale **3**, 4088 (2011).
[201] H.-S. Kim, C.-R. Lee, J.-H. Im, K.-B. Lee, T. Moehl, A. Marchioro, S.-J. Moon, R. Humphry-Baker, J.-H. Yum, J.E. Moser, M. Grätzel, and N.-G. Park, Sci Rep **2**, 583 (2012).
[202] M. Liu, M.B. Johnston, and H.J. Snaith, Nature **501**, 395 (2013).
[203] H. Zhou, Q. Chen, G. Li, S. Luo, T.-B. Song, H.-S. Duan, Z. Hong, J. You, Y. Liu, and Y. Yang, Science **345**, 542 (2014).
[204] N.J. Jeon, J.H. Noh, W.S. Yang, Y.C. Kim, S. Ryu, J. Seo, and S. Il Seok, Nature **517**, 476 (2015).
[205] J.H. Noh, S.H. Im, J.H. Heo, T.N. Mandal, and S.I. Seok, Nano Lett. **13**, 1764 (2013).
[206] N. Pellet, P. Gao, G. Gregori, T.-Y. Yang, M.K. Nazeeruddin, J. Maier, and M. Grätzel, Angew. Chem. Int. Ed. **53**, 3151 (2014).
[207] Y. Ogomi, A. Morita, S. Tsukamoto, T. Saitho, N. Fujikawa, Q. Shen, T. Toyoda, K. Yoshino, S.S. Pandey, T. Ma, and S. Hayase, J. Phys. Chem. Lett. **5**, 1004 (2014).
[208] K. Tanaka, T. Takahashi, T. Ban, T. Kondo, K. Uchida, and N. Miura, Solid State Communications **127**, 619 (2003).

[209] S.D. Stranks, G.E. Eperon, G. Grancini, C. Menelaou, M.J.P. Alcocer, T. Leijtens, L.M. Herz, A. Petrozza, and H.J. Snaith, Science **342**, 341 (2013).
[210] G. Xing, N. Mathews, S. Sun, S.S. Lim, Y.M. Lam, M. Graetzel, S. Mhaisalkar, and T.C. Sum, Science **342**, 344 (2013).
[211] W.A. Laban and L. Etgar, Energy Environ. Sci. **6**, 3249 (2013).
[212] P. Gao, M. Grätzel, and M.K. Nazeeruddin, Energy Environ. Sci. **7**, 2448 (2014).
[213] G.E. Eperon, V.M. Burlakov, P. Docampo, A. Goriely, and H.J. Snaith, Adv. Funct. Mater. **24**, 151 (2013).
[214] S. Pang, H. Hu, J. Zhang, S. Lv, Y. Yu, F. Wei, T. Qin, H. Xu, Z. Liu, and G. Cui, Chem. Mater. **26**, 1485 (2014).
[215] Q. Chen, H. Zhou, Z. Hong, S. Luo, H.-S. Duan, H.-H. Wang, Y. Liu, G. Li, and Y. Yang, J. Am. Chem. Soc. **136**, 622 (2014).
[216] S.R. Raga, M.-C. Jung, M.V. Lee, M.R. Leyden, Y. Kato, and Y. Qi, Chem. Mater. **27**, 1597 (2015).
[217] A.T. Barrows, A.J. Pearson, C.K. Kwak, A.D.F. Dunbar, A.R. Buckley, and D.G. Lidzey, Energy & Environmental Science **7**, 2944 (2014).
[218] J. Burschka, N. Pellet, S.-J. Moon, R. Humphry-Baker, P. Gao, M.K. Nazeeruddin, and M. Grätzel, Nature **499**, 316 (2013).
[219] D. Liu, M.K. Gangishetty, and T.L. Kelly, Journal of Materials Chemistry a: Materials for Energy and Sustainability **2**, 19873 (2014).
[220] B. Conings, L. Baeten, C. De Dobbelaere, J. D'Haen, J. Manca, and H.-G. Boyen, Adv. Mater. **26**, 2041 (2013).
[221] M.M. Tavakoli, H. Aashuri, A. Simchi, S. Kalytchuk, and Z. Fan, J. Phys. Chem. C **119**, 18886 (2015).
[222] B.R. Sutherland, S. Hoogland, M.M. Adachi, P. Kanjanaboos, C.T.O. Wong, J.J. McDowell, J. Xu, O. Voznyy, Z. Ning, A.J. Houtepen, and E.H. Sargent, Adv. Mater. **27**, 53 (2014).
[223] T. Salim, S. Sun, Y. Abe, A. Krishna, A.C. Grimsdale, and Y.M. Lam, Journal of Materials Chemistry a: Materials for Energy and Sustainability **3**, 8943 (2015).
[224] H.M. Christen, S.D. Silliman, and K.S. Harshavardhan, Review of Scientific Instruments **72**, 2673 (2001).
[225] H. Koinuma and I. Takeuchi, Nature Materials **3**, 429 (2004).
[226] B.L. Zhu and X.Z. Zhao, Phys. Stat. Sol. (a) **208**, 91 (2010).
[227] U. Bansode, R. Naphade, O. Game, S. Agarkar, and S. Ogale, J. Phys. Chem. C **119**, 9177 (2015).
[228] J.H. Heo, S.H. Im, J.H. Noh, T.N. Mandal, C.-S. Lim, J.A. Chang, Y.H. Lee, H.-J. Kim, A. Sarkar, M.K. Nazeeruddin, M. Grätzel, and S. Il Seok, 1 (2013).
[229] M. Shkir, H. Abbas, Siddhartha, and Z.R. Khan, Journal of Physical and Chemistry of Solids **73**, 1309 (2012).
[230] W. Nie, H. Tsai, R. Asadpour, J.-C. Blancon, A.J. Neukirch, G. Gupta, J.J. Crochet, M. Chhowalla, S. Tretiak, M.A. Alam, H.-L. Wang, and A.D. Mohite, Science **347**, 522 (2015).
[231] Z. Xiao, C. Bi, Y. Shao, Q. Dong, Q. Wang, Y. Yuan, C. Wang, Y. Gao, and J. Huang, Energy Environ. Sci. **7**, 2619 (2014).
[232] J. Haruyama, K. Sodeyama, L. Han, and Y. Tateyama, J. Phys. Chem. Lett. **5**, 2903 (2014).

[233] K.M. Boopathi, M. Ramesh, P. Perumal, Y.-C. Huang, C.-S. Tsao, Y.-F. Chen, C.-H. Lee, and C.-W. Chu, Journal of Materials Chemistry a: Materials for Energy and Sustainability **3**, 9257 (2015).
[234] S. Hossain, A.M. Abdalla, S.N.B. Jamain, J.H. Zaini, and A.K. Azad, Renewable and Sustainable Energy Reviews **79**, 750 (2017).